

UNIVERSITY OF CAPE COAST



SYNTHESIS, CHARACTERIZATION AND APPLICATION OF NOVEL
METAL-ORGANIC FRAMEWORKS FOR PHOTO-TRANSFORMATION
OF ORGANIC POLLUTANTS IN WATER

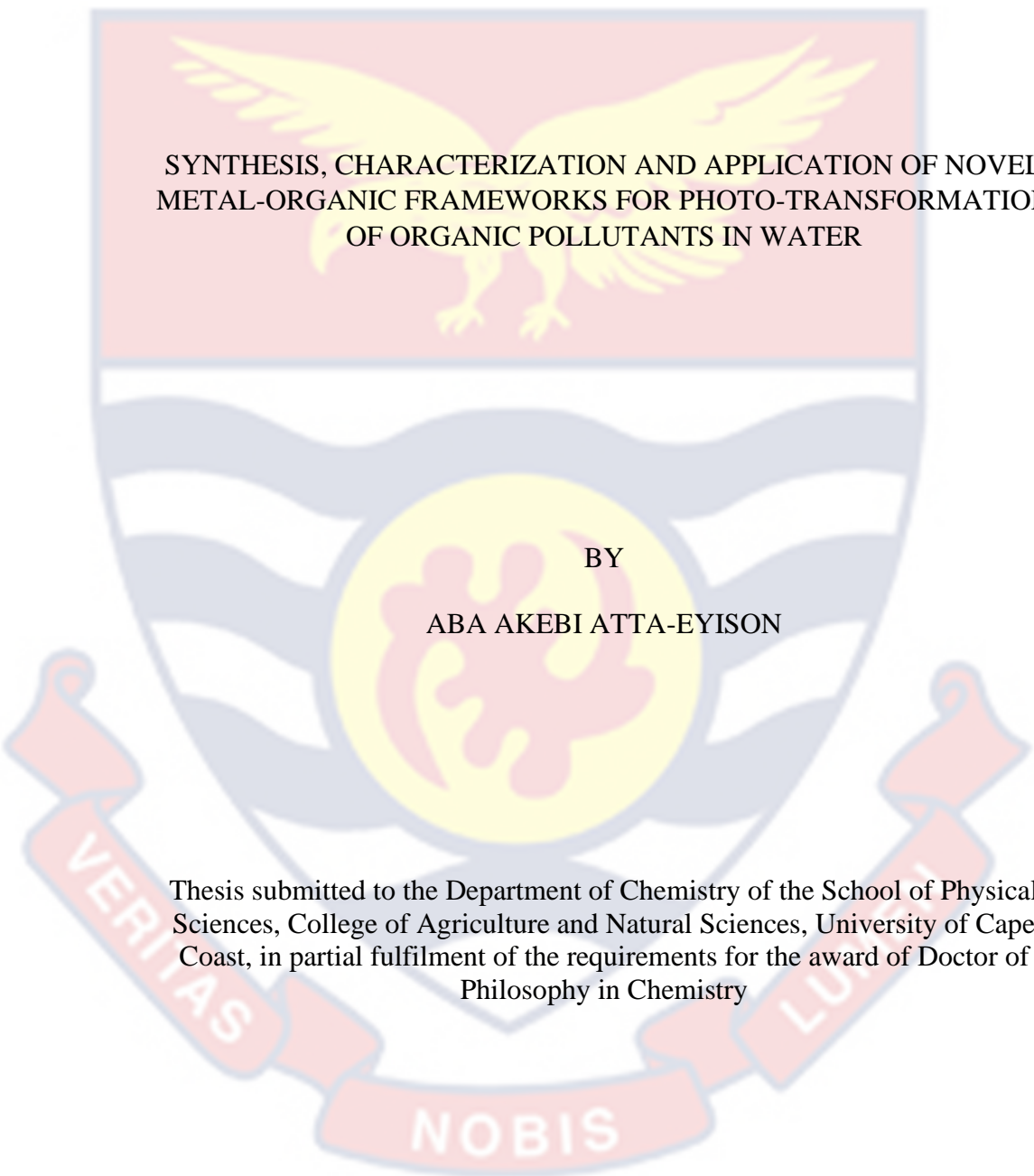
ABA AKEBI ATTA-EYISON

2023



© Aba Akebi Atta-Eyison
University of Cape Coast

UNIVERSITY OF CAPE COAST



SYNTHESIS, CHARACTERIZATION AND APPLICATION OF NOVEL
METAL-ORGANIC FRAMEWORKS FOR PHOTO-TRANSFORMATION
OF ORGANIC POLLUTANTS IN WATER

BY

ABA AKEBI ATTA-EYISON

Thesis submitted to the Department of Chemistry of the School of Physical
Sciences, College of Agriculture and Natural Sciences, University of Cape
Coast, in partial fulfilment of the requirements for the award of Doctor of
Philosophy in Chemistry

OCTOBER 2023

DECLARATION

Candidate's Declaration

I hereby declare that this thesis is the result of my own original research and that no part of it has been presented for other degree in this university or elsewhere.

Candidate's Signature..... Date.....

Name: Aba Akebi Atta-Eyison

Supervisors' Declaration

We hereby declare that the preparation and the presentation of the thesis were supervised in accordance with the guidelines on supervision of thesis laid down by University of Cape Coast.

Principal Supervisor's Signature..... Date.....

Name: Prof. Ruphino Zugle

Co-supervisor's Signature..... Date.....

Name: Dr Samuel Tetteh

ABSTRACT

The release of coloured organic pollutants from the production and application industries into water bodies is extremely worrying. Recently, metal-organic frameworks (MOFs) have attracted exceptional attention as heterogeneous catalysts in the removal of organic and inorganic pollutants through photocatalysis. As a result of this emerging technique, research to synthesize MOFs with photocatalytic functionalities to efficiently transform coloured organic pollutants found in water was studied. Six MOFs namely Zr-BTC, Zr-5abdc, Ce-BTC, Ce-5abdc, Cu-BTC and Cu-5abdc were synthesized using the solvothermal synthetic technique. The synthesized MOFs were characterized by Fourier transform infrared (FTIR) to investigate the bond formation between metals and organic ligands, by X-ray diffraction (XRD) to assess their crystallinity, by Scanning Electron Microscope-Energy Dispersive X-ray (SEM-EDX) to investigate their morphology, by Single crystallography to evaluate their topology and by Thermogravimetric analysis to assess their thermal stability. The photocatalytic activity of MOFs to transform Lissamine green SF (LGSF), Tetraethylrhodamine (TeRh), and Remezol Brilliant Violet 5R (RBV5R) into less toxic compounds was investigated. The photoactivity was subjected to three parameters which included the pH, dye concentration and catalyst loading. Various intermediates were detected from the breakdown of LGSF, TeRh, and RBV5R during their transformation using the GC/MS. The kinetics and isotherms of LGSF, TeRh, and RBV5R adsorption by the MOFs were studied. The removal activity, kinetics and isotherm study of mixed textile dye by Zr-BTC MOFs was also investigated. Conclusively, the MOFs were proven to be effective catalysts in transforming the pollutants into less toxic compounds.

KEY WORDS

Adsorption

Characterization

Light irradiation

Metal-organic frameworks

Photo-transformation

Solvothermal synthesis



ACKNOWLEDGEMENTS

I would like to express my sincere gratitude to my supervisors, Prof. Ruphino Zugle and Dr Samuel Tetteh both with the Department of Chemistry, for their time, effort, professional guidance, and understanding throughout my studies. Their availability and readiness to discuss inputs and issues to what you see as a final research output with me whenever I needed them were tremendous and have inspired me throughout my studies. I am extremely grateful to my employer Takoradi Technical University for granting me study leave with fee funding to pursue the Ph.D. study. This grant with support has aided me to complete my study within the set time frame.

I am also grateful to Dr Joseph Adjei, Prof. Michael Akrofi Anang, and Dr Robertson Akrofi for their technical assistance and encouragement throughout my research. I extend my appreciation to the various laboratory analysts and technicians, Madam Linda Osei, Madam Beatrice Agyapomah, Madam Gloria Manu, Mr Danial Nimarko Amprako, Madam Benedicta Egoh, Madam Elizabeth Davordzi, and Mr Mandela Toku, for their invaluable technical feedbacks and interpretation of the research analytical results obtained. I thank Madam Alberta Dayie, Mr Jesse Azebiik Anak, and Mr Justice Hayfron for the assistance they rendered during my laboratory work and the writing of my thesis.

Finally, I wish to thank the Almighty God for the grace, guidance, and protection granted me, as well as my family, especially, my husband, Brian Atta-Eyison, my parents Dr John Kofi Borsah and Mrs Elizabeth Nana Borsah, as well as my mother-in-law, Madam Hannah Annan for their unwavering support throughout my study.

DEDICATION

To my husband, Brian Atta-Eyison, my parents, Dr John Kofi Borsah and Mrs Elizabeth Nana Borsah, my mother-in-law, Hannah Annan and my children.



TABLE OF CONTENTS

	Page
DECLARATION	ii
ABSTRACT	iii
KEY WORDS	iv
ACKNOWLEDGEMENTS	v
DEDICATION	vi
LIST OF TABLES	xiv
LIST OF FIGURES	xvii
LIST OF SYMBOLS	xxv
LIST OF CHEMICAL SYMBOLS	xxvi
LIST OF ABBREVIATIONS	xxvii
CHAPTER ONE: INTRODUCTION	
Background of the Study	1
Statement of the Problem	8
Purpose of the Study	11
Research Objectives	11
Significance of the Study	12
Delimitations	13
Limitations	15
Definition of Terms	15
Organization of the Study	16
CHAPTER TWO: LITERATURE REVIEW	
Introduction	18
Coordination Polymers	18
Metal-Organic Frameworks	20

Building Units of Metal-Organic Framework	25
Metal for Metal-Organic Frameworks	26
Organic Ligands for Metal-Organic Framework	29
Metal-Organic Frameworks Constructed from Carboxylate Ligands	30
Benzene-1, 3, 5- tricarboxylic acid (H ₃ BTC)	32
5-Amino benzene -1, 3 - dicarboxylic acid	34
Copper Base Metal-Organic Framework	36
Cerium-Based Metal-Organic Framework	38
Zirconium-Based Metal-Organic Framework	40
Solvothermal Synthesis of Metal-Organic Framework	42
Synthetic Condition in Solvothermal Technique	45
The role of the solvent in solvothermal processes	46
The role of the counter ion of the reactants in solvothermal processes	47
The role of modulators used in solvothermal processes	48
The role of the pH value in different solvothermal processes	50
The role of the temperature of the reactants in solvothermal processes	51
The role of the pressure of the reactants in solvothermal processes	53
Metal-Organic Frameworks (MOFs) as Heterogeneous Catalysts	53
Coloured Organic Pollutants in Water	55
MOF as Photocatalyst	58
Mechanism of Metal-Organic Frameworks as Heterogeneous Photocatalyst for Organic Pollutant Degradation	60
Chapter Summary	63
CHAPTER THREE: RESEARCH METHODS	
Introduction	65
Reagents and Chemicals	65

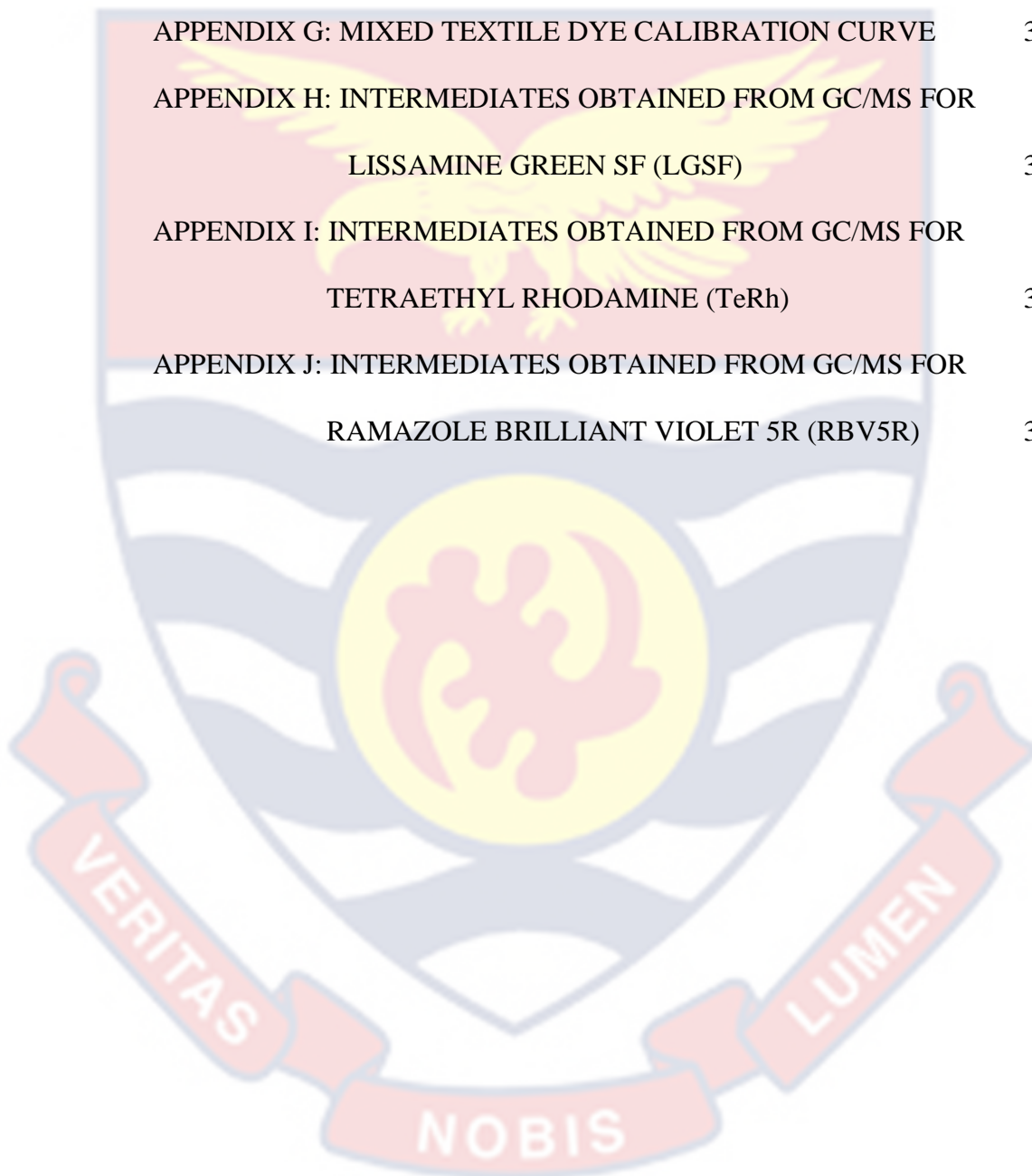
Instrumentation	66
Hydrothermal autoclave	67
Magnetic stirrer hot plate	67
Oven	68
Centrifuge	69
Fourier transform infrared (FTIR) spectrometer	70
X-ray diffractometer (XRD)	71
Thermogravimetric analyzer (TGA)	71
Scanning electron microscope-energy dispersive spectrometer (SEM-EDS)	72
Single crystal diffractometer	72
Photocatalytic system	72
The pH meter	73
Spectrophotometer	73
Gas chromatography/mass spectrum (GC/MS)	74
Synthesis of Metal-Organic Frameworks	74
Synthesis of copper metal-organic frameworks	75
Synthesis of cerium metal-organic frameworks	75
Synthesis of zirconium metal-organic framework	76
Characterization Analysis of Synthesized Metal-Organic Frameworks	77
Functional group and bond formation analysis	77
Crystal phase analysis	78
Morphology and elemental analysis	78
Single crystallography analysis	79
Thermal stability analysis	79
Coloured Organic Pollutant Transformation Analysis	80
Parameter Variation Analysis	80

Catalyst amount variation analysis	81
Pollutant concentration variation analysis	81
Solution pH variation analysis	81
Adsorption and Kinetic Study	81
Adsorption Isotherms	84
GC-MS Analysis	86
Quality Control Methodology	86
Chapter Summary	87
CHAPTER FOUR: RESULTS AND DISCUSSION	
Introduction	88
Synthesized Metal-Organic Framework	88
Characterization of Synthesized Metal-Organic Framework	92
Fourier Transform Infrared (FTIR) Analysis of Organic Linkers and Synthesized Metal-Organic Framework	92
Fourier transform infrared analysis of organic linkers	93
Fourier transform infrared (FTIR) analysis of metal-organic frameworks formed with 5-aminobenzene-1, 3-dicarboxylic acid	96
Fourier transform infrared (FTIR) analysis of metal-organic frameworks formed with 1, 3, 5- benzene tricarboxylic acid	100
X-ray diffraction (XRD) Analysis of Organic Linkers and Synthesized Compounds	103
X-ray diffraction (XRD) analysis of organic linkers	103
X-ray diffraction (XRD) analysis of metal-organic framework formed with 5-aminobenzene-1, 3-dicarboxylic acid	104
X-ray diffraction (XRD) analysis of metal-organic framework formed with 1, 3, 5-benzene tricarboxylic acid	107

SEM-EDS Analysis of Organic Linkers and Synthesized Metal-Organic Frameworks	110
SEM-EDS analysis of organic linker	111
SEM-EDS analysis of metal-organic framework formed with 5-aminobenzene-1, 3-dicarboxylic acid	113
SEM-EDS analysis of metal-organic framework formed with 1, 3, 5-benzene tricarboxylic acid	116
Single Crystallography Analysis of Synthesized Cu-BTC Metal-Organic Framework	120
Thermogravimetric (TGA) Analysis of Synthesize Metal-Organic Frameworks	121
Thermogravimetric analysis (TGA) of copper metal-organic frameworks	121
Thermogravimetric analysis (TGA) of cerium metal-organic frameworks	124
Thermogravimetric analysis (TGA) of zirconium metal-organic frameworks	127
Photoactivity of Metal-Organic Framework on Selected Pollutants	129
Metal Organic-Framework Amount Variation Analysis on Selected Pollutants	134
Pollutant Concentration Variation Analysis under Photocatalysis	139
Results of the pH Variation of Pollutants under Photocatalysis	144
Kinetic and Isotherm Study on the Adsorption of Coloured Organic Pollutants by Cu-5abdc, Ce-5abdc and Zr-5abdc MOFs	149
Kinetic and Isotherm Study on the Adsorption of Coloured Organic Pollutants by Cu-BTC, Ce-BTC and Zr-BTC MOFs	168

Kinetic Study on the Removal of Coloured Organic Pollutants at Optimum Parameter Set Conditions	187
Intermediates Obtained from the Pollutant Transformation Process	197
Photoactivity of Zr-BTC on Industrial Mixed Textile Dye	201
Effect of Initial Dye Concentration on Rate Adsorption of Mixed Textile Dye by Zr-BTC	203
Chapter Summary	208
CHAPTER FIVE: SUMMARY, CONCLUSIONS AND RECOMMENDATIONS	
Overview	209
Summary	209
Conclusion	214
Recommendations	215
REFERENCES	217
APPENDICES	311
APPENDIX A: UV-VISIBLE ABSORPTION SPECTRA OF LISSAMINE GREEN SF (LGSF) AT 640 nm UNDER PHOTODEGRADATION	311
APPENDIX B: UV-VISIBLE ABSORPTION SPECTRA OF TETRAETHYLRHODAMINE (TeRh) AT 554 nm UNDER PHOTODEGRADATION	312
APPENDIX C: UV-VISIBLE ABSORPTION SPECTRA OF RAMAZOLE BRILLIANT VIOLET 5R (RBV5R) AT 540 nm UNDER PHOTODEGRADATION.	313
APPENDIX D: LISSAMINE GREEN SF (LGSF) CALIBRATION CURVE	314

APPENDIX E: TETRAETHYLRHODAMINE (TeRh) CALIBRATION CURVE	315
APPENDIX F: RAMAZOLE BRILLIANT VIOLET 5R (RBV5R) CALIBRATION CURVE	316
APPENDIX G: MIXED TEXTILE DYE CALIBRATION CURVE	317
APPENDIX H: INTERMEDIATES OBTAINED FROM GC/MS FOR LISSAMINE GREEN SF (LGSF)	318
APPENDIX I: INTERMEDIATES OBTAINED FROM GC/MS FOR TETRAETHYL RHODAMINE (TeRh)	321
APPENDIX J: INTERMEDIATES OBTAINED FROM GC/MS FOR RAMAZOLE BRILLIANT VIOLET 5R (RBV5R)	324



LIST OF TABLES

	Page
1	Some Commonly used Organic Dyes that Pollute Water 57
2	List of Reagents and Chemicals Employed in the Present Study 65
3	The Parameters for Pseudo-first-order Adsorption Kinetics of Cu-5abdc, Ce-5abdc and Zr-5abdc for for LGSF at Varying Concentration 150
4	The Parameters for Pseudo-second-order Adsorption Kinetics of Cu-5abdc, Ce-5abdc and Zr-5abdc for for LGSF at Varying Concentration 152
5	The Parameters from Langmuir and Freundlich Isotherms of Cu-5abdc, Ce-5abdc and Zr-5abdc for LGSF 154
6	The Parameters for Pseudo-first-order Adsorption Kinetics of Cu-5abdc, Ce-5abdc and Zr-abdc for TeRh at Varying Concentration 157
7	The Parameters for Pseudo-second-order Adsorption Kinetics of Cu-5abdc, Ce-abdc and Zr-abdc for TeRh at Varying Concentration 159
8	The Parameters from Langmuir and Freundlich Isotherms of Cu-5abdc, Ce-5abdc and Zr-5abdc for TeRh 161
9	The Parameters for Pseudo-first-order Adsorption Kinetics of Cu-5abdc, Ce-5abdc and Zr-5abdc for RBV5R at Varying Concentration 163
10	The Parameters for Pseudo-second-order Adsorption Kinetics of Cu-5abdc, Ce-5abdc and Zr-5abdc for RBV5R at Varying Concentration 165

11	The Parameters from Langmuir and Freundlich Isotherms of Cu-5abdc, Ce-5abdc and Zr-5abdc for RBV5R	167
12	The Parameters for Pseudo-first-order Adsorption Kinetics of Cu-BTC, Ce-BTC and Zr-BTC for LGSF at Varying Concentration	170
13	The Parameters for Pseudo-second-order Adsorption Kinetics of Cu-BTC, Ce-BTC and Zr-BTC for LGSF at Varying Concentration	172
14	The Parameters from Langmuir and Freundlich Isotherms of Cu-BTC, Ce-BTC and Zr-BTC for LGSF	174
15	The Parameters for Pseudo-first-order Adsorption Kinetics of Cu-BTC, Ce-BTC and Zr-BTC for TeRh at Varying Concentration	176
16	The Parameters for Pseudo-second-order Adsorption Kinetics of Cu-BTC, Ce-BTC and Zr-BTC for TeRh at Varying Concentration	178
17	The Parameters from Langmuir and Freundlich Isotherms of Cu-BTC, Ce-BTC and Zr-BTC for TeRh	180
18	The Parameters for Pseudo-first-order Adsorption Kinetics of Cu-BTC, Ce-BTC and Zr-BTC for RBV5R at Varying Concentration	182
19	The Parameters for Pseudo-second-order Adsorption Kinetics of Cu-BTC, Ce-BTC and Zr-BTC for RBV5R at Varying Concentration	184
20	The Parameters from Langmuir and Freundlich Isotherms of Cu-BTC, Ce-BTC and Zr-BTC for RBV5R	186

21	The Parameters for Pseudo-first-order Adsorption Kinetics of LGSF	189
22	The Parameters for Pseudo-second-order Adsorption Kinetics of LGSF	190
23	The Parameters for Pseudo-first-order Adsorption Kinetics of TeRh	192
24	The Parameters for Pseudo-second-order Adsorption Kinetics of TeRh	193
25	The Parameters for Pseudo-first-order Adsorption Kinetics of RBV5R	195
26	The Parameters for Pseudo-second-order Adsorption Kinetics of RBV5R	196
27	Summary of Intermediates after 180 min Photoactivity on LGSF	198
28	Summary of Intermediates after 180 min Photoactivity on TeRh	199
29	Summary of Intermediates after 180 min Photoactivity on RBV5R	201
30	The Parameters for Pseudo-first-order and Pseudo-second-order Adsorption Mixed Textile Dye (MTD) by Zr-BTC	205
31	The Parameters from Langmuir Isotherms for Mixed Textile Dye (MTD)	206
32	The Parameters from Freundlich Isotherms for Mixed Textile Dye (MTD)	208

LIST OF FIGURES

		Page
1	The different dimensional structures of coordination polymers	19
2	The self-assembly of a three-dimensional metal-organic framework	21
3	The structural framework of MOF-5	22
4	Metal-organic framework publications from 2000 to 2020	23
5	Representative of building units and the related building blocks of metal-organic frameworks	25
6	A representative of categories of organic ligands	30
7	Different binding modes of a metal with a carboxylate ligand. (a) ionic state (b); Monodentate (c); Bidentate(d); Syn-syn bridging (e); Anti-anti bridging (f); Anti-syn bridging	31
8	The structure of Benzene-1, 3, 5- tricarboxylic acid	33
9	The structure of 5-aminobenzene -1, 3 – dicarboxylic acid	35
10	Development of synthetic techniques used for the formation of MOFs.	43
11	Comparison of the use of the solvothermal synthetic technique and other synthetic techniques for the synthesis of MOFs	44
12	The solvothermal procedure for the synthesis of MOFs	45
13	Formation of MOF-2 and MOF-5 crystals	52
14	Structural motifs of MOFs used for photocatalysis	60
15	Mechanism of photocatalytic dye degradation	63
16	Hydrothermal autoclave	67
17	Heidolph MR Hei-Standard magnetic stirrer hot plate	68
18	Ecocell 55 oven	69

19	VWR [®] Mega Star 600 centrifuge	70
20	Images of synthesized Cu-5abdc (a) before activation (b) after activation	89
21	Images of synthesized Cu-BTC (a) before activation (b) after activation	89
22	Images of synthesized Ce-5abdc (a) before activation (b) after activation	90
23	Images of synthesized Ce-BTC (a) before activation (b) after activation	90
24	Images of synthesized Zr-5abdc (a) before activation (b) after activation	91
25	Images of synthesized Zr-BTC (a) before activation (b) after activation	91
26	FTIR of 5-Aminobenzene-1, 3-dicarboxylic acid (H ₂ 5abdc)	93
27	FTIR of benzene -1, 3, 5- tricarboxylic acid (H ₃ BTC)	95
28	FTIR comparison of 5-aminobenzene-1, 3-dicarboxylic acid and synthesized MOFs ((a) H ₂ 5abdc; (b) Cu-5abdc; (c) Ce-5abdc and (d) Zr-5abdc)	97
29	Proposed structure formation of Cu-5abdc, Ce-5abdc and Zr-5abdc MOFs (M: Cu, Ce, Zr)	99
30	FTIR comparison of 1, 3, 5- benzene tricarboxylic acid and synthesized MOFs ((a) H ₃ BTC; (b) Cu-BTC; (c) Ce-BTC; (d) Zr-BTC)	101
31	Proposed structure formation of Cu-BTC, Ce-BTC and Zr-BTC MOFs (M: Cu, Ce, Zr)	102
32	XRD of 5-aminobenzene-1, 3-dicarboxylic acid (H ₂ 5abdc)	103

33	XRD of 1, 3, 5- benzene tricarboxylic acid (H ₃ BTC)	104
34	XRD of (a) 5-aminobenzene-1, 3-dicarboxylic acid (H ₂ 5abdc) and (b) synthesized Cu-5abdc	105
35	XRD of (a) 5-aminobenzene-1, 3-dicarboxylic acid (H ₂ 5abdc) and (b) synthesized Ce-5abdc	106
36	XRD of (a) 5-aminobenzene-1, 3-dicarboxylic acid (H ₂ 5abdc) and (b) synthesized Zr-5abdc	107
37	XRD of (a) 1, 3, 5-benzene tricarboxylic acid and (b) synthesized Cu-BTC	108
38	XRD of (a); 1, 3, 5-benzene tricarboxylic acid and (b); synthesized Ce-BTC	109
39	XRD of (a); 1, 3, 5-benzene tricarboxylic acid and (b); synthesized Zr-BTC	110
40	SEM image of 5-aminobenzene-1, 3-dicarboxylic acid (H ₂ 5abdc)	111
41	EDS of 5-aminobenzene-1, 3-dicarboxylic acid (H ₂ 5abdc)	112
42	SEM image of 1, 3, 5- Benzene tricarboxylic acid (H ₃ BTC)	112
43	EDS of 1, 3, 5- Benzene tricarboxylic acid (H ₃ BTC)	113
44	SEM image of synthesized Cu-5abdc	113
45	EDS synthesized of Cu-5abdc	114
46	SEM image of synthesized Ce-5abdc	114
47	EDS of synthesized Ce-5abdc	115
48	SEM image of synthesized Zr-5abdc	115
49	EDS of synthesized Zr-5abdc	116
50	SEM images of synthesized Cu-BTC	117
51	EDS of synthesized Cu-BTC	117
52	SEM images of synthesized Ce-BTC	118

53	EDS of synthesized Ce-BTC	118
54	SEM image of synthesized Zr-BTC	119
55	EDS of synthesized Zr-BTC	119
56	A grown view of the copper complex found within Cu-BTC	120
57	A 3D network of Cu-BTC metal-organic framework	121
58	TGA-DSC of synthesized Cu-5abdc	122
59	TGA-DSC of synthesized Cu-BTC	123
60	TGA-DSC of synthesized Ce-5abdc	125
61	TGA-DSC of synthesized Ce-BTC	126
62	TGA-DSC of synthesized Zr-5abdc	128
63	TGA-DSC of synthesized Zr-BTC	129
64	Percentage removal of Lissamine green SF (LGSF) under (a) white light and (b) solar light ([LGSF] = 0.2 g/L; MOF loading = 0.010 g/L; Solution pH = 6).	130
65	Percentage removal of Tetraethylrhodamine (TeRh) under (a) white light and (b) solar light ([TeRh] = 0.20 g/L; Photocatalyst loading = 0.010 g/L; Solution pH = 8)	132
66	Percentage removal of Ramazole Brilliant Violet 5R (RBV5R under (a) white light and (b) solar light ([RBV5R] = 0.2 g/L; Photocatalyst loading = 0.010 g/L; Solution pH = 6).	133
67	Effect of MOF loading on Lissamine green SF (LGSF) removal ([LGSF] = 0.20 g/L; Solution pH = 6).	135
68	Effect of MOF loading on Tetraethylrhodamine (TeRh) removal ([TeRh] = 0.20 g/L; Solution pH = 8).	137

69	Effect of MOF loading on Ramazole Brilliant Violet 5R (RBV5R) removal ([RBR5R] = 0.20 g/L; Solution pH = 6).	138
70	Effect of Lissamine green SF (LGSF) concentration variation on photoactivity (MOF Loading = 0.010 g/L; Solution pH = 6).	140
71	Effect of Tetraethylrhodamine (TeRh) concentration variation on photoactivity (MOF Loading = 0.010 g/L; Solution pH = 8).	141
72	Effect of Ramazole Brilliant Violet 5R (RBV5R) concentration variation on photoactivity (MOF Loading = 0.010 g/L; Solution pH = 6).	142
73	Effect of solution pH on Lissamine green SF (LGSF) percentage removal (MOFs Loading = 0.010 g/L; [LGSF] = 0.20 g/L).	144
74	Effect of solution pH on Tetraethylrhodamine (TeRh) percentage removal (MOFs Loading = 0.010 g/L; [TeRh] = 0.20 g/L).	146
75	Effect of solution pH on Ramazole Brilliant Violet 5R (RBV5R) percentage removal (MOFs Loading=0.10 g/L; [RBV5R] = 0.20 g/L).	147
76	Pseudo-first-order graph for the adsorption of LGSF by Cu-5abdc, Ce-5abdc and Zr-5abdc (MOF loading = 0.1g/L, Solution pH = 6).	149
77	Pseudo-second-order graph for the adsorption of LGSF by Cu-5abdc, Ce-5abdc and Zr-5abdc (MOF loading = 0.1g/L, Solution pH = 6).	151
78	The Langmuir isotherm for the adsorption of LGSF by Cu-5abdc, Ce-5abdc and Zr-5abdc	153
79	The Freundlich isotherm for the adsorption of LGSF by Cu-5abdc, Ce-5abdc and Zr-5abdc	153

80	Pseudo-first-order graph for the adsorption of TeRh by Cu-5abdc, Ce-5abdc and Zr-5abdc (MOF loading = 0.1g/L, Solution pH = 8)	156
81	Pseudo-second-order graph for the adsorption of TeRh by Cu-5abdc, Ce-5abdc and Zr-5abdc (MOF loading = 0.1g/L, Solution pH = 8).	158
82	The Langmuir isotherm for the adsorption of TeRh by Cu-5abdc, Ce-5abdc and Zr-5abdc	160
83	The Freundlich isotherm for the adsorption of TeRh by Cu-5abdc, Ce-5abdc and Zr-5abdc	160
84	Pseudo-first-order graph for the adsorption of RBV5R by Cu-5abdc, Ce-5abdc and Zr-5abdc (MOF loading = 0.1g/L, Solution pH = 6)	162
85	Pseudo-second-order graph for the adsorption of RBV5R by Cu-5abdc, Ce-5abdc and Zr-5abdc (MOF loading = 0.1g/L, Solution pH = 6).	164
86	The Langmuir isotherm for the adsorption of RBV5R by Cu-5abdc, Ce- 5abdc and Zr-5abdc	166
87	The Freundlich isotherm for the adsorption of RBV5R by Cu-5abdc, Ce-5abdc and Zr-5abdc	166
88	Pseudo-first-order graph for the adsorption of LGSF by Cu-BTC, Ce-BTC and Zr-BTC (MOF loading = 0.1g/L, Solution pH = 6).	169
89	Pseudo-second-order graph for the adsorption of LGSF by Cu-BTC, Ce-BTC and Zr-BTC (MOF loading = 0.1g/L, Solution pH = 6).	171
90	The Langmuir isotherm for the adsorption of LGSF by Cu-BTC, Ce-BTC and Zr-BTC	173

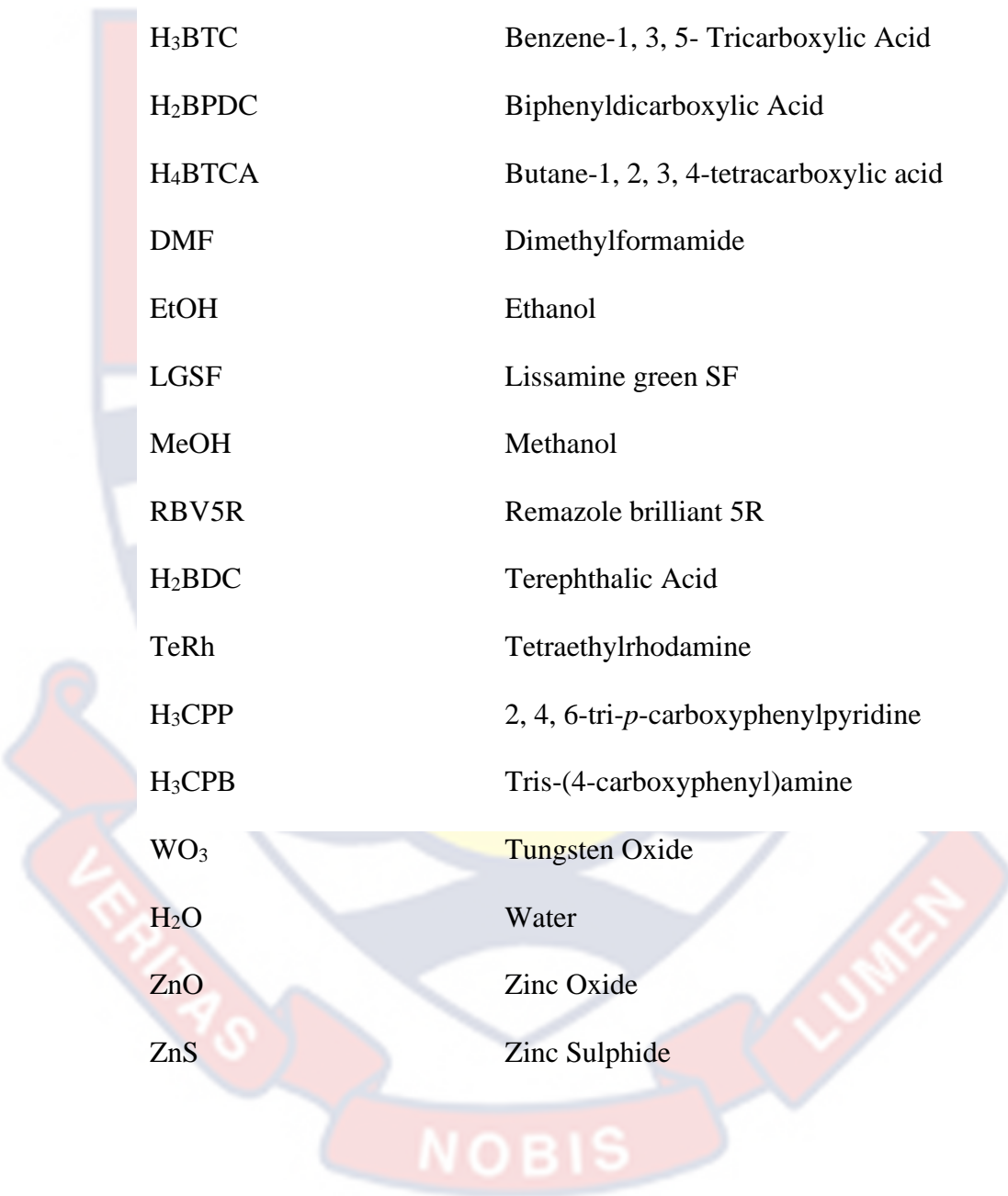
91	The Freundlich isotherm for the adsorption of LGSF by Cu-BTC, Ce-BTC and Zr-BTC	173
92	Pseudo-first-order graph for the adsorption of TeRh by Cu-BTC, Ce-BTC and Zr-BTC (MOF loading = 0.1g/L, Solution pH = 6).	175
93	Pseudo-second-order graph for the adsorption of TeRh by Cu-BTC, Ce-BTC and Zr-BTC (MOF loading = 0.1g/L, Solution pH = 6).	177
94	The Langmuir isotherm for the adsorption of TeRh by Cu-BTC, Ce-BTC and Zr-BTC	179
95	The Freundlich isotherm for the adsorption of TeRh by Cu-BTC, Ce-BTC and Zr-BTC	179
96	Pseudo-first-order graph for the adsorption of RBV5R by Cu-BTC, Ce-BTC and Zr-BTC (MOF loading = 0.1g/L, Solution pH = 6).	181
97	Pseudo-second-order graph for the adsorption of RBV5R by Cu-BTC, Ce-BTC and Zr-BTC (MOF loading = 0.1g/L, Solution pH =6).	183
98	The Langmuir isotherm for the adsorption of RBV5R by Cu-BTC, Ce- BTC and Zr-BTC	185
99	The Freundlich isotherm for the adsorption of RBV5R by Cu-BTC, Ce-BTC and Zr-BTC	185
100	Pseudo-first-order graph for the adsorption of LGSF by MOFs ([LGSF] = 0.20 g/L, MOF loading = 0.01g/L, Solution pH =6)	188
101	Pseudo-second-order graph for the adsorption of LGSF by MOFs ([LGSF] = 0.20 g/L, MOF loading = 0.1g/L, Solution pH = 6)	189

102	Pseudo-first-order graph for the adsorption of TeRh by MOFs ([TeRh] = 0.20 g/L, MOF loading = 0.1g/L, Solution pH = 6).	191
103	Pseudo-second-order graph for the adsorption of TeRh by MOFs ([TeRh] = 0.20 g/L, MOF loading = 0.1g/L, Solution pH = 8)	192
104	Pseudo-first-order graph for adsorption of RBV5R by MOFs ([RBV5R] = 0.20 g/L, MOF loading = 0.1g/L, Solution pH = 6)	194
105	Pseudo-second-order graph for the adsorption of RBV5R by MOFs ([RBV5R] = 0.20 g/L, MOF loading = 0.1g/L, Solution pH = 6)	195
106	Effect of MTD concentration variation on removal activity of Zr-BTC (Zr-BTC Loading = 0.10 g/L; Solution pH = 6.2).	202
107	UV-visible absorption spectra showing the reduction of a mixed textile dye from water ([dye] =0.10 g/L; Zr-BTC amount = 0.010 g/L; Solution pH = 6.2).	203
108	Pseudo-first-order graph for the removal of MTD by Zr-BTC (Zr-BTC loading = 0.1g/L, Solution pH = 8)	204
109	Pseudo-second-order graph for the removal of MTD by Zr-BTC (Zr-BTC loading = 0.1g/L, Solution pH = 8)	204
110	The Langmuir-Hinshelwood isotherm for the removal of MTD by Zr-BTC	206
111	The Freundlich isotherm for the removal of MTD by Zr-BTC	207

LIST OF SYMBOLS

E_{abs}	Absorbed Energy
E_{LMCT}	Ligand LUMO/Metal LUMO transition energy
K_f	Adsorption capacity constant
E_g	Band Gap Energy
R^2	Coefficient of Linear Correlation
C_t	Concentration at a given time
C_i	Initial Concentration
C_e	Concentration at Equilibrium
q_t	Adsorbed Concentration at a given time
q_e	Adsorbed Concentration at equilibrium
K	Rate Constant
n	Adsorption Energy Constant
Q_0	Maximum Adsorption Capacity Constant
h^+	Positive Hole
K_L	Langmuir Reaction Rate Constant

LIST OF CHEMICAL SYMBOLS



H ₂ -5abdc	5-Amino-1, 3-Benzene Dicarboxylic acid
H ₂ ADC	Anthracenedicarboxylic Acid
H ₂ ABDC	Azobenzene Dicarboxylic Acid
H ₃ BTC	Benzene-1, 3, 5- Tricarboxylic Acid
H ₂ BPDC	Biphenyldicarboxylic Acid
H ₄ BTCA	Butane-1, 2, 3, 4-tetracarboxylic acid
DMF	Dimethylformamide
EtOH	Ethanol
LGSF	Lissamine green SF
MeOH	Methanol
RBV5R	Remazole brilliant 5R
H ₂ BDC	Terephthalic Acid
TeRh	Tetraethylrhodamine
H ₃ CPP	2, 4, 6-tri- <i>p</i> -carboxypyridine
H ₃ CPB	Tris-(4-carboxyphenyl)amine
WO ₃	Tungsten Oxide
H ₂ O	Water
ZnO	Zinc Oxide
ZnS	Zinc Sulphide

LIST OF ABBREVIATIONS

AB	Acid/Base
AOP	Advanced Oxidation Process
ATR	Attenuated Total Reflection
BOD	Biochemical Oxygen Demand
CB	Conduction Band
COD	Chemical Oxygen Demand
EDS	Energy-Dispersive X-ray Spectroscopy
FTIR	Fourier Transform Infrared
GC	Gas Chromatography
L-H	Langmuir-Hinshelwood
LMCT	Ligand-to-Metal Charge Transfer
LUMO	Unoccupied Molecular Orbital
MOFs	Metal-Organic Frameworks
MOPs	Metal-Organic Polyhedrons
MS	Mass Spectrometry
PCPs	Porous Coordination Polymers
POMs	Polyoxometalates
SEM	Scanning Electron Microscope
SBU	Secondary-Building Unit
TGA	Thermogravimetric Analysis
UV	Ultraviolet
VB	Valence Band
VIS	Visible
XRD	X-Ray Diffraction

CHAPTER ONE

INTRODUCTION

Recently, metal-organic frameworks (MOFs) have proven and aroused outstanding attention in the area of catalysis. Metal-organic frameworks (MOFs) are complexes of porous coordination polymers consisting of metal cations (inorganic nodules) linked to ligands (organic linkers) to form extended one, two or three-dimensional metal-ligand networks. The wide variety of organic linkers and metals available for the formation of MOFs enables them to be tuned as heterogeneous photocatalysts. These frame networks yield complexes with exceptional properties such as effective donor-acceptor interface, huge surface area, great active sites and structural diversities which makes them promising as heterogeneous catalysts for catalysis. Most of these catalytic processes with MOFs as catalysts are simple, environmentally friendly and can be carried out under ambient temperature and pressure. Based on their rich properties, MOFs can be formed as heterogeneous photocatalysts to transform organic pollutants such as dyes in water under environmentally friendly conditions into less toxic substances.

Background of the Study

The fabrication of porous materials for industrial applications has been an interesting research subject. This is due to the additional surface area the pores give to these materials and the ability of the pores to host guest molecules for diverse functionalities. There are different types of materials with different pore sizes. These materials have the ability to carefully select which small particles they can hold inside their pores (Kitagawa, 2017;

Siegelman, Kim & Long, 2021; Singh, et al., 2020; Yang, et al., 2017). Three categories based on the sizes of the pores of these materials are known. These categories include microporous (tiny holes) with sizes less than 20 Å (2nm) in diameter, mesoporous (medium-sized holes) with sizes greater than 20 Å (2nm) but less than 500 Å (50nm) in diameter, and macroporous (large holes) with sizes greater than 500 Å (50nm) in diameter (Cychosz, Guillet-Nicolas, García-Martínez & Thommes, 2017; Engström, et al., 2013; Huskić, Pekov, Krivovichev & Frišćić, 2016; Schlumberger, & Thommes, 2021)

There is a wide range of materials that have different levels of porosity. These materials range from zeolites, aluminophosphates, and germanates, which are microporous to porous siliceous materials and ceramics that have macro pores. Different types of functional groups can be added directly to these porous structures, however, this can sometimes be difficult for zeolites. Zeolites contain an ordered arrangement of aluminium and silicon compounds. Consequently, zeolites have restrictions on their size and limited options to add complex features to their structure due to their ordered inorganic nature (Koohsaryan, & Anbia, 2016; Opanasenko, 2018; Weissenberger, Machoke, Reiprich, & Schwieger, 2021). Porous siliceous materials, on the other hand, have over 100 Å (10 nm) pore sizes that can take up enzymes. However, these materials have walls that are amorphous which makes their characterization study difficult. In addition, the wide pores can make it difficult to control the occupancy of guests and there are limits to the pores' functional tunability. (Engström, et al., 2013; Furukawa, Cordova, O'Keeffe, & Yaghi, 2013; Kumar, Malik, & Purohit, 2017; Varga, 2016).

Metal-organic frameworks (MOFs) which are porous coordination polymers (PCPs) are special types of porous materials made from metals and multidentate organic ligands (Chen, Kirlikovali, Li, & Farha, 2022; Feizbakhsh Bazargani, 2019; Liu, et al., 2021). They are usually crystalline and have a structure similar to zeolites. MOFs are mostly mesoporous compounds having pore sizes ranging between 20 Å and 500 Å (AlKaabi, Wade & Dincă, 2016; Li et al., 2020; Liu, Zou, Zhu, & Zhang, 2018). The adsorption capacity and selectivity of porous material are associated with the particular surface area and surface chemistry of the material. MOFs have been found to have a higher surface area of 1500–7000 m²/g range per unit weight compared with that of zeolites which is up to 1500 m²/g which makes them potentially have higher adsorption capacity. It is presently seen as having ultra-high porosity with as high as 90% of free volume (Senkovska, & Kaskel, 2014).

The systematic tuning of MOFs' pore size, pore shape, network topology, and surface functionalities allows for the customization of their structures and properties to meet the demands of particular applications, such as gas adsorption, storage processes, separation processes, catalysis among others. (Mahreni, & Ristianingsih, 2020; Soni, Bajpai, & Arora, 2020; Tombesi, & Pettinari, 2021; Zheng et. al., 2019). The crystal structure of MOFs has a specific arrangement of atoms. This arrangement can often be determined and connected to the observed properties of the material. MOFs, therefore, have systematic structures that can be identified through crystallography (Allendorf, Stavila, Witman, Brozek, & Hendon, 2021; Bloch, Champness, & Doonan, 2015; Moghadam, et al., 2017).

MOFs are known for their ability to trap and separate different molecules due to their high porosity. The strong structural nature and the functional tunability of MOFs have led to the fast growth of research in the field of porous coordination polymers (PCPs) and have, consequently, become one of the rapidly growing areas explored in chemistry (Chen, et al., 2022; Sánchez-Serratos, Álvarez, González-Zamora, & Ibarra, 2016). The largest reported surface area of MOFs so far is more than 6,000 square meters per gram. The stability of the pores associated with MOFs makes them reliable for a variety of applications.

MOFs with empty spaces that stay empty even after removing other foreign substances can have larger empty spaces that can allow larger molecules to move freely. Usually, the space inside a MOF crystal is more than half of its volume. The surfaces of the space inside a MOF can cover an area between 1,000 and 10,000 m²/g (Furukawa, Cordova, O’Keeffe, & Yaghi, 2013; Varga, 2016). The exceptional porosity has given MOFs the nickname of "Swiss-cheese-like materials" (Peplow, 2015; Varga, 2016). Additionally, because organic linkers are part of the forming structures of MOFs, a wide range of compounds can be incorporated inside these pores through organic synthesis (Jiao, Wang, Jiang & Xu, 2018; Vakili, 2020). This has been very helpful in making MOFs more useful because the inner surface can be customized to fit specific guests. Another benefit is the ability to adjust the organic linkers to make different MOFs with larger pores, but still have the same structure (Furukawa, et al., 2013; Yaghi, 2019). The availability of a large variety of organic linkers and metals produces different MOFs with diverse properties for a variety of applications.

Rigid MOFs having persistent porosity and substrate-accessible with coordinatively unsaturated metal active sites have been the main focus of research into catalytic applications (Jiao, et al., 2018; Vakili, 2020). MOF catalytic activity has been extensively studied and their numerous uses as catalysts have been established, including the manufacture of fine compounds, the definition of potential new green procedures, and the replacement of unfriendly catalysts (Dhakshinamoorthy, Opanasenko, Čejka, & Garcia, 2013; Tombesi, & Pettinari, 2021). The structure of MOFs has a key role in determining variations in activity and selectivity toward particular organic processes (Tombesi, & Pettinari, 2021). When used in catalysis, the fundamental benefit of MOFs is the ability to design and anticipate structural characteristics based on the metal geometry, linker structure and coordination number.

A variety of synthetic techniques have been developed since the inception of metal-organic frameworks. Some of these techniques include hydrothermal, solvothermal, mechanochemical, electrochemical, microwave, sonochemical, slow diffusion and slow evaporation techniques (Adegoke & Maxakato, 2021; Emam, Abdelhameed, & Ahmed, 2020; Osman, et al., 2019; Panda, Patra, Awasthi & Singh, 2020; Tripathy, Subudhi, & Parida, 2021). Most of these developed techniques although exhibiting the advantages of synthesizing MOFs at low temperatures, under milder conditions and mostly at a short time have the disadvantage of forming amorphous and less crystalline metal-organic frameworks unsuitable for X-ray structural characterization (Raptopoulou, 2021; Vakili, 2020). Solvothermal synthesis of MOFs has shown to be very effective for the formation of very stable well-

crystalline MOFs due to the presence of solvents to aid solute solubility under high temperatures and pressure. (Denisov, Primakov, Korlyukov, Novikov & Nelyubina, 2019; McKinstry, et al., 2016; Rojas-Buzo, et al., 2021; Zhou, et al., 2017). These well-crystalline stable MOFs formed are suitable for X-ray structural characterization.

Due to their large inner pore surfaces and their customizable structure, MOFs have become an attractive choice for novel heterogeneous catalysts. The existence of single-site active species inside the crystalline lattice is one appealing characteristic of these materials. (Corma, Iglesias, Llabrés Xamena, & Sánchez, 2010). The solid nature of MOFs coupled with their high porosity, high surface area, high chemical stability, and high thermal stability makes them promising heterogeneous catalysts. Additionally, MOF crystals are simple to modify (Mahreni, & Ristianingsih, 2020; Soni, et al., 2020). MOFs can be used as heterogeneous catalysts in a variety of chemical processes, including esterification and transesterification reactions, synthesis of cyclohexanone derivatives, oxygen reduction reactions and catalytic oxidation reactions (Ahmed, Begum, & Kim, 2020; Fang et al., 2020; Gao, Di, Zhang, Mo, & Zhang, 2020; Jamil, et al., 2020; Jiang et. al., 2020; Mahreni, & Ristianingsih, 2020)

Recently, the focus on MOFs as heterogeneous photocatalysts to transform organic pollutants in water is being keenly researched (Huo, et al., 2016; Majee, Singha, Mondal, & Mahata, 2019; Su, et al., 2023; Yang, et al., 2020; Zhao, Wang & Pei, 2022; Zhao, Wang, Zhu, Liu & Pei, 2021). The high porosity and high surface area of MOFs gives them an advantage over metal oxides and zeolites (Chen, et al., 2022; Gautam, 2020; Liu, Xu, & Shao,

2020; Zheng, Li, Xue, Pang, & Xu, 2020). There is also no limit to the number of crystalline MOFs with microporous or mesoporous structures since hundreds of frameworks from different clusters of metal ions with organic linkers can be synthesized.

Furthermore, diverse functional groups in the metal node and organic linkers act as adsorption sites for various organic pollutants (Huang, et al., 2020; Ohtani, 2010; Wang, et al., 2022; Zhang, Huang, Jin, Gan & Zhang, 2021). Due to the functionalities of the organic linkers, MOFs also provide selective adsorption of organic molecules and may even form inclusion complexes with the guest adsorbate molecules. Covalent bonds, hydrogen bonds, dative bonds, and Van der Waals forces of interactions are the most common mechanisms for adsorption interactions (Ahmed, & Jhung, 2017; Ohtani, 2010; Wang, Lin, Zhao, Wang, & Zhang, 2020; Woo & Jhung, 2021).

Among the groups of metals used in the formation of MOFs, transition metals and rare-earth metals have been known to form highly fluorescent and photoactive compounds. Transition elements commonly used in the construction of metal-organic frameworks for various applications include copper (Cu), zinc (Zn), iron (Fe), cobalt (Co), nickel (Ni) and zirconium (Zr). Rare-earth (RE) metals especially lanthanides have been used to generate extraordinary topologies due to their high coordination numbers from 7 to 10. The extensive use of rare earth metals is due to strong bond formation between the oxygen and nitrogen donor ligands with their ions (Jacobsen, Ienco, D'Amato, Costantino & Stock, 2020; Janicki, Mondry & Starynowicz, 2017).

Carboxylic acid linkers among oxygenated linkers, are frequently used for MOF formation due to their characteristic ability to enable metal cluster

formation to form stable frameworks with binding properties that strongly bond with metal ions (Gangu, Maddila & Jonnalagadda, 2017; Ghasempour, et al., 2021). The strategic combination of appropriate organic linkers and metals using the appropriate synthetic technique can lead to the formation of highly stable MOFs with rich photocatalytic properties for the effective mineralization of organic pollutants.

Statement of the Problem

The permeation of organic pollutants such as synthetic dyes into the environment results in broad detection of varying concentrations in the water bodies. These dyes are used as colourants by many industries which include the textiles, printing, rubber, plastics paper, cosmetics, pharmaceutical and leather industries. Some of these are also used as pH indicators, tracers and stains in various scientific fields. (Fakin & Ojstršek, 2013; Goswami, Deepika, Chandra, Babu & Kothamasi, 2023; Gusain, Gupta, Joshi, & Khatri, 2019; Hanafi & Sapawe, 2020; Kaur, Badru, Singh & Kaushal, 2020; Le, Duy, Cheong & Pung, 2022). The dye effluents released into the environment from the dye production and through their usage in industries contain a varied range of organic pollutants with the dyes dominating is extremely worrying due to their potential ecotoxicological hazards (Mehra, Singh & Chadha, 2021; Saxena & Gupta, 2022; Singh, Kumar & Srivastava, 2017; Varjani, Rakholiya, Ng, You & Teixeira, 2020)

These dyes may break down into harmful intermediates in aquatic animals when consumed, consequently, having a negative health impact on both animals and their consumers (Affat, 2021; Al-Tohamy, et al., 2022;

Avallone, et al., 2022; Berardi, et al., 2019; Chavan, 2013; Hassaan, El Nemr & Hassaan, 2017; Olas, Bialecki, Urbańska & Bryś, 2021). These harmful intermediates may be carcinogenic and mutagenic to consumers. Toxicity research on some of these dyes revealed effects such as reproductive toxicity, genotoxicity, cancerous tumours and neurotoxicity (Al-Tohamy, et al., 2022; Jiku et al., 2021; Wu, et al., 2017). Increasing demand for timely and accurate environmental pollution control requires new techniques with outstanding performance (i.e., high sensitivity, high selectivity, and reliability) as well as high-value chemical transformation qualities to degrade pollutants and convert them into useful products or less harmful products.

Heterogeneous photocatalysis, an advanced oxidation process (AOPs) has shown encouraging outcomes in the complete mineralization of wide ranges of organic pollutants including azo dyes (Jallouli, et al., 2018; Karim, Krishnan & Shriwastav, 2022; Reddy, et al., 2016; Velegraki, Hapeshi, Fatta-Kassinos & Poulios, 2015; Xie, et al., 2020). The major advantage of photocatalysis is the fact that pollutants are completely broken down into harmless compounds such as carbon dioxide, water and inorganic ions with no further secondary disposal techniques requirement. Other treatment methods such as adsorption by activated carbon do not transform these pollutants into nontoxic wastes and therefore require secondary treatments. Expensive oxidation techniques are not needed as atmospheric oxygen and water are used. Metal oxide semiconductors including zinc oxide (ZnO), titanium dioxide (TiO₂), zinc sulphide (ZnS) and tungsten oxide (WO₃) have been efficiently used as heterogeneous photocatalysts to transform organic pollutants into less toxic compounds (Adhikari, Chandra, Kim, Madras &

Sarkar, 2018; Atta-Eyison, Anukwah & Zugle, 2021; Das, Nikhil & Nair, 2019; Guo, Zhou, Ma, & Yang, 2019; Ye, Kong, Chen, Chen, Lin & Liu, 2018).

Recently, metal-organic frameworks (MOFs) have demonstrated and attracted exceptional attention as heterogeneous catalysts for the mineralization of organic and inorganic compounds due to their exceptional features that outperform the drawbacks of metal oxide semiconductors. MOFs have extremely high surface area and porosity, and can, therefore, have a large number of active sites (Rocío-Bautista, Taima-Mancera, Pasán & Pino 2019; Yuan et al., 2018). Conduction and valence bands, which are typical of semiconductors, have been demonstrated in MOFs (Huo, et al., 2016; Wang, et al., 2022; Zhao, et al., 2022). MOFs may exhibit photocatalytic capabilities directly from their metal centres or organic linker active sites. They might also function as carrier transporters as a result of the photoexcitation of metal clusters or organic linkers. As heterogeneous photocatalysts, MOFs can absorb light and have a light excitation period that results in charge separation. (Bouider, et al., 2023; Huo, et al., 2016; Wang, et al., 2022; Zhang, Huang, Jin, Gan & Zhang, 2021; Zhao, et al., 2022).

Recent development in the photoactivity of MOFs has revealed that a variety of MOFs display remarkable charge-separation characteristics under light radiation when various light-harvesting functional components are incorporated into them (Ferreira da Rosa, et al., 2021; Su, et al., 2023; Surib, Kuila, Saravanan, Sim & Leong, 2018). MOFs with promising adsorption properties have been selectively used for the removal of contaminants in water. Their stabilities, adsorption capacities, and ease of reusability have

been reported (Abdi, Vossoughi, Mahmoodi, & Alemzadeh, 2017; Guo, et al., 2022; Ramanayaka, 2019; Wanigarathna, Gao & Liu, 2020; Zhao, et al., 2021; Zheng, et al., 2022). For the past 10 years, publications were principally on adsorptions compared to photocatalytic degradation (Zango, et al., 2020).

Research into the mineralization of organic dye pollutants by MOFs into less toxic substances in water is a new area with few publications. Drawbacks such as the stability of MOFs in water during the processes have been reported (Lee, Tang, & Huo, 2014; Yao, et al., 2022; Yu, et al., 2021; Wang, et al., 2022). As a result of this emerging exploitation, research into the synthesis of stable MOFs with rich photocatalytic properties which could be used as highly effective stable heterogeneous photocatalysts to transform coloured organic compounds into less toxic compounds in water through heterogeneous photocatalysis is intended.

Purpose of the Study

The purpose of the study was to synthesize metal-organic frameworks (MOFs) with photocatalytic properties to be used as heterogeneous photocatalysts to transform toxic organic dye pollutants in water under environmentally friendly conditions into less toxic products.

Research Objectives

1. To synthesize copper, cerium and zirconium metal-organic frameworks using benzene-1, 3, 5- tricarboxylic acid as an organic linker through the solvothermal synthetic approach.

2. To synthesize copper, cerium and zirconium metal-organic frameworks using 5-amino benzene -1, 3-dicarboxylic acid as organic linker through the solvothermal synthetic approach.
3. To characterize the various synthesized metal-organic frameworks to ascertain whether the frameworks are satisfactorily formed using the solvothermal synthetic technique.
4. To investigate the catalytic ability of the metal-organic frameworks to phototransform various coloured organic pollutants.
5. To investigate the catalytic ability of the most photoactive metal-organic frameworks to transform mixed textile dye.
6. To study the adsorption kinetics and isotherms of the metal-organic frameworks on the various coloured organic pollutants.

Significance of the Study

The findings from the study would:

1. Help minimize the extent of pollution by related organic effluents from corresponding industries into water bodies by treating the effluents before being discharged into the water bodies.
2. Provide a simple and environmentally friendly method for complete mineralization of selected organic pollutants with no extreme conditions and to obtain less harmful products.
3. Help prevent the excess usage and waste of water significantly in the corresponding industries by reusing the water freed from the pollutants after treatment.

4. Help increase the production of carbon dioxide which is the major end product after the photocatalytic treatment by harnessing it to be used for purposes such as to be used to promote plant growth in greenhouses, refrigerants, carbonated beverages and fire extinguishers.

Delimitations

The research is focused on the synthesis, characterization and photocatalytic application of metal-organic frameworks. Various synthetic methods can be used to synthesize the frameworks. The synthesis was however limited to the use of the solvothermal synthetic method. This synthetic technique offers high solubility of the precursors and the formation of good-quality MOF crystals suitable for structural characterization (Denisov, et al., 2019; McKinstry, et al., 2016; Rojas-Buzo, et al., 2021; Zhou, et al., 2017). Two carboxylic acid ligands were used as linkers for the formation of metal-organic frameworks. These ligands include benzene-1, 3, 5-tricarboxylic acid and 5-aminobenzene-1, 3-dicarboxylic acid. The organic ligands used for the formation of the framework were limited to the use of benzene carboxylic acid linkers. Benzene carboxylate groups are commonly used in MOF formation due to their rigidity and hence their ability to form rigid MOFs (Gangu, et al., 2017; Ghasempour, et al., 2021; Vizuet, Lewis, McCandless & Balkus Jr, 2019). These two linkers were chosen to observe the dynamics of the metal-organic frameworks formed with them and the selected metals on photocatalysis.

Three metal nitrates hydrates which included copper (II) nitrate trihydrate (a divalent transition metal), cerium (III) nitrate hexahydrate cerium

(a trivalent lanthanide) and zirconium (IV) oxynitrate hydrate (a tetravalent transition metal) were selected as metal clusters for the MOF synthesis. Copper was chosen because the first-row transition metals are well known to be able to coordinate with carboxylate groups under hydro and solvothermal conditions to form crystals. Copper-based MOFs are easy to synthesize due to the remarkable complexation property of copper (Taher, Kim, & Lee, 2017; Xu, et al., 2021; Zhang, et al., 2019). Cerium represents a potential candidate for the synthesis of stable MOFs at relatively low cost. It is the most accessible rare earth element and is similar to metals such as copper, zinc and tin (Kateshali, Dogaheh, Soleimannejad, & Blake, 2020; Kohantorabi & Gholami, 2017). Zirconium-based MOFs have shown higher thermal and chemical stability in comparison with other MOFs. This is due to the strength of the Zr-O coordination bonds caused by acid-hard base interactions between Zr (IV) atoms and oxygen atoms (Ahmadijokani, et al., 2022; Bon, et al., 2019; Dreischarf, Lammert, Stock, & Reinsch, 2017).

In all, the three selected metals and the two linkers were combined to form six metal-organic frameworks. The six synthesized metal-organic frameworks were characterized. The characterization tests included Fourier transform infrared (FTIR) analysis, X-ray diffraction (XRD) analysis Scanning electron microscope and energy-dispersive X-ray spectroscopy (SEM-EDS) analysis, Single-crystal X-ray diffraction analysis and Thermogravimetric (TGA) analysis. The application of the synthesized metal-organic frameworks was limited to the heterogeneous photocatalytic transformation of azo dyes into less toxic compounds. Azo dyes are the most produced and most used dye due to their easy application (Hashemi, &

Kaykhaii, 2022; Yamjala, Nainar, & Ramiseti, 2016). An acid azo dye (Lissamine green SF), a basic azo dye (Tetraethylrhodamine), a reactive textile dye (Remazole brilliant violet 5R) as well as a dye mixture from the textile studio were selected for the mineralization process under visible light.

Limitations

The occasional power outages during the synthesis of the MOFs could affect the formation of the MOFs. The light meter used to measure the intensity of light from the sun had a testing range of 200/20000 Lux. The intensity of the light from the sun during the pollutant transformation under solar conditions was mostly above 20000 Lux. Consequently, the light meter was unable to read the intensity of the light above 20000 Lux. Light meters of higher intensity above 20000 Lux reading should therefore be employed when photoactivity is being done under solar energy.

Definition of Terms

Adsorption: The process by which ions, atoms or molecules adhere to the surface of a solid material (Zarrouk, & Mclean, 2019).

Catalysis: The acceleration of a chemical reaction by a catalyst (Oxford Languages, 2023).

Catalyst: A substance that increases the rate of a chemical reaction without itself undergoing any permanent chemical change (Oxford Languages, 2023).

Characterization: The use of techniques to probe into the internal structure and properties of a material (chemeurope.com, 2023)

Photocatalyst: A material that is capable of absorbing light, producing electron-hole pairs or other reactive species that enable chemical transformations of the reaction participants and regenerate its chemical composition after each cycle of such interactions (Wang, Li, Lv, Zhang & Guo 2014).

Heterogeneous catalyst: Chemical catalysts whose physical phase is different from the physical phase of the reactants and/or products that take part in the catalyzed chemical reaction (Julkapli & Bagheri, 2015)

Ligand: An ion or molecule which donates a pair of electrons to the central metal atom or ion to form a coordination complex (Chemicool Chemistry Dictionary, 2023)

Multidentate ligand: A ligand capable of donating two or more pairs of electrons in a complexation reaction to form coordinate bonds (McGraw-Hill Dictionary of Scientific & Technical Terms, 2003)

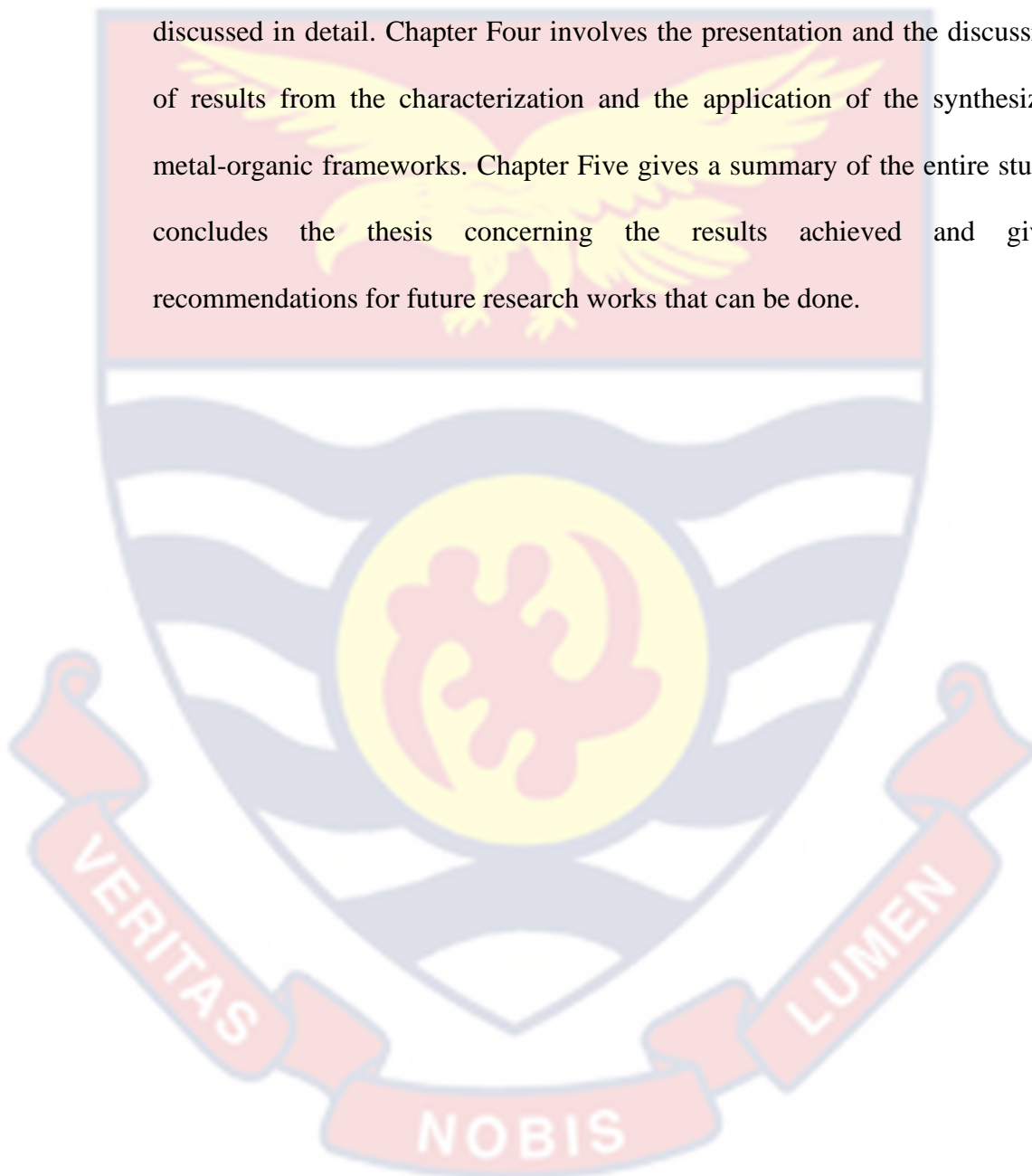
Self-assembly: The process in which a system's components, be it molecules, polymers, colloids, or macroscopic particles, organize into ordered and/or functional structures or patterns as a consequence of specific, local interactions among the components themselves, without external direction (Varga, 2016).

Reticular chemistry: The linking of well-defined molecular building blocks by strong bonds into crystalline extended frameworks. (Yaghi, 2019).

Organization of the Study

This thesis consists of five chapters. Chapter One introduces the general background information, and also includes the main objectives of this

study. Chapter Two provides a detailed review of metal-organic frameworks, their various synthetic technologies and their applications. In Chapter Three, the experimental materials, instruments and methods used for the synthesis and characterization of the synthesized metal-organic frameworks have been discussed in detail. Chapter Four involves the presentation and the discussion of results from the characterization and the application of the synthesized metal-organic frameworks. Chapter Five gives a summary of the entire study, concludes the thesis concerning the results achieved and gives recommendations for future research works that can be done.



CHAPTER TWO

LITERATURE REVIEW

Introduction

Chapter Two reviews literature on metal-organic frameworks and their catalytic application. Some of the topics that have been reviewed include inorganic metals used for metal-organic frameworks with attention focused on copper, cerium and zirconium base metal-organic frameworks. A review of organic bridging ligands for a metal-organic framework was done with an emphasis on carboxylate ligands. The Synthetic techniques for metal-organic framework focusing on the solvothermal synthesis technique have been elaborated. A review of the catalytic application of metal-organic framework targeting its oxidative application with a focus on photocatalytic oxidation has been provided.

Coordination Polymers

Coordination polymers are simply derived from the repeated combination of coordination compounds (Soares & Pérez, 2013). Coordination compound formation is very vital in inorganic chemistry. A coordination compound is formed when a ligand which has a lone electron pair to donate to form a bond with mostly transition metals in their ionic form through the sharing of the ligand's lone electron pairs (Batten & Champness, 2017; Morrill, Michaels & Freitag, 2022). Coordination polymers are therefore building blocks formed from infinite interactions between metal ions and ligands through covalent and non-covalent weak bonds (Dawood, 2020; Feizbakhsh Bazargani, 2019; Morrill, et al., 2022; Tatikonda, 2018).

Coordination polymer formation typically yields well-ordered solid-state crystalline materials in one, two or three-dimensional space (Batten & Champness, 2017; Dalai, 2011; Fromm, Sague, & Mirolo, 2010; Kostakis, 2018; Kuznetsova, Matveevskaya, Pavlov, Yakunenkov & Potapov, 2020).

Figure 1 shows the different structural dimensionalities of coordination polymer. Their designs and assumed dimensions are determined by the coordinative arrangement of their building blocks (Dawood, 2020; Fan, Zhang, Chen, Wu & Wang, 2021; Guan, 2021; Soares & Pérez, 2013).

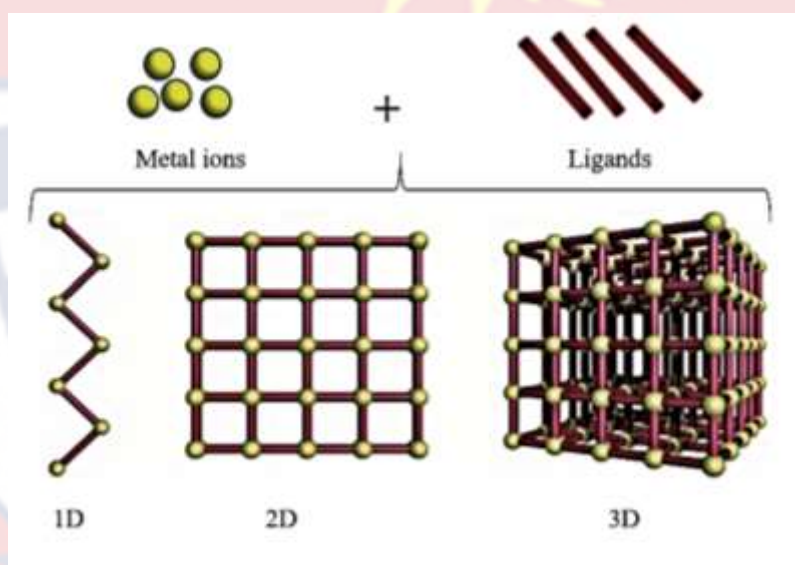


Figure 1: The different dimensional structures of coordination polymers (Henke, 2012)

The name coordination polymers was coined by J. C. Bailer in 1964 upon his realization of the disparity between organic polymers and coordination polymeric compounds (Batten, et al., 2012). Prussian blue, a dye compound discovered during the 18th century was realized to belong to the coordination polymer family. Prussian blue is a face-centred cubic mixed-valence iron hexacyanoferrate ($K_xFe^{III}[Fe^{II}(CN)_6]_{(3+x)/4}$) crystal structure having Fe^{III} and Fe^{II} bridged by cyanide ligands (Catala & Mallah, 2017;

Demirkıran, 2016; Doveri, et al., 2023; Piernas Muñoz, Castillo Martínez, Piernas Muñoz, & Castillo Martínez, 2018).

The coordination polymer field of research gained significant growth with the emergence of a new porous coordination polymer with tailoring functional properties (Cui, Ren, Sun & Jia, 2018; Gao, Xu & Bu, 2019; Gao, et al., 2020; Guan, 2021; Kuznetsova, et al., 2020; Lin, Xiang, Zhou & Chen, 2020; Pei, et al., 2020; Tsivadze, et al., 2019). Porous coordination polymers are now mostly referred to as metal-organic frameworks (MOFs) (Chen, Kirlikovali, Li, & Farha, 2022; He, et al., 2018; Li, et al., 2019). Research into the area of coordination polymers has moved through an advanced transformation over twenty-five years and has become the most extensively studied area in materials chemistry (Głuchowska, Łyszczek, Mazur, & Kirillov, 2021; Kuznetsova, et al., 2020; Soares & Pérez, 2013).

Metal-Organic Frameworks

Metal-organic frameworks (MOFs) are crystalline porous coordination polymers (Chen, et al., 2022; He, et al., 2018; Li, et al., 2019). The frameworks are developed by the self-assembly of inorganic metal clusters and organic molecule ligands to form hybrid organic-inorganic structures (Feizbakhsh Bazargani, 2019; Liu, et al., 2021; Sánchez-Serratos, Álvarez, González-Zamora & Ibarra, 2016; Zhang, et al., 2018). MOFs are formed by the attachment of inorganic metal clusters onto organic ligands through strong covalent and weak bond interactions to produce a secondary-building unit (SBU) that self-assembles to yield mostly scaffold-like three-dimensional frameworks with pores (Diercks & Yaghi, 2017; Hendon, Rieth, Korzynski &

Dinca, 2017; Hungerford, 2019; Lian, Chen, Liu & Zhou, 2016; Liu, et al., 2020; Sharmin & Zafar, 2016; Zarei-Shokat & Ganjali, 2023). Figure 2 shows the self-assembly of a three-dimensional metal-organic framework.

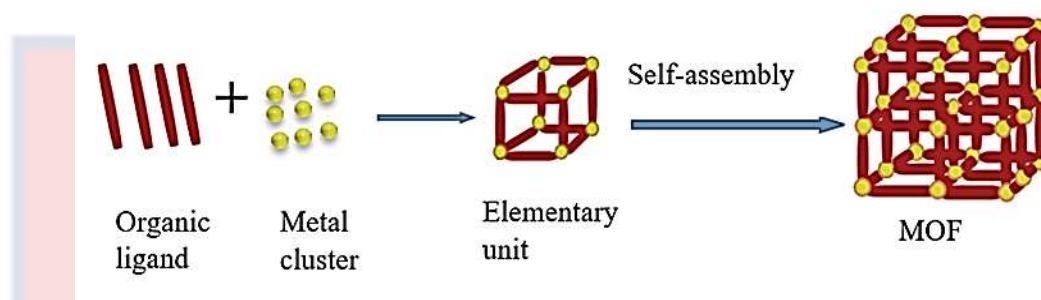


Figure 2: The self-assembly of a three-dimensional metal-organic framework (Zarei-Shokat & Ganjali, 2023)

These frameworks show exceptional stability with high permanent pore size and volume resulting in a large surface area of the frameworks (Abdollahi, Razavi, Morsali, & Hu, 2020; Dutta, Pan, Liu, & Kumar, 2021; Knebel, et al., 2017; Singh, Singh, Liu & Kumar, 2021; Zhang, et al., 2018). The varying bonding energies found in the formation of these frameworks include strong coordinative covalent bonds with an average bond strength of 50 kJ mol^{-1} , hydrogen bonds with varying bond strength from 15 to 40 kJ mol^{-1} and π - π bond interactions between $5\text{--}10 \text{ kJmol}^{-1}$. (Ahmed, & Jhung, 2017; Raptopoulou, 2021; Servati Gargari, et al., 2015; Sharmin & Zafar, 2016; Vogel, Nenoff, & Rimsza, 2020)

The name metal-organic framework was first used by Omar Yaghi in 1995 when he synthesized MOF-5 which was a three-dimensional structure with $2900 \text{ m}^2/\text{g}$ surface area and 0.60 cm^3 pore volume (Liu, et al., 2012; Villemot, Hamel, Pansu, Leray, & Bertrand, 2020; Yang, Fang, Ma, Ganz & Han, 2014; Zhao, Ma, Kasik, Li, & Lin, 2013). The high surface area was

historical since it exceeded the surface area of traditional zeolites and amorphous carbon. Further investigations into the full crystal structure of the MOF-5 with empty pores showed a surface area above $7000\text{m}^2/\text{g}$ (Furukawa, Cordova, O’Keeffe & Yaghi, 2013; Yaghi, 2019). The new high porosity for MOF-5 brought excitement and attention to the field of the metal-organic framework. Figure 3 shows the structural framework of MOF-5.

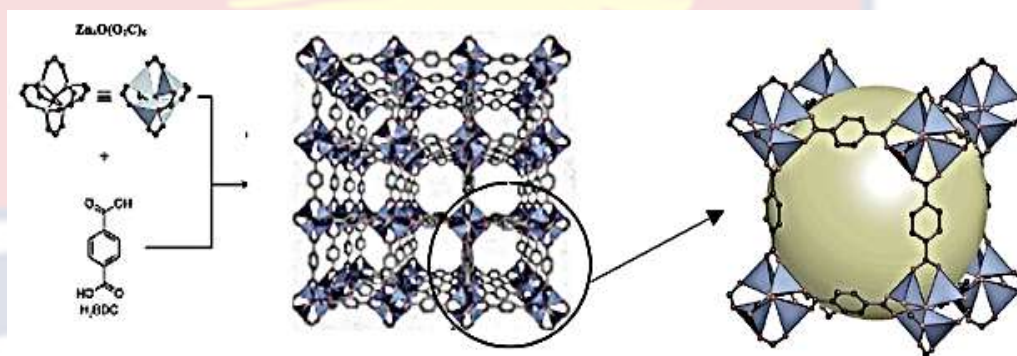


Figure 3: The structural framework of MOF-5 (Sugamata, Kobayashi, Iihama, & Minoura, 2021; Yaghi, 2019)

The structure of MOF-5 consists of zinc cluster units linked by 1, 4-benzenedicarboxylic acid linker to develop a cubic extended three-dimensional framework (Aghajanloo, Rashidi, & Moosavian, 2014; Sugamata, Kobayashi, Iihama, & Minoura, 2021; Yaghi, 2019) There has been a rapid growth of research into MOFs in the field of reticular chemistry after the discovery of MOF-5 due to their remarkable characteristics such as high porosity, abundant surface area and rich tunability (Chen, Li, Modica, Drout & Farha, 2018; Liu, et. al., 2022; Ma, et al., 2017; Qin, et al., 2021). The combinations of the large range of inorganic metals and the organic linkers under different techniques with different synthetic conditions allow for the vast tailoring of MOF pore size and surface area. The diversity in structure, compositions and functionalization of MOFs has led to the development of

thousands of MOFs. Figure 4 shows the number of MOF articles published in the past twenty years. A rapid increase in MOF publications has been observed over the years.

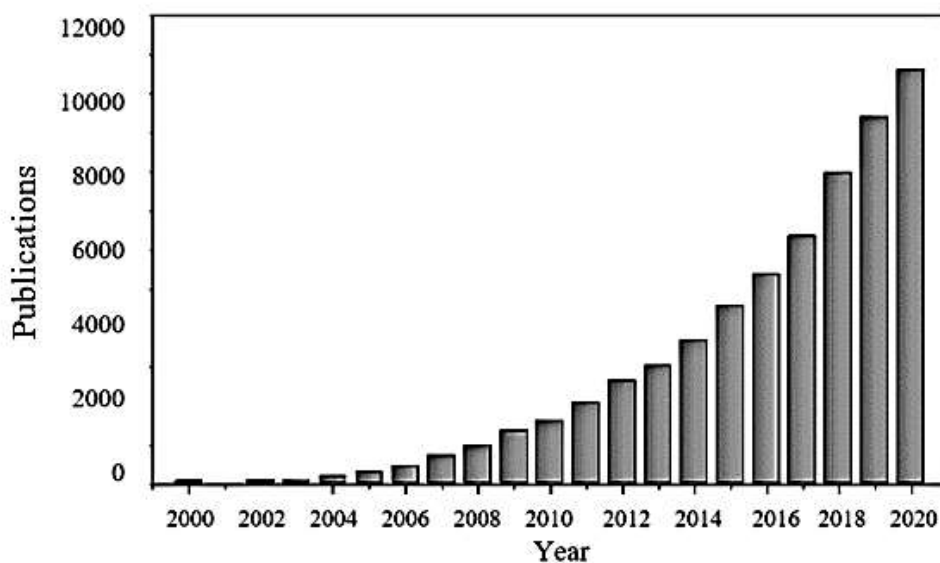


Figure 4: Metal-organic framework publications from 2000 to 2020 (Dai, Tissot & Serre, 2021)

There are a wide variety of metals and organic linkers available for the formation of MOFs. Almost all the metals from the periodic table of elements can be used in the cluster form for MOF synthesis (Manousi, Giannakoudakis, Rosenberg & Zachariadis, 2019; Lu, et al., 2014; Yuan, Qin, Lollar, & Zhou, 2018). Also, a wide variety of oxygen and nitrogen donor ligands can serve as linkers for the synthesis (Feizbakhsh Bazargani, 2019; Gu, et al., 2015; Meng, et al., 2015; Semitut, Sukhikh, Filatov, Ryadun & Potapov, 2017). Different MOF synthetic techniques with different synthetic conditions have been developed since the inception of MOFs (Dey, Kundu, Biswal, Mallick & Banerjee, 2014; Emam, Abdelhameed & Ahmed, 2020; Hammond, Edler, Bowron, & Torrente-Murciano, 2017; Huo, Xiu, Meng & Quan, 2023;

Raptopoulou, 2021; Safaei, et al., 2019). Some of these techniques include hydrothermal, solvothermal, mechanochemical, electrochemical, sonochemical, microwave, slow diffusion and slow evaporation. All these techniques have different controlling synthetic conditions and largely depend on factors such as reaction solvents, modulators, counterions, temperature, pH, pressure and time.

The coordination number and geometry of the metal clusters and the nature of the organic ligands under suitable synthetic conditions determine the geometries of MOFs. Consequently, the final topology of MOF is mostly directed by the metal clusters and organic linkers under suitable set conditions (Sharmin & Zafar, 2016; Noa, et al., 2021). MOF possible tunability generates various structures of different geometries such as triangle, square paddle-wheel, and trigonal prism for more suitable applications including gas storage, separations, drug delivery, catalysis, and, sensing (Dawood, 2020; Gautam, Singhal, Lee & Chae, 2022; Jiang, Alezi & Eddaoudi, 2021; Vakili, R. 2020; Peralta, Huxley, Albalad, Sumbly & Doonan, 2021; Raptopoulou, 2021; Zhang, et al., 2019). Figure 5 shows the possible geometries of some building units and the building blocks of metal-organic frameworks.

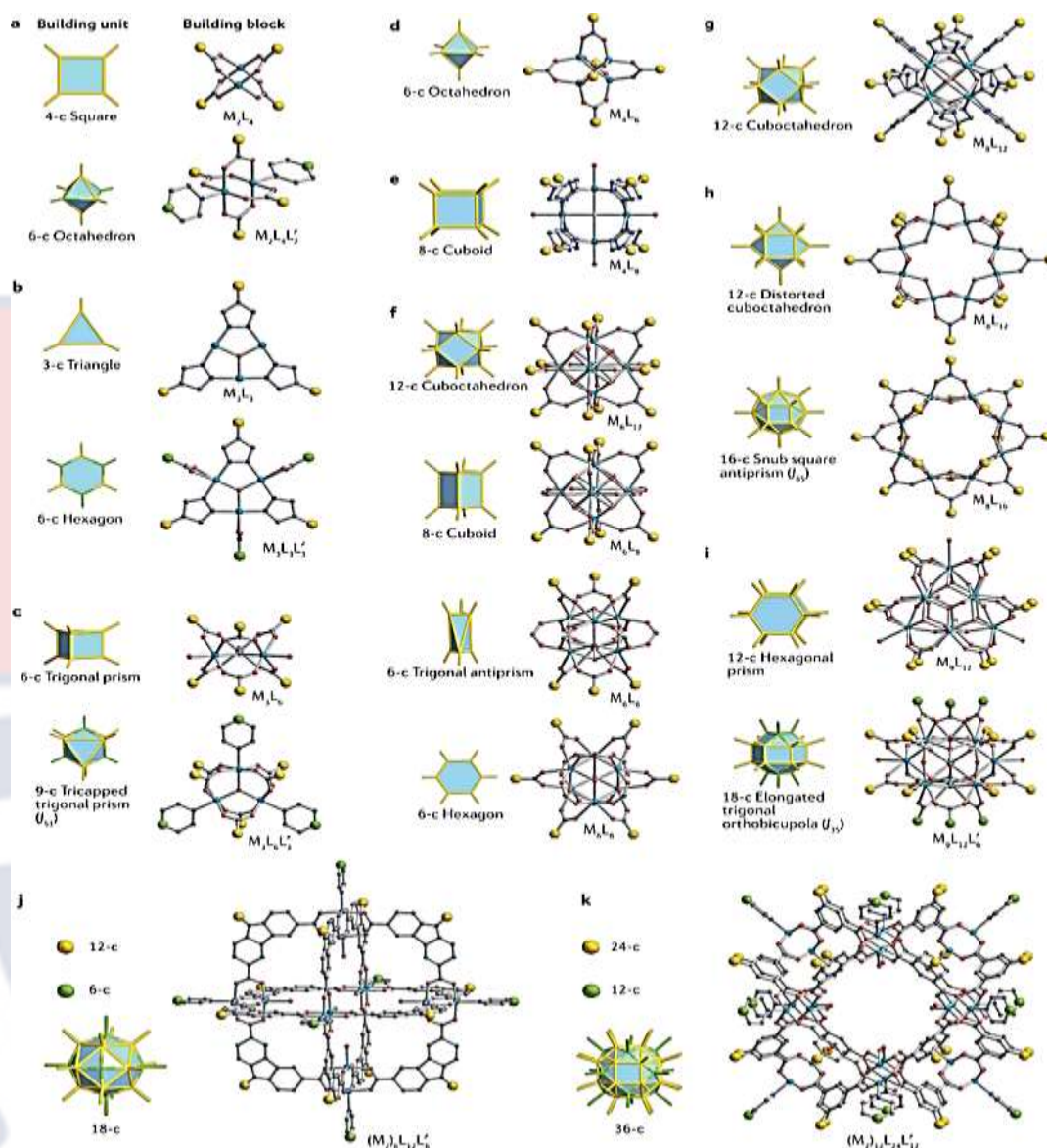


Figure 5: Representative of building units and the related building blocks of metal-organic frameworks (Jiang, Alezi & Eddaoudi, 2021)

Building Units of Metal-Organic Framework

Metal-organic frameworks (MOFs) consist of secondary building units (SBUs). Secondary building units (SBUs) have become an important concept for MOF structural topology classification. They form the elementary design that predicts MOF topologies (Guo, et al., 2022; Ha, Lee & Moon, 2020; Kalmutzki, Hanikel, & Yaghi, 2018; Yan, et al., 2018). The SBUs generate the

directional design for the final frameworks of MOFs (Kalmutzki, et al., 2018; Peng, Song, Yin, Zhang & Fei, 2019; Schoedel, Li, Li, O’Keeffe & Yaghi, 2016). Secondary building units (SBUs) have been described as a moiety consisting of the metal cluster and organic linker coordination sites (Bour, Wright, He, & Dincă, 2020; Brozek & Dincă, 2014; Ha, Lee & Moon, 2020; Kalmutzki, et al., 2018; Peng, et al., 2019). SBUs are, therefore, the units that are linked up making the scaffold structure of the MOF with each unit comprising metal ions with bridging organic ligands. Each SBU is joined to a neighbouring SBU by the bridging organic ligands.

SBUs determine how stable and versatile MOFs are subject to the characteristics of the metal ions and the organic linker (Ha, et al., 2020; Schoedel, et al., 2016; Yan, et al., 2018). The extensive MOFs formed with diversified structures result from the availability of a broad range of SBU geometries. Consequently, by the selection of appropriate building units with established reaction conditions targeted structures can be attained (Chen & Zhang, 2019; Lv, et al., 2021; Yu, et al., 2022; Yan, et al., 2018). The SBU approach, therefore, makes it possible to control the geometry of the building units to form MOFs with predetermined topologies.

Metal for Metal-Organic Frameworks

Metals used for MOF synthesis exist either in the form of metal ions, metal clusters with multinuclearity, metal cluster chains or metal cluster layers (Manousi, Giannakoudakis, Rosenberg & Zachariadis, 2019). Metal species for the formation of MOFs cover a wide spectrum ranging from alkali, alkaline-earth, transition and rare-earth metals. Among the metal groups, the

transition metals are the most used inorganic metals for MOF synthesis (Lu, et al., 2014; Manousi, et al., 2019; Rocío-Bautista, González-Hernández, Pino, Pasán, & Afonso, 2017; Yuan, Qin, Lollar, & Zhou, 2018).

Transition elements commonly used in the construction of metal-organic frameworks include copper (Cu), zinc (Zn), iron (Fe), cobalt (Co), nickel (Ni) and zirconium (Zr) (Du, Chai, Li, Zhang, & Tang, 2022; Jia, Han, Luo, Cong & Deng, 2022; Rocío-Bautista, et al., 2017; Singha & Mahata, 2015; Valvekens, Vandichel, Waroquier, Van Speybroeck & De Vos, 2014). Other transition elements such as chromium (Cr), manganese (Mn), molybdenum (Mo), platinum (Pt), silver (Ag), palladium (Pd), and cadmium (Cd) have also been employed to construct MOFs (Du, et al., 2022; Jing, et al., 2022; Li, Han & Wang, 2021; Pan, et al., 2022; Seyedpour, et al., 2020; Zhang, Lv, Bi, Lu & Wang, 2020). Transition metals have diversified coordination forms leading to different forms of secondary building units (SBUs) (Bour, Wright, He, & Dincă, 2020; Ha, Lee, & Moon, 2020).

Rare-earth (RE) metals which comprise the lanthanides, scandium (Sc) and yttrium have recently been largely used for MOF synthesis with outstanding outcomes (Chen, Li, Chen, Tan, Wu, & Qiu, 2022; Elsaidi, et al., 2018; Mahata, Mondal, Singha & Majee, 2017; Saraci, Quezada-Novoa, Donnarumma & Howarth, 2020; Shi, Cao, Liu, Zhang & Du, 2021; Yang, Zhuang, Li & Gu, 2019). The lanthanides include promethium (Pm), erbium (Er), ytterbium (Yb), thulium (Tm), lutetium (Lu), holmium (Ho), gadolinium (Gd), dysprosium (Dy) samarium (Sm), cerium (Ce), europium (Eu), lanthanum (La), terbium (Tb), praseodymium (Pr) and neodymium (Nd). The extensive use of rear earth metals is due to strong bond

formation between the oxygen and nitrogen donor ligands with their ions (Jacobsen, Ienco, D'Amato, Costantino & Stock, 2020; Janicki, Mondry & Starynowicz, 2017).

Rare-earth (RE) metals especially lanthanides have been used to generate extraordinary topologies due to their high coordination numbers from 7 to 10 (Gao, et al., 2020; Gorai, Schmitt, & Gunnlaugsson, 2021; Zhao, Wang, Poelman & Voort, 2018; Wang, et al., 2022; Xu, Cao, Kang & Zhao, 2016). Generally, MOFs are formed from monovalent, divalent, trivalent, or tetravalent metal cations among the metal classes. High-valent metal cations are observed to generate stronger coordination bonds due to their large charge densities resulting in extra stable frameworks (Ding, Cai & Jiang, 2019; Hansen & Das, 2014; Jia, et al., 2023; Lin, et al., 2019; Yan, et al., 2022). MOFs designed from a trivalent metal cation such as Ce^{3+} and tetravalent metal cations such as Zr^{4+} are, therefore, likely to have higher stabilities than MOFs constructed from divalent metal cations such as Cu^{2+} .

The coordination strength between the organic linkers and the metal ions can be explained using the hard/soft and acid/base (HSAB) principles (Dhakshinamoorthy, Asiri, & Garcia, 2019, Manousi, Giannakoudakis, Rosenberg & Zachariadis, 2019). High valent metal ions such as Fe^{3+} , Al^{3+} , Zr^{4+} and Cr^{3+} are considered hard acidic metal ions, while low valent metal ions such as Mn^{2+} , Cu^{2+} , Ag^+ , Zn^{2+} and Ni^{2+} are considered soft acidic metal ions (Feng, Zhang, Zhou, & Sharma, 2018; Manousi, et al., 2019).

Organic Ligands for Metal-Organic Framework

The organic ligands used for metal-organic frameworks must bridge the metal ions through coordination to form a strong framework. Multidentate ligands are therefore required to form such frameworks (Feizbakhsh Bazargani, 2019; Ramathulasamma, Bommakanti & Das, 2023; Wang, et al., 2022; Zhang, et al., 2021). Several organic ligands that can be used as linkers for metal-organic frameworks have been reported (Feizbakhsh Bazargani, 2019; Pervez, Chen, Li, Naddeo & Zhao, 2022; Ramathulasamma, et al., 2023; Shi, Ji, Wang & Li, 2020; Yang, et al., 2020; Zhan, et al., 2021). Rigid organic ligands are, however, desired for easy prediction of the geometries of MOFs before synthesis due to their certain induced steric effect in the framework formation process (Jornet-Molla, & Romero, 2015; Kaur, Anthwal, Kandwal & Sud, 2023; Kokado, 2017; Lin, Lü, Hong, & Cao, 2014; Sun & Sun, 2015). Strong open pores are, therefore, obtained after inclusive solvent removal from synthesized MOFs when rigid organic ligands are used.

Organic ligands exist in cationic, anionic and neutral forms. Cationic and neutral organic ligands are less used for the construction of metal-organic frameworks. Cationic ligands have low affinities for metal cations while neutral organic ligands are usually weak donors. Anionic organic ligands however are largely used. Common anionic ligands include oxygen and nitrogen-containing ligands such as carboxylic acid, phosphonic acid, sulfonic acid, pyridine, thiophene and furan (Feizbakhsh Bazargani, 2019; Gu, et al., 2015; Meng, et al., 2015; Semitut, et al., 2017). Oxygenated organic ligands lead as linkers for MOF synthesis due to the ability of most metals to coordinate with oxygen with varying bond strength. Among these oxygenated

linkers, carboxylic acids linkers are widely used because of their ability to form strong bonds with metal ions (Decker, Lorzing, Deegan & Bloch, 2020; Ding, et al., 2019; Mouchaham, Wang & Serre, 2018; Wang, et al., 2021; Zhao, et al., 2023). Figure 6 shows a representative of the various categories of common oxygen and nitrogen-contained anionic ligands used for metal-organic frameworks.

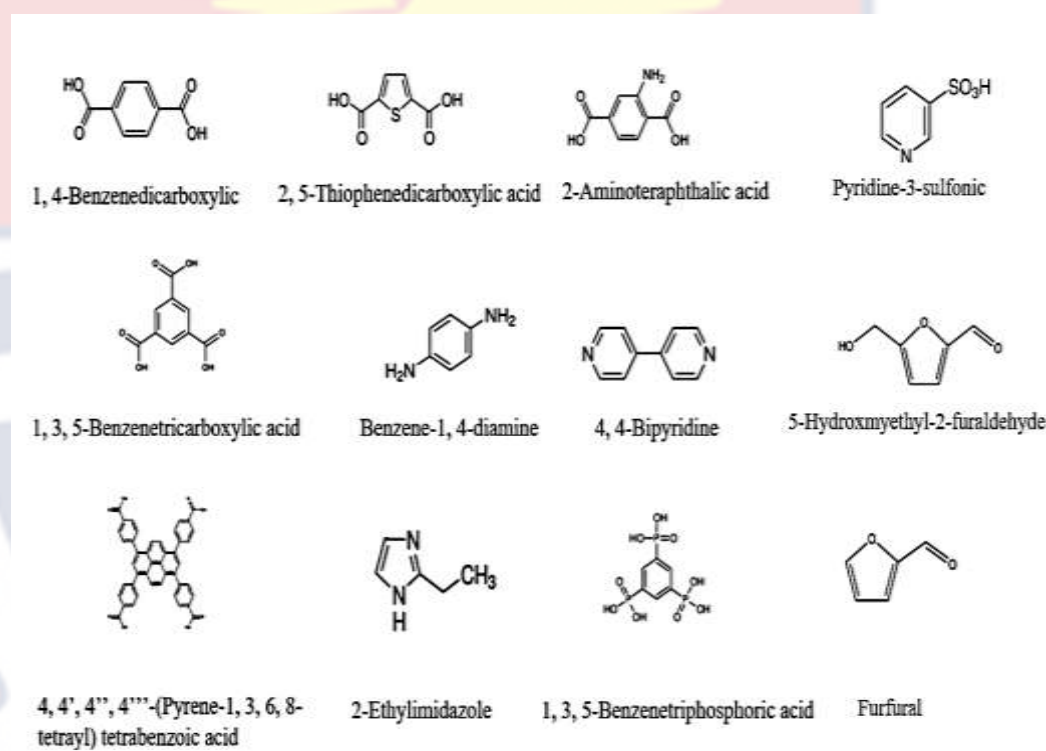


Figure 6: A representative of categories of organic ligands

Metal-Organic Frameworks Constructed from Carboxylate Ligands

Carboxylate linkers are frequently used for MOF formation due to their characteristic ability to enable metal cluster formation to form stable frameworks. They are commercially available and less expensive (Ghasempour, et al., 2021; Yang, et al., 2021). Carboxylate ligands possess monodentate and polydentate binding properties that strongly bond with metal

ions (Gangu, Maddila & Jonnalagadda, 2017; Ghasempour, et al., 2021; Janiak, 2013; Vizuet, Lewis, McCandless & Balkus Jr, 2019; Yan, Li, Wu, Gao, & Zhang, 2020; Ramathulasamma, et al., 2023). The carbonyl oxygen atoms on carboxylate ligands can hold the metal clusters firmly in place resulting in rigid frameworks. (Ghasempour, et al., 2021; Gangu, et al., 2017).

Carboxylate ligands are classified as hard Lewis bases in relation to hard and soft acid and base (HSAB) theory. The hard Lewis bases property of carboxylate ligands enables the formation of extra stable MOFs when linked with hard Lewis acids such as Ti^{4+} , Fe^{3+} , Zr^{4+} and Cr^{3+} (Balto, et al., 2021; Chen, et al., 2020; De, et al., 2021; Liu, et al., 2018; Yuan, et al., 2018; Zhang, et al., 2017). Carboxylate linkers can bond to metal ions in different modes to yield a rich diversity of MOF topologies (Gao, et al., 2021; Li & Zuo, 2020; Lu, et al., 2013). Figure 7 shows the different binding modes of a carboxylate ligand with a metal. Carboxylate ligands can bind to metal ions in monodentate, bidentate, syn-syn bridging, anti-anti bridging and anti-syn bridging modes.

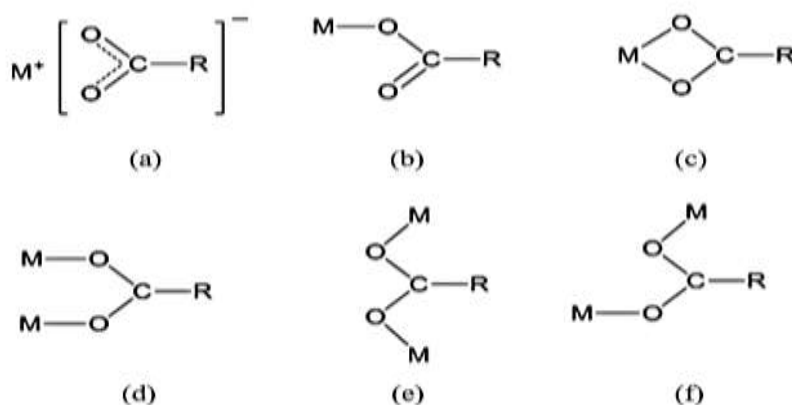


Figure 7: Different binding modes of a metal with a carboxylate ligand. (a) ionic state (b); Monodentate (c); Bidentate(d); Syn-syn bridging (e); Anti-anti bridging (f); Anti-syn bridging (Li & Zuo, 2020).

Aromatic multicarboxylic acids ligands have been widely used to form a large number of MOFs with varying properties (Ghasempour, et al., 2021; Gu, Gu, & Kirillov, 2020; Gu, et al., 2019; Lu, et al., 2021; Luo, et al., 2014; Ru, et al., 2022; Wei, Wang, & Duan, 2013; Yan, Li, & Yong, 2021; Yin, Li, Yan, & Yong, 2021). High MOF performance due to the high surface area and strong porosity of MOFs has been synthesized using aromatic multicarboxylic acids ligands as linkers (Ghasempour, et al., 2021; Gu, et al., 2020; Yin, et al., 2021; Luo, et al., 2014). Generally, using aromatic multicarboxylate linkers for MOFs makes them more stable and rigid through stronger connections to metal clusters. The incorporation of aromatic multicarboxylate ligands as linkers for MOFs has the advantages of greater porosity, reduced dead space in pores and interpenetration as well as enhanced tunability through linker functionalization (Ghasempour, et al., 2021; Gu, et al., 2019; Lu, et al., 2021; Ru, et al., 2022). Factors such as the nature of carboxylate behaviour, size, deprotonation characteristics, rigidity and presence of other functional groups, however, control the bonding behaviour of the linkers.

Benzene-1, 3, 5- tricarboxylic acid (H₃BTC)

Benzene-1, 3, 5- tricarboxylic acid is a tricarboxylic aromatic compound with the carboxylic acid groups positioned at the 1, 3 and 5 carbons found in the benzene ring. Intermolecular hydrogen bonds exist among the carboxylic acids to form a two-dimensional network structure within the crystals. Benzene-1, 3, 5- tricarboxylic acid is an oxygen-containing rigid ligand due to the rigid planar arrangement of the symmetrical carboxylic acid

groups (Xu, Wang, Yu, Wang & Zhou, 2023). The structure of Benzene-1, 3, 5- tricarboxylic acid is shown in Figure 8.

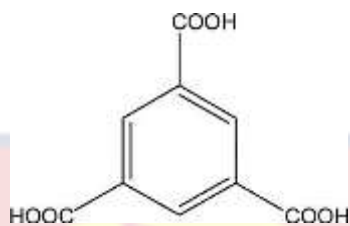


Figure 8: The structure of Benzene-1, 3, 5- tricarboxylic acid (Xu, Wang, Yu, Wang & Zhou, 2023)

Benzene-1, 3, 5- tricarboxylic acid has been used as an organic linker to synthesize metal-organic frameworks (Alammar, et al., 2018; Lestari, Winarni, & Rahmawati, 2017; Liu, Li, Oh, Fang & Xi, 2016; Manyani, Siwatch, Rana, Sharma & Tripathi, 2023; Nozohour Yazdi, Yamini, Asiabi & Alizadeh, 2018; Wang, Yang & Dong, 2021). HKUST-1 which is among one of the earliest MOFs discovered was synthesized using benzene-1, 3, 5- tricarboxylic acid as the linker. HKUST-1 is a three-dimensional porous structure formed from benzene-1, 3, 5- tricarboxylic acid ligands and copper metal clusters (Ghasempour, et al., 2021). HKUST-1 has become a standard of adsorption studies for MOFs.

Several frameworks involving benzene-1, 3, 5- tricarboxylic acid and a wide variety of metal ions for various applications have been researched after the production of HKUST-1 (Arroussi, Gaffour, Mokhtari & Boukli-Hacene, 2020; Jeyaseelan, Albaqami & Viswanathan, 2021; Kumar, Mezni, Periyasamy & Viswanathan, 2022; Lestari, Inayah, Rahmawati & Purwanto, 2020; Murad et al., 2022). Benzene-1, 3, 5- tricarboxylic acid is highly reactive and has multiple coordination modes and has been used in recent

times as a linker for the formation of MOFs and complexes with Polyoxometalates (POMs). In a recent study, various synthetic methods with POMs modified by Benzene-1, 3, 5- tricarboxylic acid and a summary of the applications of synthetic compounds in different fields have been analyzed (Xu, et al., 2023).

Benzene-1, 3, 5- tricarboxylic acid bonded to POMs in four different modes which include serving as a template support, coordinating with elements found in POMs, coordinating with transition metal ions in unsaturated POM to form POM-BTC, coordinating with other transition metals to form M-BTC covalent bond with POMs to form POM-M-BTC with hydrogen bonding and supramolecular interaction as well (Li, Ma, Niu, & Wang, 2019; Ma, Hu, Wang & Niu, 2019; Ullah, et al., 2023; Walsh, Bond, Forster & Keyes, 2016; Xu, et al., 2023; Yang, et al., 2021). Benzene-1, 3, 5- tricarboxylic acid can modify POM the formation of through metal-organic frameworks, metal-organic polyhedrons (MOPs) and organic molecular cages formations with superior hydrolysis resolution, electron transfer ability and catalytic performance to improve applications in various prospective fields (Das, Kaushik & Hussain, 2020; Ge, Li, & Zheng, 2021; Lai, et al., 2021; Ma, et al., 2019; Ullah, et al., 2023; Xu, et al., 2023; Yang, et al., 2021).

5-Amino benzene -1, 3 - dicarboxylic acid

5-amino benzene -1, 3 – dicarboxylic acid is an aromatic amino carboxylic acid compound. 5-aminobenzene -1, 3 – dicarboxylic acid is an aromatic compound having carboxylic acid groups positioned on the first and third carbons with an amino group on the fifth carbon of the benzene ring (Jin,

2012 et al.,). Figure 9 shows the molecular structure of 5-aminobenzene -1, 3 – dicarboxylic acid.

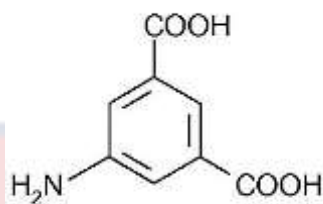


Figure 9: The structure of 5-aminobenzene -1, 3 – dicarboxylic acid (Jin, 2012 et al.,)

The rigidity of 5-aminobenzene -1, 3 – dicarboxylic acid has been observed as an excellent polycarboxylic acid for various gatherings of distinctive secondary building units (SBUs) for the building of a large range of metal-organic frameworks. The presence of the amino group in its structure is mostly uncoordinated giving it a rich coordination property (Ferrer, Alvaro, Baldovi, Reinsch & Stock, 2014; Jin, et al., 2012; Phan, Nguyen, Kim, Park, Kim, & Lee, 2021; Sheta, El-Sheikh, Abd-Elzaher & Wassel, 2019; Wei, Hui-Ming, Li, Qing-Wei & Lei, 2018). The amino group can occupy the voids of the expected networks which enable the network to undergo further synthetic modifications for particular properties and functions. The amino groups also form hydrogen bonds with the adjacent SBU units to enhance connectivity for stable framework formations.

Several frameworks involving 5-aminobenzene -1, 3 – dicarboxylic acid and lanthanide ions for various applications have been researched (Jin, et al., 2012; Qiu, et al., 2009; Queirós, et al., 2021; Rowe 2013; Wang et al., 2019). Other transition metals in combination with 5-aminobenzene -1, 3 – dicarboxylic acid as organic linkers have also been synthesized for various

applications. Copper and cadmium MOF with good electrochemical, fluorescent and photocatalytic properties have been synthesized using 5-aminobenzene -1, 3 – dicarboxylic acid as linkers (Lin, et al., 2015). A novel 2D Ag (I)-5-aminoisophthalate MOFs have also been synthesized with good photoluminescence, good antimicrobial activity against gram-positive and negative bacteria, mould and clinic isolated yeast as well as good antifungal activity against mould and yeast (Günay, Çolak, Yeşilel, Tunç & Çolak, 2015). Three novel MOFs Zn-ant, CdBa-aip and Cd-aipox with photoluminescent properties have also been formulated for sensing activity (Zhou, Geng, Zhang, &Bo, 2016).

Copper Base Metal-Organic Framework

Copper (Cu) is one of the popular transition metal elements used to develop MOFs. Copper is abundant, less expensive, non-toxic and has amazing complexation strength (Abdelmoaty, El-Beih & Hanna, 2022; Taher, Kim & Lee, 2017). Copper forms varying ranges of +1 and +2 oxidation states coordination to form cuprous and cupric compounds (Al Hageh, et al., 2018; Liu, Gu, Jia, & Zhang, 2016; Pushie, et al., 2019). Cu(I) easily coordinate with nitrogen donor ligands to form attractive networks. Cu(I) strongly coordinate with halides to form stable neutral coordination compounds (Feng, Cai, Gao & Zheng, 2018; Jiang, Wang, Bai & Hor, 2013; Pushie, et al., 2019; Schlachter, et al., 2020 Wang, et al., 2017; Wang, et al., 2019) Further combinations of these neutral coordination compounds and bridging ligands commonly result in one dimensional (CuX)_n chains or two dimensional (Cu₂X₂)_n rings networks (Ji, Qu, Jing, Zhu, & Huang, 2016; Schlachter, et

al., 2020; Xu, et al., 2022; Soltani, Ghorbanpour, Bagheri, Ebadi-Nahari, & Ziegler, 2023; Wang, et al., 2017)

Copper-based MOFs are easy to synthesize due to the remarkable complexation property of copper (Taher, et al., 2017). The d9 system of Cu(II) complexes leads to diversified structural geometries. Geometries such as square planar, tetrahedral, octahedral, trigonal planar, square pyramidal and trigonal bipyramidal have been found (Datta, et al., 2023; Hua, et al., 2019; Peralta, et al., 2021; Vizuet, et al., 2019; Xu, et al., 2021; Zhang, et al., 2019). The Cu(II) coordination sphere usually consists of *N* donor groups with counter anions or solvent molecules also present (Tatikonda, 2018). The MOFs from Cu can be tuned to possess biocompatibility, redox activity, high chemical stability, photochemical and electrochemical properties. This has expanded its exploration into various applications in hydrogen storage, photovoltaics, ammonia sensing, CO₂ reduction, absorption and catalysis (Abbasi, Karimi & Daasbjerg, 2017; Nivetha, et al., 2020; Roy, et al., 2018).

Copper is one of the first transition elements to be used with benzene-1, 3, 5- tricarboxylic acid to synthesize HKUST-1 ([Cu₃(BTC)₂3H₂O]_n), which has served as a standard for adsorption studies for many years. After the discovery of the promising adsorption property of HKUST-1, numerous research into Cu₃(BTC)₂ MOFs with different synthetic techniques and parameters for different applications such as gas adsorption, storage, separation and catalysis with a recent focus on catalysis have been employed (Chen, et al., 2017; Denning, et al., 2020; Gautam, et al., 2022; Hendon & Walsh, 2015; Kar & Srivastava, 2018; Li, et al., 2019; Ma, et al.,

2022; Mosleh, Rahimi, Ghaedi & Dashtian, 2016; Nivetha et al., 2020; Zhao, et al., 2019).

Recently the use of $\text{Cu}_3(\text{BTC})_2$ MOFs and other copper MOFs as photocatalyst for the degradation of pollutants in water is keenly investigated (Chang, Zheng, Zhao & Yang, 2019; Ebrahimi, Sheikhshoae & Mehran, 2017; Garg, Rekhi, Kaur, Singh & Malik, 2022; Samuel, Savunthari, & Ethiraj, 2021; Wei, Chen, Liang, Zhao & Luo, 2017). The investigations into various catalytic applications of Cu (II) with dicarboxylic acids and other linkers have also been made for various applications including post-synthesis application and decarboxylation application (Mollabagher, Taheri, majid Mojtahedi & Seyedmousavi, 2020; Saini, Jojeph & Bhatia, 2018; Yang, Ruess & Carreon, 2015).

Cerium-Based Metal-Organic Framework

In the past few years, several Ce(III)-MOFs research have been published. The rapid emergence of Ce(III)-MOFs is due to the high availability of cerium among the rare earth elements and the reasonable cost of Ce(III) salts which makes it capable of being used for applications on a large scale (Kateshali, Dogaheh, Soleimannejad, & Blake, 2020; Kohantorabi & Gholami, 2017)). Cerium has an electronic configuration of $[\text{Xe}]4f^15d^16s^2$, and adopts stable Ce^{3+} and Ce^{4+} oxidation states with configurations of $[\text{Xe}]4f^1$ and $[\text{Xe}]$ (Jacobsen, et al., 2020; Singh, et al., 2021; Tu, et al., 2019; Wu, Zhang, Zhang, Ma & Alonso-Vante, 2022; Zhang, et al., 2019)

Several Ce(III)-MOFs have been synthesized with di, tri, and tetracarboxylate ions. Some of the commonest dicarboxylate ions that have

been employed include terephthalic acid (H_2BDC) and its substituted derivatives (H_2BDC-X and heterocyclic 1, 4-dicarboxylic acids). Terephthalic acid (H_2BDC) has been used for the synthesis of Ce(III)-MOFs by slow diffusion of Ce(III) nitrate and Na_2BDC in a water/DMF mixture forming rhombic channels (d'Arras, et al., 2014; Jacobsen, et al., 2020). Aminoterephthalic acid ($H_2BDC-NH_2$) has also been employed for the synthesis of Ce (III)-MOFs among other rare earth metals to obtain square-shaped channels (Tan, Zhao, Liu & Dai, 2015). Other dicarboxylate ligands such as 2,5-pyrazine dicarboxylic acid and 2, 3, 5, 6-tetrafluoroterephthalic acid have been employed to yield 3- dimensional mononuclear frameworks with topologies different from those of dicarboxylate containing compounds (Jacobsen, et al., 2020; Marinho, et al., 2017; Seidel, Lorbeer, Cybińska, Mudring & Ruschewitz, 2012) Aromatic dicarboxylic acids such as 9,10-anthracenedicarboxylic acid (H_2ADC), azobenzene dicarboxylic acid (H_2ABDC) and biphenyldicarboxylic acid (H_2BPDC) have been employed for Ce(III)-MOFs synthesis with varying topologies (Atzori, et al., 2018; Jacobsen, et al., 2020).

Among the tricarboxylates, Benzene-1, 3, 5- tricarboxylic acid (H_3BTC) is the most used ligand for the synthesis of Ce(III)-MOFs (Chevinly, Mobtaker, Yousefi, Shirani & Aghayan, 2017; Ethiraj, et al., 2016; Zhou, Shi, Xu & Cheng, 2013). Tricarboxylates linkers such as tris(2-carboxyethyl)isocyanurate (H_3TCI), 4,4',4''-{[(2,4,6-trimethylbenzene-1,3,5-triyl)tris-(methylene)]tris (oxy)}tribenzoic acid ($H_3TMOBTC$), tris-(4-carboxyphenyl)amine (H_3CPB), 2,4,6-tri-*p*-carboxyphenylpyridine (H_3CPP) and 1,3,5-tris(4-carboxyphenylethynyl) benzene (H_3CPEB) have been reported

for the synthesis of potentially porous Ce(III)-MOF (He, Tan & Zhang, 2013; Jacobsen, et al., 2020; Liang, Xu, Xue, Tao & Chen, 2016; Yao, et al., 2015) Tetracarboxylates linkers have also been used to synthesized cerium MOFs. Some include butane-1, 2, 3, 4-tetracarboxylic acid (H₄BTCA) (Jacobsen, et al., 2020; Rhauderwiek, et al., 2017; Wang, et al., 2015). Ce(III)-MOFs have been used in the sorption and separation of alkanes and CO₂. They have been employed as catalysts in reactions which include oxidation, asymmetric cyanosilylation and acetylation (Jacobsen, et al., 2020).

Zirconium-Based Metal-Organic Framework

Zirconium (Zr) 4+ ions and carboxylate ligands show strong coordination bonds due to their strong acidic and basic characteristics. Zr MOFs, therefore, exhibit high chemical and thermally stability with resistance decomposition in water as well as temperature up to 450 °C (Bon, et al., 2019; Dreischarf, Lammert, Stock, & Reinsch, 2017; Mouchaham, et al., 2015; Song, et al., 2019; Vakili, 2020; Xin, et al., 2021). The first Zr-MOF synthesized was UiO-66 from the University of Oslo. This is regarded as one of the most stable MOFs that has been reported (Ahmadijokani, et al., 2022; De Vos, Hendrickx, Van Der Voort, Van Speybroeck, & Lejaeghere, 2017; Dhakshinamoorthy, Santiago-Portillo, Asiri, & Garcia, 2019; Feng, et al., 2021). The UiO-66 was formed from the combination Zr₆O₄(OH)₄ clusters and 1, 4-benzenedicarboxylic acid (BDC) ligands to form a face-centred-cubic MOF structure.

The research into Zr-MOFs was unattractive some years back due to the formation of most often amorphous MOFs (Hu, et al., 2021; Li, Cai, Jiang,

He, & Zhu, 2019; Liu, Wang, Li, Chu & Zhou, 2023; Ozdemir, 2022; Shortall, Otero, Bendl, Soulimane, & Magner, 2022). Crystal formation is hindered due to the retardation of the rate of exchange of the ligand caused by Zr forming a strong bond with Oxygen from the ligand. Recently, crystalline Zr-MOFs are being synthesized upon the introduction of modulators in their synthesis (Liu, et al., 2020; Shan, et al., 2018; Nemiwal & Kumar, 2020). [74, 75]. These modulators either competitively bind with the metal clusters or repress the linkers' deprotonation. Terminal carboxylic such as formic acid, acetic acid and benzoic acid is most often used as modulators (Gutiérrez, et al., 2023; Hu, et al., 2021; Mohebbali, Moussavi, Karimi, & Giannakis, 2023; Piciorus, Alexandru, Ianasi, Szerb & Cretu, 2020; Shan, 2019; Zhong, Liu, & Zhang, 2018).

The research into the application of benzoic acid and modulators for the formation of UiO MOFs has been investigated. It was observed that benzoic acid hindered deprotonation by linkers by bonding with the metals allowing the formation of crystalline product. The increase in benzoic acid concentration increased the MOF's crystallinity (Shearer, Chavan, Bordiga, Svelle, Olsbye & Lillerud, 2016; Vakili, 2020). Large crystals were also obtained for UiO-68-NH₂ using benzoic acid as a modulator. UiO-68-NH₂ became the first Zr-based MOF with its single-crystal structure determined (Mansouri, Sadeghian, Mansouri, & Setareshenas, 2021; Yuan, et al., 2018). Modulators can be removed by the activation of the synthesized MOFs thermally. This thermal activation generates pores to improve adsorption and catalytic properties. (Fang, Bueken, De Vos, & Fischer, 2015; Vakili, 2020). .

Few synthetic methods have been employed to synthesize Zr MOFs. This includes solvothermal, microwave-assisted and electrochemical synthesis (da Trindade, et al., 2020; Li, et al., 2014; Rojas-Buzo, et al., 2021; Tan, bin Mohammad Latif & Rashid, 2022; Varsha & Nageswaran, 2020; Wang, et al., 2018; Zhou, et al., 2021) The solvothermal technique is however commonly used. The applications of Zr MOFs for catalysis are promising due to their proven chemical and thermal stability, abundant surface area, high pore volume and rich tunability.

Solvothermal Synthesis of Metal-Organic Framework

A variety of synthetic techniques have been developed since the inception of metal-organic frameworks. The hydrothermal process was the first technique used in developing nanomaterials including MOFs. With this technique, water was used as the solvent for the synthetic process. The hydrothermal technique was followed by the solvothermal technique where organic solvents rather than water were used as solvents in the synthesis (Li, Wu & Wu, 2016; Taghavi Fardood, Ramazani, & Woo Joo, 2017). Other new synthetic techniques which include mechanochemical, electrochemical, microwave, sonochemical, slow diffusion, slow evaporation methods and others have been developed in recent years (Adegoke & Maxakato, 2021; Emam, et al., 2020; Osman, et al., 2019; Panda, Patra, Awasthi & Singh, 2020; Tripathy, Subudhi, & Parida, 2021). Figure 10 shows the various synthetic methods since the inception of the metal-organic framework (Raptopoulou, 2021; Vakili, 2020).

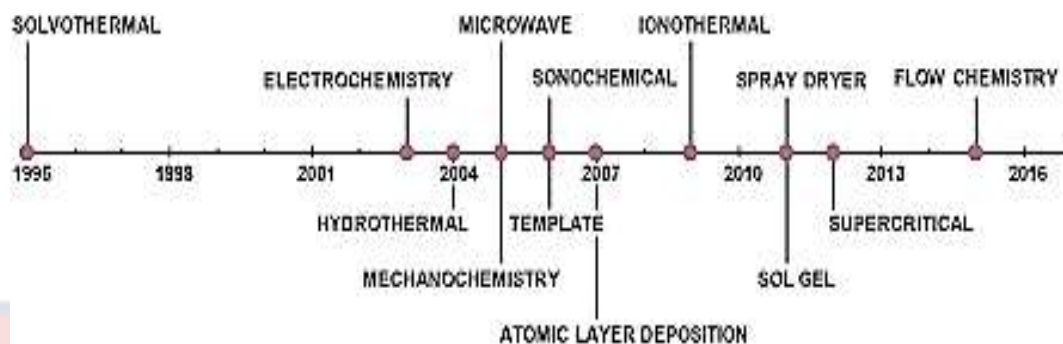


Figure 10: Development of synthetic techniques used for the formation of MOFs (Carreon & Venna, 2020)

The synthetic techniques for MOFs are however limited since MOFs should be good crystals chemically stable and easy to characterize hence one-step process is required for the complete formation and crystallization of MOFs (Li, 2013). Most of these developed techniques although exhibiting the advantages of synthesizing MOFs at low temperatures, under milder conditions and mostly at a short time have the disadvantage of forming amorphous and less crystalline metal-organic frameworks unsuitable for X-ray structural characterization (Raptopoulou, 2021; Vakili, 2020). Solvothermal synthesis of MOFs has shown to be very effective for the formation of well-crystalline MOFs due to the presence of solvents to aid solute solubility under high temperatures and pressure (Denisov, Primakov, Korlyukov, Novikov & Nelyubina, 2019; McKinstry, et al., 2016; Rojas-Buzo, et al., 2021; Zheng, et al., 2023; Zhou, et al., 2023; Zorainy, Sheashea, Kaliaguine, Gobara & Boffito, 2022).

The requirement of a well-formed MOF crystal has made the solvothermal synthetic technique the most used (Kareem, & Abd Alrubaye, 2019). Figure 11 shows the high percentage usage of the solvothermal technique compared with the other techniques. Publications on the use of the

solvothermal technique with related hydrothermal techniques show a great increase in the usage of the solvothermal techniques.

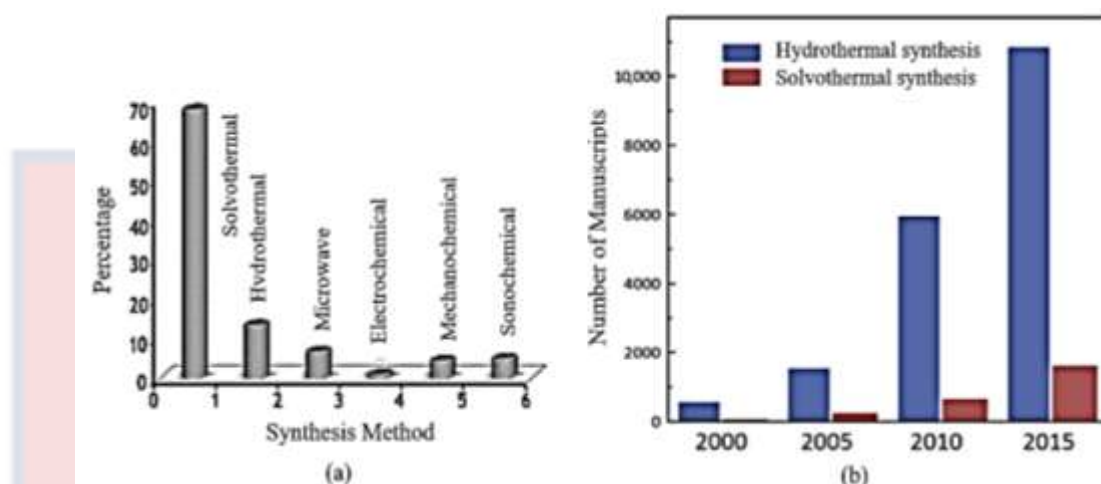


Figure 11: Comparison of the use of the solvothermal synthetic technique and other synthetic techniques for the synthesis of MOFs (Anish Khan, et al., 2019; Nunes, et al., 2019; Yanai, et al., 2012)

In the solvothermal process, the metal salt together with the organic linker in a suitable solvent is sealed in a closed system usually a hydrothermal autoclave at an elevated temperature and pressure for several hours to produce a crystalline product (Hsieh, Law, Lin & Tsai, 2022; Jiang, Wang, Wang, Chen & Zhang, 2016; Ma, Huang, Zhang, Wang & Wang, 2023; Shen, Guo, & Pang, 2022; Wang, et al., 2020). Polar solvents with high boiling points such as dimethylformamide (DMF), methanol (MeOH), water (H₂O), ethanol (EtOH), or their mixtures are mostly used. The synthesis is done at a temperature in the range between 50 and 260°C usually above the solvent boiling point and with an autogenous pressure. (Rocío-Bautista, Taima-Mancera, Pasán & Pino, 2019; Vakili, 2020). An elevated temperature and pressure in the sealed vessel are assumed to enhance the construction of quality stable crystals due to the increased solubility of reactants and intermediates. A reversible reaction process that slows the rate of product

formation leading to large crystal acquisition appropriate for X-ray analysis is acquired when solubility is high (Li, 2013; Jiang, et al., 2016; Ma, et al., 2023; Wang, et al., 2020). Synthesized MOFs are usually collected through filtration or by centrifuge, cleaned with suitable solvents such as methanol or DMF and then activated by heating. In the activation process, excess solvent held in the MOF pores is removed. A schematic diagram of the solvothermal synthetic procedure for the formation of MOFs is shown in Figure 12 (Rocío-Bautista, et al., 2019; Vakili, 2020).

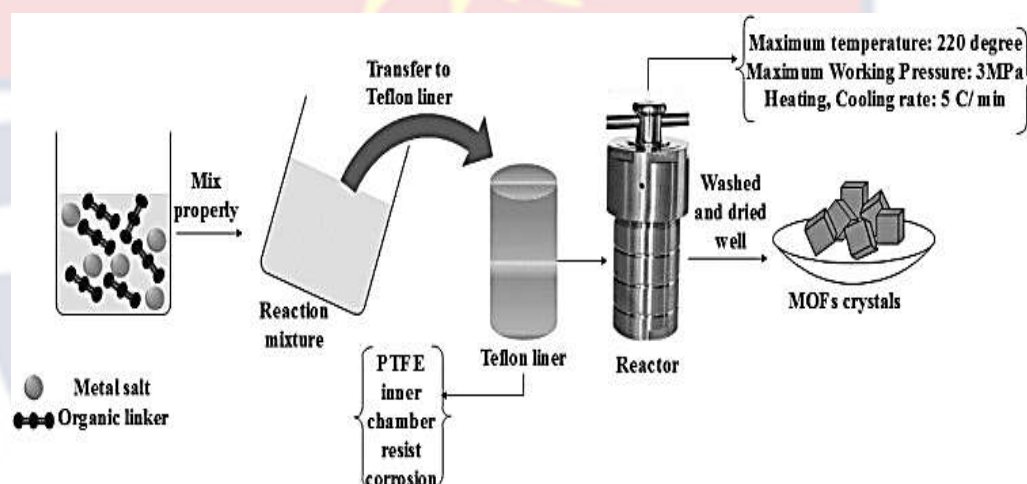


Figure 12: The solvothermal procedure for the synthesis of MOFs (Sud, & Kaur, 2021)

Synthetic Condition in Solvothermal Technique

MOF formation is not only dependent on the building units but also on other experimental conditions. (Feizbakhsh Bazargani, 2019). Consequently, a successful solvothermal synthesis depends on chemical and thermodynamic factors. The major chemical factors include the chemical and physicochemical properties of the solvent, the nature of the precursors, the pH value of the reaction medium and the characteristics of additives. The thermodynamic factors are mainly temperature and pressure (Hammond, Edler, Bowron &

Torrente-Murciano, 2017; Huo, Xiu, Meng & Quan, 2023; Jensen, Tyrsted, Bremholm, & Iversen, 2014; Kareem & Abd Alrubaye, 2019; Nandihalli, Gregory & Mori, 2022).

The role of the solvent in solvothermal processes

The selection of suitable solvents for MOF synthesis is vital since they affect the coordinate bonding between metal ions and organic ligands. The organic solvents for synthesis either coordinately bond to metals or behave as guests in the framework structure (Broge, Søndergaard-Pedersen, Roelsgaard, Hassing-Hansen, & Iversen, 2020; Vaquero, Navarro & Fierro, 2017; Bahramzadeh, Abdizadeh & Golobostanfard, 2015). The solvent mostly does not form part of the synthesized MOFs but directs the structural growth of the crystals during MOF formation (Kareem, & Abd Alrubaye, 2019; Seetharaj, Vandana, Arya, & Mathew, 2019). The solvents mostly used for MOF syntheses are polar with high boiling points. Polar solvents such as dimethylformamide (DMF), methanol (MeOH), water (H₂O), ethanol (EtOH), or their mixtures are mostly used. The presence of solvent promotes metal salt and organic ligand solubility hence increasing their reactivity at high temperatures and pressure (Anandan, Rajesh, & Rajendran, 2017; Bondesgaard, et al., 2016; Ding, et al., 2018; Huo, et al., 2023; Li, et al., 2016; Lu, Li, Hoang, Suib & Gao, 2021).

The physical and chemical properties possessed by the solvent can have diverse effects on the reaction media. The solvent affects reaction kinetics due to its ability to control the chemical species concentration in the reacting solution. It is capable of altering the solvated species coordination to

generate specific structures (Bahramzadeh, et al., 2015; Ding, et al., 2018; Feizbakhsh Bazargani, 2019; Kareem & Abd Alrubaye, 2019; Seoane, Castellanos, Dikhtiarenko, Kapteijn & Gascon, 2016). For instance, the carboxylate ligands deprotonation rate can be controlled by the appropriate application of related solvents such as DMF. At elevated temperatures, the DMF can be changed to its resultant amines leading to carboxylate deprotonation (Seetharaj, et al., 2019). Mixed solvents promote the nucleation of solvated species and enhance the process of crystal growth (Baloch, et al., 2021; Ding, et al., 2018; Nohara, Takeshita & Isobe, 2014). Solvent, therefore plays a vital role in the crystallization process by providing a rich crystallization environment during MOF formation and also in controlling the configurations of the MOFs leading to a variety of geometries.

The role of the counter ion of the reactants in solvothermal processes

The transition metals used for the metal-organic framework are usually positively charged and must be accompanied by anions to counterbalance the charge on the metal. These anions are therefore called counter ions. Most counter ions are inorganic anionic species which may act as coordination units, free guests, and hydrogen-bond acceptors (Al-Assy, Mahmoud, Husein & Mostafa, 2018; Bøjesen & Iversen, 2016; He, Hashemi, Hu, & Morsali, 2018; Lin, Usov & Morris, 2018; Rachuri, Parmar, Bisht & Suresh, 2017; Walton, 2020). Examples include N^{3-} , ClO_4^- , PF_6^- , BF_4^- , NO_3^- , NCS^- , NO_2^- , CN^- , SO_4^{2-} , and halides, which are combined with the metal cations ions from the corresponding metal salts.

Although counter ions do not participate in the coordination between the metal cations and the organic linkers they can lead to diverse coordination structures through their effect on the coordination products crystallization (Brandi, Antonietti & Al-Naji, 2021; Catto, et al., 2020; El-Berry, Sadeek, Abdalla & Nassar, 2021; Gupta & Paul, 2014; Mruthunjayappa, Kotrappanavar & Mondal, 2022; Zhang, et al., 2020). The Counter ions have a vital characteristic of the behaviour of forming hydrogen bonds due to electron-donating atoms. Different counter ions exhibit diverse hydrogen bonding behaviour and coordinate differently with metal cations and the other components of the complex which diversify the rate of crystallization for the formation of different complexes (Feizbakhsh Bazargani, 2019).

The role of modulators used in solvothermal processes

Modulators are commonly monocarboxylic acids which are used as auxiliaries in a reaction mixture during the synthesis of MOF to improve crystal formation and reproducibility of the MOF. The modulators prevent impurity formation and slow reaction rate for the formation of the MOFs through their competition with the organic ligands to bind to the metal centres (Bagherzadeh, Zebarjad, & Hosseini, 2018; Bagherzadeh, Zebarjad, Hosseini & Chagnon, 2019; Bao, Cai, Shi & Pang, 2017; Li, et al., 2014; Ji, et al., 2021; Majewski, Noh, Islamoglu & Farha, 2018; Marshall, Staudhammer & Brozek, 2019; Tajnšek, Zabukovec, Logar & Mazaj, 2023; Wasson, et al., 2020; Zahn, et al., 2014; Zhou, et al., 2020). Generally, two modulation mechanisms are possible which include deprotonation and coordination.

In the deprotonation, the modulators behave as bases to improve organic linker deprotonation consequently, aiding the organic linker attachment to the metal clusters to accelerate the formation of MOFs. The deprotonation modulation mechanism was observed in ZIF-8 synthesis using formic acid as a modulator (Zahn, et al., 2014). In the coordination mechanism of modulation, the modulator contests with the organic linkers to form bonds with the metal clusters. The competition leads to a slow rate of nucleation and crystal growth which yields large crystals. This is common in zirconium MOF synthesis. The coordination mechanism impedes amorphous or gel precursor formation (Liu, et al., 2020; Nemiwal & Kumar, 2020; Shan, et al., 2018; Zahn, et al., 2014).

The acidic property of Modulators has been observed to affect MOF defects (Assaad, Sabeh & Hmadeh, 2020; Cox, Slavich, Macreadie, McKemmish & Lessio, 2023; Hu, Kundu, Wang, Sun, Zeng & Zhao, 2020; Liu, et al., 2021; Morris, et al 2017). A study on four modulators with varying acidity was performed to investigate their effect on the defect in zirconium (UiO) MOFs which has $Zr_6(OH)_4O_4(CO_2)_{12}$ as metal clusters and 1, 4-dicarboxylic acid (H_2BDC) as the linker. Difluoroacetic acid ($pK_a = 1.24$), trifluoroacetic acid ($pK_a = 0.23$), formic acid ($pK_a = 3.77$) and acetic acid ($pK_a = 4.76$) as modulators were accessed. Difluoroacetic acid and trifluoroacetic acid were easily deprotonated due to their lower acidity compared with H_2BDC linkers ($pK_{a1} = 3.51$, $pK_{a2} = 4.82$), dominating the competition to bond to $Zr_6(OH)_4O_4(CO_2)_{12}$ clusters than carboxylates, hence, producing high defects in UiO MOF. The acetic acid, with pK_a comparable to that of H_2BDC linker, had close competition with the carboxylate to bond to

the Zr clusters, resulting in comparatively low defects (Shearer et al., 2016; Vakili, 2020).

The role of the pH value in different solvothermal processes

Acid-base reactions form an important part of the formation coordination assembly of MOFs. MOF synthesis involves the coordination between acidic metal ions and basic organic linkers. The formation of MOF crystals is greatly influenced by how acidic or basic a reaction medium operates. The rate of reaction can be influenced by variations in pH conditions (Demazeau, 2011; Guo, Wu, Xie, Zhang, Cao & Zhao, 2014; Jin, Chen, Pei, & Xu, 2012; Li, et al., 2021; Liu, Zhao, An & Chang, 2015; Sarmadi, Msoudpanah & Alamolhoda, 2022; Venkateshalu, Kumar, Kollu, Jeong & Grace, 2018; Weixia, Gaoling, Qifu, & Xingyong, 2015; Yang, Yang, Li, Li & Cao, 2016). Extremely low pH will hinder the coordination of N-donor ligands owing to protonation. Additionally, there is a slow formation of anionic ligands due to the inability of organic ligands to deprotonate efficiently. Extremely high pH also results in quick deprotonation of organic ligands producing less crystalline MOFs (Makal, 2015).

The pH of a reaction solution for the synthesis of MOFs has a significant impact on determining the modes of coordination of organic ligands employed in the synthesis. Appropriate reaction pH adjustment causes organic ligand deprotonation and occasionally OH-bonding of the ligand in an aqueous environment to enhance the coordination between the organic ligand and metal clusters (Feizbakhsh Bazargani, 2019; Guo, et al., 2014; Li, et al., 2021, Weixia, et al., 2015). The pH of a reaction media for distinct

solvothermal processes can result in the formation of particular compositions in MOF synthesis, encourage the formation of specific stabilized structural forms and control the crystal formation (Guo, et al., 2014; Jin, et al., 2012; Kareem & Abd Alrubaye, 2019).

The role of the temperature of the reactants in solvothermal processes

Temperature plays a vital role in the synthesis and the properties acquired by the synthesized MOFs. The rate of crystal formation and growth is influenced by the temperature of the synthetic reaction medium (Arumugam, Raj, Irudayaraj & Thambidurai, 2018; Aslibeiki, et al., 2016; Bincy, 2017; Fan, Meng, Zhang, Wu, Sun, & Li, 2016; Khatter & Chauhan, 2020; Lai, et al., 2019; Olatunde & Onwudiwe, 2021;). The temperature for solvothermal reactions can have a great influence on the synthetic process. Such influence includes the solubility and stability of the metal salts and the organic ligands, the chemical reaction kinetics, the solvent chemical composition, crystal morphology as well as the oxidation state of the metals (Kareem, & Abd Alrubaye, 2019; Raptopoulou, 2021).

The temperature variation can change the topologies of MOFs formed from the same kind of metal clusters and linkers (Schweighauser, Harano, & Nakamura, 2017; Xing, Schweighauser, Okada, Harano & Nakamura, 2019). A typical example is the formation of a square lattice MOF-2 and a cubic lattice MOF-5 shown in Figure 13. Both MOFs formed from heating a reaction mixture of zinc nitrate and 1, 4- benzene dicarboxylic acid (H_2BDC) in dimethylformamide (DMF) at different temperatures. MOF-2 is formed by

heating the mixture at 95 °C for several hours while MOF-5 is formed by heating the mixture at 120 °C for several hours.

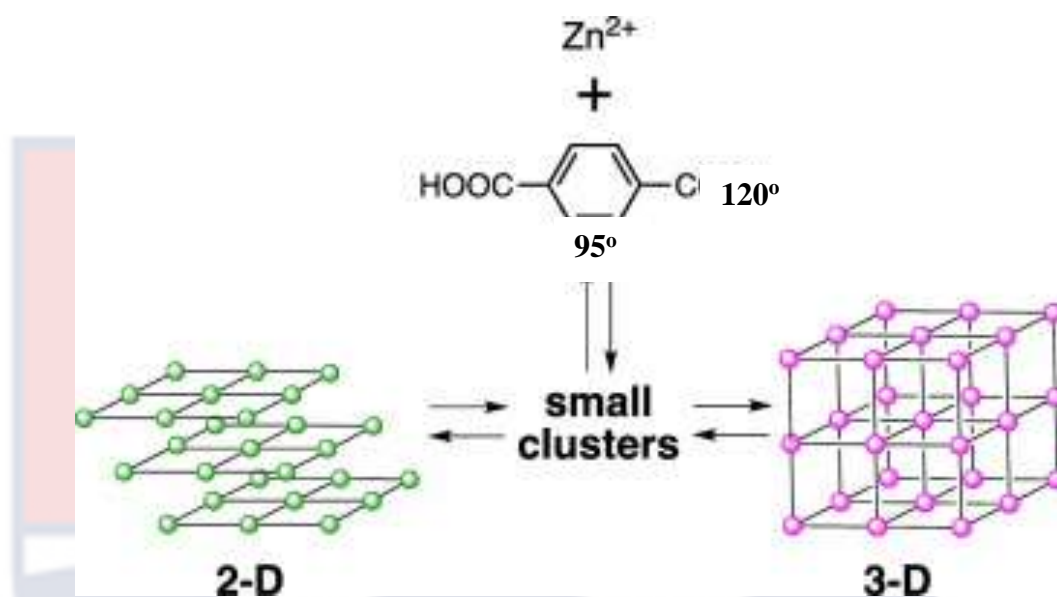


Figure 13: Formation of MOF-2 and MOF-5 crystals (Schweighauser, et al., 2017)

High temperature yields high reactant solubility which slows crystal growth kinetics. The slow crystal growth accelerates the formation of bonds and enhances crystallization producing superior crystals (Bagherzadeh, Zebarjad, Hosseini, & Khodaei, 2022; Cao, et al., 2020; Fan, et al., 2016; NaderiNasrabadi, Mortazavi & Khodadadi, 2016; Pang, et al., 2015).

Inappropriate high temperatures may however result in the decomposition of synthesized product. Improper cooling of synthesized products may also affect the growth of crystals (Feizbakhsh Bazargani, 2019; Soni, Bajpai, & Arora, 2020; Raptopoulou, 2021). Slow cooling of the product is required to ensure good crystal growth. Temperature variations can lead to different synthesized MOF morphologies from MOFs produced from the same reactant.

The role of the pressure of the reactants in solvothermal processes

In solvothermal processes, a large pressure range help stabilizes more condensed complexes (Assat, & Manthiram, 2015; Demazeau, 2010; Silmi, et al., 2021; Wang, Li, Xu, Xu, & Li, 2019; Wang, et al., 2016; Zhou, et al., 2017). The domain of reactants' thermal stability is enlarged when the pressure has a large operating range. The reactants' chemical reactivity kinetics for the reactions are also enhanced under large pressure (Demazeau, 2010; Silmi, et al., 2021; Zhou, et al., 2017). In a solvothermal reaction, the pressure may depend on the reaction vessel filling (autogenous) or be applied at a value above 1 bar (105 Pa) at the beginning of the reaction through to the end (imposed) (Demazeau, 2010).

Metal-Organic Frameworks (MOFs) as Heterogeneous Catalysts

Catalysis has become one major industrial element for several essential chemical processes. About 90% of industrial catalytic application processes have been reported annually with the chemical industry having a major share followed by the refinery and environmental industries (Cermelj, Ruengkajorn, Buffet, & O'Hare, 2019; Vakili, 2020). The catalysts used for industrial processes are mostly heterogeneous catalysts, homogeneous catalysts and biocatalysts. Among these three catalysts, the use of heterogeneous catalysts which are mostly in the solid form dominates in application (Bhushan, Kumar & Thakur, 2020; Chen, Xu, & Mavrikakis, 2020; Chen, et al., 2014; Corma, 2016; Friend, & Xu, 2017 Wang, Li, Xu, Xu, & Li, 2019; Lalhriatzuala, & Agarwal, 2021; Li, et al., 2018; Ma, et al., 2018; Védrine, 2017; Vakili, 2020; Van Santen, 2017). The stability of these heterogeneous catalysts as

well as the ease of separation from the reaction mixture makes them more desirable (Cermelj, et al., 2019; Vakili, 2020; Waclawek, Padil, & Černík, 2018).

MOFs have recently been found to be promising as solid heterogeneous catalysts. This is due to the ability to smoothly manipulate the inorganic metals and the organic ligands to produce different stable solid structural MOFs with remarkably large surface areas of about $10,000 \text{ m}^2 \text{ g}^{-1}$, 90% high porosity and 0.13 g cm^{-3} low density. These qualities make MOFs to be easily tuned to function as heterogeneous catalysts for adsorption with easy separation and recovery (Bhattacharya, et al., 2020; Guo, et al., 2021; Luo, et al., 2019; Rao & Mandal, 2019; Vakili, 2020; Zhang, Yang, & Zhou, 2018). The inorganic metals or the organic ligands of the MOFs can be designed to possess the catalytic property by direct synthesis, post-synthesis modification or the introduction of diverse catalytic functions such as metal nanoparticles into the MOFs pores with the MOFs serving as host (Jiao, Wang, Jiang & Xu, 2018; Vakili, 2020).

The great tunability property of MOFs concerning their physicochemical properties can enhance the production of MOFs with multifunctional catalytic properties. This is achieved through stern manipulation of the various catalysts' active sites based on their nature and inter-distances in a chronological reaction. Consequently, the flexible control over the MOFs to incorporate catalytic active sites in them offers a brilliant advantage of producing novel catalysts with high catalytic performance for various applications

Coloured Organic Pollutants in Water

Water pollution is a serious environmental problem worldwide. Rapid advancement in industrial and economic activities causes a drastic increase of inorganic and organic pollutants in water bodies which poses a great health threat to humans as a result of insufficient amount of hygienic or quality water. Over 1.2 billion people are experiencing water scarcity worldwide (Tesh & Scott, 2014). The permeation of organic pollutants into the environment may result in the detection of varying concentrations in water bodies and this is extremely worrying due to their substantial toxicological effect on plants, animals and humans (Affat, 2021; Alharbi, Khattab, & Ali, 2018; Kaur, Badru, Singh & Kaushal, 2020; Lu, & Astruc, 2020; Sousa, Ribeiro, Barbosa, Pereira & Silva, 2018; Wang, Li, Lv, Zhang, & Guo, 2014; Wang, et al., 2019).

These organic pollutants mainly emanate from industries that produce organics and industries that use organics for their production activities. Some of these major industries include the pharmaceutical, petroleum, agrochemical, petrochemical, dye and dyeing industries. Out of these organic pollutants, organic colours mainly dyes pose much danger to the water bodies and the environment due to the high level of effluents discharged from dye production and various dye application industries (Fakin & Ojstršek, 2013; Goswami, Deepika, Chandra, Babu & Kothamasi, 2023; Gusain, Gupta, Joshi, & Khatri, 2019; Hanafi & Sapawe, 2020; Le, Duy, Cheong & Pung, 2022). Above 7×10^5 tons of over 10000 kinds of dyes are estimated to be produced worldwide with approximately 10% lost as industrial effluents (Saxena & Gupta, 2022).

These dyes are used as colourants by many industries which include the textiles, printing, rubber, plastics paper, cosmetics, pharmaceutical and leather industries. Some of these are also used as pH indicators, tracers and stains in various scientific fields. The dye effluents released through dye production and application in industries may contain a varied range of organic pollutants with dyes dominating with the potential to cause severe ecotoxicological hazards (Mehra, Singh & Chadha, 2021; Saxena & Gupta, 2022; Singh, Kumar & Srivastava, 2017; Varjani, Rakholiya, Ng, You & Teixeira, 2020). Table 1 shows some commonly used organic dyes that pollute our water bodies. The presence of these dye effluents in the water bodies causes a reduction in sunlight penetration and upsurges biochemical oxygen demand (BOD) as well as chemical oxygen demand (COD). These obstructions affect photosynthetic activity and obstruct the growth of aquatic plants.

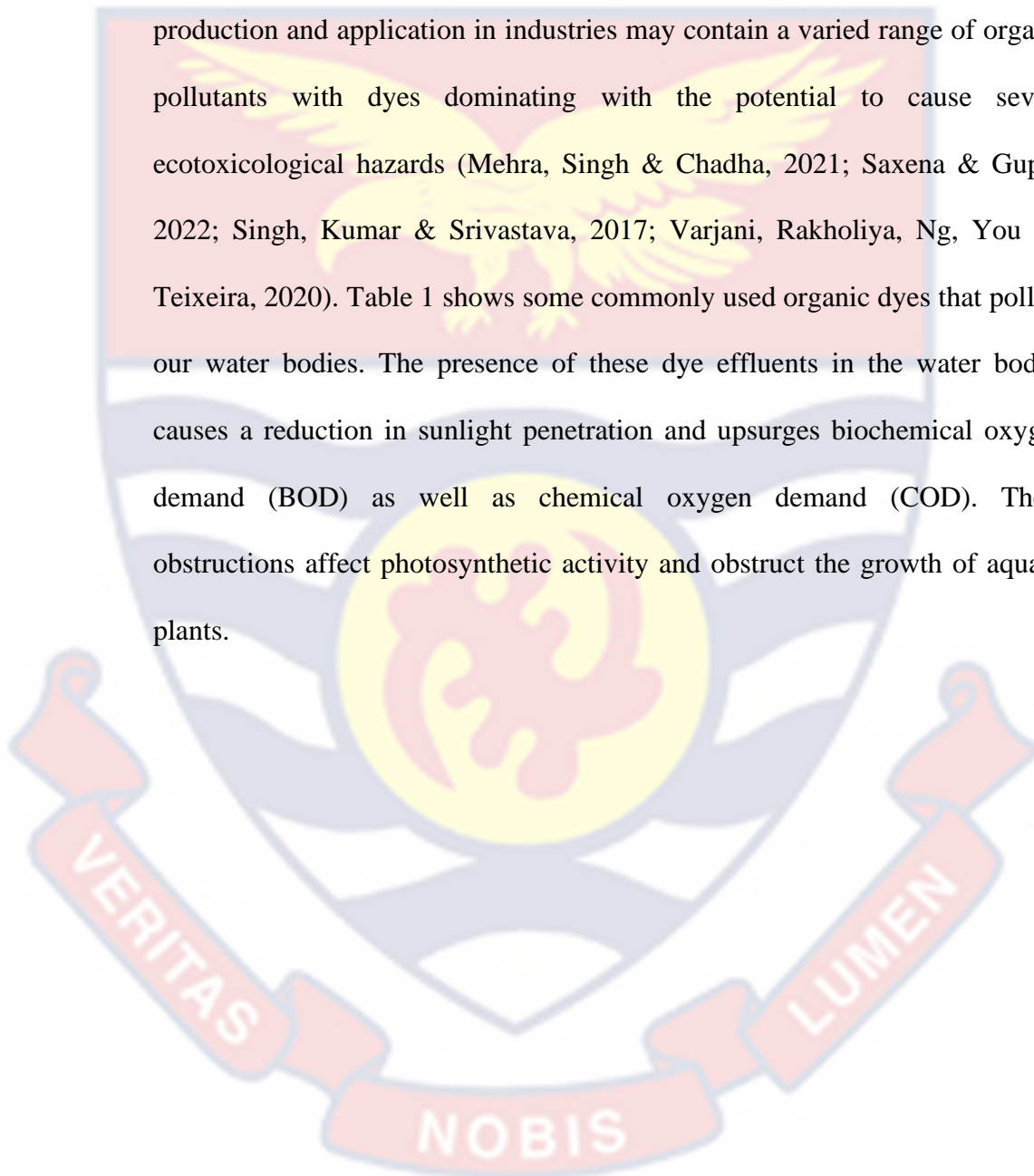
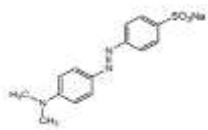
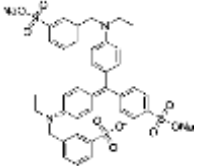
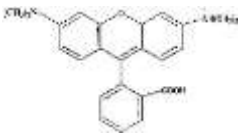
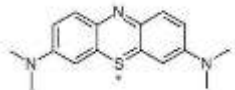
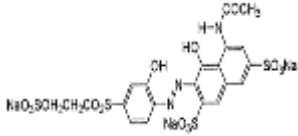
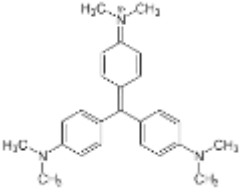


Table 1: Some Commonly used Organic Dyes that Pollute Water

Dyes	Type	Application
 Helianthine B (Methyl orange)	Acid dye	Acid-base indicator in titration
 Lissamine green (Light green SF)	Acid dye	Staining of bacteria, algae and yeast.
 Tetraethylrhodamine (Rhoamine B)	Basic dye	Tracer in water to define the rate and direction of flow
 Chromosmon (Methylene Blue)	Basic dye	Bacteriologic stain for bacterial cells under the microscope. Test the purity of milk
 Remazole brilliant violet 5R	Reactive dye	As a textile dye for colouring cellulosic fibres.
 Pyoktanin (Gentian violet)	Basic Dye	Treating fungal infections of the skin and minor cuts to prevent infection

Source: Industrial dyes (Hunger, 2003)

Additionally, these dyes can break down into harmful intermediates in aquatic animals when consumed, consequently, having a negative health impact on both animals and their consumers (Affat, 2021; Al-Tohamy, et al., 2022; Avallone, et al., 2022; Berardi, et al., 2019; Chavan, 2013; Hassaan, El Nemr & Hassaan, 2017; Olas, Bialecki, Urbańska & Bryś, 2021). These

harmful intermediates may be carcinogenic and mutagenic to consumers. Furthermore, most farmers in developing countries use untreated industrial effluents containing dyes for irrigation which has a damaging effect on crop growth. Toxicity research on some of these dyes revealed effects such as reproductive toxicity, genotoxicity, cancerous tumours and neurotoxicity (Al-Tohamy, et al., 2022; Jiku et al., 2021; Wu, et al., 2017)

MOF as Photocatalyst

Recent developments in the photoactivity of MOFs have revealed that a variety of MOFs display remarkable charge separation characteristics under light irradiation when various light-harvesting functional components are incorporated into them (Ferreira da Rosa, et al., 2021; Su, et al., 2023; Surib, Kuila, Saravanan, Sim & Leong, 2018). The MOFs may exhibit photocatalytic properties directly from their metal centres or organic linker active sites. They may also act as carrier transports as a result of metal clusters or organic linkers' photoexcitation. MOFs have been shown to have conduction and valence bands which are typical with semiconductors (Bouider, et al., 2023; Huo, et al., 2016; Wang, et al., 2022; Zhang, Huang, Jin, Gan & Zhang, 2021; Zhao, Wang & Pei, 2022). The conduction band in the MOFs relates to the metal centre empty outer orbitals while the valence band refers to the organic linker outer orbitals. The abundance of a variety of organic linkers and metal centres gives MOFs the advantage of being tuned to possess a high light absorption capacity as compared with traditional inorganic photocatalysts (Huang, et al., 2020; Wang, et al., 2022; Zhang, et al., 2021). The photoactive behaviour of MOFs has made them possible to be used as photocatalysts for

activities such as for photodegradation of water pollutants, photogeneration of oxygen and hydrogen gases and photoreduction (Dong, Shi, Li, & Wang, 2019; Ramalingam, et al., 2022; Wang, et al., 2022; Wu, et al., 2017; Zhang, et al., 2021)

Recently, the synthetic applications of MOFs photocatalysts for the production of organic molecules with varying complexity have been explored (Chen, Wang, Deng & Li, 2017; Dhakshinamoorthy & Garcia, 2018). MOF photocatalysts have also been employed for artificial photosynthesis and the reduction of CO₂ (Chen, et al., 2017; Cui, Zhang, He & Qian, 2018; Samanta, Desai, Let, & Ghosh, 2019). The photocatalytic activity of synthesized MOFs-based photocatalysts for efficient production of hydrogen from water has been investigated with a detailed summary of related works reviewed showing an impressive achievement in the application of such MOFs for efficient photolysis of water to yield hydrogen (Chen et al., 2022; Shi, Yang, Cao & Zhao, 2019). Multivariate MOF-based nanostructures have been used as photocatalysts for multifunctional applications in environmental remediation and renewable energy such as organic pollutant degradation, reduction of CO₂ to produce largely CH₄ and reduction of Cr (VI) (Patial, et al., 2021). Figure 14 shows the structural motifs of some MOF photocatalysts that have been used for various catalytic organic reactions.

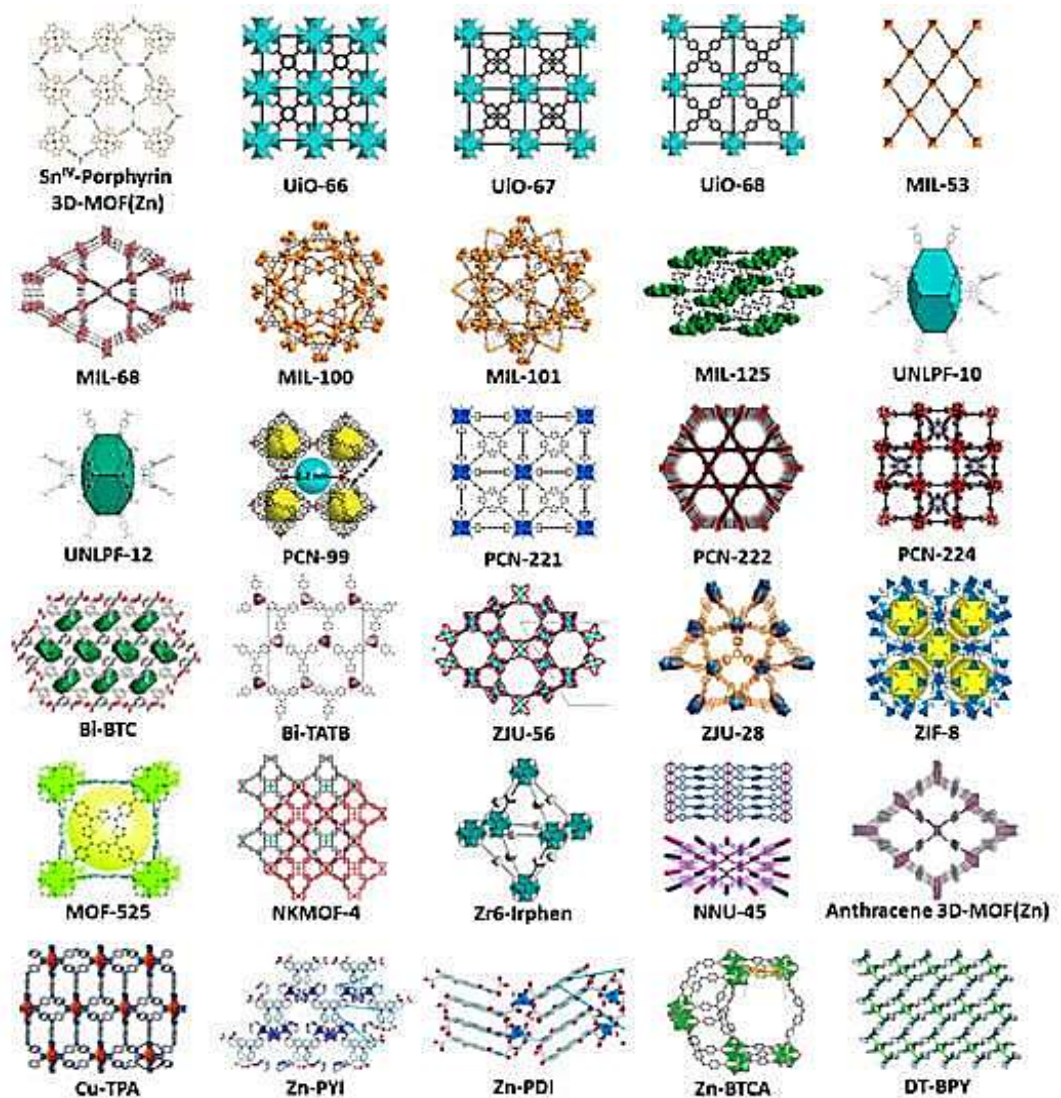


Figure 14: Structural motifs of MOFs used for photocatalysis (López-Magano, Jiménez-Almarza, Alemán & Mas-Ballesté, 2020)

Mechanism of Metal-Organic Frameworks as Heterogeneous Photocatalyst for Organic Pollutant Degradation

Metal-organic frameworks (MOFs) as heterogeneous photocatalysts should have the ability to capture light and have a light excitation period that produces charge separation. An efficient electron-hole separation is obtained in MOFs by the transfer of photogenerated electrons from the organic ligands onto the surfaces of metal clusters through ligand-to-metal charge transfer

(LMCT) (Huo, et al., 2016; Majee, Singha, Mondal, & Mahata, 2019; Su, et al., 2023; Yang, et al., 2020; Zhao, et al., 2022; Zhao, Wang, Zhu, Liu & Pei, 2021). The amount of energy absorbed by MOF for excitation is given as E_{abs} . This energy is directly related to E_g , the band gap between the highest occupied molecular orbital (HOMO) and lowest unoccupied molecular orbital (LUMO) of ligands and E_{LMCT} , the energy necessary to transfer the photogenerated electrons from the LUMO of the ligands to the LUMO of the metal clusters (An, et al., 2021; Ferreira da Rosa, et al., 2021; Su, et al., 2023; Surib, et al., 2018; Wu, Gagliardi & Truhlar, 2018; Zhao, et al., 2022; Zhang, et al., 2023). A relationship from the three parameters can be expressed in equation (1);

$$E_{\text{abs}} = E_g + E_{\text{LMCT}} \quad (1)$$

Charge separation is better when E_g is constant with E_{LMCT} approaching zero or negative. This condition results in a smaller absorbed excitation energy (E_{abs}) to enhance visible light absorption. (Chanu, et al., 2020; Das, Manna, Pathak & Nagaraja, 2022; Miyasaka, 2013; Qiu, et al., 2018; Yin, et al., 2021; Wang, et al., 2020) MOFs comprising high-energy lone pair carrier ligands and low-lying empty orbital metals show efficient photocatalysis resulting from favourable E_{LMCT} . Ligand manipulation, metal-node substitution and defect engineering are possible approaches to enhance the LMCT activity (Mezenov, Krasilin, Dzyuba, Nominé & Milichko, 2019; Ortega-Guerrero, Fumanal, Capano, Tavernelli, & Smit, 2020; Treto-Suárez, et al., 2023; Tripathy, Subudhi, Ray, Behera, Bhaumik & Parida, 2022; Usman, Mendiratta & Lu, 2017; Wang, Gao, Al-Enizi, Nafady & Ma, 2020; Zhuang & Liu, 2020).

The photocatalysis mechanism of MOF photocatalyst operates on principles similar to that of traditional semiconductors. The HOMO/LUMO in MOFs performs a similar function as the CB/VB in semiconductors (Gautam, et al., 2020; Hang, et al., 2022; Hou, Yuan, Niu, Li, Wang & Zhang, 2022; Qian, et al., 2019; Zhang, Wang, Dong & Lv, 2020). In MOF photocatalysis electrons transit from the highest occupied molecular orbital (HOMO) to the lowest unoccupied molecular orbital (LUMO) when excited by an incident light (Dong, et al., 2019; Huang, et al., 2020; Ramalingam, et al., 2022; Wang, et al., 2022; Zhang, et al., 2021; Zhang, et al., 2021).

The transition of electrons generated from the HOMO leaves holes in the HOMO. The transitioned electron in the LUMO during photolysis is trapped by oxygen molecules reducing the molecules to yield superoxide radical ($\bullet\text{O}_2^-$) which is a strong oxidant (Endashaw & Girma, 2020). The holes (h^+) generated in the HOMO after the transition of photogenerated electrons to LUMO possess a strong oxidant ability. This gives it the ability to directly adsorb pollutants as well as oxidize the surface hydroxyl group or water to generate hydroxyl radicals ($\bullet\text{OH}$). The hydroxyl radicals ($\bullet\text{OH}$) formed are also a strong oxidant which is capable of reacting eagerly with surface-adsorbed pollutants. The activity of these generated radicals and holes can lead to pollutant degradation. (Endashaw, & Girma, 2020; Qiu, et al., 2018; Saha, Chaudhary, Kumar & Khanuja, 2020). The overall mechanism of the active species generation for the degradation process is shown in Figure 15.

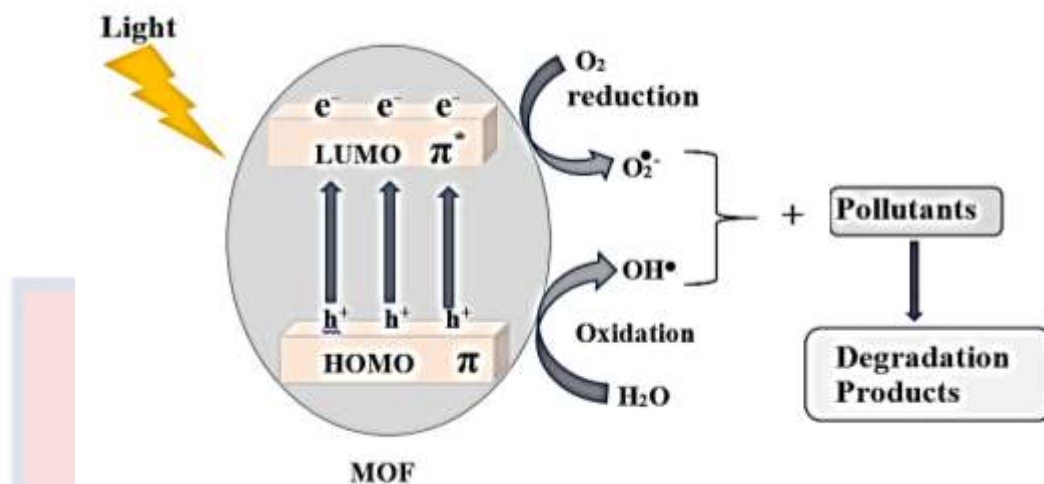


Figure 15: Mechanism of photocatalytic dye degradation (Saha, et al., 2020)

The overall heterogeneous catalytic process can be categorized into five autonomous steps (Endashaw & Girma, 2020). These steps include the transfer of the pollutants to the catalyst surface from solution, adsorption of the pollutants on the photoactivated catalyst surface, photocatalytic degradation of the adsorbed pollutants by photoactivated catalyst, desorption of pollutant intermediates product from the catalyst surface and transfer of the pollutant intermediates product from catalyst surface to the solution.

Chapter Summary

In this chapter, literature on metal-organic frameworks as porous coordination polymers has been reviewed. A review of inorganic metals and organic bridging ligands for a metal-organic framework with an emphasis on carboxylate ligands has been outlined. Literature on copper, cerium and zirconium as the metal clusters for the synthesis of the metal-organic frameworks was highlighted. A review of the synthetic techniques for metal-organic framework focusing on the solvothermal synthesis technique has been

made. Literature on the catalytic application of metal-organic frameworks focusing on their photocatalytic application has also been captured.



CHAPTER THREE

RESEARCH METHODS

Introduction

The experimental materials, chemicals, equipment and procedures used in the present study are discussed in this chapter.

Reagents and Chemicals

All reagents used were of HPLC grade and were used as obtained. All chemicals were used as obtained. The reagents and chemicals used in this study are shown in Table 2.

Table 2: List of Reagents and Chemicals Employed in the Present Study

Reagents/ Chemical	Purity (%)	Supplier	Purpose
5-Aminobenzene-1, 3- dicarboxylic acid	94.0	Aldrich Chemistry, China	Linker for MOF synthesis
Benzene- 1, 3, 5- tricarboxylic acid	95.0	Aldrich Chemistry, China	Linker for MOF synthesis
Copper (II) nitrate trihydrate	98.0	Sigma Aldrich. Spain	Metal for MOF synthesis
Cerium (III) nitrate hexahydrate	99.9	Central Drug House (P) Ltd. India	Metal for MOF synthesis
Zirconium (IV) oxynitrate hydrate	99.0	Sigma Aldrich, USA	Metal for MOF synthesis
N, N- Dymethylformamide (DMF)	99.0	Daejung Chemicals and Metals Co. LTD, Korea	Solvent for MOF synthesis and purification
Methyl alcohol (CH ₃ OH)	99.9	Daejung Chemicals and Metals Co. LTD, Korea	Solvent for MOF purification

Ethyl alcohol anhydrous (C ₂ H ₅ OH)	99.9	Daejung Chemicals and Metals Co. LTD, Korea.	Solvent for MOF synthesis and purification
Acetone	99.8	Daejung Chemicals and Metals Co. LTD, Korea	Solvent for MOF purification
Acetic acid	99.7	. T. Baker, Avantor Performance Materials. Inc, USA	Modulator for MOF synthesis
Ultrapure water	100	Department of Chemistry, University of Cape Coast, Ghana	Solvent for MOF synthesis
Sodium Hydroxide (NaOH)	50	Quality Reagent Chemical	pH adjuster
Hydrochloric acid (HCl)	37	Quality Reagent Chemical	pH adjuster
Lissamine green	65.0	Paskem Finechemical Industries, India	Pollutant
Tetraethylrhodamine	≥95	Paskem Finechemical Industries, India	Pollutant
Remazole brilliant violet 5R	~35	Santa Cruz Biotechnology, Inc. USA	Pollutant

Source: Reagents and chemicals suppliers (2021)

Instrumentation

Various instruments were used for the experimental and analyses of the results of the study. All instruments used were of standard quality to give accurate results.

Hydrothermal autoclave

A 100 ml Teflon lined hydrothermal autoclave reactor manufactured by Shanghai Shenheng Biological Technology Co., Ltd is shown in Figure 16. The autoclave was used as a vessel for the metal-organic framework synthetic process. The reactor mainly consists of the outer stainless steel vessel and inner Teflon liner. The Teflon liner has a maximum operating temperature of 240° C and pressure of 3MPa with a heating and cooling rate of 5 c/min. The reactor also has an upper and lower stainless steel disc to provide stable sealing, a high-quality stainless steel cap and a stainless steel rod for locking the cup.



Figure 16: Hydrothermal autoclave

Magnetic stirrer hot plate

The Heidolph MR Hei-Standard magnetic stirrer hot plate at the Chemistry Department Laboratory, University of Cape Coast is displayed in Figure 17. The magnetic stirrer hot plate was used to heat and/or stir substances to a specified temperature and/or speed. It consists of a main

switch, a speed control knob to set speed and, a heating button to set and regulate heat. The device has a maximum heating temperature of 300 °C and a speed capacity of 1400 rpm.



Figure 17: Heidolph MR Hei-Standard magnetic stirrer hot plate

Oven

The Ecocell 55 oven manufactured by MMM Medcenterat at the Chemistry Department Laboratory, University of Cape Coast is shown in Figure 18. The oven was used as the heating source for the syntheses and drying of the metal-organic frameworks. It has external dimensions of (W) x (D) x (H): 62 x 64 x 68 cm and interior dimensions of (W) x (D) x (H): 40 x 37 x 36 cm. The Ecocell 55 oven has two shelves of 55-litre capacity. The oven has a heating indicator light, a power indicator light and a setting mode activation key for operational use. It has a voltage of 230 V, a power of 1290 W and a nominal temperature of +250 °C.



Figure 18: EcoCell 55 oven

Centrifuge

The VWR[®] Mega Star 600 centrifuge is displayed in Figure 19. The centrifuge located at the Chemistry Department Laboratory, University of Cape Coast was used for filtration and recovery of synthesized compounds. The VWR[®] Mega Star 600 centrifuge is a 370 × 490 × 310 mm size system with a TX-150 rotor, a set of glove-friendly buckets and ClickSeal[®] caps. The TX-150 rotor with a maximum capacity of 4x 145ml and speed of 4350 min⁻¹ offers high speed and high capacity combined with the flexibility of a wide range of adapters. The ClickSeal[®] bucket caps and rotor lid sealing system are glove-friendly with one-handed open and close ability. The Mega Star 600 centrifuge has an Auto-Lock[®] III rotor locking system and a Large, bright LED that provides a reflective backlit to easily aid parameter readings.



Figure 19: VWR[®] Mega Star 600 centrifuge

Fourier transform infrared (FTIR) spectrometer

Fourier Transform Infrared (FTIR) analyses of the synthesized compounds were measured with the Bruker Alpha Spectrometer at the Central Lab., located at the Kwame Nkrumah University of Science and Technology. The Bruker Alpha Spectrometer is a tabletop single reflection ECO-Attenuated Total Reflection (ATR) compact spectrometer. The spectrometer consists of a ZnSe ATR crystal, an anvil and a surface area. The ZnSe ATR crystal has a focal plane array of 6000 to 400 cm^{-1} and a single point detector ranging from 7500-400 cm^{-1} . The spectrometer has an analyzing area of 128 x 128 in 2D format on the sample plane 300 x 300 μm . It has a spectral resolution of 0.2 cm^{-1} and a rapid scan of 65 spectra/sec at 16 cm^{-1} . The Bruker Alpha FTIR Spectrometer does not need any sample preparation and is easy to use to analyze both solids and liquids.

X-ray diffractometer (XRD)

X-ray diffraction (XRD) analysis was done to study the crystal phase of synthesized metal-organic frameworks. The XRD analysis was carried out using Empyrean X-ray Diffractometer at the Department of Physics, University of Ghana. The Empyrean X-ray Diffractometer consists of a steel diffractometer enclosure with two interlocking front doors and the electronics and support unit. The doors of the diffractometer enclosure have transparent lead glass windows. The diffractometer enclosure contains the incident beam optical module, goniometer, diffracted beam optical module, detector, sample stage and tube housing with an X-ray tube. The electronics and support unit contains the knobs for the operation of the machine.

Thermogravimetric analyzer (TGA)

The thermal stability of the synthesized metal-organic frameworks was assessed by decomposing them using the SDT Q600 V20.9 analyzer located at the Department of Materials Science Engineering, University of Ghana. The SDT Q600 can simultaneously measure heat flow (DSC) and weight changes (TGA) during the decomposition process. The simultaneous measurement of two properties not only improves productivity but also simplifies the interpretation of results. The SDT Q600 analyzer has a maximum operating temperature at 1500 °C with heating rates from 100 °C /min to 1000 °C and from 25 °C to 1500 °C. The SDT Q600 has 110 μ l platinum and 90 μ l alumina sample cups with weight and temperature sensitivity of 0.1 μ g and 0.001 °C. The TGA Instruments SDT Q600 analyzer operates on helium, nitrogen, air

and argon gases with a 20 to 1000ml/min flow rate measured by a mass flow regulator with gas switching ability.

Scanning electron microscope-energy dispersive spectrometer (SEM-EDS)

The ZEISS EVO MA 15 Scanning Electron Microscope was used to analyze the morphology of the synthesized metal-organic frameworks. It has an electron optical column, a specimen chamber, and a plinth which displays the control buttons of the machine. The SEM machine is connected to the Bruker Quantax EDS to identify elements present in the synthesized complex compounds. The SEM-EDS analyzer used was located at the University of Mines and Technology Laboratory, Tarkwa Ghana.

Single crystal diffractometer

The single crystal analysis was done by the National Crystallography Service, United Kingdom, using the Rigaku 007VHF diffractometer. The Rigaku 007VHF diffractometer is equipped with Varimax confocal mirrors, a UG2 Universal goniometer, a HyPix 6000 detector and an Oxford Cryosystems low-temperature device.

Photocatalytic system

The Chromato-Vue cabinet C-70G located at the Molecular Biology Department Laboratory, University of Cape Coast was used for the photo-irradiation activity analysis. The Chromato-Vue cabinet C-70G is a black rectangular box with a rectangular opening at the top covered by a transparent

plate and an opening at the front covered with black leather with a bar holding the leather in place which prevents penetration of light from outside to ensure the reaction is solely facilitated by the inner light source. The cabinet has three measuring light modes which consist of a short UV wave at 254 nm, a long UV wave at 365 nm and an interior overhead white light with a range from 400-700 nm. Photocatalytic transformation of the coloured pollutants was carried out in this system using the white light mode.

The pH meter

The pH of the solution was monitored by using VWR® pHEMOMENAL® pH/mV/°C Meter from Avantor® at the Laboratory of Water and Sanitation Department, University of Cape Coast. The meter has a big graphic LCD with an uninterrupted LED backlight which displays pH/mV with temperature value. It has selectable data logging between one minute and one hour and a memory ability of 5,000 data sets. It has 24-hour automatic adjustable power shut-off and automated identification of DIN and NIST buffers of 1.68, 4.00, 6.86, 9.18 and 12.54 with three extra buffers of 4.00, 7.00, 10.00 at 25 °C in memory. It has an efficient drift control diagnostic electrode with a calibration symbol displaying for recalibration.

Spectrophotometer

The T70 UV/VIS Spectrometer by PG Instruments Ltd. shown in Plate 2 located at the Chemistry Department Laboratory, University of Cape Coast was used for all spectrophotometric measurements. The T70 UV/VIS Spectrometer is a split beam UV-Vis spectrophotometer with a wavelength

range from 200 to 1000 nm. The model has five measurement modes which include photometry, spectrum, quantitative, kinetics and spectrum bandwidth with eight Multi-cells. The spectrum mode of the spectrophotometer was employed to measure the absorbance of the dye solution before and after irradiation and the absorbance of the photocatalyst.

Gas chromatography/mass spectrum (GC/MS)

Gas chromatography/mass spectrometry (SHIMADZU GC-MS QP 2010 Plus) located at the School of Physical Sciences Laboratory, University of Cape Coast was used to identify intermediate compounds from the degraded coloured samples. The gas chromatograph for mass spectrometer uses an AOC-20s autosampler, an AOC 20i autoinjector, a DB-5ms column as the stationary phase and helium as the carrier gas (mobile phase). The mass spectrometer has a metal quadruple mass filter with pre-rods analyzer, an electron ionization source with an electron energy of 10 to 200 eV and a dual automatic switching filament. It has a differential vacuum system with a main pump (turbo molecular pump 58 L/sec (He)) and a fore pump (oil rotary pump, 30 L/min (60 Hz)). The mass spectrometer also has a secondary electron multiplier with a patented overdrive lens and conversion dynode 8×10^6 dynamic range detector.

Synthesis of Metal-Organic Frameworks

The solvothermal synthetic process was used to synthesize the various compounds. Six metal-organic frameworks were synthesized using this

process. Different parameters relating to temperature and time with different solvents were used for the metals to form the complexes with the linkers.

Synthesis of copper metal-organic frameworks

The synthesis of the copper metal-organic frameworks was a modification of the synthetic procedure reported from previous works (Kar & Srivastav, 2018; Furuawa, Cordova, Keeffe, & Yaghi, 2013; Yang, Ruess & Carreon, 2015). Parameters such as the type and amount of metal salt, linker, and solvent as well as temperature and time were varied in relation to previous works. A 0.63 g (3.5 mmol) of 5-aminoisophthalic acid was dissolved in a solution of 15 ml ethanol and 15 ml ultrapure water. A 1.21 g (5 mmol) of Copper (II) Nitrate trihydrate was separately dissolved in 30 ml ultrapure water. The first solution was added to the second and stirred for 15 min. The stirred solution with a pH of 6.4 was poured into a Teflon liner autoclave and heated at 120 °C for 18 hours. The autoclave was allowed to cool to normal room temperature. The synthesized compound was filtered off, washed twice with methanol to remove impurities and dried in the oven at 80°C overnight to obtain a leafy green powdery compound. The procedure was repeated using 0.76g (3.5 mmol) of 1, 3, 5-benzenetricarboxylic acid as an organic linker to produce a blue crystal product.

Synthesis of cerium metal-organic frameworks

The procedure used for the synthesis of the cerium metal-organic frameworks was similar to procedures reported in literature (Lin, Ibrahim, Arab, El-Kaderi & El-Shall, 2017; Santos & Luz, 2019). Parameters such as

the type and amount of metal salt, linker, and solvent as well as temperature and time were varied in relation to previous works. A mixture of 0.866g (2 mmol) cerium nitrate hexahydrate and 0.181 (1 mmol) 5-aminoisophthalic acid was dissolved in 40 ml N, N-Dimethylformamide (DMF) to form a solution with pH of 7.8. The solution mixture was sealed in 100 ml Teflon liner autoclave and heated in the oven for 24 hours at a constant temperature of 140°C. The autoclave was allowed to cool to room temperature after the required heating process. The acquired product was filtered off, washed thrice with DMF and dried in the oven at 120°C for 2 hours to obtain a marble white-coloured powdery compound. The procedure was repeated using 0.420g (2 mmol) 1, 3, 5-benzenetricarboxylic acid as an organic linker to obtain a creamy powdery compound.

Synthesis of zirconium metal-organic framework

The synthesis of the zirconium metal-organic frameworks was a modification of the synthetic procedure reported in previous studies (Ardila-Suárez, Alem, Baldovino-Medrano & Ramírez-Caballero, 2020; Ganesh, Hemalatha, Peng, Cha & Jang, 2014; Larasati, Winarni, Putri, Hanif, Lestari, 2017). Parameters such as the type and amount of metal salt, linker, solvent and modulator as well as temperature and time were varied in relation to previous works. A mixture of 0.8155g (3.5 mmol) Zirconium (IV) oxynitrate hydrate and 0.2129g (1.2 mmol) 5-aminoisophthalic acid was added to a solution of 35 mL DMF and 20 ml acetic acid in a 100ml Teflon liner autoclave to form a solution with pH of 7.5. The mixture was stirred at 1000 rpm for 15 min, sealed and heated at 140°C for 24 hours. The autoclave was

allowed to cool at room temperature to remove the resulting compound. The obtained compound was centrifuged, washed 15 ml with DMF, 15 ml acetone and 15 ml methanol to remove unreacted materials, and finally dried in an oven at 200 °C for 2 hours to obtain a pastel-coloured block. The procedure was repeated using 0.2471g (1.2 mmol) 1, 3, 5-benzenetricarboxylic acid as the organic linkers to obtain cream block products.

Characterization Analysis of Synthesized Metal-Organic Frameworks

Various analytical procedures were performed to investigate the bond formation, crystal phase, morphology and thermal stability to characterize and confirm that the various synthesized complex compounds were metal-organic frameworks.

Functional group and bond formation analysis

Fourier Transform Infrared (FTIR) analysis was done for the organic linkers and the various synthesized metal-organic frameworks to determine the various functional groups present in the organic linkers and the synthesized metal-organic framework and also determine the possibility of bond formation between the metals and organic linkers. The FTIR analysis was carried out using Bruker Alpha Spectrometer. The sampling surface, ATR crystal and anvil of the spectrometer were cleaned with propanol before the analysis. About 1mg of the sample was carefully placed on the ATR crystal in the middle of the sampling surface. The anvil was pressed against the sample for suitable contact pressure against the ATR crystal to acquire a spectrum. The anvil was raised against the ATR crystal after obtaining a spectrum. The

sample was removed and the sampling surface, ATR crystal and anvil were cleaned again with propanol.

Crystal phase analysis

X-ray powder diffraction (XRD) analysis was performed to study the crystal phase for the organic linkers and the various synthesized complex compounds. The XRD analysis was executed using the Empyrean X-ray Diffractometer. The sample powder was packed tightly into the sample holder and scanned from 10° to 70° at 2θ angle (2θ) λ 48 geometry using Cu-K α radiation at kilovoltage of 45 kV and tube current of 20 mA. The pattern obtained from the detector was analyzed using high score plus software to identify and match the sample peaks.

Morphology and elemental analysis

The ZEISS EVO MA 15 Scanning Electron Microscope/Energy Dispersive Spectroscopy analysis was used to determine the surface morphology and elements found in the organic linkers and the synthesized metal-organic frameworks. Before imaging, the samples were sputter coated with gold/palladium alloy to provide a conduction path for the non-conductive samples to be imaged at high voltages (30kV). The samples were exposed to electron irradiation which resulted in X-ray emissions specific to the elements existing in the samples. The emitted energies were converted into spectral peaks of varying intensities and used to identify the different inorganic elements present in the samples.

Single crystallography analysis

Single crystallography analysis was used to determine the topology of atoms in the metal-organic frameworks (MOFs). A small portion of the synthesized MOF was suspended in NVH oil; a suitable pale blue trapezoid-shaped crystal of size $0.10 \times 0.09 \times 0.07 \text{ mm}^3$ was selected and mounted on a MITIGEN holder with NVH oil then aligned on a Rigaku 007VHF diffractometer. The crystal was kept at a steady $T = 100(2) \text{ K}$ during data collection. The structure was solved with the ShelXT 2018/2 (Sheldrick, 2015a) solution program using dual methods and by using Olex2 1.5 (Dolomanov, Bourhis, Gildea, Howard & Puschmann, 2009) as the graphical interface. The model was refined with ShelXL 2018/3 (Sheldrick, 2015b) using full matrix least squares minimisation on F^2 to obtain the required results.

Thermal stability analysis

The thermal stability of the synthesized metal-organic complexes was examined using the SDT Q600 V20.9 System under a nitrogen atmosphere. A required amount of samples about 15 mg were loaded into an alumina pan and heated in a furnace programmed for a linear temperature change from room temperature to $800 \text{ }^\circ\text{C}$ at a heating rate of $5 \text{ }^\circ\text{C/minute}$ over some time. Nitrogen gas was utilized to create a uniform environment while the sample was being heated.

Coloured Organic Pollutant Transformation Analysis

The photocatalytic activity of the synthesized metal-organic frameworks was studied on Lissamine green SF (LGSF), Tetraethylrhodamine (TeRh) and Remazole brilliant 5R (RBV5R) as models for acidic, basic and reactive coloured organic pollutants and also on mixed textile dye. For each photocatalytic activity, a 150 mL beaker containing 100 mL from sample pollutant stock solutions containing an amount of the synthesized metal-organic framework as catalyst was prepared. The solution of the pollutant was stirred in the Chromato-Vue cabinet without light for an hour and then under white light for 180 min. Before the photocatalytic reaction under white light, a 5 mL aliquot was drawn and this amount was drawn at 30 min intervals under white light reaction for 180 min. The drawn sample was filtered and poured into a quartz cell 10.0 cm cuvette. The absorbance of the filtered sample was analyzed using the T70 UV/VIS Spectrometer. The T70 UV/VIS Spectrometer is connected to monitors and a personal computer with results interpreted using the UVWin 6 Spectrophotometer Software. The single scanning mode with a maximum displayed range of 3.00 and a medium speed at 2.0 nm interval was set as parameters for the UV/VIS absorbance measurements.

Parameter Variation Analysis

Three major parameters including catalyst amount, pollutant concentration and solution pH were varied to obtain the optimum pollutant transformation conditions. The experiment was repeated with solar light for all the pollutants using the optimum set conditions.

Catalyst amount variation analysis

The amount of the synthesized metal-organic frameworks which was used as catalysts varied from 0.005 to 0.020 g/L. The selected catalyst amounts for the study were 0.005, 0.010, 0.015 and 0.020 g/L. The catalyst amounts were selected to define the optimum amount of the metal-organic framework that could be able to remove the selected organic pollutants from water under photolysis after 180 min.

Pollutant concentration variation analysis

The pollutant concentration after degradation was studied by varying the concentrations of sampled pollutant solutions. The selected pollutant concentrations for the study were 0.10 g/L, 0.20 g/L, 0.30 g/L and 0.40 g/L to define the optimum concentration for the photo-transformation study

Solution pH variation analysis

The pH of the pollutants was varied from 4.0 to 10.0 whilst factors such as pollutant concentration and MOF amounts kept constant. The selected pH for the study were pH4, pH6, pH7, pH8 and pH10. The pH of the solution was adjusted using 1.0 M HCl and 1.0 M NaOH solution.

Adsorption and Kinetic Study

The quantities of pollutants adsorbed on the surfaces of the MOFs at a given time t , and at equilibrium, were obtained using equation (2) and equation (3).

$$q_t = \frac{(C_i - C_t)}{m} \times V \quad (2)$$

$$q_e = \frac{(C_i - C_e)}{m} \times V \quad (3)$$

Where q_t (mg/g) is the concentration of pollutants adsorbed by the MOFs at a given time, q_e (mg/g) is the concentration of pollutants adsorbed by the MOFs at equilibrium, C_i (mg/L) is the initial concentration of pollutant in solution, C_t (mg/L) is the concentration of pollutant in solution at time t , C_e (mg/L) is the concentration of pollutant in solution at equilibrium, V is volume of solution (L) and m is the mass of MOF (g). The efficiency of the pollutant removal as a result of their transformation was calculated using Equation (4)

$$\text{Pollutant removal efficiency (\%)} = \frac{C_i - C_t}{C_i} \times 100 \% \quad (4)$$

Where C_i is the initial concentration of the pollutant at $t = 0$ (g/L), C_t is the concentration at a given time (g/L).

The rate of pollutant removal in water with time was determined using the pseudo-first-order adsorption and pseudo-second-order adsorption reaction rate equations. These equations examine the relationship between pollutant adsorption rate and rate changes at a specific reaction time. Pseudo-first-order model considers intramolecular force interactions during adsorption (physisorption) to limit the rate of adsorption. Pseudo-second-order model, however, considers chemical bond interaction during adsorption (chemisorption) to limit the rate of adsorption (Liu et al., 2019; Sumalinog, Capareda, & de Luna, 2018). The pseudo-first-order adsorption and pseudo-second-order adsorption reaction rate equations as proposed by Lagergren (1898) and Ho McKay (1999) were used to kinetically analyze the rate of pollutant transformation by the synthesized MOFs.

The pseudo-first-order adsorption is given in equation (5) when $n=1$

$$\frac{dq_t}{dt} = K_1 (q_e - q_t) \quad (5)$$

The q_e represents the amount of pollutants adsorbed by the MOFs at equilibrium (mg/g). The q_t denotes the amount of pollutants adsorbed on the MOFs at a given time t (mg/g). The K_1 is the rate constant for pseudo-first-order adsorption (min^{-1}).

Integrating equation (5) with boundary conditions set at $t = 0$ to $t = t$ and $q_t = 0$ to $q_t = q_e$ leads to give linear equation:

$$\ln (q_e - q_t) = \ln(q_e) - k_1 t \quad (6)$$

A linear relationship can be obtained when $\ln (q_e - q_t)$ is plotted against t . The slope and intercept obtained from the plot can be used to determine k_1 and q_e .

The pseudo-second-order is expressed in equation (7), where $n = 2$.

$$\frac{dq_t}{dt} = K_2 (q_e - q_t)^2 \quad (7)$$

The K_2 is the rate constant for pseudo-second-order adsorption (min^{-1}).

Integration of equation (7) with boundary conditions when $t = 0$ to $t = t$ and $q_t = 0$ to $q_t = q_e$ gives equation (8).

$$\frac{1}{q_e - q_t} = \frac{1}{q_e} + K_2 t$$

(8)

The rearrangement of the linear form of equation (8) gives equation (9).

$$\frac{t}{q_t} = \frac{1}{k_2 q_e^2} + \frac{1}{q_e} (t) \quad (9)$$

From equation (9) a linear relationship can be obtained when $\log (t/qt)$ is plotted against t . The slope and intercept obtained from the plot can be used to determine K_2 and q_e .

Adsorption Isotherms

Langmuir adsorption model is known to describe isotherm concerning adsorption studies. The Langmuir theory assumes that the adsorption of adsorbate within an adsorbent occurs at specific uniform sites in solutions when equilibrium is attained at constant temperature (Mahmood, Wang, Xie & Sun, 2021; Musah, 2022; Thompson, Fernandez & Maroto-Valer, 2020). The linear expression of the Langmuir equations is displayed in equations (10):

$$\frac{C_e}{Q_e} = \frac{1}{K_L Q_o} + \frac{C_e}{Q_o} \quad (10)$$

C_e is the concentration of the adsorbate in solution at equilibrium, q_e is the amount of pollutant (adsorbate) removed per unit weight of MOF (adsorbent), Q_o represents maximum single layer adsorption capacity constant and K_L is the surface energy of the adsorption process constant. A linear relationship can be obtained when C_e/Q_e is plotted against C_e from equation (10). The slope and intercept obtained from the plot can be used to determine K_L and Q_o respectively. An equilibrium factor, R_L can be used to express the Langmuir adsorption isotherm using the expression in equation (11)

$$R_L = \frac{1}{(1 + K_L C_o)} \quad (11)$$

R_L is the dimensionless separation factor, C_o (mg/dm^3) is the highest initial concentration and K_L (dm^3/mg) is the Langmuir constant. The adsorption

isotherm is favourable for the Langmuir model when $0 < R_L < 1$, unfavourable when $R_L > 1$, irreversible when $R_L = 0$ and linear when $R_L = 1$ (Musah et al., 2022; Prasath, Muthirulan, & Kannan, 2014).

Another well-known isotherm model used for adsorption study is the Freundlich isotherm model. The Freundlich adsorption isotherm usually measures the relationship between the adsorption capacity of adsorbent per unit weight and the concentration of remaining adsorbate in heterogeneous gas surfaces at equilibrium (Ahamad, Singh, Baruah, Choudhury & Sharma, 2018; Elbana et al., 2018; Musah, 2022). Data acquired from heterogeneous solution mostly fit the Freundlich adsorption isotherm empirical equation expressed as:

$$Q_e = K_f C_e^{1/n} \quad (12)$$

Where:

n is the efficiency of adsorption and adsorption energy constant, K_f is the adsorption capacity constant, Q_e is the adsorption capacity per unit weight of adsorbent and C_e is the concentration of the adsorbate (pollutant) in solution at equilibrium.

The logarithm linear expression of equation (12) is given in equation (13)

$$\log Q_e = \log K_f + \frac{1}{n} \log C_e \quad (13)$$

The plot of $\log q_e$ versus $\log C$ will give a straight line with $1/n$ and $\log K_f$ as slope and intercept respectively. The K_f value increases as the capacity of the adsorbent to remove adsorbate also increases (Musah, 2022; Paudel and Shrestha, 2020). The adsorption isotherm is termed favourable for the Freundlich isotherm when $1 < n > 10$. A larger n value (smaller $1/n$ value) is

favourable while a smaller n value (larger $1/n$ value) is unfavourable (Anah, & Astrini, 2018; Ramadoss & Subramaniam, 2019). Both the Langmuir and the Freundlich isotherms were applied for the adsorption study to assess whether the adsorption process was homogeneous or heterogeneous.

GC-MS Analysis

Before the pollutant intermediate determination analysis, 10 ml of degraded samples were loaded onto a cartridge. The cartridge was conditioned with 2 ml methanol followed by 1 ml deionized water before the loading of the samples. The loaded sample was washed with 2 ml deionized water and left for 3 min to dry using the manifold. The samples were eluted by gravity with 2 ml methanol twice followed by 2 ml acetone. Extracted samples were concentrated using a stream of nitrogen gas over a water bath set at 45 °C. The sample was reconstituted with ethylacetate to 30ul and put into vials for GC analysis.

SHIMADZA GC-MS QP 2020 was used to identify intermediate compounds from the transformed dyes. For the GC, a DB-5ms column of 30 m × 0.25 mm, 0.25 μm film thickness was employed. An injection pot temperature of 250° C and splitless injection mode were employed with helium as the carrier gas. For the MS, the ion source temperature was 210° C. It was run on scan mode set from m/z 50.00 to m/z 1030.

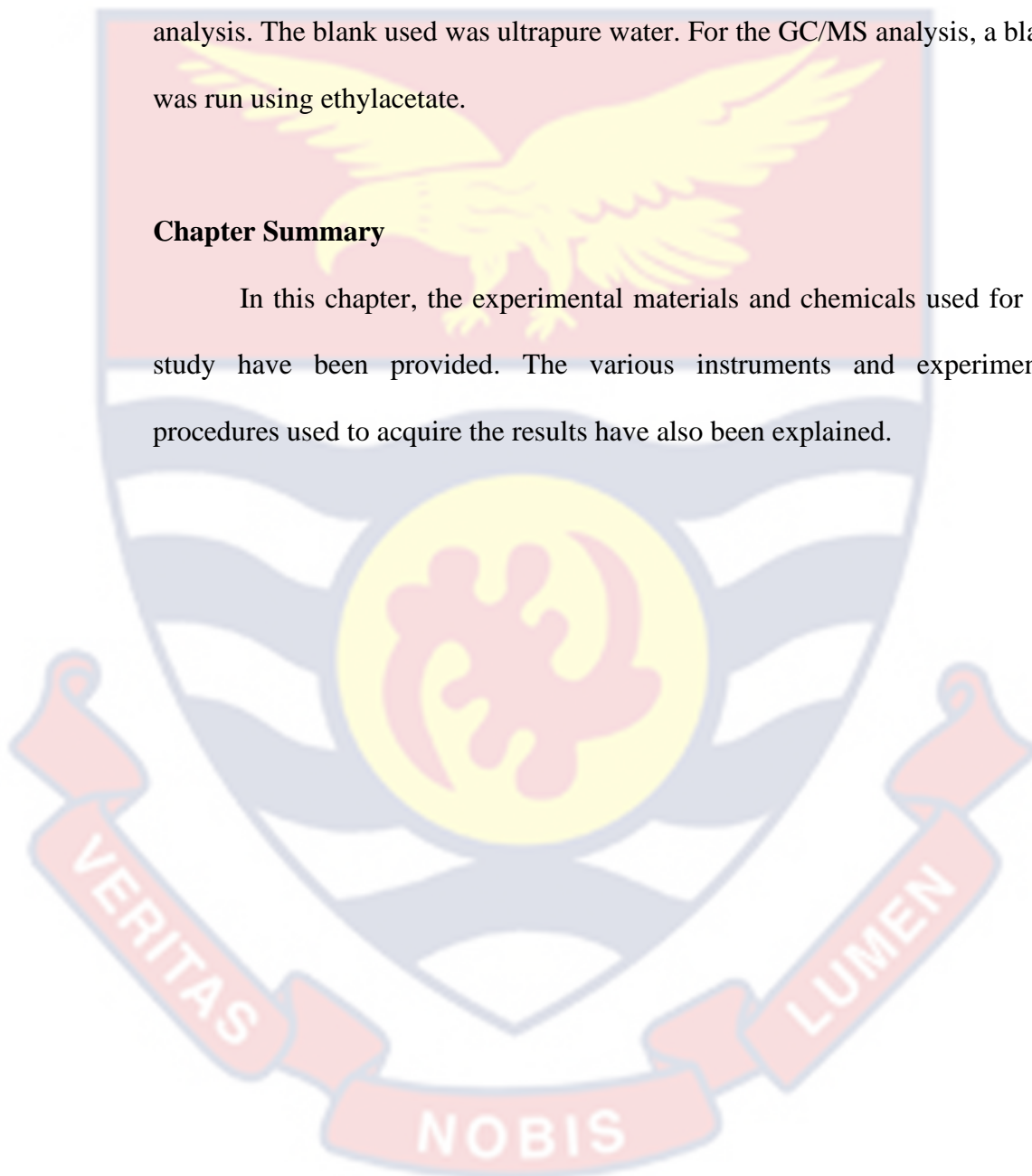
Quality Control Methodology

Various quality control measures were carried out to ensure the quality of data generated. For the synthesis of the MOFs, the oven was preheated to acquire a

stable desired temperature before the preparation of the MOF solutions to avoid heat fluctuations which may affect the formation of the MOFs. Blanks of dye solutions were run in the visible light and the dark for the photocatalytic process. A blank was also run before the UV-visible absorption analysis. The blank used was ultrapure water. For the GC/MS analysis, a blank was run using ethylacetate.

Chapter Summary

In this chapter, the experimental materials and chemicals used for the study have been provided. The various instruments and experimental procedures used to acquire the results have also been explained.



CHAPTER FOUR

RESULTS AND DISCUSSION

Introduction

This chapter involves the interpretation of results obtained from the characterization and the application of the synthesized metal-organic framework. Results from Fourier transform infrared (FTIR) analysis, X-ray diffraction (XRD) analysis, Scanning electron microscope and energy-dispersive X-ray spectroscopy (SEM-EDS) analysis, Single-crystal X-ray diffraction analysis and Thermogravimetric analysis on the synthesized metal-organic frameworks (MOFs) have been discussed. A discussion on the results of the photoactivity of the synthesized MOFs on the transformation of coloured organic compounds as pollutants into less toxic substances in water has been made. The kinetic and isotherm study on the transformation rate as well as intermediates obtained during the transformation was also discussed.

Synthesized Metal-Organic Framework

Figure 20 shows the synthesized copper-5-amino-1, 3-benzene dicarboxylic acid metal-organic framework (Cu-5abdc) before and after activation. A leafy green colour precipitate was obtained as seen (a) which resulted in leafy green powder after activation (b) having a percentage mass yield of 49.89%.



(a)

(b)

Figure 20: Images of synthesized Cu-5abdc (a) before activation (b) after activation

Figure 21 shows the synthesized copper-1, 3, 5-benzenetricarboxylic acid metal-organic framework (Cu-BTC) before and after activation. A pale blue colour precipitate (a) was obtained after synthesis which resulted in pale blue crystals (b) after activation with a percentage mass yield of 55.84%.



(a)

(b)

Figure 21: Images of synthesized Cu-BTC (a) before activation (b) after activation

Figure 22 shows the synthesized cerium-5-amino-1, 3-benzene dicarboxylic acid metal-organic framework (Ce-5abdc) before and after activation. A linen white precipitate (a) yielded a marble white coloured powder (b) after activation having a percentage mass yield of 43.17%.



(a)

(b)

Figure 22: Images of synthesized Ce-5abdc (a) before activation (b) after activation

Figure 23 shows the synthesized cerium-1, 3, 5-benzenetricarboxylic acid metal-organic framework (Ce-BTC) before and after activation. A cream colour precipitate (a) which resulted in a cream powder (b) after activation with a percentage yield of 56.07%.



(a)

(b)

Figure 23: Images of synthesized Ce-BTC (a) before activation (b) after activation

Figure 24 shows the synthesized zirconium-5-amino-1, 3-benzene dicarboxylic acid metal-organic framework (Zr-5abdc) before and after activation. A walnut cream jellylike precipitate (a) was obtained which resulted in pastel-coloured blocks (b) after activation having a percentage yield of 41.91 %.

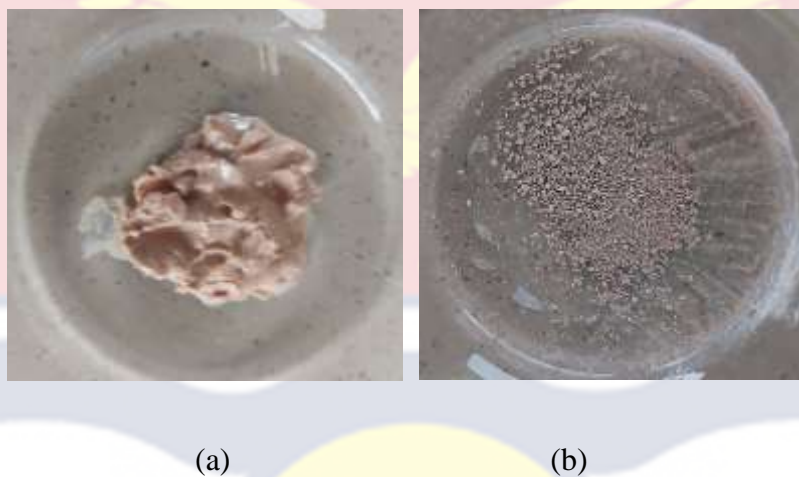


Figure 24: Images of synthesized Zr-5abdc (a) before activation (b) after activation

Figure 25 shows the synthesized zirconium-1, 3, 5-benzenetricarboxylic acid metal-organic framework (Zr-BTC) before and after activation. A white jelly-like precipitate (a) was obtained which resulted in cream blocks (b) after activation with a percentage mass yield of 44.34 %.

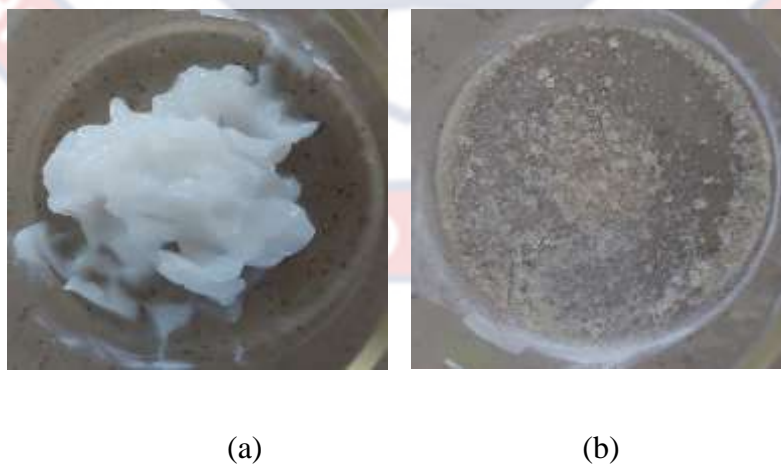


Figure 25: Images of synthesized Zr-BTC (a) before activation (b) after activation

All activated synthesized metal-organic frameworks formed powdered compounds except Cu-BTC which produced crystals suitable for single crystal XRD analysis. The activated synthesized Zr-5abdc and Zr-BTC yielded blocks that needed grinding into powdered form for characterization.

Characterization of Synthesized Metal-Organic Framework

Fourier transform infrared (FTIR) analysis was done on synthesized compounds to investigate the various components and functional groups found in the synthesized compounds. The crystallinity of the synthesized compounds was examined through X-ray diffraction (XRD) analysis. Scanning electron microscope and energy-dispersive X-ray spectroscopy (SEM-EDS) analysis were also conducted to investigate the surface morphology and the various elements found in the synthesized compounds. Analysis of bond formation between metals and organic linkers of synthesized samples that appeared crystalline was carried out by single-crystal X-ray diffraction test. The thermal stability of the synthesized compounds was also determined.

Fourier Transform Infrared (FTIR) Analysis of Organic Linkers and Synthesized Metal-Organic Framework.

Fourier Transform Infrared (FTIR) is an important technique used to identify the functional groups and confirm the components of compounds. Fourier Transform Infrared (FTIR) test for the organic linkers and the various synthesized compounds was done to determine the various functional groups present in the organic linkers and the synthesized compounds and also

ascertain the possibility of bond formation between the various metals and organic linkers.

Fourier transform infrared analysis of organic linkers

Fourier Transform Infrared (FTIR) analysis of 5-Aminobenzene-1, 3-dicarboxylic acid (H₂5abdc) and 1, 3, 5- Benzene tricarboxylic acid (H₃BTC) has been done. The FTIR spectrum of H₂5abdc shown in Figure 26 indicates bands distinctive of H₂5abdc from CAS DataBase lists (Chemical Book, 2017). The broad band from 3500 cm⁻¹ to 2220 cm⁻¹ indicates the presence of the hydroxyl group (O-H) stretch typical of carboxylic acids (Coates, 2000; Nandiyanto, Oktiani, & Ragadhita, 2019; Nandiyanto, Ragadhita & Fiandini, 2023; Stuart, 2004). The revealing double peaks within the broad band at 2830 cm⁻¹ and 2600 cm⁻¹ indicate the N-H stretch characteristic of primary aromatic amine.

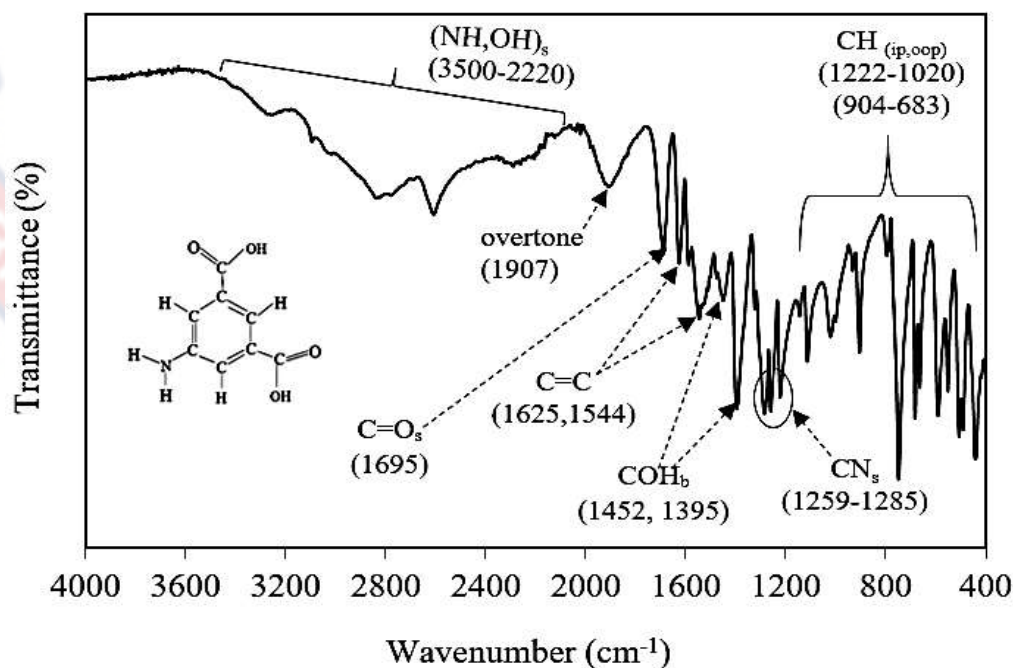


Figure 26: FTIR of 5-Aminobenzene-1, 3-dicarboxylic acid (H₂5abdc)

There is however a shift to the right which indicates a change in bond strength (Chen et al., 2022; Han et al., 2022; Kaur, Yusuf & Malik, 2021; Saber-Samandari, & Gazi, 2015; Sahil, Prashant, Akanksha, Premjeet & Devashish, 2012; Zhang et al., 2018). The band at 1695 cm^{-1} could be attributed to the presence of a C=O stretch carboxylic acid group (Nandiyanto, Ragadhita & Fiandini, 2023; Segneau et al., 2012). A slightly lower absorption frequency of C=O with a shift to the right other than the region 1700 cm^{-1} to 1730 cm^{-1} could be due to conjugation of the benzene ring found in 5-Aminobenzene-1, 3-dicarboxylic acid as well as the presence of the amine group (NH_2) attached to the benzene ring (Nandiyanto, Oktiani, & Ragadhita, 2019; Sahil, Prashant, Akanksha, Premjeet & Devashish, 2012).

The bands observed at 1625 cm^{-1} and 1544 cm^{-1} indicate C=C stretching present in the aromatic ring of the compound (Sahil, Prashant, Akanksha, Premjeet & Devashish, 2012). The bands detected at 1452 cm^{-1} and 1395 cm^{-1} depict the bending of C-O-H (Nandiyanto, Ragadhita & Fiandini, 2023). A C-N stretch could be related to bands at 1285 cm^{-1} and 1258 cm^{-1} (Coates, 2000; Nandiyanto, Oktiani, & Ragadhita, 2019; Segneau et al., 2012). The bands from 1222 cm^{-1} to 1020 cm^{-1} could be attributed to the in-plane bending of the aromatic C-H bond while bands from 903.65 cm^{-1} to 683.35 cm^{-1} could be associated with the out-of-plane bending of aromatic C-H (Nandiyanto, Ragadhita & Fiandini, 2023; Sahil, Prashant, Akanksha, Premjeet & Devashish, 2012). The band found at 1907 cm^{-1} could be due to an overtone which is typical for aromatic compounds (Stuart, 2004).

FTIR spectra of H_3BTC shown in Figure 27 indicates band patterns typical of 1, 3, 5- benzene tricarboxylic acid (Andriamitantsoa, Dong, Gao, &

Wang, 2017; Santos and Luz, 2019). The characteristic band region for the identification of OH stretching vibrations of the carboxylic acids found on the benzene ring was observed from 3050 cm^{-1} to 2450 cm^{-1} (Mahalakshmi & Balachandran, 2014; Nandiyanto, Oktiani, & Ragadhita, 2019; Sahil, Prashant, Akanksha, Premjeet & Devashish, 2012; Segneanu et al., 2012). The band at 1701 cm^{-1} is attributed to the presence of a C=O stretch of the carboxylic acid groups attached to the benzene ring in the 1, 3, 5- benzene tricarboxylic acid (Mat Yusuf, Ng, Ayub, Ngalim, & Lim, 2017; Nandiyanto, Oktiani, & Ragadhita, 2019; Segneanu et al., 2012). The COH bending from the carboxylic groups could be observed at 1440 cm^{-1} to 1397 cm^{-1} (Coates, 2000; Nandiyanto, Oktiani, & Ragadhita, 2019).

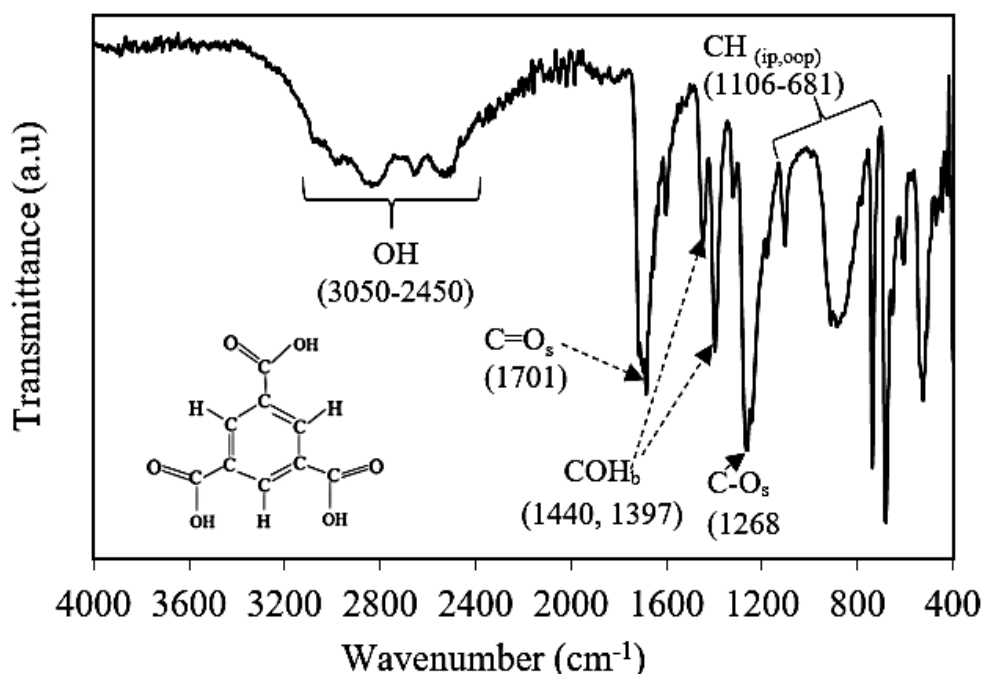


Figure 27: FTIR of benzene -1, 3, 5- tricarboxylic acid (H₃BTC)

The C-O stretch from the carboxylic acid groups could also be assigned to the band at 1268 cm^{-1} (Segneanu et al., 2012). The band at 1106 cm^{-1} is attributed to in-plane bending of the aromatic C-H bond while bands

from 889.37 cm^{-1} to 685.39 cm^{-1} are associated with out-of-plane bending of aromatic C-H of the benzene ring found in 1, 3, 5- benzene tricarboxylic acid (Coates, 2000; Nandiyanto, Oktiani, & Ragadhita, 2019).

Fourier transform infrared (FTIR) analysis of metal-organic frameworks formed with 5-aminobenzene-1, 3-dicarboxylic acid

A comparative analysis of the FTIR spectrum of 5-aminobenzene-1, 3-dicarboxylic acid ($\text{H}_2\text{5abdc}$) and that of the copper (Cu), cerium (Ce) and zirconium (Zr) metal-organic frameworks (MOFs) formed using $\text{H}_2\text{5abdc}$ as an organic linker is shown in Figure 28. A shift of a broad band to the left with the absence of double peaks is observed for all the synthesized compounds compared to that observed in $\text{H}_2\text{5abdc}$. The broad band was found between 3650 cm^{-1} and 2862 cm^{-1} further left to that found in 5-aminobenzene-1, 3-dicarboxylic acid between 3500 cm^{-1} and 2220 cm^{-1} .

The broad bands shift could relate to OH vibrational stretch due to water molecules adsorbed on the surface of synthesized MOFs from their metal hydrate salts which is typical of most MOFs (Aghajanzadeh et al., 2018; Autie-Castro, Autie, Rodríguez-Castellón, Aguirre, & Reguera, 2015; Li et al., 2016; Nandiyanto, Oktiani, & Ragadhita, 2019; Nivetha et al., 2020; Sangeetha & Krishnamurthy, 2020; Rezaei Kahkha, Oveisi, Kaykhali, & Rezaei Kahkha, 2018). The bands observed from 1587 cm^{-1} to 1652 cm^{-1} indicate C=C-C stretching present in the aromatic ring of the synthesized MOFs as well as $\text{H}_2\text{5abdc}$ (Coates, 2000; Nandiyanto, Oktiani, & Ragadhita, 2019; Sahil, Prashant, Akanksha, Premjeet & Devashish, 2012).

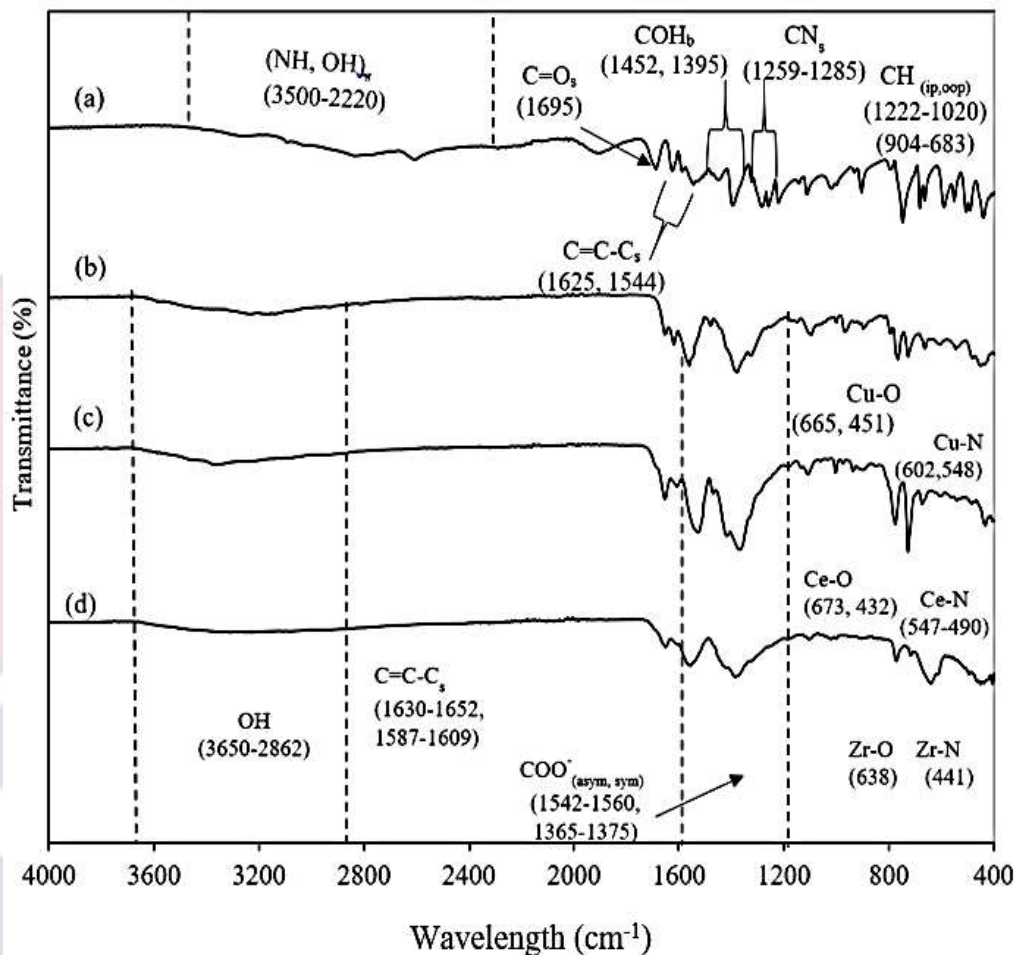


Figure 28: FTIR comparison of 5-aminobenzene-1, 3-dicarboxylic acid and synthesized MOFs ((a) H₂5abdc; (b) Cu-5abdc; (c) Ce-5abdc and (d) Zr-5abdc)

Strong absorption bands between 1365 cm^{-1} and 1560 cm^{-1} in the synthesized MOFs could be related to the asymmetric and symmetric vibrational modes of carboxylate (COO^-) found on the benzene of 5-aminobenzene-1, 3-dicarboxylate (5abdc) present in the synthesized MOFs which was absent in H₂5abdc (Ganesh, Hemalatha, Peng, Cha, & Jang; 2014; Nandiyanto, Oktiani, & Ragadhita, 2019; Zhang et al., 2018; Sangeetha & Krishnamurthy, 2020). The bands between 1220 cm^{-1} to 680 cm^{-1} found in both synthesized MOFs and H₂5abdc are associated with the bending vibrational modes in the benzene ring. The bands from 1126 cm^{-1} to 930 cm^{-1}

could relate to the in-plane C–H vibrational mode while bands from 900 cm^{-1} to 680 cm^{-1} are out-of-plane vibrational modes (Coates, 2000; Nandiyanto, Oktiani, & Ragadhita, 2019)

The stretching vibration of the Cu–O and Cu–N bonds in Cu-5abdc from Figure 28 (b) could be attributed to vibrational bands from 665 cm^{-1} to 451 cm^{-1} similar to copper metal-organic frameworks synthesized (Al-Obaidy, Ibraheem, & Mesher, 2020; Ganesan & Lee, 2006; Jurca, Marian, Vicaş, Mureşan & Fritea, 2017; Köse & Necefoğlu, 2008; Nzikayel, Akpan & Adams, 2017) The low-intensity stretching vibrational bands of Ce–O could be seen at 673 cm^{-1} and 432 cm^{-1} (Lin et al., 2017) while the very weak vibrational stretch of Ce–N could be observed from 547 cm^{-1} to 490 cm^{-1} Ce-5abdc from Figure 28 (c). This is similar to metal-nitrogen (M–N) bond vibrations obtained in literature (Köse & Necefoğlu, 2008; Nzikayel, Akpan & Adams, 2017).

The band observed at 630 cm^{-1} in Zr-5abdc from Figure 28 (d) could be related to the Zr–O vibrational stretch similar to reports related to zirconium complexes (Ardila-Suárez, Alem, Baldovino-Medrano & Ramírez-Caballero, 2020; Heu, Ateia, & Yoshimura, 2020; Yang, Jiang, Huang, Guo, & Shao, 2017). The band at 428 cm^{-1} could be related possibly to the Zr–N vibrational stretch (Köse & Necefoğlu, 2008; Nzikayel, Akpan & Adams, 2017). From the various functional groups observed in Figure 28, a proposed structure for the MOFs is shown in Figure 29.

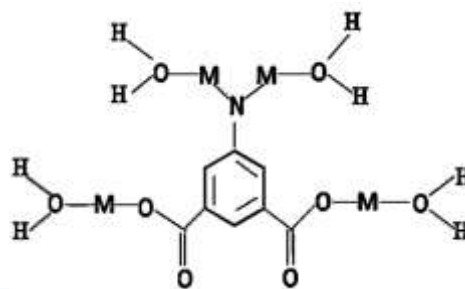


Figure 29: Proposed structure formation of Cu-5abdc, Ce-5abdc and Zr-5abdc MOFs (M: Cu, Ce, Zr)

The absence of NH primary amines in the various frameworks formed with H₂5abdc linker indicates the presence of a tertiary amine. It is highly possible, therefore, that the primary amine found in the linker was deprotonated to enable nitrogen (N) to form bonds with the metals. There was, however, the absence of CN around 1335 cm⁻¹ to 1250 cm⁻¹ (Coates, 2000; Nandiyanto, Oktiani, & Ragadhita, 2019; Nandiyanto, Ragadhita & Fiandini, 2023; Stuart, 2004) which could be due to the overlap of the broad intense symmetric vibrational bands of COO⁻ found around the region in these frameworks. The absence of COH in all the synthesized MOFs indicates the deprotonation of COOH to yield COO⁻ which can bond to the metals. The various metals bonding with the oxygens and nitrogens to form a link in the frameworks were identified at the fingerprint region per documented literature (Köse & Necefoğlu, 2008; Nzikayel, Akpan & Adams, 2017).

Generally, the infrared bands for inorganic materials appear at lower wavenumbers than those observed for organic materials (Ardila-Suárez, Alem, Baldovino-Medrano & Ramírez-Caballero, 2020; Nzikayel, Akpan & Adams, 2017; Stuart, 2004). Oxygen-metal bonds were however seen as a bit sharper and stronger than nitrogen-metal bonds since oxygen generally tends to form

stronger bonds with metals than nitrogens (Fulton, Holland, Fox & Bergman, 2002; Nimmermark, Öhrström & Reedijk, 2013). Oxygen will therefore have a stronger interaction with the metals than nitrogen in the fingerprint region.

Fourier transform infrared (FTIR) analysis of metal-organic frameworks formed with 1, 3, 5- benzene tricarboxylic acid

A comparative analysis of FTIR spectrum of 1, 3, 5- benzene tricarboxylic acid (H₃BTC) and that of the copper (Cu), cerium (Ce) and zirconium (Zr) metal-organic frameworks formed using H₃BTC as an organic linker is shown in Figure 30. A shift of a broad band to the left is observed for all the synthesized compounds compared to that observed in H₃BTC. The broad band between 3650 cm⁻¹ to 2840 cm⁻¹ could be due to the presence of OH group from water molecules adsorbed on the surface of the synthesized MOFs from their hydrate salts (Almáši et al., 2015; Ardila-Suárez et al., 2019; Guo et al., 2021; Li et al., 2016; Lin et al., 2017; Nivetha et al., 2020; Peng et al., 2019; Ragon et al., 2015; Sangeetha & Krishnamurthy, 2020; Santos and Luz, 2019; Vellingiri, Kumar, Deep & Kim, 2017).

A sharper band around 1640 cm⁻¹ for water was however not observed owing to the overlapping broad sharper COO⁻ bands around the same band area (De Marco, Carpenter, Liu, Biswas, Bowman & Tokmakoff, 2016; Dimitrova, 2006; Wang, Sivakumar, Redding, Hastings, 2003; Gupta, Jelle, & Gao, 2022). The bands between 1644 cm⁻¹ and 1656 cm⁻¹ indicate the presence of C=C-C vibrational stretch of the benzene rings found in the MOFs. The intense bands from 1370 cm⁻¹ to 1609 cm⁻¹ could be associated with the asymmetric and symmetric vibrational stretch of the carboxylate (COO⁻)

groups of the 1, 3, 5- benzene tricarboxylate (BTC^-) found in the synthesized MOFs (Al Cheikh et al., 2019; Nandiyanto, Oktiani, & Ragadhita, 2019; Segneanu et al., 2012).

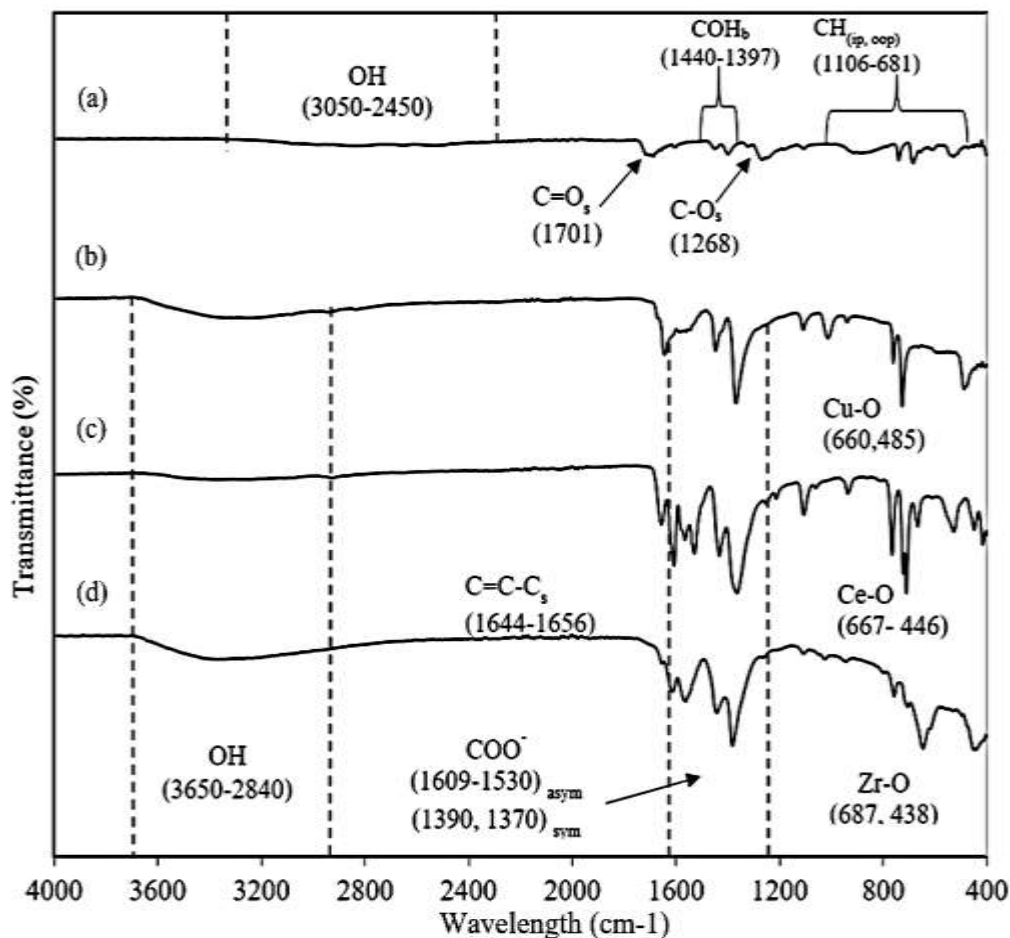


Figure 30: FTIR comparison of 1, 3, 5- benzene tricarboxylic acid and synthesized MOFs ((a) H_3BTC ; (b) Cu-BTC ; (c) Ce-BTC ; (d) Zr-BTC)

The bands between 1100 cm^{-1} to 680 cm^{-1} could relate to the in and out of plane vibrations of CH in the benzene ring found in H_3BTC as well as in BTC^- of the synthesised MOFs (Coates, 2000; Nandiyanto, Oktiani, & Ragadhita, 2019). The bands at 660 cm^{-1} and 480 cm^{-1} in Cu-BTC from Figure 30 (b) could be a result of Cu–O bending and stretching vibrations similar to reports related to copper complexes (Al-Obaidy, Ibraheem, &

Meshar, 2020; Ganesan & Lee, 2006; Jurca, Marian, Vicaş, Mureşan & Fritea, 2017; Köse & Necefoğlu, 2008; Nivetha et al., 2020; Nzikayel, Akpan & Adams, 2017). The stretching vibrations of Ce–O could be seen at a less intense peak range from 667 cm^{-1} to 446 cm^{-1} (Almási et al., 2015; Lin et al., 2017; Peng et al., 2019) in Ce-BTC from Figure 30 (c). The presence of the band at 687 cm^{-1} and 646 cm^{-1} in Zr-BTC from Figure 30 (d) could be attributed to Zr–O stretching vibration. (Ardila-Suárez, Alem, Baldovino-Medrano & Ramírez-Caballero, 2020; Heu, Ateia, & Yoshimura, 2020; Yang, Jiang, Huang, Guo, & Shao, 2017). From the various functional groups observed in Figure 30 a proposed structure for the synthesized MOFs is shown in Figure 31.

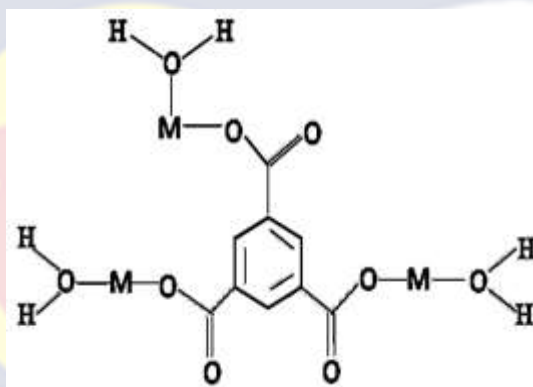


Figure 31: Proposed structure formation of Cu-BTC, Ce-BTC and Zr-BTC MOFs (M: Cu, Ce, Zr)

The absence of COH in all the synthesized MOFs indicates the deprotonation of COOH to yield COO^- which can bond to the metals. The various metals bonding with the oxygens to form a link in the frameworks were identified at the fingerprint region per documented literature (Köse & Necefoğlu, 2008; Nzikayel, Akpan & Adams, 2017).

X-ray diffraction (XRD) Analysis of Organic Linkers and Synthesized Compounds

X-ray diffraction (XRD) analysis tests for the organic linkers and the various synthesized compounds were done to ascertain the crystallinity of the organic linkers and formed compounds.

X-ray diffraction (XRD) analysis of organic linkers

The XRD spectrum of 5-aminobenzene-1, 3-dicarboxylic acid (H_25abdc) is shown in Figure 32. The XRD analysis shows diffraction peaks typical of 5-aminoisophthalic acid comparing the measured and documented pattern (Electronic Supplementary Material (ESI) for CrystEngComm, 2009). Major peaks were observed at 12.82° , 18.81° , 20.28° , 23.95° , 24.79° , 25.74° and 27.84° .

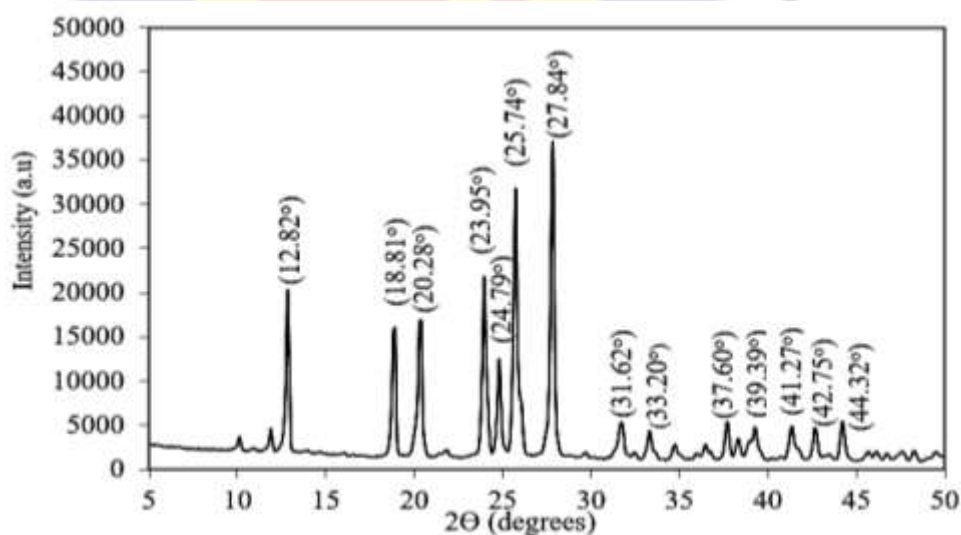


Figure 32: XRD of 5-aminobenzene-1, 3-dicarboxylic acid (H_25abdc)

Minor peaks were seen at 31.62° , 33.20° , 37.60° , 39.39° , 41.27° , 42.75° and 44.32° . The intensity of the major peaks indicates that H_25abdc is highly crystalline. The XRD spectrum of 1, 3, 5- benzene tricarboxylic acid

(H₃BTC) is shown in Figure 33. The X-ray diffraction (XRD) pattern shows bands typical of 1, 3, 5- benzene tricarboxylic acid. Major peaks were observed at 6.73 °, 10.83 °, 24.16 °, 26.89 ° and 27.52 ° which showed bands similar to results reported (Wei, Chen, Liang, & Zhao 2018; Xu, Yang, Wang, Cao & Chen, 2019). Minor peaks were observed at 9.25 °, 11.77 °, 12.61 °, 13.35 °, 21.01 ° and 29.73 °. The intensity of the peaks indicates that H₃BTC is crystalline.

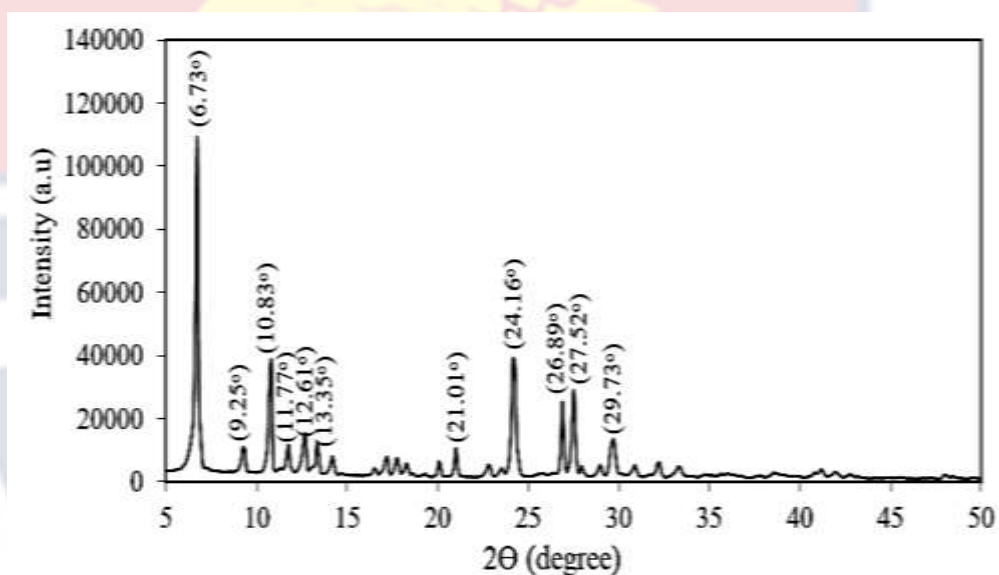


Figure 33: XRD of 1, 3, 5- benzene tricarboxylic acid (H₃BTC)

X-ray diffraction (XRD) analysis of metal-organic framework formed with 5-aminobenzene-1, 3-dicarboxylic acid

The XRD pattern of Cu-5abdc (b) in comparison with 5-aminobenzene-1, 3-dicarboxylic acid (H₂5abdc) (a) is displayed in Figure 34. Well resolved intense 2θ peaks at 10.62°, 13.66°, 15.87°, 29.52°, 36.34° and 42.22° were observed for Cu-5abdc (b). The peaks at 29.52°, 36.34° and 42.22° are similar to some peaks obtained for copper-containing amine metal-organic framework (Han, 2022).

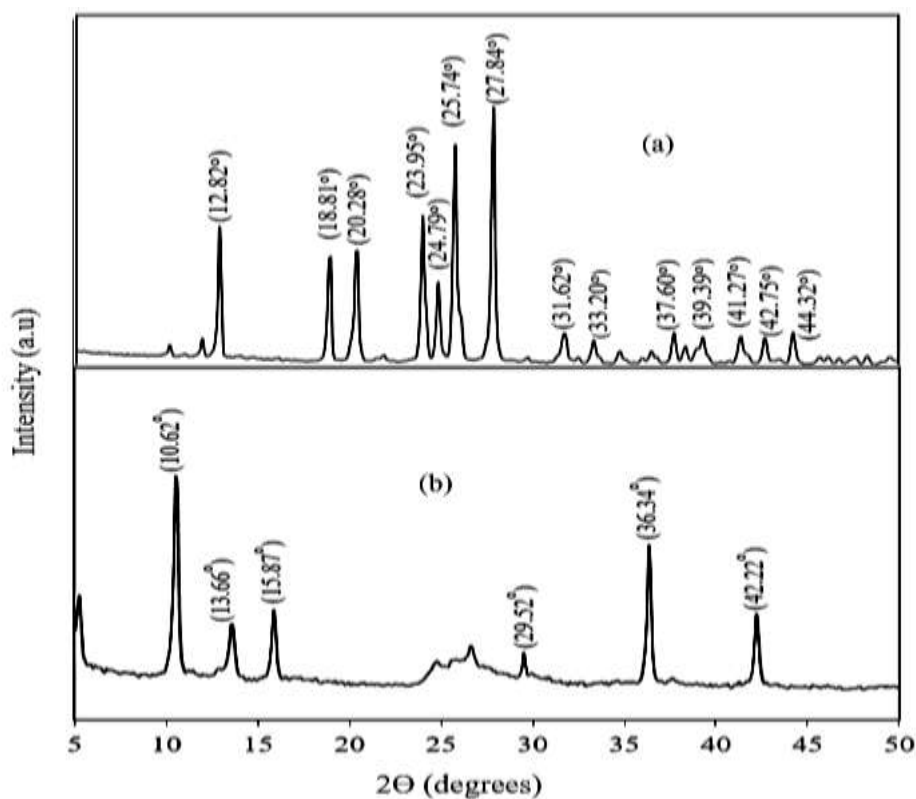


Figure 34: XRD of (a) 5-aminobenzene-1, 3-dicarboxylic acid (H_25abdc) and (b) synthesized Cu-5abdc

The peak angles obtained for Cu-5abdc varied compared to the peaks of H_25abdc . A close peak around 42° was however observed for both. The changes in 2θ peak values and intensity could indicate Cu-5abdc is formed and that, it is a highly crystalline compound.

The XRD pattern of the Ce-5abdc (b) in comparison with 5-aminobenzene-1, 3-dicarboxylic acid (H_25abdc) (a) is displayed in Figure 35. The diffractogram from 10° to 50° shows a 2θ peak pattern similar to the cerium-containing amine metal-organic frameworks reported (Dong & Huang, 2020). The 2θ peaks at 16.13° , 23.28° , 28.56° , 33.16° , 41.07 , 44.59° and 47.79° were observed for Ce-BTC (a). These peaks indicate that the Ce-5abdc is a crystalline compound. Different peak patterns were observed for Ce-5abdc

(a) and (H₂5abdc) (b) with close peak angles around 23.00°, 33.00°, 41.00° and around 44.00°.

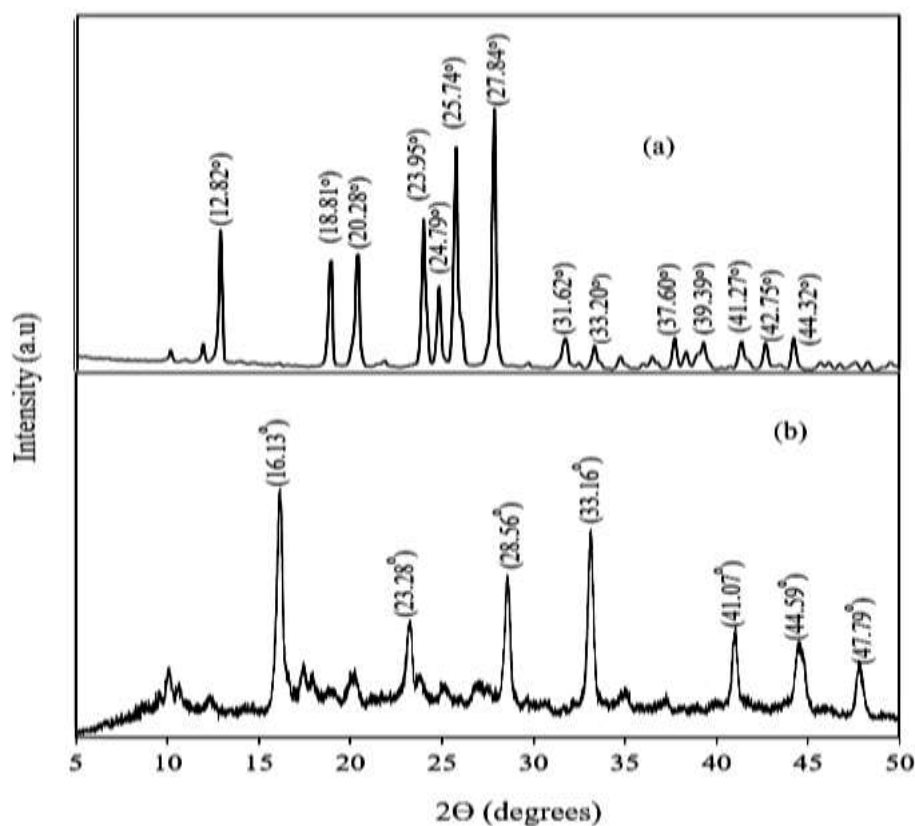


Figure 35: XRD of (a) 5-aminobenzene-1, 3-dicarboxylic acid (H₂5abdc) and (b) synthesized Ce-5abdc

The XRD of synthesized Zr-5abdc (b) in comparison with 5-aminobenzene-1, 3-dicarboxylic acid (H₂5abdc) (a) is shown in Figure 36. The diffractogram reveals amorphous characteristics with few peaks as observed in other related works on zirconium metal-organic frameworks (Ardila-Suárez et al., 2019; Ardila-Suárez, Alem, Baldovino-Medrano & Ramírez-Caballero, 2020; Ganesh, Hemalatha, Peng, Cha & Jang, 2014). The major peak at 6.52° was revealed with the amorphous phase which could be attributed to the partial crystallization of the Zr-5abdc (Ganesh, Hemalatha, Peng, Cha & Jang, 2014; Wißmann et al., 2012).

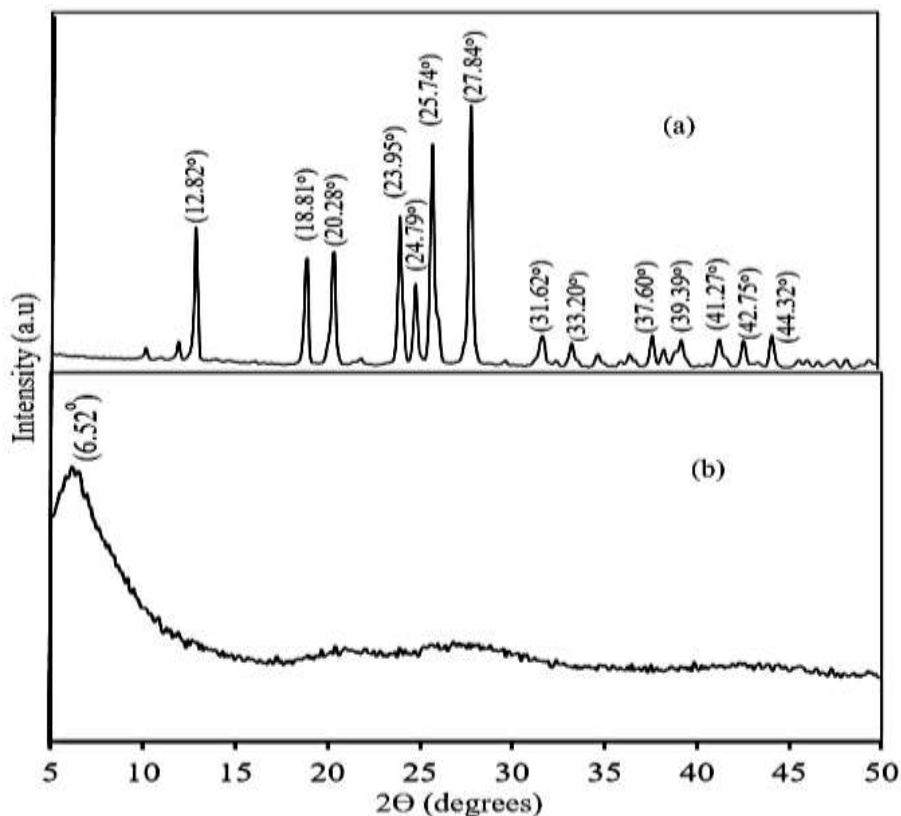


Figure 36: XRD of (a) 5-aminobenzene-1, 3-dicarboxylic acid (H_25abdc) and (b) synthesized Zr-5abdc

X-ray diffraction (XRD) analysis of metal-organic framework formed with 1, 3, 5-benzene tricarboxylic acid

The XRD pattern of the Cu-BTC (b) in comparison with 1, 3, 5-benzene tricarboxylic acid (a) is displayed in Figure 37. Results obtained from experimental XRD analysis in Figure 37 are agreeable with previous results (Kar & Srivastava, 2018; Li, Huang, Tang, Song, Lv & Ling, 2019; Nivetha et al., 2020).

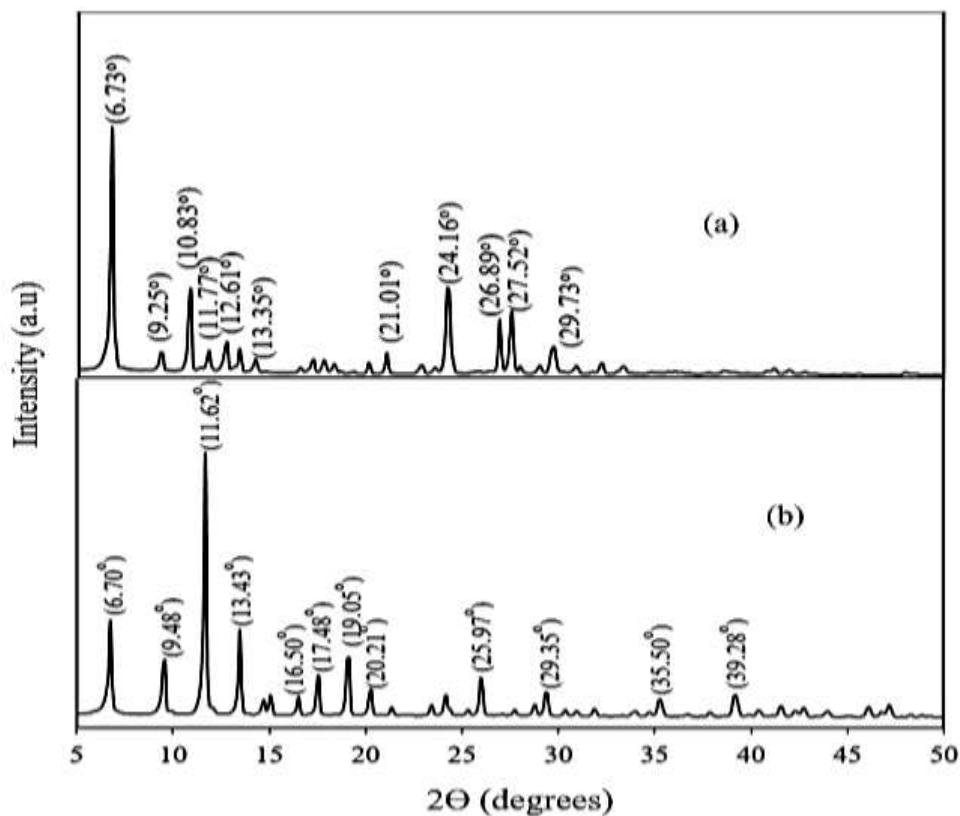


Figure 37: XRD of (a) 1, 3, 5-benzene tricarboxylic acid and (b) synthesized Cu-BTC

The XRD result indicates the formation of well-resolved peaks with main diffraction peaks at 6.70° , 9.48° , 11.62° , 13.43° , 16.50° , 17.48° , 19.05° , 20.21° , 24.16° , 25.97° , 29.35° , 35.50° and 39.28° which indicate a high degree of crystallinity (Nivetha et al., 2020). The diffraction peaks 6.70° , 9.48° , 11.62° , 13.43° and 29.35° were identifiable to similar angles for H_3BTC . It is reported that the observed low peaks indicate the existence of CuO bond formation and a slight occurrence of Cu_2O due to high temperature during the development of Cu-BTC (Alfè, Gargiulo, Lisi & Di Capua, 2014; Nivetha et al., 2020; Yang et al., 2013).

The X-ray diffraction (XRD) pattern of Ce-BTC (b) in comparison with H_3BTC (a) is shown in Figure 38. The diffractogram depicts peaks

typical of Ce-BTC per literature reports (Almási, Zelenák, Kuchár, Bourrelly, Llewellyn, 2016; Fonseca, Gaspar, Raimundo Jr, & Luz, 2019; Khan, Haque & Jhung, 2010; Lin et al., 2017; Peng, Ganesh, Vinodh, Palanichamy & Jang, 2019; Santos and Luz, 2020; Zhang et al., 2017; Zhang et al., 2018).

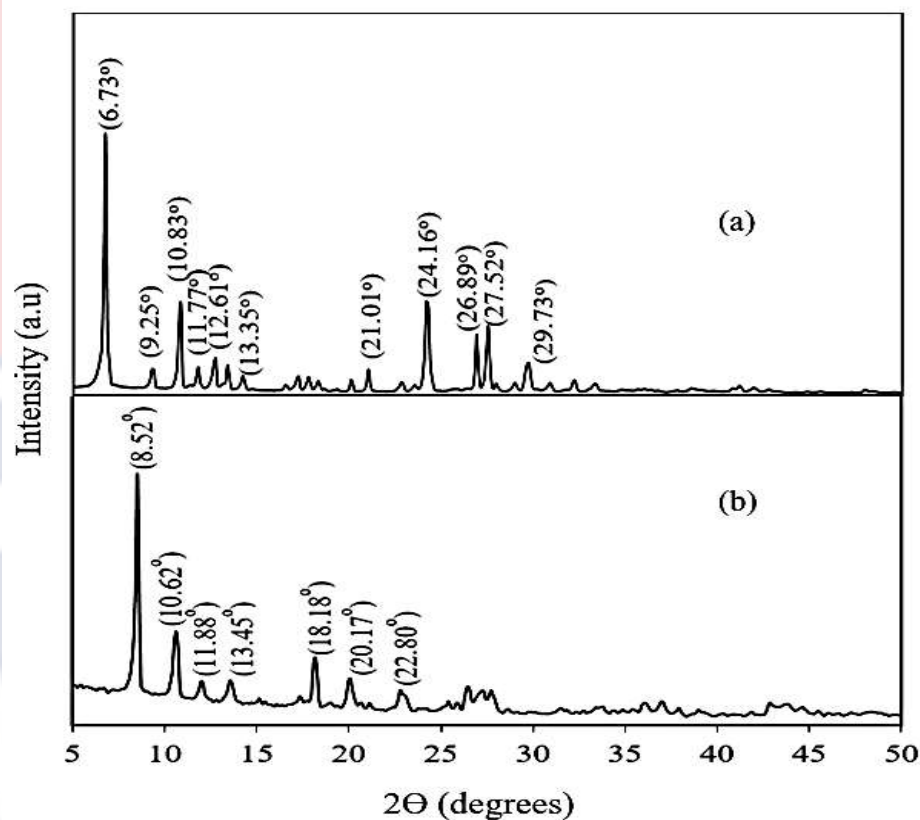


Figure 38: XRD of (a); 1, 3, 5-benzene tricarboxylic acid and (b); synthesized Ce-BTC

Characteristic 2θ peaks at 8.52° , 10.62° , 11.88° , 13.45° , 18.18° , 20.17° and 22.80° were identified. The diffraction peaks 10.62° , 11.88° and 13.45° were identifiable to similar angles for H_3BTC . The diffraction peak pattern observed indicates that Ce-BTC is a crystalline compound.

The XRD of synthesized Zr-BTC (b) in comparison with H_3BTC (a) is shown in Figure 39. The 2θ peaks at 7.13° , 8.24° , 9.98° , 10.09° , 19.67° , 20.76° , 27.18° and 28.67° were observed for Ce-BTC (a).

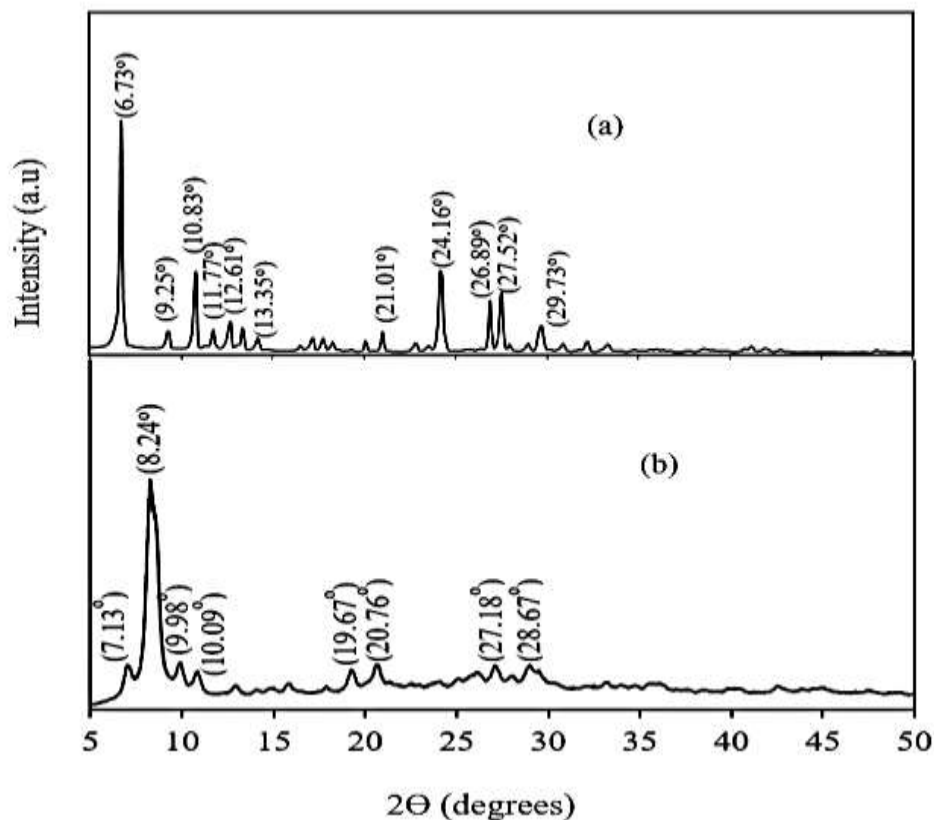


Figure 39: XRD of (a); 1, 3, 5-benzene tricarboxylic acid and (b); synthesized Zr-BTC

The diffraction peaks 9.98°, and 27.18 ° were identifiable to similar angle ranges for H₃BTC. The diffraction peaks pattern observed indicate that Zr-BTC is a crystalline compound with a similar diffraction pattern obtained in literature (Ganesh, Hemalatha, Peng, Cha & Jang, 2014; Wißmann et al., 2012).

SEM-EDS Analysis of Organic Linkers and Synthesized Metal-Organic Frameworks

The morphology of the organic linkers and the synthesized metal-organic frameworks were characterized by SEM images. The EDS analysis

was taken to confirm the element present in the synthesized metal-organic frameworks.

SEM-EDS analysis of organic linker

The SEM image of 5-aminobenzene-1, 3-dicarboxylic acid (H_25abdc) is shown in Figure 40.

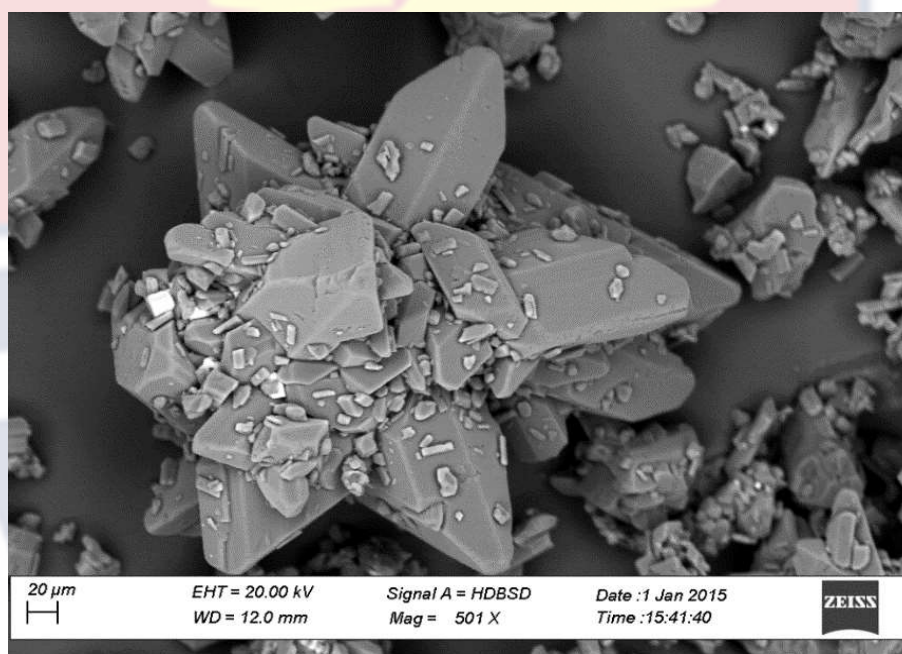


Figure 40: SEM image of 5-aminobenzene-1, 3-dicarboxylic acid (H_25abdc)

It was observed that 5-aminobenzene-1, 3-dicarboxylic acid shows a close-packed arrangement of particles with ends similar to a square pyramid shape. The EDS spectrum of 5-aminobenzene-1, 3-dicarboxylic acid (H_25abdc) is shown in Figure 41. Figure 41 revealed the presence of carbon (C) copper, oxygen (O) and nitrogen (N) with atomic percentages of 57.31% for carbon, 31.66% for oxygen and 11.03% for nitrogen.

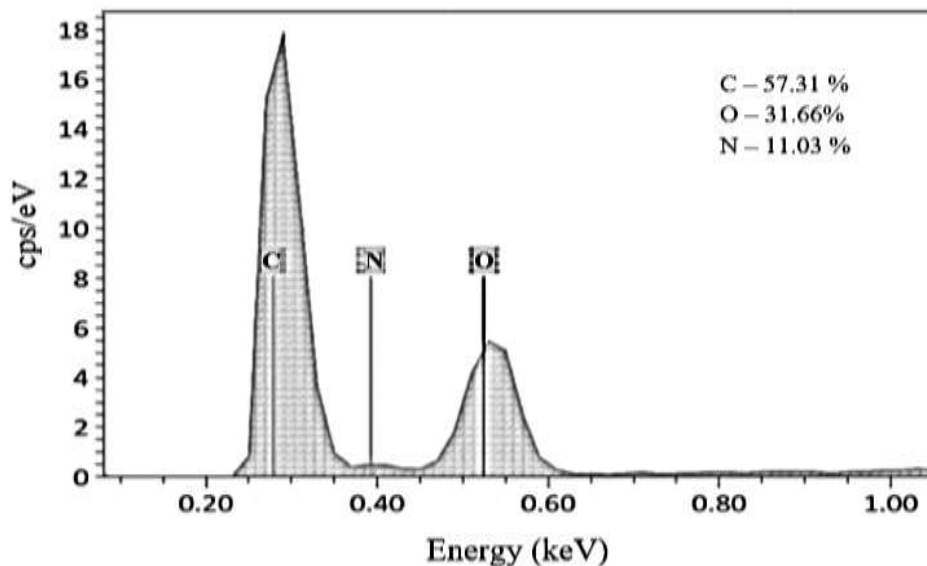


Figure 41: EDS of 5-aminobenzene-1, 3-dicarboxylic acid (H_25abc)

The SEM image of 1, 3, 5- Benzene tricarboxylic acid (H_3BTC) is shown in Figure 42. It is observed that H_3BTC shows a close-packed arrangement with a cuboid-shaped morphology.

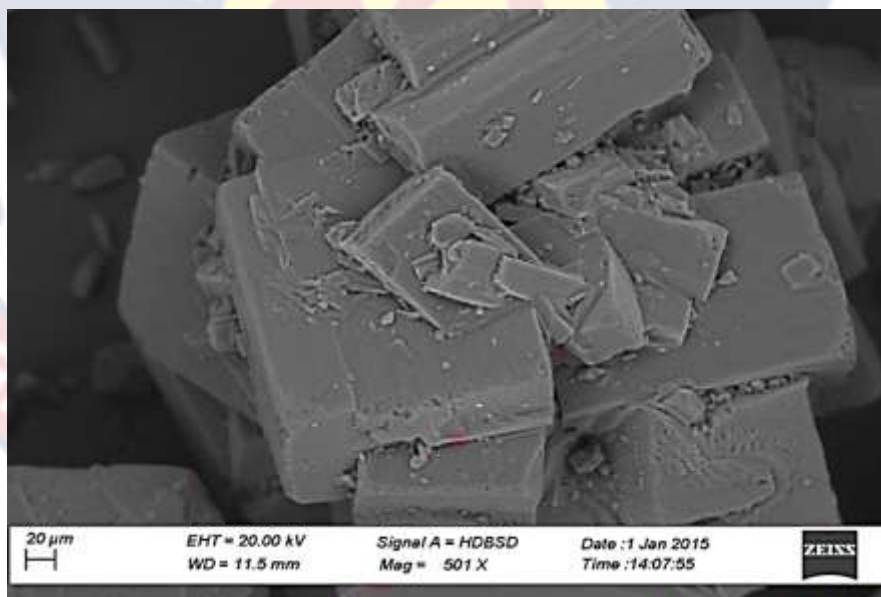


Figure 42: SEM image of 1, 3, 5- Benzene tricarboxylic acid (H_3BTC)

The EDS spectrum of 1, 3, 5- Benzene tricarboxylic acid in Figure 43 revealed the presence of carbon (C) and oxygen (O) with atomic percentages of 64.62 % for carbon and 35.38 % for oxygen.

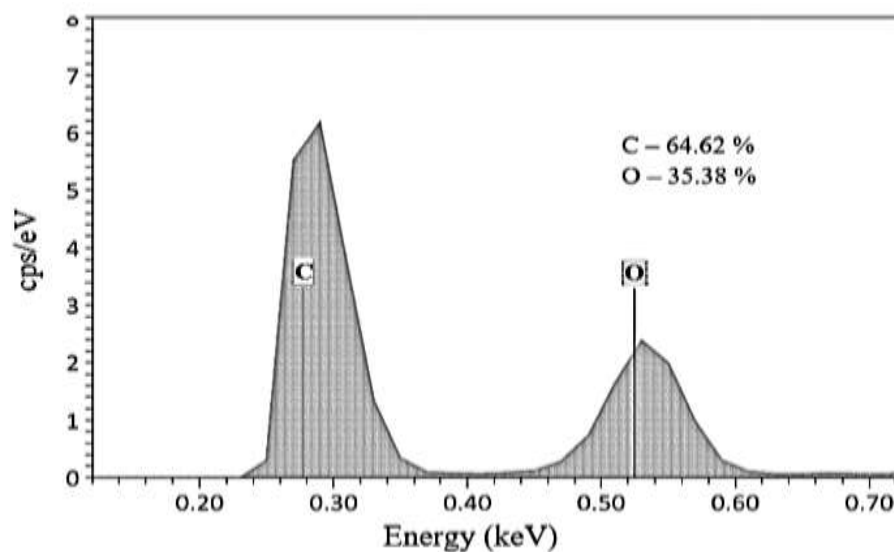


Figure 43: EDS of 1, 3, 5- Benzene tricarboxylic acid (H₃BTC)

SEM-EDS analysis of metal-organic framework formed with 5-aminobenzene-1, 3-dicarboxylic acid

The SEM image for synthesized Cu-5abdc is shown in Figure 44.

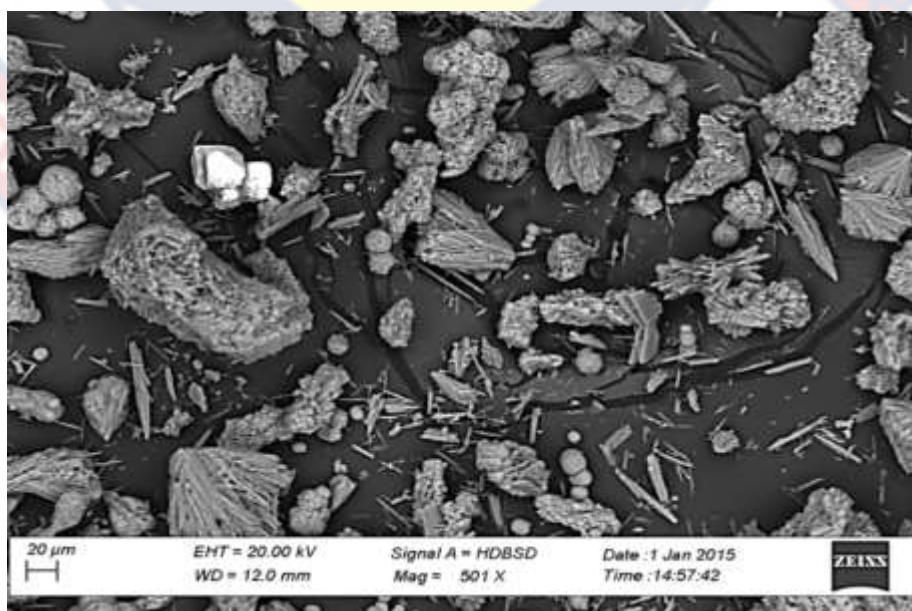


Figure 44: SEM image of synthesized Cu-5abdc

The SEM image shows that Cu-5abdc exhibited a calendula flowering shape morphology similar to the reported work (Kaur, Yusuf & Malik, 2021). The EDS spectrum of Cu-5abdc is shown in Figure 45. The spectrum revealed the presence of carbon (C), copper (Cu) and oxygen (O) with atomic percentages of 57.82 % for carbon, 29.81 % for oxygen and 12.38% for copper (C).

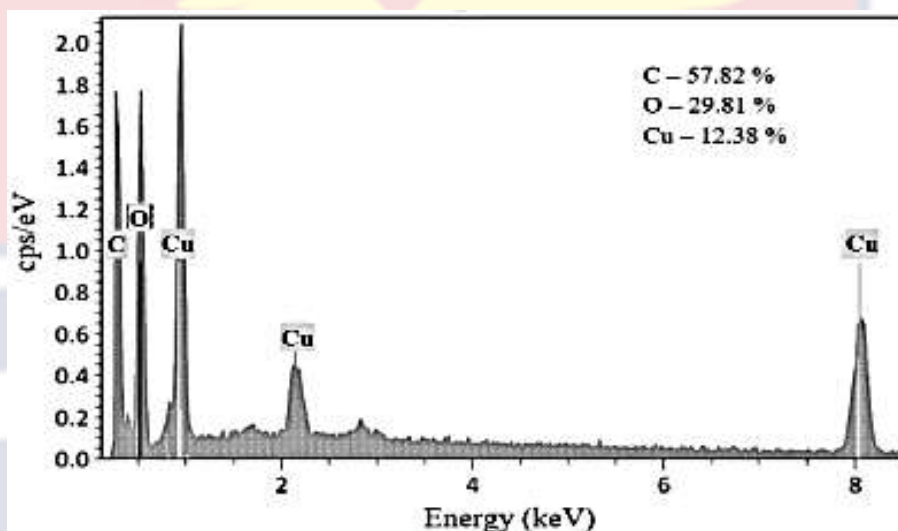


Figure 45: EDS synthesized of Cu-5abdc

The SEM image of synthesized Ce-5abdc is shown in Figure 46.

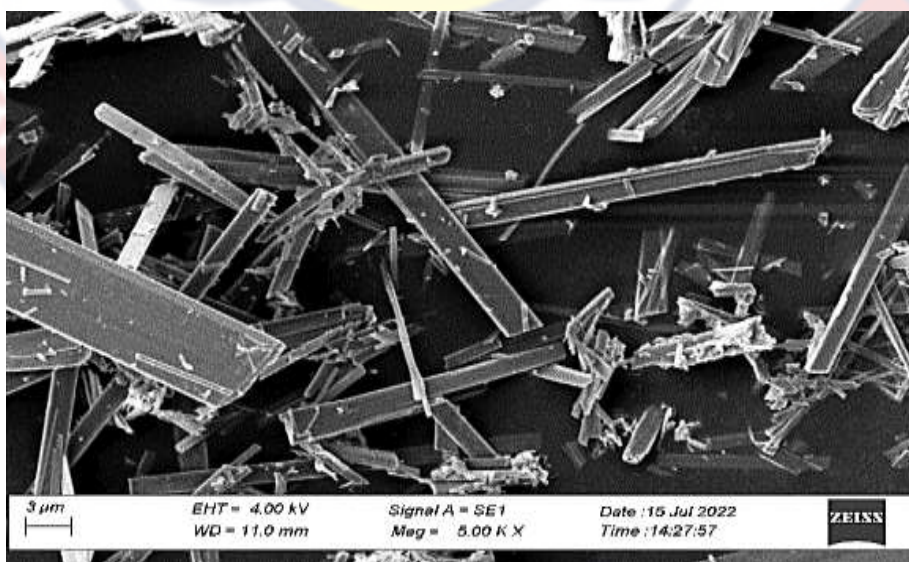


Figure 46: SEM image of synthesized Ce-5abdc

The SEM image of Ce-5abdc shows rod-like rectangular prism shape morphology similar to other reported works related to cerium MOFs (Dong & Huang, 2020; Ramachandran et al., 2018; Xie et al., 2021). The EDS spectrum of Ce-5abdc shown in Figure 47 revealed the presence of carbon (C), cerium (Ce) and oxygen (O) with atomic percentages of 67.01 % for carbon, 23.76 % for oxygen and 7.22% for cerium (Ce).

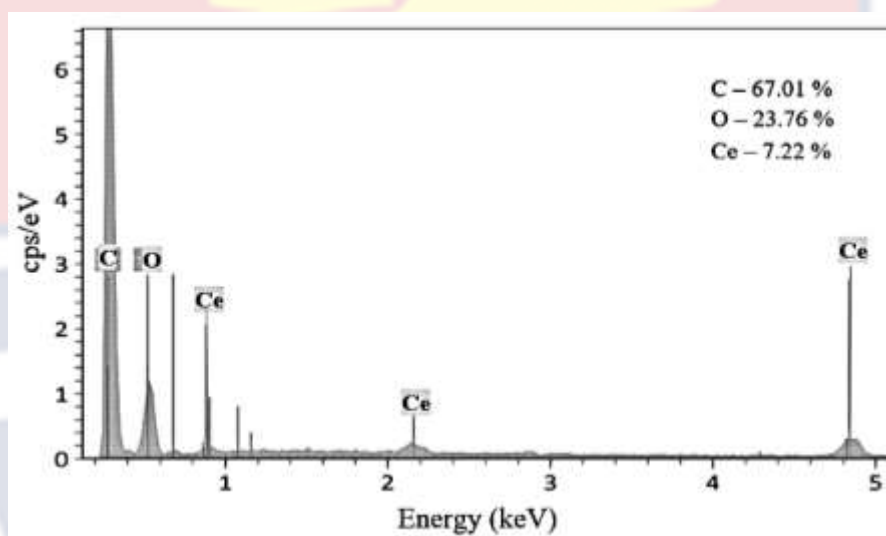


Figure 47: EDS of synthesized Ce-5abdc

The SEM image of synthesized Zr-5abdc is shown in Figure 48.

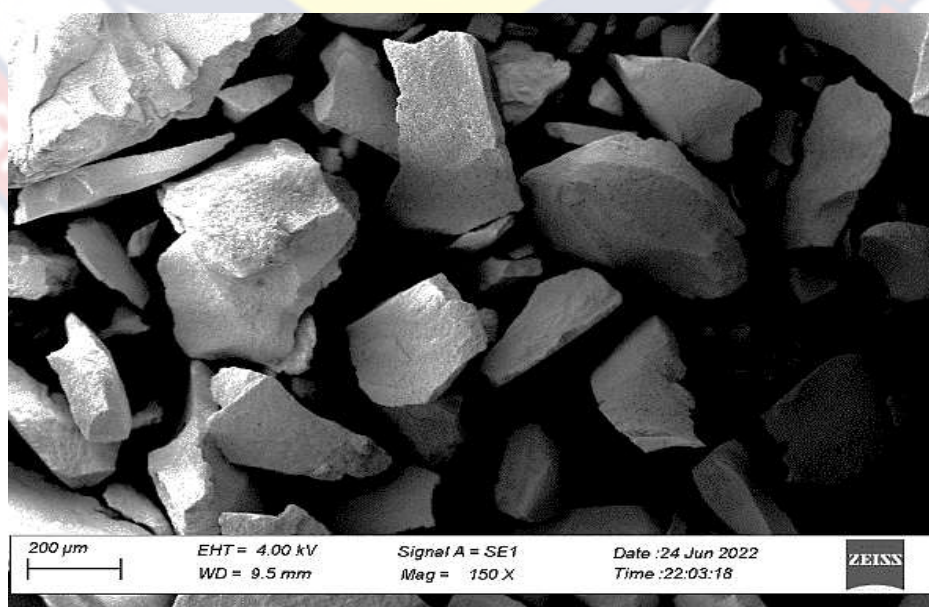


Figure 48: SEM image of synthesized Zr-5abdc

The SEM image exhibited irregular flake-shape morphology. The EDS spectrum of Zr-5abdc shown in Figure 49 revealed the presence of carbon (C), zirconium (Zr) and oxygen (O) with atomic percentages of 53.90 % for carbon, 40.04% for oxygen and 6.07 % for zirconium (Zr).

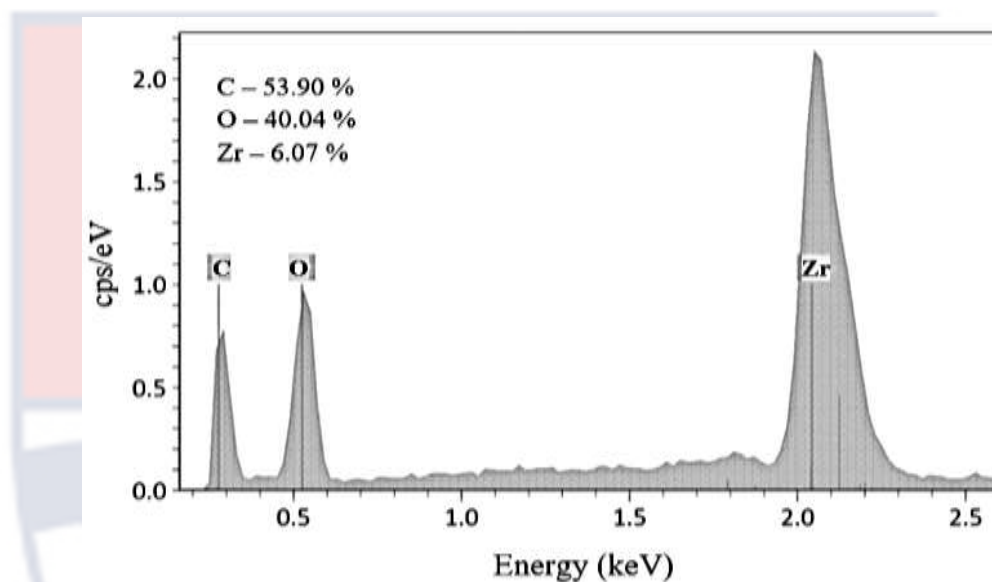


Figure 49: EDS of synthesized Zr-5abdc

Nitrogen was not identified from the EDS shown for the synthesized frameworks. The absence of nitrogen is due to an overlap of C and O k-alpha peaks which are heavier than nitrogen and fall close to it. It is also possible the nitrogen in the samples was absorbed by the beryllium window that separated the sample chamber from the analyzer during the EDS analysis (Gazulla, Rodrigo, Blasco & Orduña, 2013; Makhlof & Aliofkhazraei, 2015).

SEM-EDS analysis of metal-organic framework formed with 1, 3, 5-benzene tricarboxylic acid

SEM images of synthesized Cu-BTC are shown in Figure 50. The crystals image exhibited cubic crystal particles with an octahedral geometry

similar to reported results (Chang, Zheng, Zhao, Yang, 2019; Ge et al., 2018; Gu, Li & Ma, 2022; Hu, Peng, Tan & Zhao, 2015; Nivetha et al., 2020; Sun et al., 2019; Yang et al., 2018)

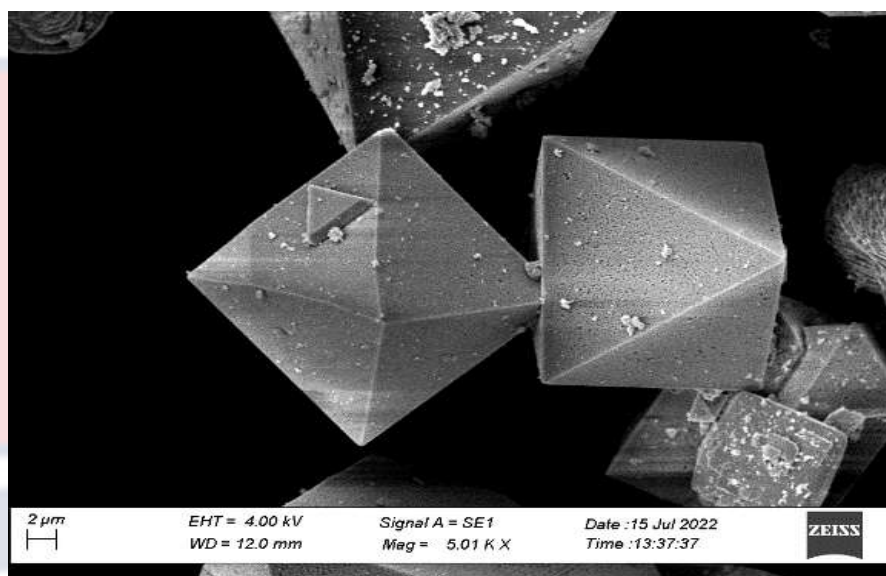


Figure 50: SEM images of synthesized Cu-BTC

The EDS spectrum of Cu-BTC shown in Figure 51 revealed the presence of carbon (C), copper (Cu) and oxygen (O) with atomic percentages of 58.22 % for carbon, 34.21 % for oxygen and 7.57% for copper.

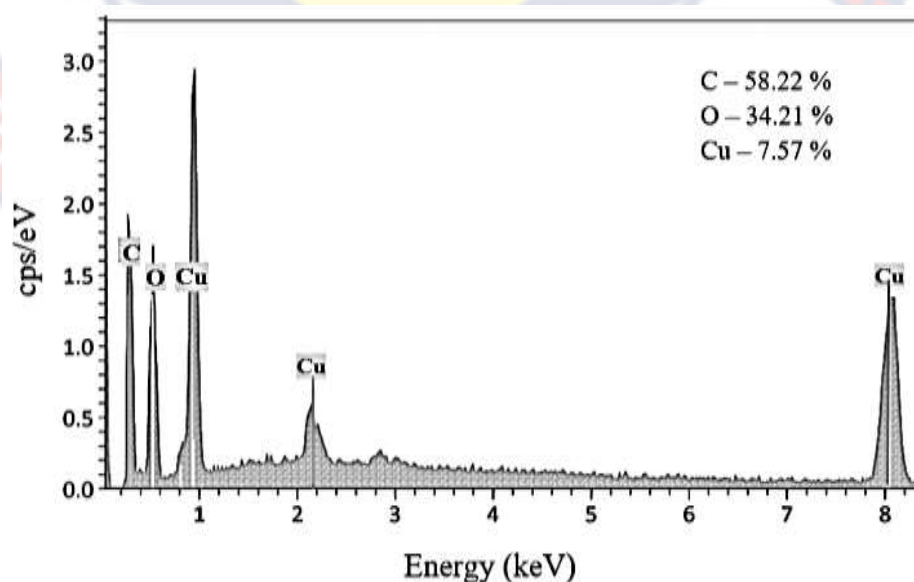


Figure 51: EDS of synthesized Cu-BTC

SEM images of Ce-BTC are displayed in Figure 52. The SEM images of Ce-BTC exhibited rod-like needle-shaped particles with ends similar to a square pyramid similar to reports from literature (Peng, Ganesh, Vinodh, Palanichamy & Jang, 2019; Ramachandran et al., 2018).

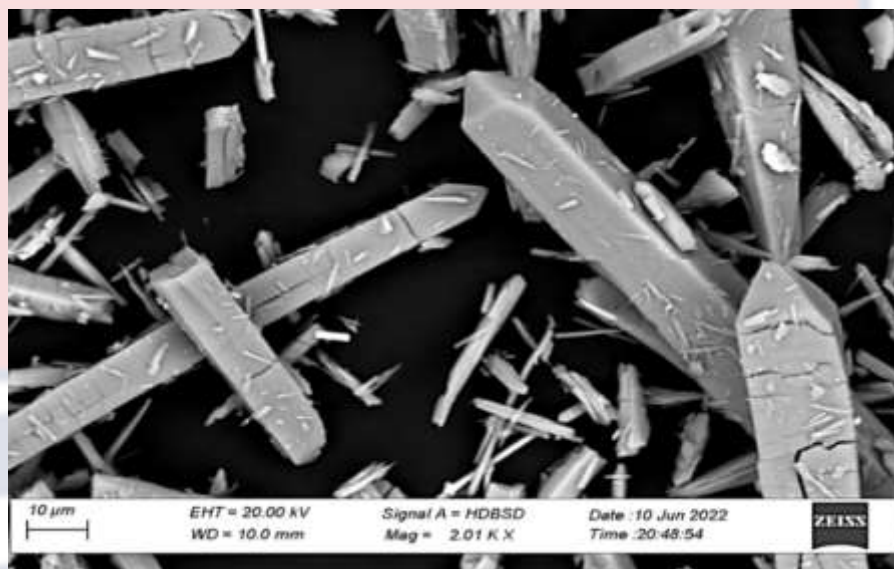


Figure 52: SEM images of synthesized Ce-BTC

The EDS spectrum of Ce-BTC shown in Figure 53 revealed the presence of carbon (C), cerium (Ce) and oxygen (O) with atomic percentages of 66.72 % for carbon, 32.73 % for oxygen and 6.55 % for cerium (Ce).

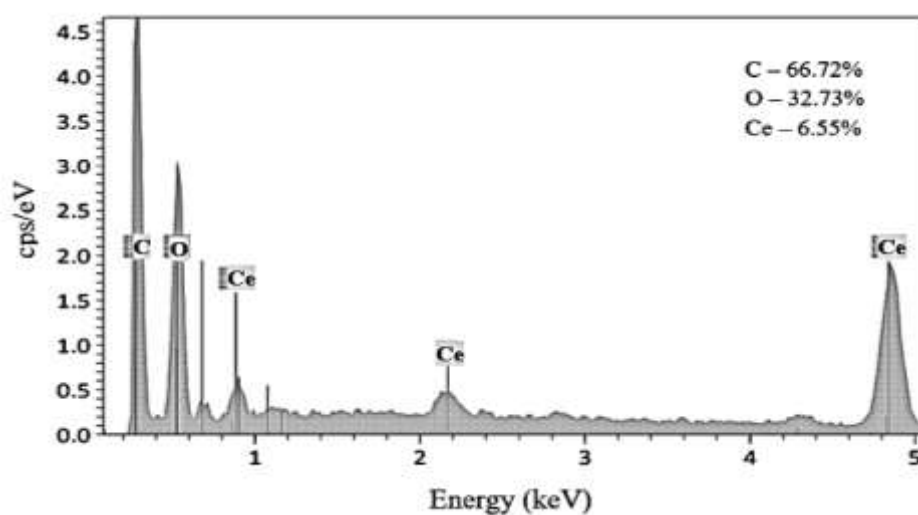


Figure 53: EDS of synthesized Ce-BTC

The SEM image of synthesized Zr-BTC is shown in Figure 44. The SEM image shows irregular rock shape morphology.

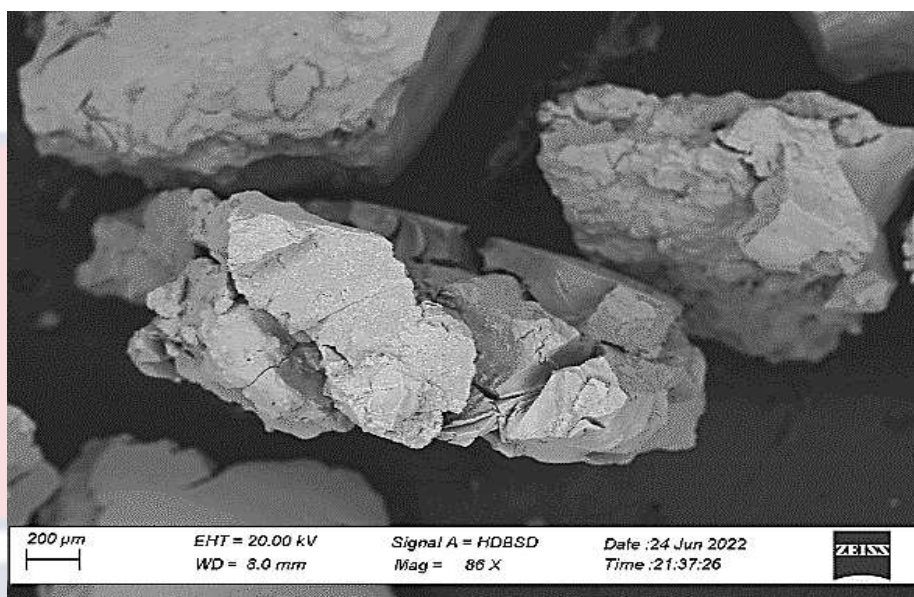


Figure 54: SEM image of synthesized Zr-BTC

The EDS spectrum of Zr-BTC shown in Figure 55 revealed the presence of carbon (C), zirconium (Zr) and oxygen (O) with atomic percentages of 50.61 % for carbon, 40.66% for oxygen and 8.72 % for zirconium (Zr).

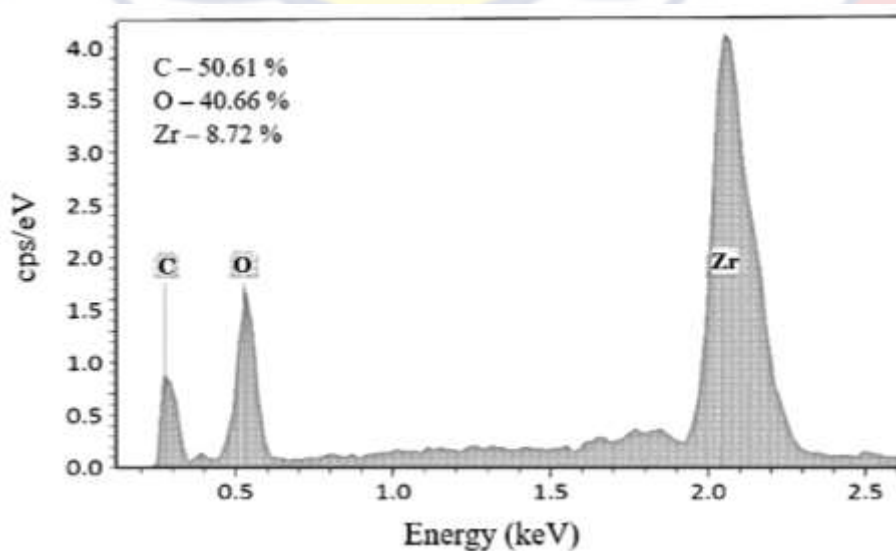


Figure 55: EDS of synthesized Zr-BTC

Single Crystallography Analysis of Synthesized Cu-BTC Metal-Organic Framework

The Cu-BTC MOF was the most crystalline among the synthesized MOFs. The result of single crystal XRD analysis of Cu-BTC is shown in Figure 56. The Cu-BTC MOF had a formula $[\text{Cu}_3(\text{C}_9\text{H}_3\text{O}_6)_2] \cdot 3\text{H}_2\text{O} \cdot 18\text{H}_2\text{O}$ with a unit formula $\text{C}_6\text{H}_{16}\text{CuO}_{11}$. From Figure 56 it can be seen that the compound crystallizes in the $Fm-3m$ space group with each unit consisting of an assembly of two linked copper atoms (Cu1) forming coordinates with four carboxylate oxygen atoms (O1) each and one oxygen atom (O2) each from coordinated H_2O molecule (Sheldrick, 2015a; Sheldrick, 2015b). The unit assembly forms a cubic crystal system with a trapezoid shape having a size dimension of $0.10 \times 0.09 \times 0.07 \text{ mm}^3$ with a bond length of $a = 26.2891(3) \text{ \AA}$, $b = 26.2891(3) \text{ \AA}$, $c = 26.2891(3) \text{ \AA}$ and bond angle, $a = b = g = 90^\circ$. A water mask of $V = 18168.8(6) \text{ \AA}^3$ was obtained for a void per unit cell.

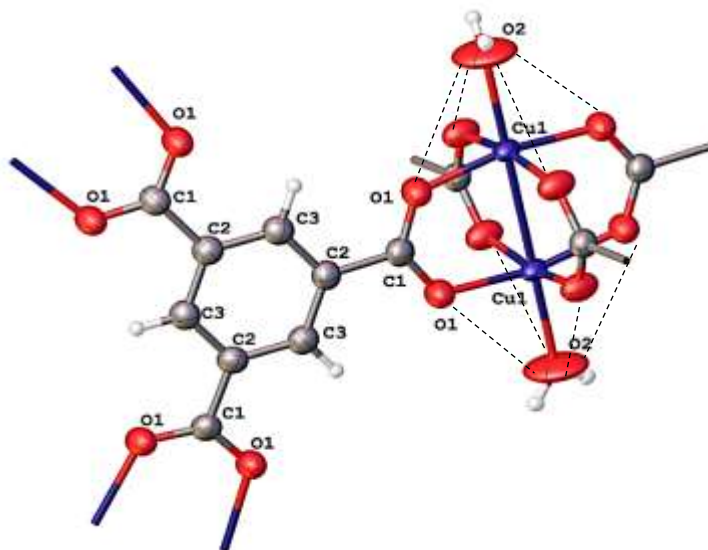


Figure 56: A grown view of the copper complex found within Cu-BTC

The coordination of the carboxylate oxygen, water oxygen and copper develops into a highly porous 3D network of metal-organic framework shown in Figure 57 having four pore centres.

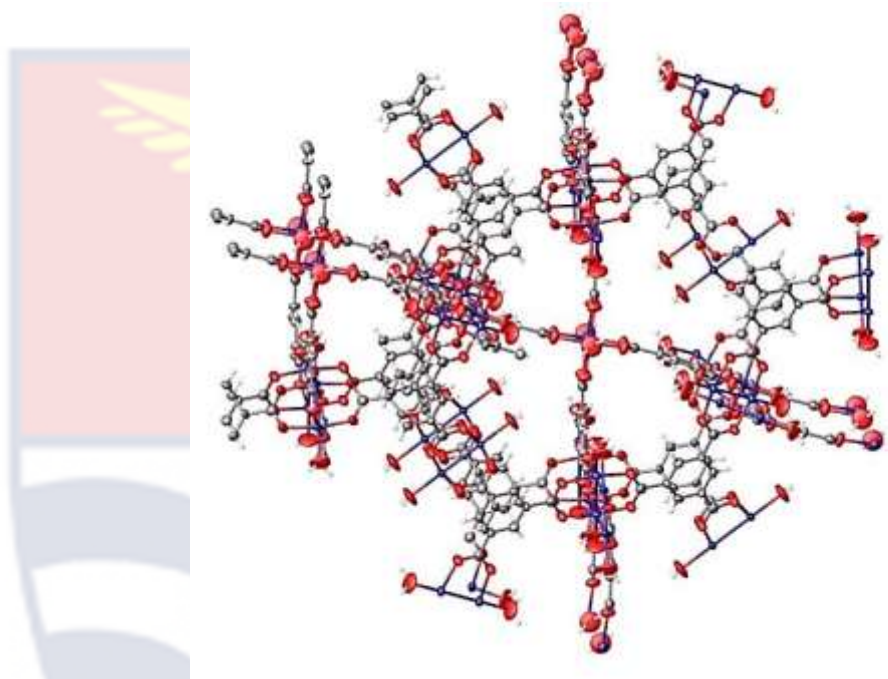


Figure 57: A 3D network of Cu-BTC metal-organic framework

Thermogravimetric (TGA) Analysis of Synthesize Metal-Organic Frameworks

Thermogravimetric (TGA) analysis was further done to investigate the thermal stability of the synthesized metal framework. The TGA analysis was done in a temperature range of 20 °C to 800 °C under nitrogen atmosphere.

Thermogravimetric (TGA) analysis of copper metal-organic frameworks

Thermogravimetric (TGA) analysis of Cu-5abdc is shown in Figure 58. Three major weight losses were observed. The weight losses began at 50 °C and ended at 800°C. The first and second weight loss percentages of

11.07% and 10.61% with corresponding exothermic rates of change of weight losses of 5.03 %/min and 4.79 %/min were observed between 50 °C and 300 °C. These weight losses are due to the removal of the absorbed water molecules and any organic solvents present in the porous Cu-5abdc structure (Gabbott, 2008; Mohamed, 2016; Saadatkah, et al., 2020; Yakuphanoglu, 2019)

A large weight loss percentage of 34.72% with a corresponding exothermic rate of change of weight loss of 26.73 %/min was observed between 300 °C to 400 °C. The sharp decrease in weight was due to the decomposition of the Cu-5abdc which could be due to the elimination of ligand molecules (5abdc) (Mohamed, 2016; Yakuphanoglu, 2019; Zainal, Saiter, Halim, Lucas & Chan, 2021). The decomposition between 300 °C to 400 °C is similar to the thermal decomposition of other copper metal-organic frameworks reported (Aarti, 2016; Al-Janabi et. al., 2016; Liu et al., 2021; Liu, Ghimire, & Jaroniec, 2019; Yang, Ruess, & Carreon, 2015).

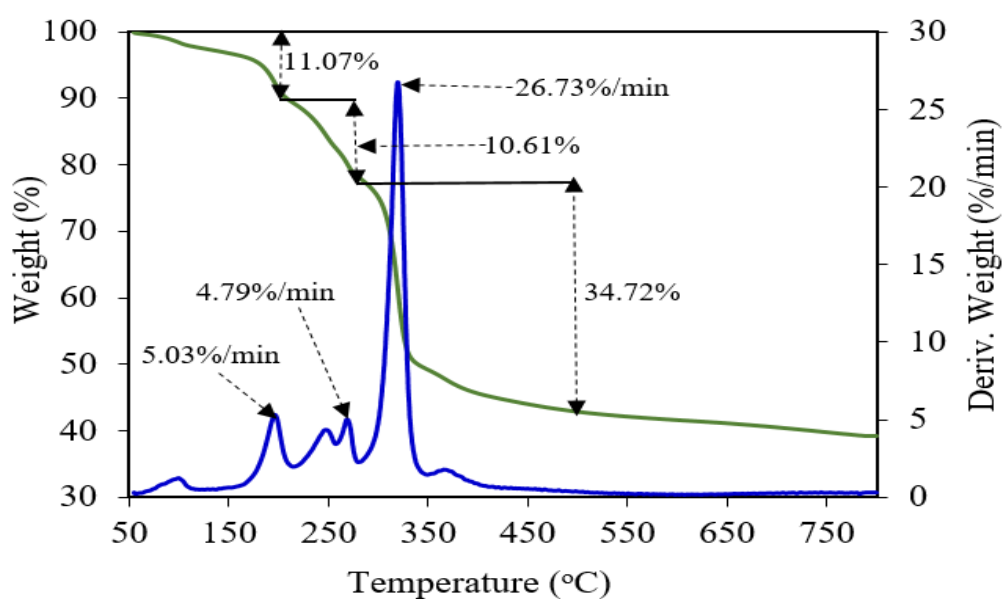


Figure 58: TGA-DSC of synthesized Cu-5abdc

A minimal weight loss decrease was observed from 500–800 °C which confirms the formation of copper oxide after the decomposition of the Cu-5abdc as reported for other copper MOFs (Huang & Wu, 2018; Kar, & Srivastava, 2018; Nivetha et al., 2020). The decomposition of Cu-5abdc around 300 °C indicates Cu-5abdc can withstand excessive heat and will only disintegrate above 300 °C.

Thermogravimetric analysis of Cu-BTC is shown in Figure 59. The weight loss pattern concurred with previous literature results (Kar, & Srivastava, 2018; Nivetha et al., 2020; Yang, Ruess & Carreon, 2015). Two main weight loss steps and corresponding rate of change of weight loss exothermic peaks were observed. The weight losses began at 50 °C and ended at 800 °C. The first weight loss percentage of 23.63% with a corresponding rate of change of weight loss of 7.31 %/min was observed between 50 °C and 200 °C.

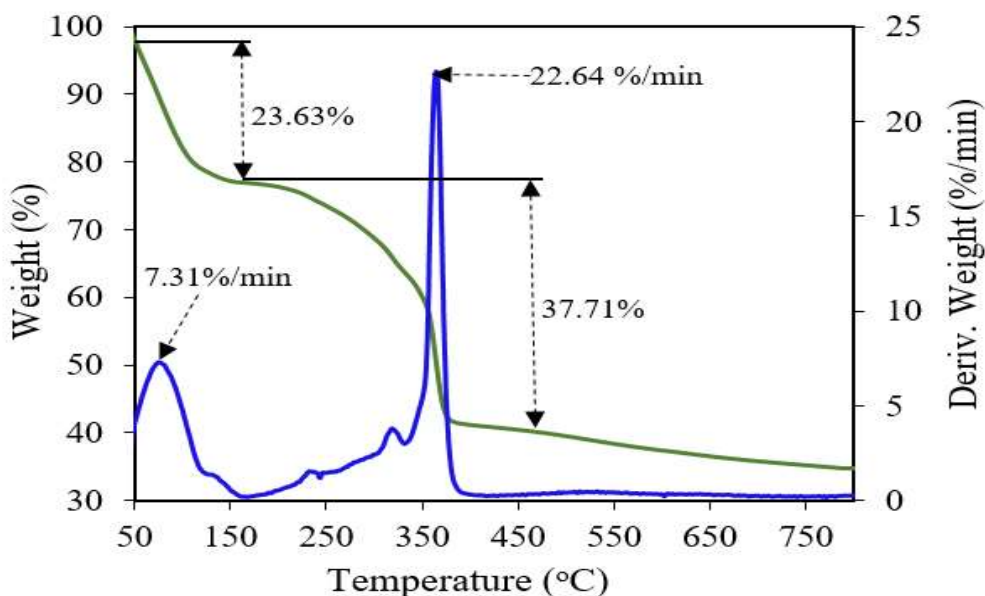


Figure 59: TGA-DSC of synthesized Cu-BTC

The loss in weight is highly a result of the elimination of water molecules and organic solvents remaining in the Cu-BTC (Kar, & Srivastava, 2018; Mukasyan, 2017). A large percentage loss of 37.71% and a correspondingly high rate of change of weight loss of 22.64 %/min was observed at between 350 °C and 400 °C. The large percentage of weight loss indicates the decomposition of Cu-BTC due to the removal of ligand molecule (BTC) from Cu-BTC (Nivetha et al., 2020; Yakuphanoglu, 2019). A slight decrease in the percentage weight loss was however observed in the range of 400–800 °C confirming the formation of copper oxide after the decomposition of the Cu-BTC (Kar, & Srivastava, 2018; Huang & Wu, 2018; Nivetha et al., 2020). The decomposition of Cu-BTC around 400 °C indicates Cu-BTC is thermally stable and will only disintegrate above 400 °C.

Thermogravimetric analysis (TGA) of cerium metal-organic frameworks

The thermogram for the decomposition of Ce-5abdc is shown in Figure 60. Three major weight losses were observed from 50 °C to 800 °C. The first and second weight loss percentages of 6.88% and 13.74% with corresponding exothermic rates of change of weight losses of 0.12 %/min and 0.09 %/min were observed between 50 °C and 350 °C. These weight losses are due to the removal of the absorbed water molecules and organic solvents present in the Ce-5abdc (Mohomed, 2016; Mukasyan, 2017). A large weight loss percentage of 42.69% with a corresponding broad exothermic rate of change of weight loss peak at 0.13 %/min was observed between 350 °C and 750 °C. The large decrease in weight was due to the decomposition of the Ce-5abdc (Mukasyan, 2017 Saadatkah, et al., 2020).

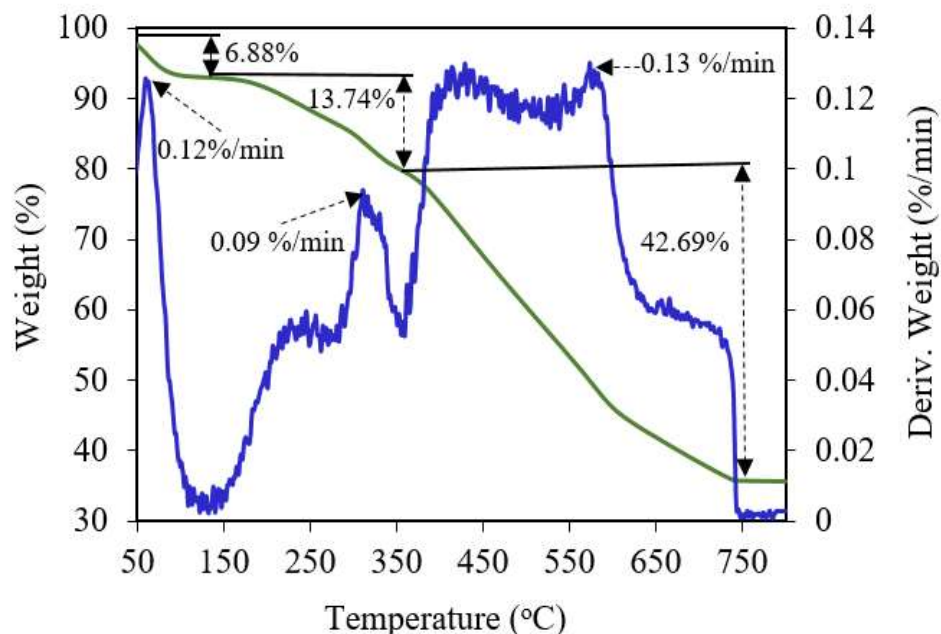


Figure 60: TGA-DSC of synthesized Ce-5abdc

The decomposition could be due to the elimination of ligand molecules (5abdc) as reported for other Ce-5abdc (Almáši, Zelenák, Kuchár, Bourrelly, & Llewellyn, 2016; Santos & Luz, 2020). A slight weight loss decrease was however observed from 750–800 °C which confirms the formation of cerium oxide after the decomposition of the Ce-5abdc relative to obtained literature (Santos & Luz, 2020; Zhang, Chen & Yang, 2019). The decomposition of Ce-5abdc around 650 °C indicates Ce-5abdc) can withstand excessive heat and will only disintegrate above 600 °C.

Thermal analysis of synthesized Ce-BTC compounds is displayed in Figure 61. The weight loss pattern agreed with previous literature results (Almáši, Zelenák, Kuchár, Bourrelly, & Llewellyn, 2016; Almáši, Zelenák, Opanasenko, Císarová, 2015; Santos & Luz, 2020). Four major weight loss steps with corresponding rates of change of weight loss exothermic peaks were observed. The weight losses began at 50 °C and ended approximately at

780 °C. The first and second weight loss percentages of 7.49% and 7.88% with corresponding rates of change of weight of 4.35 %/min and 2.02 %/min were observed between 50 °C and 200 °C. These weight losses could be a result of the removal of adsorbed water residue in Ce-BTC (Santos & Luz, 2020).

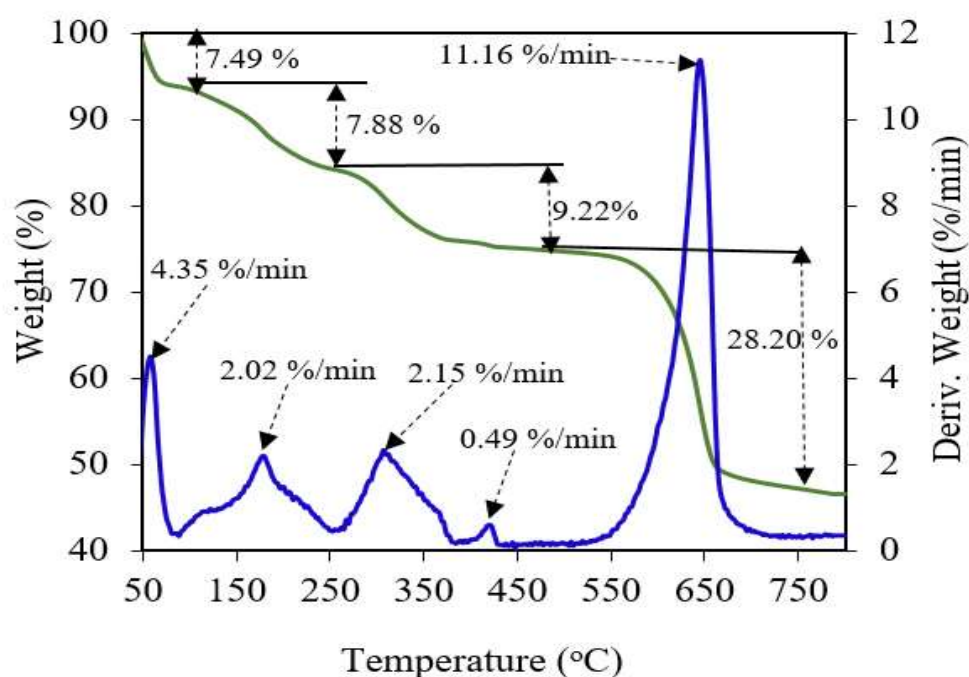


Figure 61: TGA-DSC of synthesized Ce-BTC

The third percentage weight loss of 9.22% with a corresponding exothermic rate of change of weight loss of 2.15 %/min and 0.49 %/min was observed at 480 °C. This observed weight loss could relate to the elimination of absorbed solvents such as DMF used in the synthetic process (Almási, Zelenák, Kuchár, Bourrelly, & Llewellyn, 2016; Santos & Luz, 2020). A large percentage loss of 28.20% with a correspondingly high rate of change of weight loss of 11.16 %/min was observed at between 600 °C and 650 °C. The large percentage of weight loss indicates the disintegration of Ce-BTC by the partial removal of BTC linkers from Ce-BTC (Mukasyan, 2017; Santos &

Luz, 2020). A minimal weight loss decrease was however observed from 700–800 °C which confirms the formation of cerium oxide after the disintegration of the Ce-BTC (Santos & Luz, 2020; Zhang, Chen & Yang, 2019). The decomposition of Ce-BTC around 600 °C indicates Ce-BTC can withstand excessive heat and will only disintegrate above 600 °C.

Thermogravimetric analysis (TGA) of synthesized zirconium metal-organic frameworks

The TGA thermogram for the decomposition of Zr-5abdc is shown in Figure 62. The synthesized Zr-5abdc) showed two weight losses in the temperature range between 50 °C and 800 °C. The first weight loss percentage of 5.84% with a corresponding exothermic rate of change of weight loss of 0.07%/min was observed between 50 °C and 150 °C due to the removal of absorbed water and organic solvent residue present in the sample ((Gabbott, 2008; Mohomed, 2016; Saadatkah, et al., 2020; Yakuphanoglu, 2019). A downward steady trend of weight loss was observed from 350 to 800 °C with three corresponding exothermic rates of change of weight loss of 0.15%/min, 0.09 %/min and 0.07 %/min having the highest rate of change of weight loss between 350 °C and 400 °C. The weight loss of Zr-5abdc was a result of the breakdown of the framework to form oxides (Mohomed, 2016; Yakuphanoglu, 2019; Zainal, Saiter, Halim, Lucas & Chan, 2021). The path of decomposition could be a result of the partially amorphous nature of the Zr-5abdc). The decomposition of Zr-5abdc between 350 °C to 650 °C indicates Zr-5abdc is thermally stable and will completely disintegrate only above 650 °C.

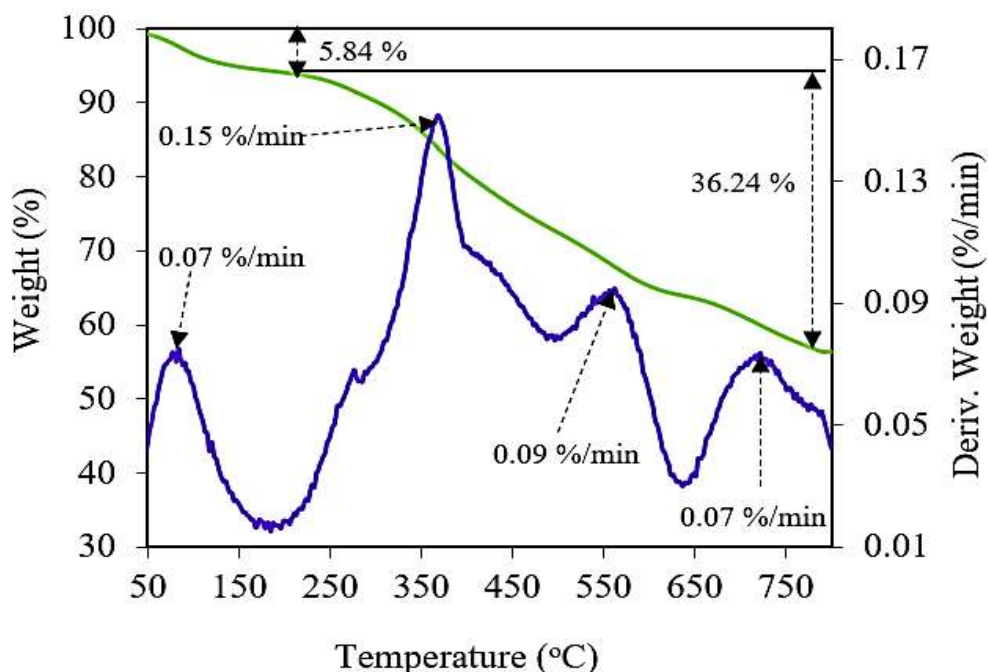


Figure 62: TGA-DSC of synthesized Zr-5abdc

Thermogravimetric analysis of Zr-BTC is shown in Figure 63. Three major weight losses were observed. The weight losses began at 50 °C and ended approximately at 800 °C. The first and second weight loss percentages of 5.17% and 14.93% with corresponding exothermic rates of change of weight losses of 0.13 %/min and 0.21 %/min were observed between 50 °C and 400 °C. These weight losses are due to the removal of the absorbed water molecules and organic solvents existent in the porous Zr-BTC structure (Mohomed, 2016; Mukasyan, 2017; Yakuphanoglu, 2019). A large weight loss percentage of 20.01% with a corresponding exothermic rate of change of weight loss of 0.32 %/min was observed between 550 °C to 650 °C. The large decrease in weight was due to the decomposition of the Zr-BTC (Mukasyan, 2017 Saadatkah, et al., 2020; Yakuphanoglu, 2019). The decomposition could be due to the elimination of BTC ligand molecules (Ardila-Suárez et al.,

2019; Ardila-Suárez, Alem, Baldovino-Medrano & Ramírez-Caballero, 2020; Ganesh, Hemalatha, Peng, Cha & Jang, 2014).

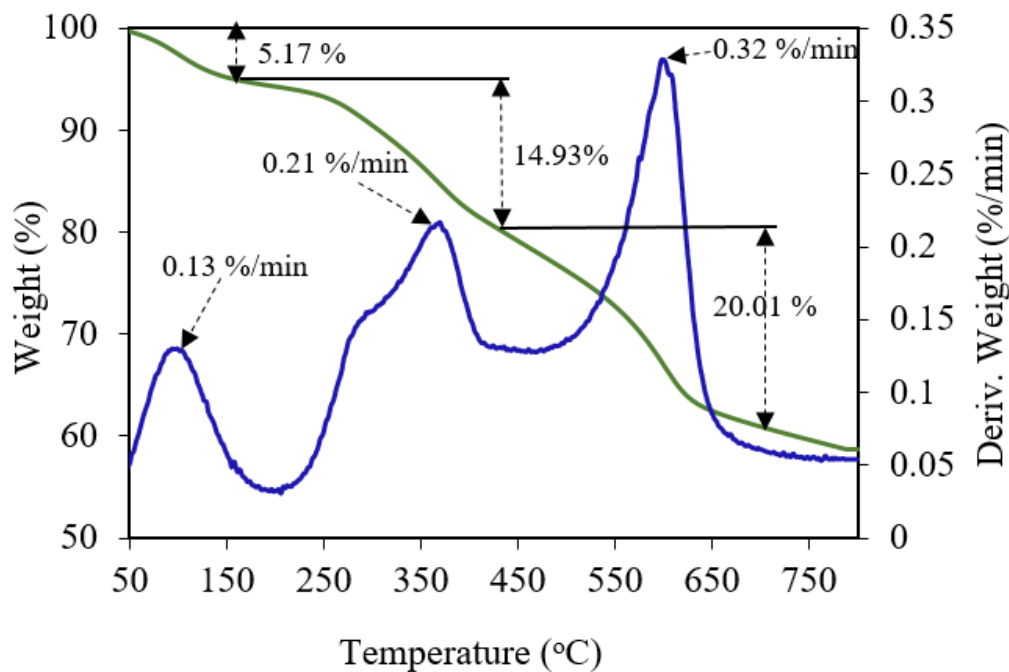


Figure 63: TGA-DSC of synthesized Zr-BTC

A minimal weight loss decrease was however observed from 650–800 °C which confirms the formation of zirconium oxide after the decomposition of the Zr-BTC (Ardila-Suárez et al., 2019; Ardila-Suárez, Alem, Baldovino-Medrano & Ramírez-Caballero, 2020). The decomposition of Zr-BTC around 600 °C indicates Zr-BTC can withstand excessive heat and will only disintegrate above 600 °C.

Photoactivity of Metal-Organic Framework on Selected Pollutants

Photocatalytic activity of synthesized metal-organic frameworks to transform three categories of coloured organic pollutants which included Lissamine green SF (LGSF), Tetraethylrhodamine (TeRh), and Remezol

Brilliant Violet 5R (RBV5R) into less toxic compounds was investigated. Figure 64 displays the transformation of Lissamine green SF (LGSF) which resulted in its removal from water under white and solar light for 180 min.

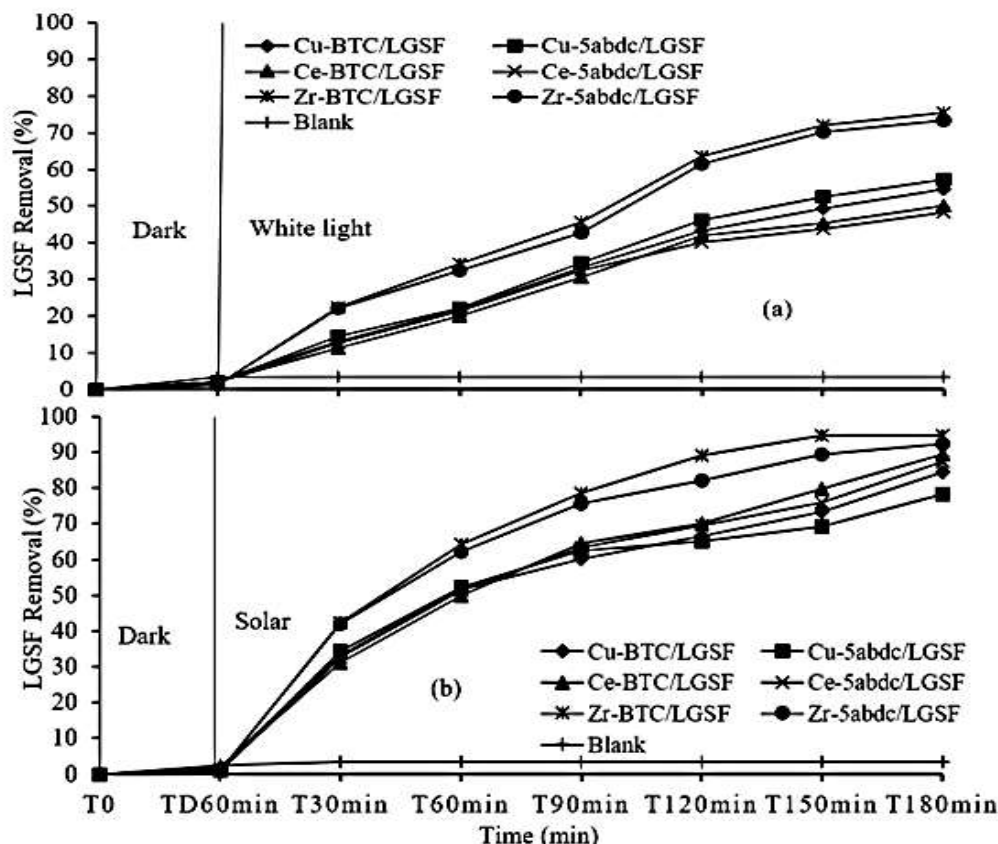


Figure 64: Percentage removal of Lissamine green SF (LGSF) under (a) white light and (b) solar light ([LGSF] = 0.2 g/L; MOF loading = 0.010 g/L; Solution pH = 6).

The percentage of LGSF removal under white light was observed to be lower for all the MOFs compared with the LGSF percentage removal under solar light after 180 min irradiation. The Zr-MOFs were observed to have the highest LGSF removal percentage under both white (a) and solar (b) light compared to the Cu-MOFs and Ce-MOFs. Above 90% removal of LGSF was observed at 180 min for the Zr-MOFs under solar compared with a lower percentage removal between 70 to 75% under white light after 180 min. Zr-

BTC removed 75.34 % LGSF under white light and 94.65 % LGSF under solar light after 180 min. A slightly lower removal of 73.34 % and 92.34 % LGSF under white and solar light was observed for Zr-5abdc.

The percentage LGSF removal values were however close among the Cu-MOFs and the Ce-MOFs. A lower LGSF removal between 40% and 60% under white light and a higher LGSF removal between 70% and 90% under solar light were observed after 180 min. The Ce-MOFs were however observed to have slightly higher LGSF removal compared to the Cu-MOFs with an LGSF removal of 50.12% and 89.48% for Ce-BTC and 48.31%, and 87.39% for Ce-5abdc under white and solar light. Cu-MOFs had the lowest LGSF removal percentages. Cu-BTC however had higher LGSF removal percentages of 84.56% compared to Cu-5abdc with LGSF removal of 78.43% under solar light after the 180 min irradiation.

Figure 65 displays the removal of Tetraethylrhodamine (TeRh) under white and solar light. The percentage of TeRh removal under white light was also observed to be lower for all MOFs compared with the percentage removal of TeRh under solar light after 180 min irradiation. The Zr-MOFs were observed to have the highest TeRh removal percentage under both lights compared to the Cu-MOFs and Ce-MOFs. Zr-BTC was however observed to have a slightly higher TeRh removal relative to Zr-5abdc. A removal of 95.13 % and 78.12% TeRh was observed for Zr-BTC while TeRh percentage removal of 93.23% and 70.95% was observed for Zr-5abdc under white and solar light. The Ce-MOFs were observed to have higher TeRh removal under both lights compared to the Cu-MOFs.

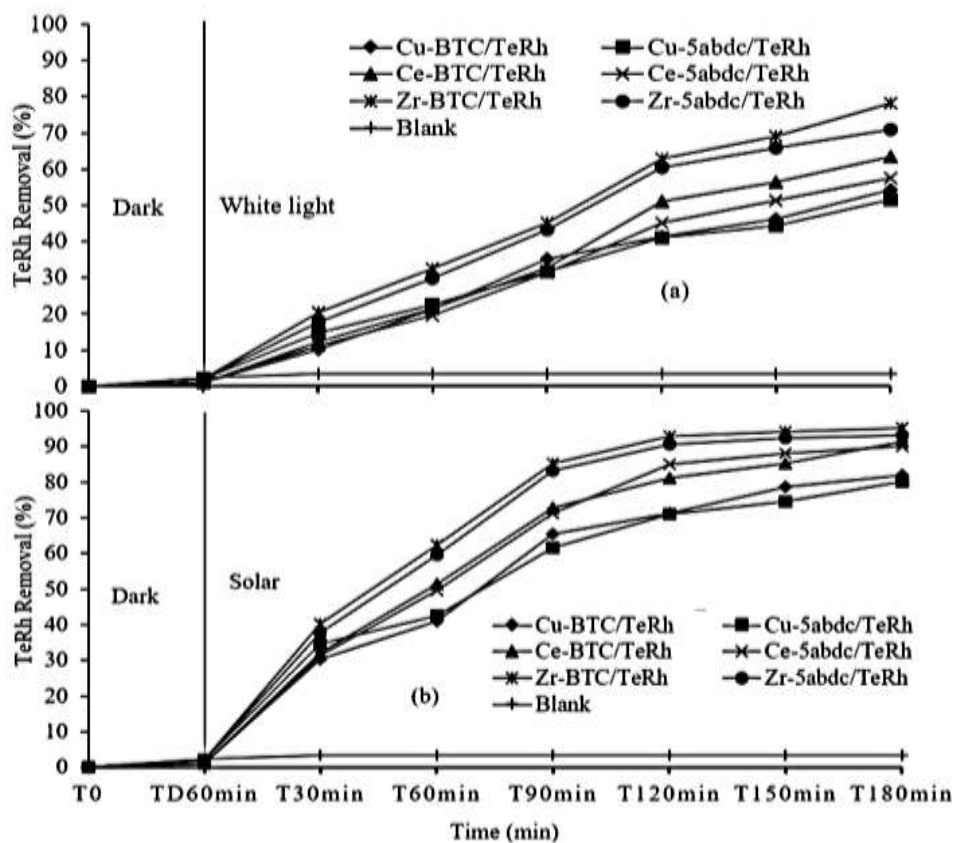


Figure 65: Percentage removal of Tetraethylrhodamine (TeRh) under (a) white light and (b) solar light ([TeRh] = 0.20 g/L; Photocatalyst loading = 0.010 g/L; Solution pH = 8)

Ce-BTC was however seen to have a higher TeRh removal of 63.56% under white light but a slightly lower TeRh removal of 89.61% under solar light relative to relative to Ce-5abdc with TeRh removal of 57.64% under white light and 90.14% under solar after 180 min irradiation. A close percentage of TeRh removal values was observed among the Cu-MOFs with a lower TeRh removal of 50% to 60% under white light and a higher TeRh removal between 80% and 85% after 180 min irradiation.

Figure 66 displays the removal of Remezol Brilliant Violet 5R (RBV5R) under white and solar light at 180 min. The percentage of RBV5R removal under white light was observed to be low for all MOFs compared

with the percentage removal of RBV5R under solar light after 180 min irradiation.

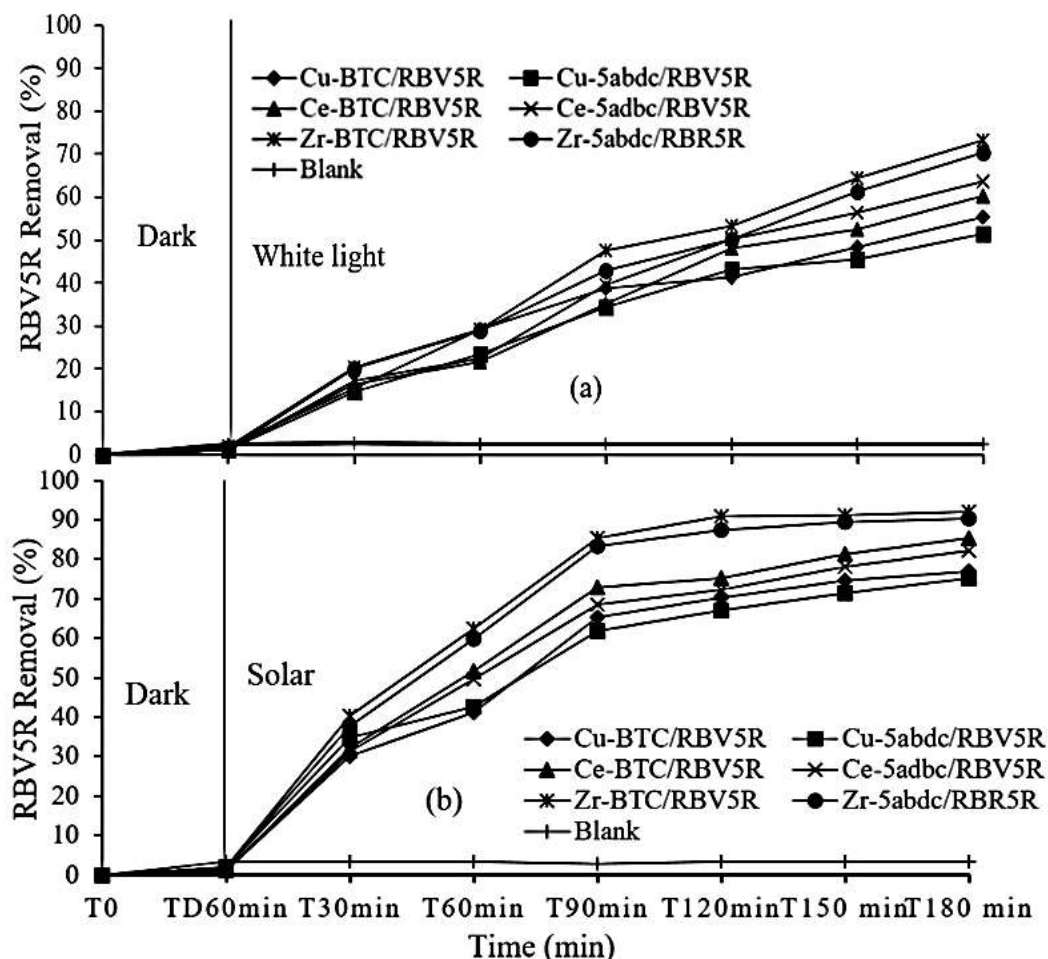


Figure 66: Percentage removal of Ramazole Brilliant Violet 5R (RBV5R) under (a) white light and (b) solar light ($[RBV5R] = 0.2 \text{ g/L}$; Photocatalyst loading = 0.010 g/L ; Solution pH = 6).

The Zr-MOFs were observed to have the highest RBV5R removal percentage under both lights compared to the Cu-MOFs and Ce-MOFs. A slightly higher RBV5R removal was observed for Zr-BTC compared to Zr-5abdc. A removal of 92.13 % and 90.23% RBV5R were observed for Zr-BTC and Zr-5abdc under solar and a lower percentage removal of 73.23 % and 70.45% RBV5R under white light after 180 min light irradiation. The Ce-MOFs were observed to have higher RBV5R removal under white and solar

light compared to the Cu-MOFs. Ce-BTC was however seen to have a lower RBV5R removal of 60.23% under white light but a slightly higher RBV5R removal of 90.14% under solar light relative to relative to Ce-5abdc with RBV5R removal of 63.52% under white light and 82.14% under solar after 180 min irradiation. A close percentage of RBV5R removal values was observed among the Cu-MOFs with a lower RBV5R removal rate of 50% to 60% under white light and a higher RBV5R removal rate between 80% and 85% under solar after 180 min irradiation.

A higher percentage removal of the coloured pollutants under solar light was observed relative to white light for all MOFs after the 180 min light irradiation. In photocatalytic processes, light irradiation is key in the number of electron-hole pair generation. Consequently, higher light intensity increases the oxidation of a compound which results in a higher photocatalytic reaction. The high photon flux from solar light may enhance the interaction between the photons and the active sites on the surfaces of the MOFs to improve photocatalytic removal of the pollutants (Endashaw & Girma, 2020; Reza, Kurny & Gulshan, 2017). The solar light may, therefore, have exhibited a higher intensity level hence the higher removal efficiency.

Metal Organic-Framework Amount Variation Analysis on Selected Pollutants

The amount of MOFs was varied from 0.005 to 0.02 g/L with 0.005 g/L increment to define the optimum amount of the MOFs that could serve as catalysts to transform the selected coloured pollutants into less toxic compounds as a result of their removal from water under photolysis after 180

min. Figure 67 shows the variation in the amount of the MOFs used to investigate their effect on the removal of Lissamine Green SF (LGSF) under photolysis. An increase in the removal of LGSF by the MOFs was generally observed with increasing MOF amounts. A sharp increase in LGSF removal percentages at 180 min with the amount increase of the MOFs from 0.005g/L to 0.010g/L was observed. Slightly higher LGSF removal was however observed for the amount increase from 0.015 g/L to 0.020 g/L for the MOFs after each 180 min light irradiation.

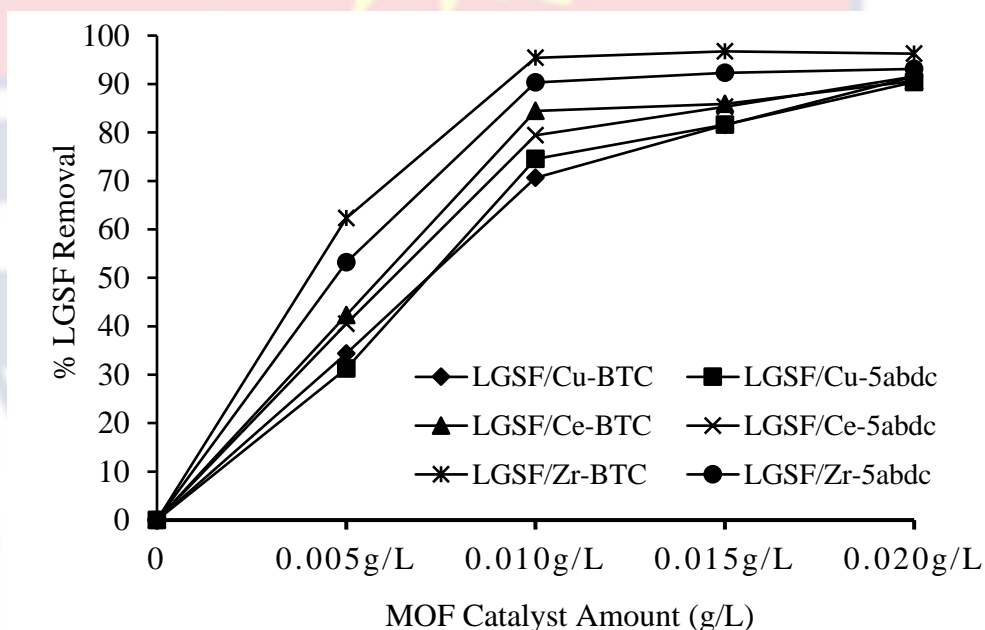


Figure 67: Effect of MOF loading on Lissamine green SF (LGSF) removal ([LGSF] = 0.20 g/L; Solution pH = 6).

The Zr-MOFs however displayed the highest LGSF removal compared to the other MOFs with a percentage LGSF removal above 90 % upon the addition of 0.010g/L and more after 180 min of light irradiation. It was observed that there was no significant change in LGSF removal percentage for the Zr-MOFs with subsequent usage of MOF amounts above 0.010g/L. A considerably lower percentage of LGSF removal was however observed for

Zr-5abdc comparing the Zr-BTC. A slight increase of LGSF removal percentage between 85% and 92% was observed for the amount increase from 0.015 g/L to 0.020 g/L after the 180 min for Ce-MOFs. A marginally higher increment of LGSF removal from 80% to 91% was observed for Cu-MOFs with higher amounts from 0.015 g/L to 0.020 g/L. The removal percentages of Ce-BTC and Ce-5abdc were not significantly different upon an increase in their amount from 0.015 g/L to 0.020 g/L after 180 min light irradiation. A similar result was observed for Cu-BTC and Cu-5abdc with 0.015 g/L and 0.020 g/L amounts.

Figure 68 exhibits the variation of MOF amount to investigate their effect on the removal of Tetraethylrhodamine (TeRh) under photolysis after 180 min light irradiation. A general increase in the removal of TeRh by the MOFs was also observed with increasing MOF amounts. A sharp increase in TeRh TR removal percentages with an increase of the MOFs from 0.005g/L to 0.010g/L was observed. Slightly higher TeRh removal was however observed for the amount increase from 0.015 g/L to 0.020 g/L. The Cu-MOFs and Ce-MOFs showed lower TeRh removal compared to the Zr-MOFs. A TeRh removal above 90% was observed for 0.010g, 0.015 g/L and 0.020 g/L of Zr-MOFs.

No significant change in percentage removal of TeRh was observed for Zr-BTC after 180 min with higher amounts of 0.010g, 0.015 g/L and 0.020g/L. A slight increase in TeRh removal was however observed for the increasing amounts of Zr-5abdc from 0.010 g/L to 0.020 g/L. Ce-BTC, Ce-5abdc, Cu-BTC and Cu-5abdc also had a slight increase for 0.010g/L MOF amount and higher with a lower percentage removal of TeRh ranging between

78% to 93%. The percentage removal of TeRh with increasing amounts of Ce-MOFs was however higher relative to Cu-MOFs.

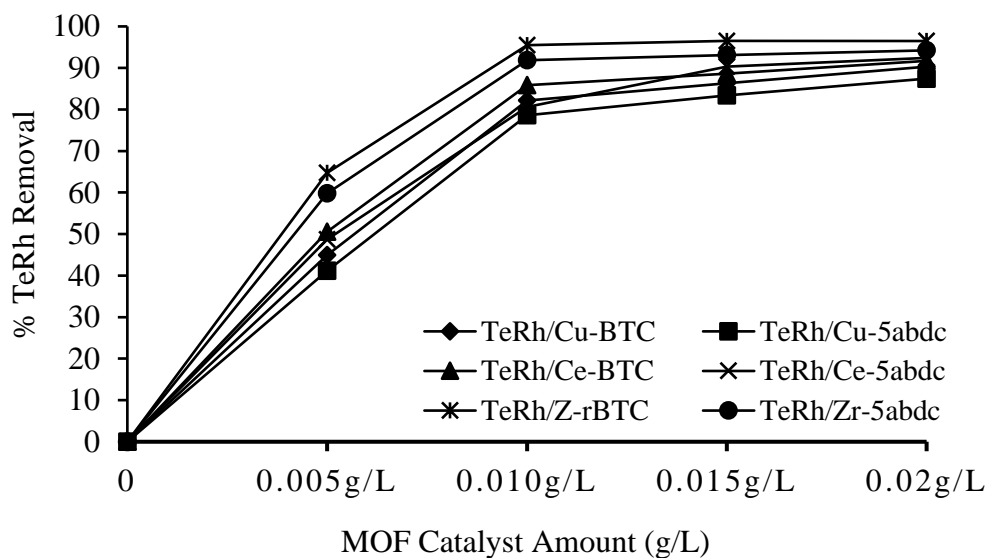


Figure 68: Effect of MOF loading on Tetraethylrhodamine (TeRh) removal ([TeRh] = 0.20 g/L; Solution pH = 8).

Figure 69 shows the variation of MOF amounts to examine their effect on the removal of Ramazole Brilliant Violet 5R (RBV5R) under photolysis after 180 min light irradiation. An increase in the removal of RBV5R by the MOFs was generally observed with increasing MOF amounts. A sharp increase in RBV5R removal percentages with an increase in the amount of MOF from 0.005g/L to 0.010g/L was observed for all the MOFs. Slightly higher RBV5R removal was however observed for the amount increase from 0.015 g/L to 0.020 g/L. The Zr-MOFs however displayed the highest RBV5R removal compared to the other MOFs with RBV5R percentage removal above 90 % upon the addition of 0.010g/L and more.

A slightly lower RBV5R removal from 76% to 92% was observed for the Cu-MOFs than for Ce-MOFs with RBV5R removal percentages ranging between 80% to 95% from 0.010g/L to 0.020g/L amount. No significant change in percentage removal for the Zr-MOFs with subsequent usage of higher amounts from 0.010g/L was observed. Zr-BTC however showed slightly higher RBV5R removal relative to Zr-5abdc. A small increase in RBV5R removal percentage was observed for the variation of Cu-MOFs and Ce-MOFs amount from 0.010 g/L to 0.020 g/L. A higher RBV5R removal was seen for Ce-MOFs with Ce-BTC having slightly higher RBV5R removal percentages of 85.27%, 93.63% and 94.45% compared to Ce-5abdc with RBV5R removal of 83.39%, 92.56% and 93.56%.

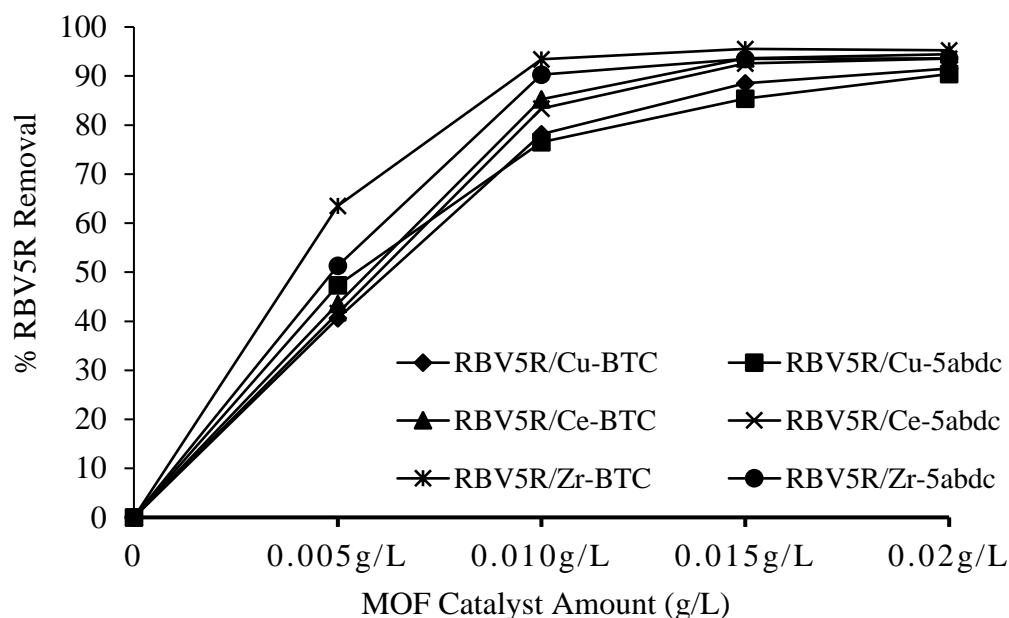


Figure 69: Effect of MOF loading on Ramazole Brilliant Violet 5R (RBV5R) removal ($[RBV5R] = 0.20$ g/L; Solution pH = 6).

Higher RBV5R removal percentages were also observed for Cu-BTC with 78.12%, 87.54% and 91.54% RBV5R removal relative to Cu-5abdc with

76.53%, 85.41% and 89.54% RBV5R removal for the amounts of 0.010g/L, 0.015 and 0.020 g/L. A high pollutant removal was observed for all coloured pollutants when the amount of the MOFs was increased from 0.005 g/L to 0.010g/L. The high pollutant removal efficiency may be due to an increase in available photoactive sites to enhance the photocatalytic transformation into less toxic compounds (Alkaykh, Mbarek & Ali-Shattle, 2020; Rafiq et al., 2021; Reza, Kurny, & Gulshan, 2017). Slow removal of the pollutants was however observed when the amount of the various MOFs was further increased from 0.015g/L to 0.020g/L. The slow removal may be a result of the turbidity generated due to excess suspended MOF particles which may limit the penetration of light radiations. The available surface area for adsorption by the MOFs may also be lost as a result of agglomeration (Endashaw & Girma 2020; Reza, Kurny & Gulshan, 2017). The 0.010 g/L MOF amount was chosen as the optimum catalyst loading for the photocatalysis.

Pollutant Concentration Variation Analysis under Photocatalysis

The pollutant amounts were varied from 0.10 to 0.40 g/L with other variables such as MOF amounts and pH concentration kept constant to define the optimum pollutant concentration that could be removed by the MOFs under photolysis after 180 min. Figure 70 displays the variation of Lissamine Green SF (LGSF) concentration to ascertain its level of removal with increasing concentration under photolysis under the set parameter conditions. The removal of LGSF by the MOFs was seen to generally decrease with increasing LGSF concentration after 180 min photocatalysis. A sharp decrease

in LGSF removal was observed with an increase in LGSF concentration from 0.20g/L to 0.30g/L for all the MOFs.

The Zr MOFs showed the highest photocatalytic activity with increasing LGSF concentration. Zr-BTC had slightly higher reduced LGSF removal from 95.24% to 44.51% relative to Zr-5abdc with LGSF removal reduced from 92.12% to 42.37%. The Ce-MOFs also exhibited a higher photoactivity relative to the Cu-MOFs with increasing LGSF concentration. Higher LGSF removal with increasing concentration was seen with Ce-BTC with removal percentages reduced from 87.63% to 35.62% compared to Ce-5abdc with LGSF removal of 80.56%, reduced to 31.71% among the Ce-MOFs. A slightly higher LGSF removal percentage reduction from 84.54% to 33.72% was also observed for Cu-BTC relative to Cu-5abdc with removal percentages reduction from 79.41% to 30.83% for Cu-MOFs.

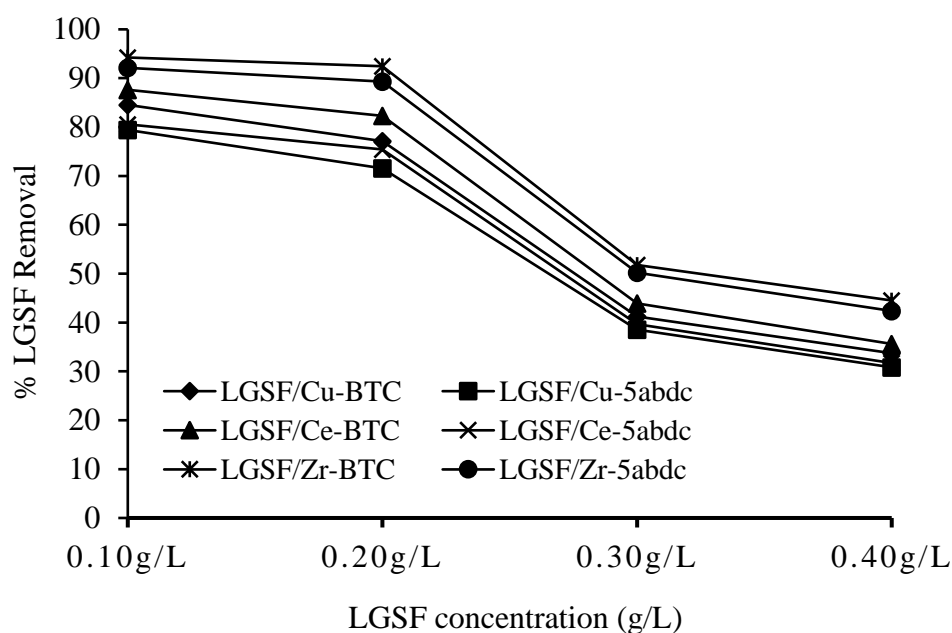


Figure 70: Effect of Lissamine green SF (LGSF) concentration variation on photoactivity (MOF Loading = 0.010 g/L; Solution pH = 6).

Figure 71 presents the variation of Tetraethylrhodamine (TeRh) concentration to investigate its level of removal with increasing concentration under photolysis with constant catalyst amount and pH after 180 min. It was observed that the removal of TeRh by the MOFs generally decreased with increasing TeRh concentration. A sharp decrease in TeRh removal was observed with a TeRh concentration increase from 0.20 g/L to 0.30 g/L for all the MOFs. The Zr-MOFs showed the highest photocatalytic activity with increasing TeRh concentration.

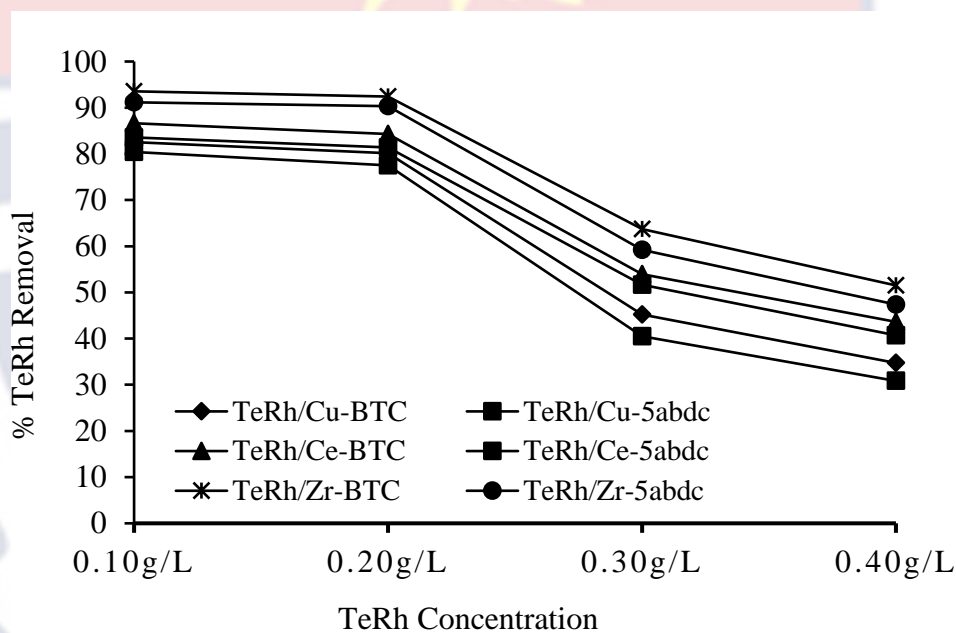


Figure 71: Effect of Tetraethylrhodamine (TeRh) concentration variation on photoactivity (MOF Loading = 0.010 g/L; Solution pH = 8).

Zr-5abdc had slightly lower TeRh removal from 91.16% to 47.37% compared to Zr-BTC with TeRh removal reduction from 93.24% to 51.51%. The Ce-MOFs exhibited a higher photoactivity relative to the Cu-MOFs. A lower TeRh removal with increasing concentration was seen for Ce-5abdc with a removal percentage from 83.56% to 40.71% compared to Ce-BTC with TeRh removal of 86.63% to 43.62% among the Ce-MOFs. A slightly lower

TeRh removal percentage from 80.41% to 30.83% was also observed for Cu-5abdc relative to Cu-BTC with removal percentages reduction from 82.54% to 34.72% for Cu-MOFs.

Figure 72 shows the variation of RBV5R concentration to examine its level of removal with increasing concentration under photolysis with constant set parameter conditions. A general decrease in the removal of RBV5R by the MOFs with increasing RBV5R concentration was observed. A sharp decrease in RBV5R removal was observed with RBV5R concentration increase from 0.20g/L to 0.30g/L for all the MOFs. The Zr-MOFs generally showed the highest photocatalytic activity with increasing RBV5R concentration relative to Cu-MOFs and Ce-MOFs. Higher RBV5R removal from 95.24% to 50.51% was observed for Zr-BTC compared to Zr-5abdc with RBV5R removal from 93.12% to 48.36%.

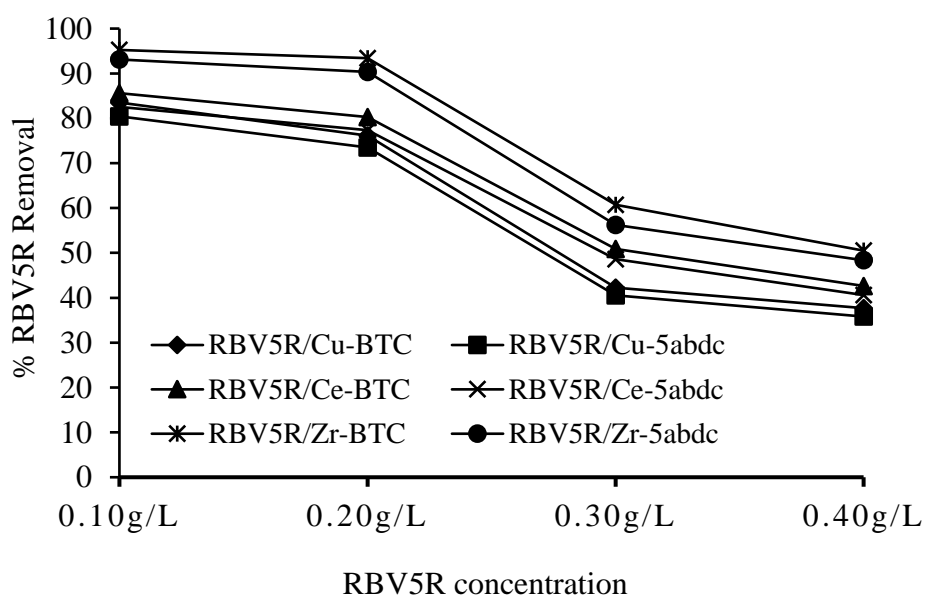


Figure 72: Effect of Ramazole Brilliant Violet 5R (RBV5R) concentration variation on photoactivity (MOF Loading = 0.010 g/L; Solution pH = 6).

A close RBV5R removal concentration was observed among the Cu-MOFs and Ce-MOFs for the various RBV5Rs. The Ce-MOFs however exhibited a higher photoactivity relative to the Cu-MOFs with increasing RBV5R concentration. A marginally higher RBV5R removal with increasing concentration was seen for Ce-BTC with a removal percentages from 85.61% to 42.64% compared to Ce-5abdc with RBV5R removal of 82.55% to 40.61% among the Ce-MOFs. A slightly higher RBV5R removal percentage from 83.52% to 37.69% was also observed for Cu-BTC relative to Cu-5abdc with removal percentages from 80.44% to 35.81% for the Cu-MOFs.

A general decrease in the removal of coloured pollutants with increasing concentrations of the coloured pollutants by the MOFs was observed. This decrease may be a result of the insufficient generation of $\bullet\text{OH}$ radicals which is dependent on a specific amount of catalyst. Excess coloured pollutant ions in solution may cover the active sites on the MOFs limiting the surface generation of holes or $\bullet\text{OH}$ radicals by the MOFs during photolysis (Mahmoodi, 2014; Tambat, Umale & Sontakke 2016). Higher coloured pollutant concentration may also prevent a sufficient amount of light radiation from reaching the surfaces of the MOFs by absorbing a substantial amount of the radiation (Mahmoodi, 2014; Endashaw & Girma 2020). This may reduce the photooxidation process. The pollutant concentration chosen as the optimum initial concentration for the photocatalysis was 0.20g/L.

Results of the pH Variation of Pollutants under Photocatalysis

The pH of the pollutants was varied from 4.0 to 10.0 with other factors such as pollutant concentration and MOF amounts kept constant. Figure 73 displays the results of the variation of pH for LGSF to ascertain its level of removal and transformation into less toxic compounds under photolysis after 180 min. The removal of LGSF by the MOFs was seen to generally decrease with increasing pH value after the 180 min photocatalysis. The Zr MOFs showed the highest LGSF removal with decreasing pH.

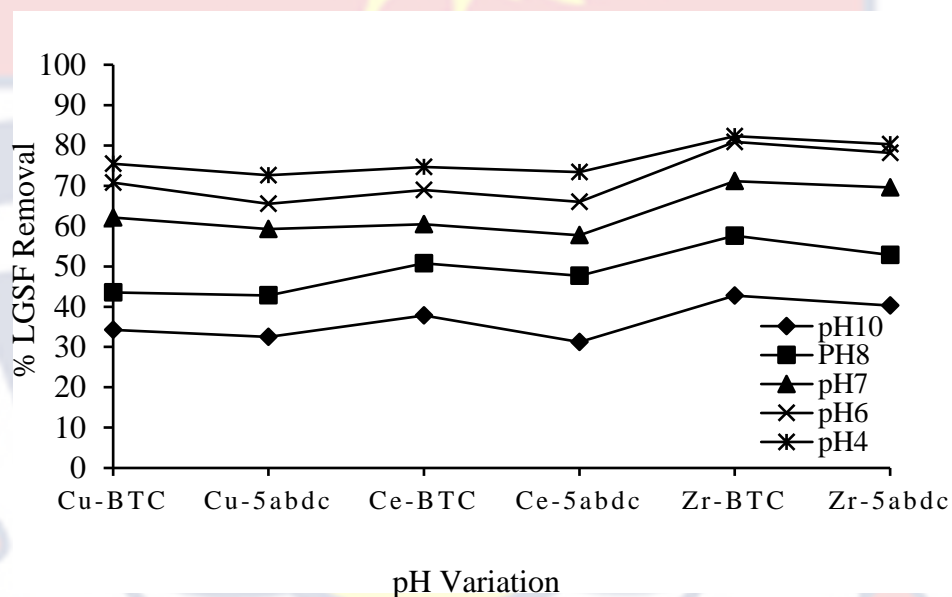


Figure 73: Effect of solution pH on Lissamine green SF (LGSF) percentage removal (MOFs Loading = 0.010 g/L; [LGSF] = 0.20 g/L).

Zr-BTC showed higher removal of 82.29 % to 42.75 % when the pH was increased from pH4 to pH10 than Zr-5abdc with LGSF removal efficiency of 80.28% to 40.25% from pH4 to pH10. The Ce-MOFs also exhibited a higher LGSF removal with lower solution pH relative to the Cu-MOFs. Higher LGSF removal of 74.64% to 37.82% was observed for Ce-BTC from pH 4 to pH 10 compared to Ce-5abdc with LGSF removal from 73.41% to 31.23%. A slightly higher LGSF removal percentage of 75.46% to 34.21%

was also observed for Cu-BTC relative to Cu-5abdc with a removal percentage of 72.61% to 32.52% from pH 4 to pH10 for Cu-MOFs.

Under acidic or basic conditions the surface of the MOFs becomes positively or negatively charged (Eassa, 2016). In acidic media, the MOF surfaces will possess positive charges which could attract anions while in basic media the MOF surfaces will possess negative charges which could attract cations. In the basic environment the generation of $\bullet\text{OH}$ is limited due to Coulombic repulsion between the negatively charged surfaces of the MOFs and the OH ions which decreases photooxidation activity. The LGSF exists in anionic form in water. Since LGSF is anionic, an electrostatic repulsion between the negatively charged surfaces of the MOFs and LGSF may occur. This repulsion may decrease LGSF adsorption onto the surfaces of the MOFs with higher pH values limiting the photooxidation process. (Eassa, 2016; Haddad, Merouani, Hannachi, Hamdaoui & Hamrouni, 2019; Mittal, Mittal, Malviya, Kaur & Gupta, 2010). At lower pH, deprotonation occurs on the surfaces of the MOFs generating positive charges. These positively charged surfaces may attract the anionic LGSF to promote the transformation of LGSF.

Figure 74 displays the variation of pH for TeRh to ascertain its level of removal under photolysis. The removal of TeRh by the MOFs was seen to generally increase with increasing pH value after 180 min photocatalysis. The Zr MOFs showed the highest TeRh removal with increasing pH. Zr-BTC showed slightly higher removal of 42.86 % to 87.79 % from pH4 to pH10 than Zr-5abdc with TeRh removal of 40.91% to 86.95% from pH4 to pH10. The Ce-MOFs exhibited a higher TeRh removal with higher solution pH relative to the Cu-MOFs. A higher TeRh removal of 32.73% to 69.45% was seen for Ce-

BTC from pH 4 to pH 10 compared to Ce-5abdc with TeRh removal of 30.81% to 72.27%. A slightly higher TeRh removal percentage of 28.86% to 67.15% was also observed for Cu-BTC relative to Cu-5abdc with removal percentages of 25.44% to 64.23% from pH 4 to pH 10 for Cu-MOFs.

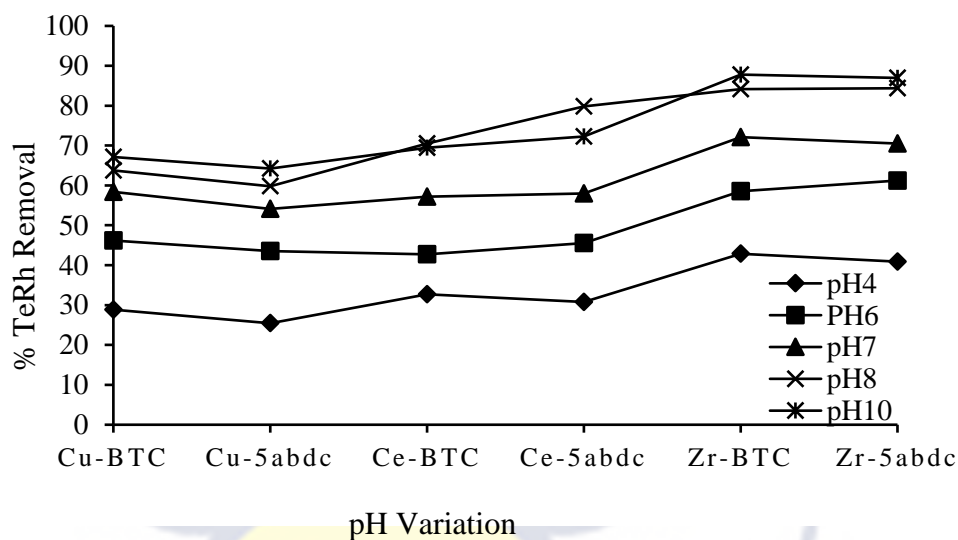


Figure 74: Effect of solution pH on Tetraethylrhodamine (TeRh) percentage removal (MOFs Loading = 0.010 g/L; [TeRh] = 0.20 g/L).

TeRh occurs in cationic (TeRh^+) form as well as zwitter ionic (TeRh^\pm) form in water (Abdullah, 2016; Hariprasad, Anju & Yesodharan, 2013). At lower pH values, the TeRh solution becomes acidic. The surfaces of the MOFs become positively charged and cationic TeRh is also produced. The positive charges from both may cause electrostatic repulsion between them which may limit the ability of the MOFs to adsorb TeRh reducing their removal efficiency. At higher pH values, the TeRh solution becomes basic. The surfaces of the MOFs become negatively charged and zwitter TeRh is also produced. The basic condition also enhances the generation of $\bullet\text{OH}$ radicals (Mugumo, Tichapondwa, & Chirwa, 2022; Khan, Valicsek & Horváth, 2021).

These conditions may promote the adsorption of TeRh onto the surfaces of the MOFs to increase the TeRh removal.

Figure 75 displays the variation of pH for RBV5R to ascertain its level of removal under photolysis. The removal of RBV5R by the MOFs was seen to generally decrease with increasing pH value after 180 min photocatalysis. The Zr MOFs showed the highest RBV5R removal with decreasing pH. Zr-BTC showed higher removal of 86.65 % to 38.51 % from pH4 to pH10 than Zr-5abdc with RBV5R removal of 78.45% to 36.15% from pH4 to pH10.

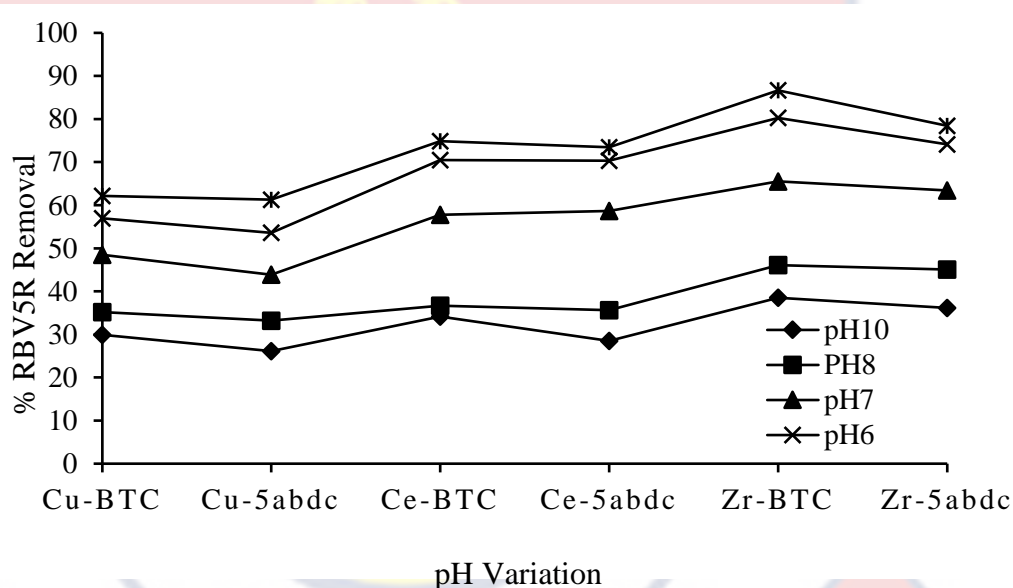


Figure 75: Effect of solution pH on Ramazole Brilliant Violet 5R (RBV5R) percentage removal (MOFs Loading=0.10 g/L; [RBV5R] = 0.20 g/L).

The Ce-MOFs also exhibited a higher RBV5R removal with lower solution pH relative to the Cu-MOFs. Higher RBV5R removal of 74.83% to 34.13% was seen for Ce-BTC from pH 4 to pH 10 compared to Ce-5abdc with RBV5R removal of 73.47% to 28.47%. A slightly higher RBV5R removal percentage of 62.18% to 29.92% was also observed for Cu-BTC relative to

Cu-5abdc with a removal percentages of 61.29% to 26.13% from pH 4 to pH10 for Cu-MOFs.

RBV5R occurs in the anionic form in water. In the basic condition of the RBV5R solution, the MOF surfaces become negatively charged. Since RBV5R is anionic, an electrostatic repulsion between the negatively charged surfaces of the MOFs and RBV5R may occur. The generation of $\bullet\text{OH}$ in the basic environment may also be limited due to Coulombic repulsion from the negatively charged surfaces of the MOFs. These limitations may deter RBV5R adsorption onto the surfaces of the MOFs at higher pH restricting the photooxidation process. (Haddad, Merouani, Hannachi, Hamdaoui & Hamrouni, 2019; Mittal, Mittal, Malviya, Kaur & Gupta, 2010; Khasri, Jamir, Ahmad & Ahmad, 2021; Rápó, et al., 2020; Zainip, Adna & Elshikh, 2021). At lower pH, deprotonation occurs on the surfaces of the MOFs generating positive charges. These positively charged surfaces may attract the anionic RBV5R to promote the transformation of RBV5R to less toxic compounds.

On the whole, the synthesized MOFs are photoactive for the removal of organic pollutants from water. The Zr-MOFs were observed to have the highest performance under various sets of conditions. The performance of Ce-MOFs was found better than Cu-MOFs. The performance of the MOFs could be related to their surface area since photocatalytic activity is much dependent on number of active sites to generate favourable radicals (Alkaykh, Mbarek & Ali-Shattle, 2020; Rafiq et al., 2021; Reza, Kurny, & Gulshan, 2017). The Zr-MOFs are therefore likely to have a larger surface area with a more active site relative to the Ce-MOFs and the Cu-MOFs followed by Ce-MOFs. Generally, a lower performance was observed for the H₂5abdc MOFs compared to the

H₃BTC MOFs. The slightly low performance of H₂5abdc MOFs could be due to the lower energy levels generated for the absorption of light by the presence of weaker metal-nitrogen bonding compared to the metal-oxygen bonding. The optimum pH selected for LGSF and RBV5R removal was pH6 and that of TeRh was pH8.

Kinetic and Isotherm Study on the Adsorption of Coloured Organic Pollutants by Cu-5abdc, Ce-5abdc and Zr-5abdc MOFs

The rate of adsorption of Lissamine green SF (LGSF), Tetraethylrhodamine (TeRh), and Remezol Brilliant Violet 5R (RBV5R) with time from water by Cu-5abdc, Ce-5abdc and Zr-5abdc was examined using the pseudo-first-order adsorption and pseudo-second-order adsorption reaction rate equations. Figure 76 shows the pseudo-first-order adsorption reaction rate of LGSF by Cu-5abdc, Ce-5abdc and Zr-5abdc at varying initial LGSF concentrations.

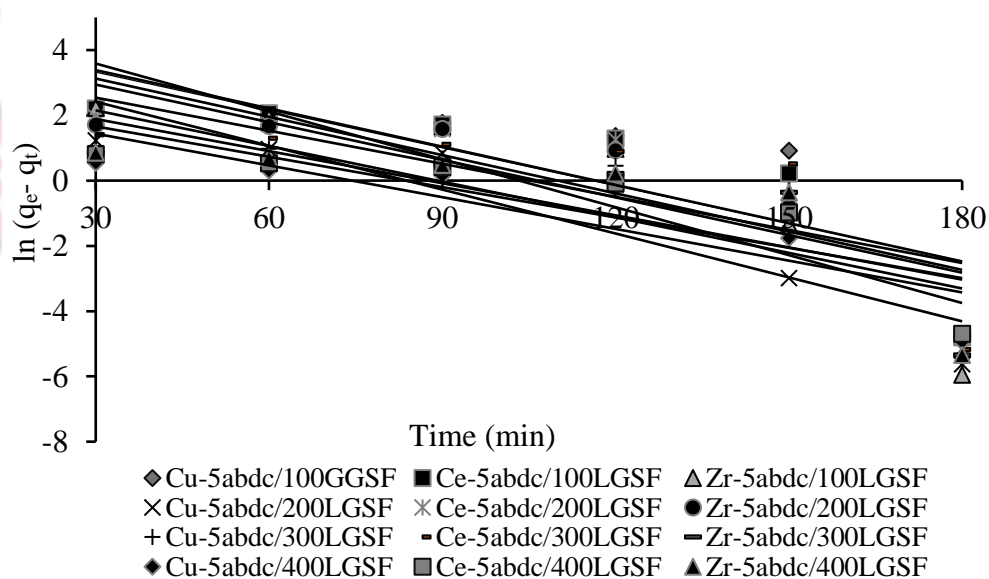


Figure 76: Pseudo-first-order graph for the adsorption of LGSF by Cu-5abdc, Ce-5abdc and Zr-5abdc (MOF loading = 0.1g/L, Solution pH = 6).

A similar trend in the rate of adsorption of LGSF was observed for the various MOFs. A summary of values for the parameters measured for the various MOFs is shown in Table 3. R^2 values below 0.9 and low experimental q_e values compared with the computed values were generally observed.

Table 3: The Parameters for Pseudo-first-order Adsorption Kinetics of Cu-5abdc, Ce-5abdc and Zr-5abdc for for LGSF at Varying Concentration

Cu-5abdc/LGSF				
[LGSF]/g/L	K_1 (min^{-1})	R^2	q_e (mg/g)	q_{ecal} (mg/g)
0.1000	0.0387	0.5642	88.6691	89.4800
0.2000	0.0449	0.8269	43.0516	183.7300
0.3000	0.0364	0.7509	25.6156	281.2700
0.4000	0.0324	0.7519	11.1440	370.7100
Ce-5abdc/LGSF				
[LGSF]/g/L	K_1 (min^{-1})	R^2	q_e (mg/g)	q_{ecal} (mg/g)
0.1000	0.0391	0.6751	95.4402	96.7800
0.2000	0.0391	0.7060	73.6556	192.7800
0.3000	0.0338	0.5490	35.0439	286.5600
0.4000	0.0310	0.7047	13.3311	383.5200
Zr-5abdc/LGSF				
[LGSF]/g/L	K_1 (min^{-1})	R^2	q_e (mg/g)	q_{ecal} (mg/g)
0.1000	0.0489	0.7614	159.8986	97.9700
0.2000	0.0384	0.7217	60.0637	192.9000
0.3000	0.0328	0.6006	17.6776	290.4300
0.4000	0.0328	0.6006	17.6776	384.8200

Source: Experimental data (2022)

Figure 77 shows the pseudo-second-order adsorption reaction rate of LGSF by Cu-5abdc, Ce-5abdc and Zr-5abdc at varying initial LGSF concentrations. An increasing LGSF adsorption rate trend was observed for the various MOFs. The R^2 values closer to 1 were observed for all the rates of adsorption reactions. The adsorption rate of LGSF seems to favour the pseudo-second-order adsorption rate.

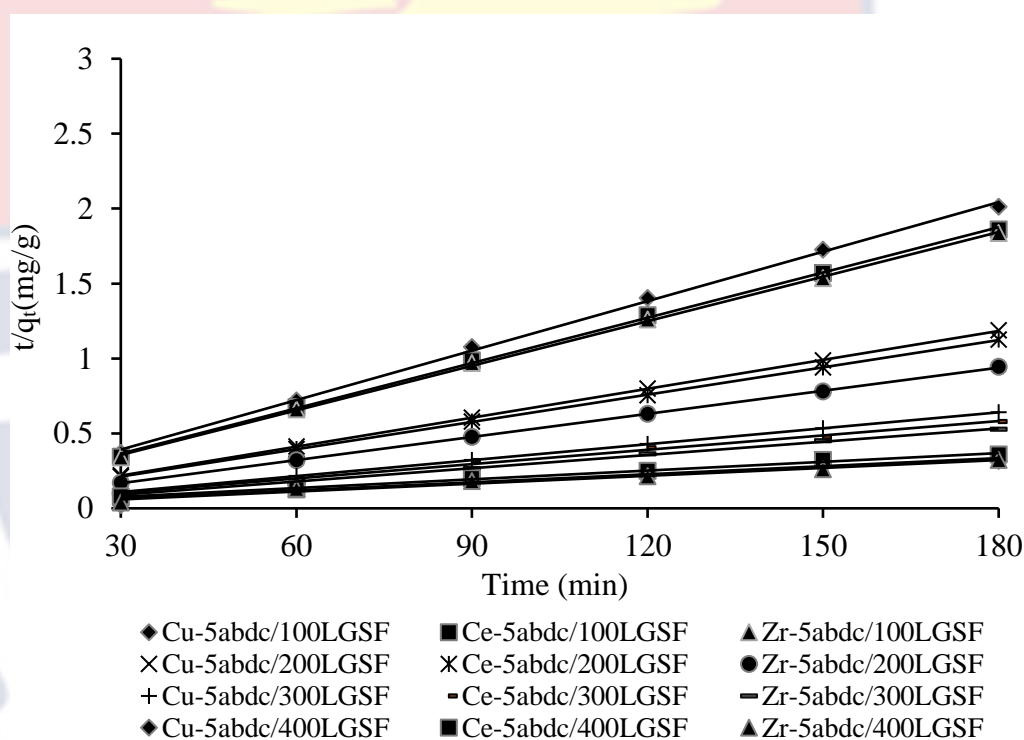


Figure 77: Pseudo-second-order graph for the adsorption of LGSF by Cu-5abdc, Ce-5abdc and Zr-5abdc (MOF loading = 0.1g/L, Solution pH = 6).

A summary of values for the parameters measured for the various MOFs is shown in Table 4. Close experimental q_e values compared with the computed values were observed with increasing initial LGSF concentration for each LGSF concentration of 0.100g /L, 0.200 g/L and 0.300 g/L. A large difference in q_e values and q_{ecal} values was, however, observed for the 0.400 g/L initial concentrations.

Table 4: The Parameters for Pseudo-second-order Adsorption Kinetics of Cu-5abdc, Ce-5abdc and Zr-5abdc for for LGSF at Varying Concentration

Cu-5abdc/LGSF				
[LGSF]/g/L	K_2 (min ⁻¹)	R^2	q_e (mg/g)	q_{ecal} (mg/g)
0.1000	0.0020	0.9986	90.9091	89.4800
0.2000	0.0016	1.0000	156.2500	183.7300
0.3000	0.0051	1.0000	285.7143	281.2700
0.4000	0.0003	0.9201	555.5556	370.7100
Ce-5abdc/LGSF				
[LGSF]/g/L	K_2 (min ⁻¹)	R^2	q_e (mg/g)	q_{ecal} (mg/g)
0.1000	0.0016	0.9991	99.0099	96.7800
0.2000	0.0012	0.9999	163.9344	192.7800
0.3000	0.0013	0.9935	312.5000	286.5600
0.4000	0.0019	0.9942	526.3158	383.5200
Zr-5abdc/LGSF				
[LGSF]/g/L	K_2 (min ⁻¹)	R^2	q_e (mg/g)	q_{ecal} (mg/g)
0.1000	0.0017	0.9994	101.0101	97.9700
0.2000	0.0019	0.9999	196.0784	192.9000
0.3000	0.0037	0.9976	344.8270	290.4300
0.4000	0.0005	0.9768	555.5556	384.8200

Source: Experimental data (2022)

The adsorption capacity of Cu-5abdc, Ce-5abdc and Zr-5abdc were further determined using the Langmuir and the Freundlich model for the pseudo-second-order adsorption which was the suitable adsorption reaction rate. As shown in Figure 78, the adsorption of LGSF by Cu-5abdc, Ce-5abdc and Zr-5abdc fit the Langmuir adsorption model for the pseudo-second-order

adsorption rate with R^2 value of 0.9436, 0.9172 and 0.8871 although the R^2 value for Zr-5abdc was lower.

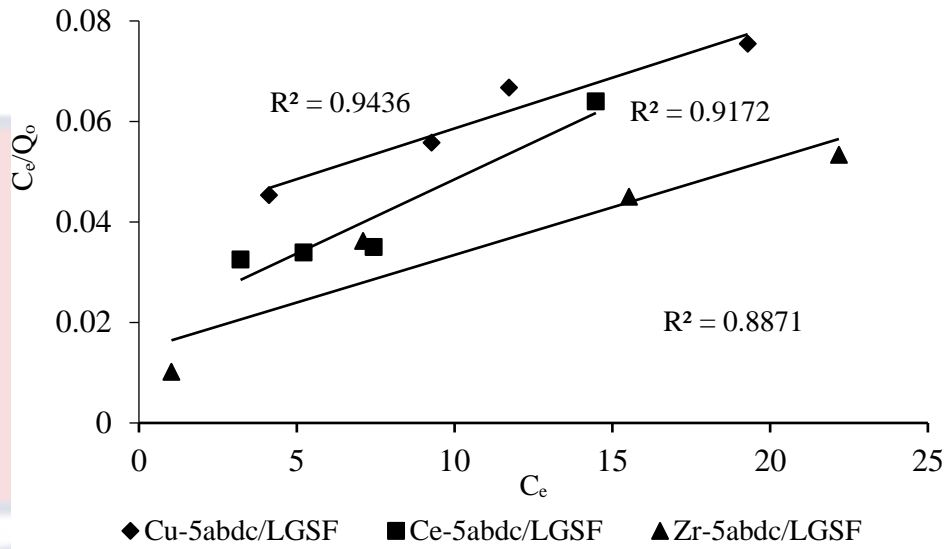


Figure 78: The Langmuir isotherm for the adsorption of LGSF by Cu-5abdc, Ce-5abdc and Zr-5abdc

The adsorption capacity of Cu-5abdc, Ce-5abdc and Zr-5abdc observed for the Freundlich model is as shown in Figure 79.

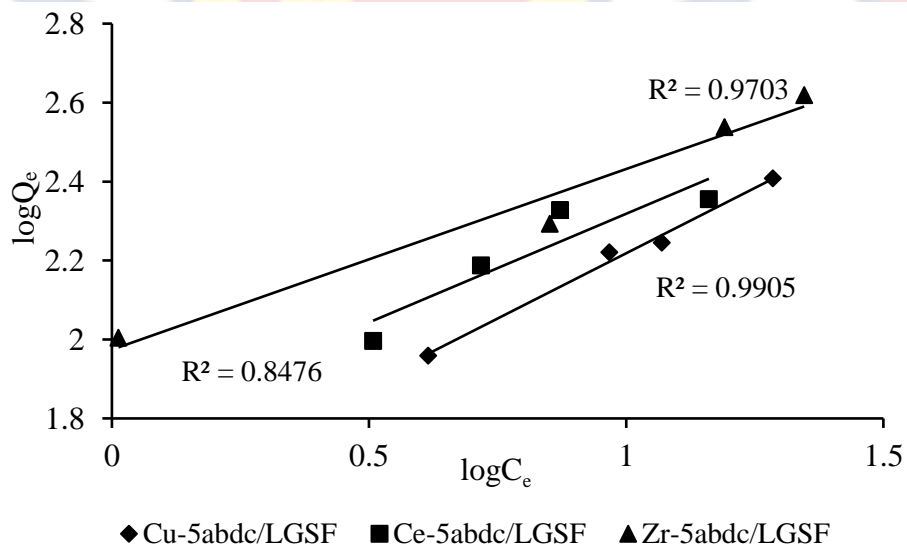


Figure 79: The Freundlich isotherm for the adsorption of LGSF by Cu-5abdc, Ce-5abdc and Zr-5abdc

The Freundlich adsorption isotherm for the pseudo-second-order adsorption rate of LGSF by of Cu-5abdc, Ce-5abdc and Zr-5abdc gave R^2 values of 0.9905, 0.8476 and 0.9703 with Ce-5abdc having a lower fit. Table 5 lists the parameters from the Langmuir isotherms and the Freundlich isotherms for the pseudo-second-order adsorption rate. The adsorption isotherm is favourable for the Langmuir model when $0 < R_L < 1$, unfavourable when $R_L > 1$, linear when $R_L = 1$ and irreversible when $R_L = 0$ (Musah et al., 2022; Prasath, Muthirulan, & Kannan, 2014). Favourable adsorption isotherm was observed for the pseudo-second-order adsorption rate for Cu-5abdc, Ce-5abdc and Zr-5abdc with R_L values of 0.9796, 0.9406 and 0.9502 although close to 1.

Table 5: The Parameters from Langmuir and Freundlich Isotherms of Cu-5abdc, Ce-5abdc and Zr-5abdc for LGSF

		Langmuir		
Pseudo-second-order	R^2	K_L	Q_o	R_L
Cu-5abdc/LGSF	0.9436	0.0521	500.0000	0.9796
Ce-5abdc/LGSF	0.9172	0.1579	333.3333	0.9406
Zr-5abdc/LGSF	0.8871	0.1310	526.3158	0.9502
		Freundlich		
Pseudo-second-order	R^2	K_f	n	1/n
Cu-5abdc/LGSF	0.9905	4.7460	1.5126	0.6611
Ce-5abdc/LGSF	0.8476	5.8585	1.8165	0.5505
Zr-5abdc/LGSF	0.9703	7.2009	2.1853	0.4576

Source: Experimental data (2022)

The lowest K_L value of 0.0521 was observed for Cu-5abdc among the MOFs which indicates that there was weak interaction between Cu-5abdc and LGSF although it had a high maximum adsorption capacity (Q_0). The high Q_0 may have interfered interaction between Cu-5abdc and LGSF due to excess LGSF adsorbed. Ce-5abdc had the highest interaction and the lowest maximum adsorption capacity for LGSF resulting in the lowest separation between Ce-5abdc and LGSF with R_L value of 0.9406 which makes it have the most favourable adsorption isotherm relative to Cu-5abdc and Zr-5abdc. The highest maximum adsorption capacity (Q_0) of LGSF was observed for Zr-5abdc with stronger interaction relative to Cu-5abdc.

The Freundlich adsorption isotherm is considered favourable for the Freundlich model when n has larger values (smaller $1/n$ value) and unfavourable when n has smaller value (larger $1/n$ value) for $1 < n < 10$ (Anah, & Astrini, 2018; Ramadoss & Subramaniam, 2019). Favourable Freundlich adsorption isotherm with n values of 1.5126, 1.8165 and 2.1853 with $1/n$ values of 0.6611, 0.5505 and 0.4576 were observed for Cu-5abdc, Ce-5abdc and Zr-5abdc respectively. The Zr-5abdc MOF was observed to have the highest K_f value of 7.2009 which indicates its highest capacity to remove LGSF compared to Cu-5abdc and Ce-5abdc. This is reflected in its highest strength of adsorption with an n value of 2.1853 relative to Cu-BTC and Ce-5abdc. A higher removal of LGSF was observed for Ce-5abdc with K_f value of 5.8585 relative to Cu-5abdc with K_f value of 4.7460. A higher adsorption strength was also observed for Ce-5abdc with an n value of 1.8165 relative to Cu-5abdc with an n value of 1.5126.

Figure 80 shows the pseudo-first-order adsorption reaction rate of TeRh by Cu-5abdc, Ce-5abdc and Zr-5abdc at varying initial TeRh concentrations. A similar trend in the rate of adsorption of TeRh was observed for the various MOFs. The R^2 values below 0.9 were observed for all the MOFs with varying initial TeRh concentrations.

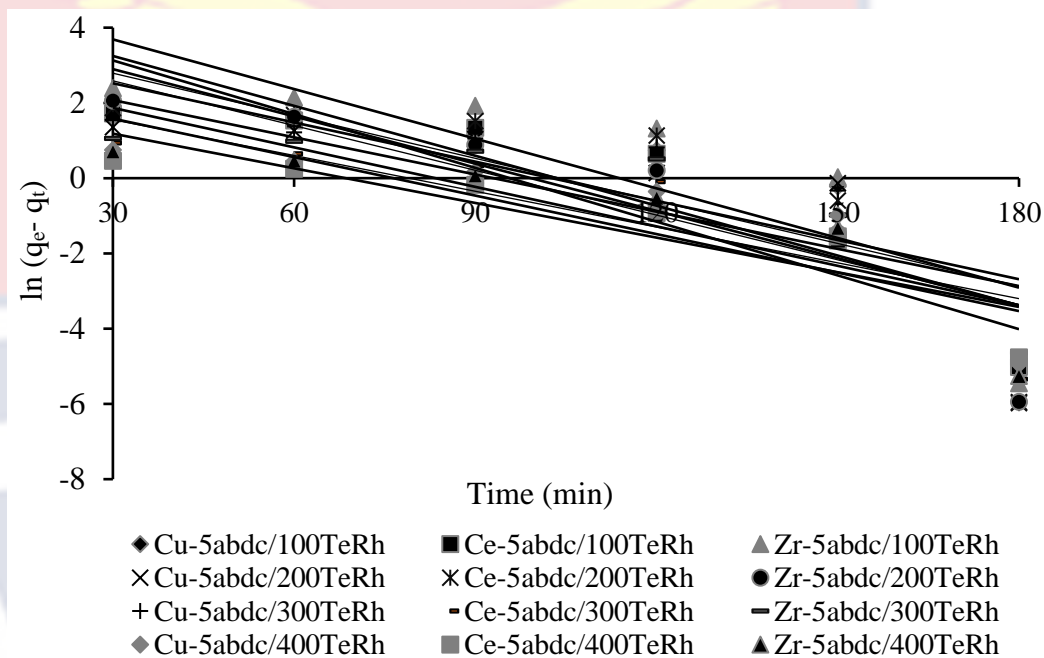


Figure 80: Pseudo-first-order graph for the adsorption of TeRh by Cu-5abdc, Ce-5abdc and Zr-5abdc (MOF loading = 0.1g/L, Solution pH = 8)

A summary of values for the parameters measured for the various MOFs is shown in Table 6. Low experimental q_e values were observed with increasing initial TeRh concentration compared with the computed values for each TeRh concentration.

Table 6: The Parameters for Pseudo-first-order Adsorption Kinetics of Cu-5abdc, Ce-5abdc and Zr-5abdc for TeRh at Varying Concentration

Cu-5abdc/TeRh				
[TeRh]/g/L	K_1 (min ⁻¹)	R^2	q_e (mg/g)	q_{ecal} (mg/g)
0.1000	0.0377	0.6666	50.4660	87.7800
0.2000	0.0397	0.6328	43.6804	184.6800
0.3000	0.0347	0.6654	35.2864	279.4600
0.4000	0.0317	0.7103	12.25703	372.6200
Ce-5abdc/TeRh				
[TeRh]/g/L	K_1 (min ⁻¹)	R^2	q_e (mg/g)	q_{ecal} (mg/g)
0.1000	0.0419	0.7867	63.6691	94.8100
0.2000	0.0442	0.6698	96.9601	191.2500
0.3000	0.0350	0.6993	18.4894	286.6300
0.4000	0.0307	0.7919	8.1997	383.2800
Zr-5abdc/TeRh				
[TeRh]/g/L	K_1 (min ⁻¹)	R^2	q_e (mg/g)	q_{ecal} (mg/g)
0.1000	0.0440	0.6837	149.5604	98.5200
0.2000	0.0476	0.8104	95.4020	193.2500
0.3000	0.0329	0.6985	21.4023	286.2800
0.4000	0.0341	0.7422	13.5448	383.1900

Source: Experimental data (2022)

Figure 81 shows the pseudo-second-order adsorption reaction rate of TeRh by Cu-5abdc, Ce-5abdc and Zr-5abdc at varying initial TeRh concentrations. A similar increasing trend of TeRh adsorption rate with decreasing initial concentration was observed for the various MOFs. The R^2

values closer to 1 were observed for all the rates of adsorption reaction. The adsorption of TeRh follows the pseudo-second-order reaction rate.

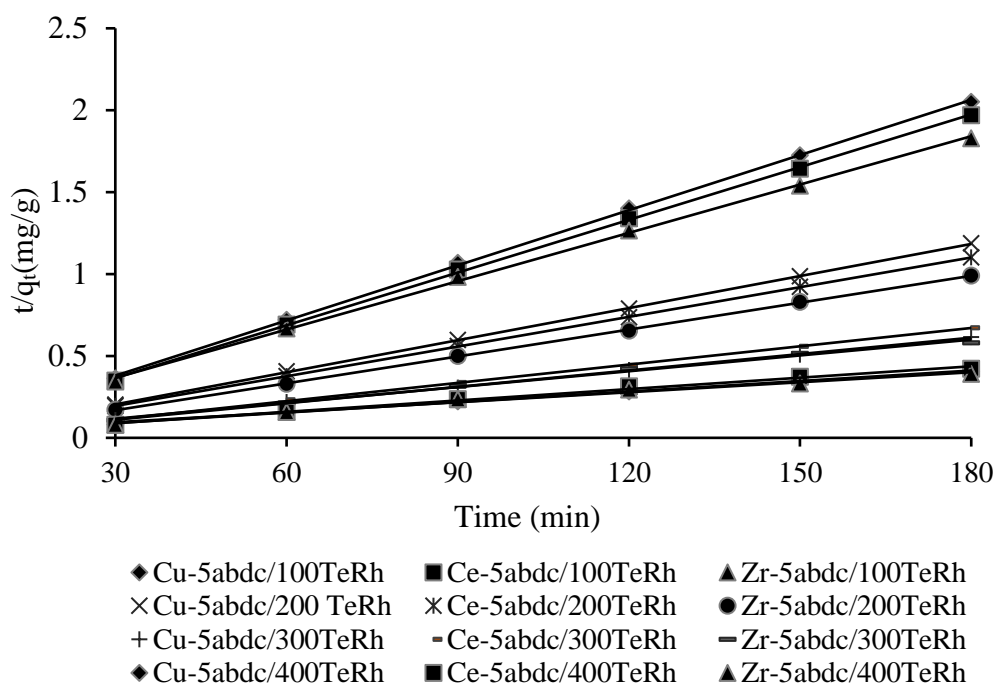


Figure 81: Pseudo-second-order graph for the adsorption of TeRh by Cu-5abdc, Ce-5abdc and Zr-5abdc (MOF loading = 0.1g/L, Solution pH = 8).

A summary of values for the parameters measured for the various MOFs is shown in Table 7. Close experimental q_e values compared with the computed values were observed with increasing initial TeRh concentration for each TeRh concentration of 0.100g /L, 0.200 g/L and 0.300 g/L. Larger q_e values were however recorded compared with the computed value q_{ecal} , especially, for the 0.400 g/L initial concentration.

Table 7: The Parameters for Pseudo-second-order Adsorption Kinetics of Cu-5abdc, Ce-5abdc and Zr-5abdc for TeRh at Varying Concentration

Cu-5abdc/TeRh				
[TeRh]/g/L	K_2 (min ⁻¹)	R^2	q_e (mg/g)	q_{ecal} (mg/g)
0.1000	0.0029	0.9996	89.2857	87.7800
0.2000	0.0050	0.9999	153.8462	184.6800
0.3000	0.0050	0.9995	312.5000	279.4600
0.4000	0.0002	0.9965	476.1905	372.6200
Ce-5abdc/TeRh				
[TeRh]/g/L	K_2 (min ⁻¹)	R^2	q_e (mg/g)	q_{ecal} (mg/g)
0.1000	0.0026	0.9996	93.4579	94.8100
0.2000	0.0027	1.0000	166.6667	191.2500
0.3000	0.0034	0.9994	270.2700	286.6300
0.4000	0.0003	0.9917	434.7826	383.2800
Zr-5abdc/TeRh				
[TeRh]/g/L	K_2 (min ⁻¹)	R^2	q_e (mg/g)	q_{ecal} (mg/g)
0.1000	0.0013	0.9989	102.0408	98.5200
0.2000	0.0069	0.9998	181.8182	193.2500
0.3000	0.0050	0.9941	312.5000	286.2800
0.4000	0.0001	0.9847	500.0000	383.1900

Source: Experimental data (2022)

The adsorption capacity of Cu-5abdc, Ce-5abdc and Zr-5abdc were further determined using the Langmuir and the Freundlich model. As shown in Figure 82, the pseudo-second-order adsorption rate of TeRh by Cu-5abdc,

Ce-5abdc and Zr-5abdc fit the Langmuir adsorption model although with low R^2 value of 0.7868, 0.8909 and 0.8047.

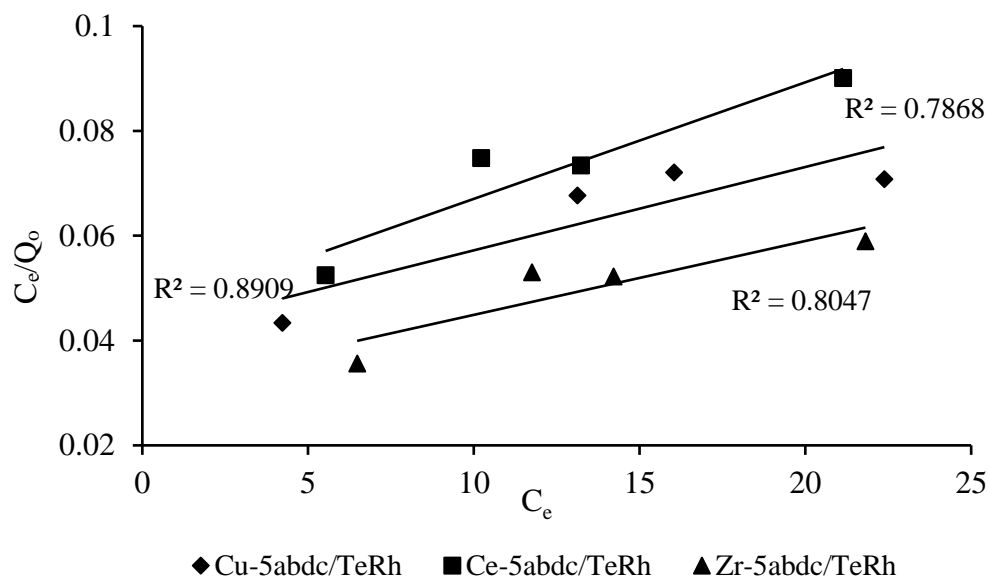


Figure 82: The Langmuir isotherm for the adsorption of TeRh by Cu-5abdc, Ce-5abdc and Zr-5abdc

The adsorption capacity of Cu-5abdc, Ce-5abdc and Zr-5abdc observed for the Freundlich model is shown in Figure 83.

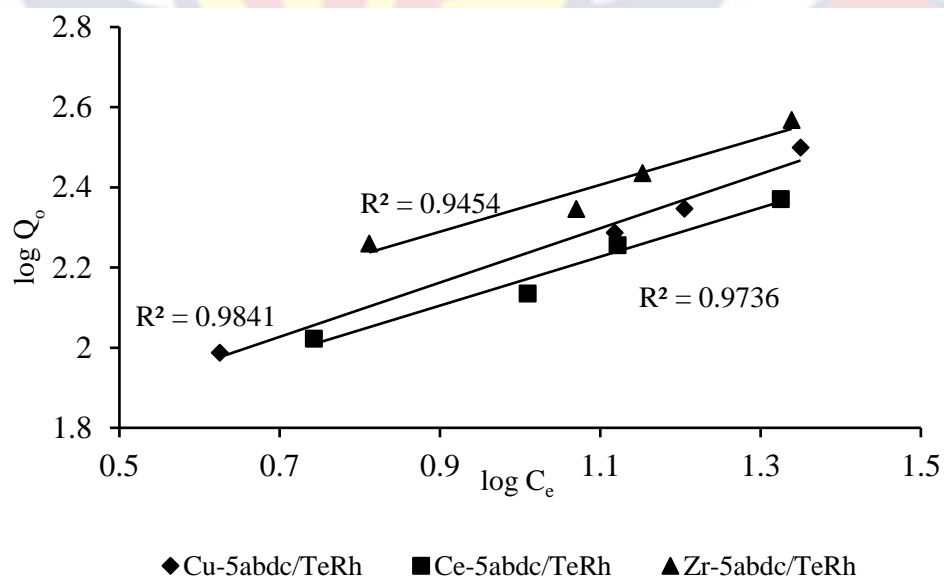


Figure 83: The Freundlich isotherm for the adsorption of TeRh by Cu-5abdc, Ce-5abdc and Zr-5abdc

The pseudo-second-order adsorption rate of TeRh by Cu-5abdc, Ce-5abdc and Zr-5abdc gave high R^2 values of 0.9841, 0.9736 and 0.9841 which fit the Freundlich model. Table 8 lists the parameters from the Langmuir and the Freundlich isotherms for the pseudo-second-order adsorption rate of TeRh by Cu-5abdc, Ce-5abdc and Zr-5abdc.

Table 8: The Parameters from Langmuir and Freundlich Isotherms of Cu-5abdc, Ce-5abdc and Zr-5abdc for TeRh

		Langmuir		
Pseudo-second-order	R^2	K_L	Q_o	R_L
Cu-5abdc/TeRh	0.7868	0.0387	625.0000	0.9848
Ce-5abdc/TeRh	0.8909	0.0491	454.5455	0.9807
Zr-5abdc/TeRh	0.8047	0.0455	714.2857	0.9821
		Freundlich		
Pseudo-second order	R^2	K_f	n	1/n
Cu-5abdc/TeRh	0.99841	4.7256	1.4767	0.6772
Ce-5abdc/TeRh	0.9736	4.7389	1.6388	0.6102
Zr-5abdc/TeRh	0.9454	5.8299	1.7097	0.5849

Source: Experimental data (2022)

Favourable Langmuir adsorption isotherm was observed for Cu-5abdc, Ce-5abdc and Zr-5abdc with R_L values of 0.9848, 0.9807 and 0.9821 since $0 < R_L < 1$. Close K_L values of 0.0387, 0.0491 and 0.0455 for the MOFs were observed with a slightly stronger interaction expressed by Ce-5abdc on TeRh relative to Zr-5abdc. The Ce-5abdc however had the highest interaction with TeRh resulting in the lowest R_L value of 0.9807 which makes it have the most

favourable Langmuir adsorption isotherm relative to Cu-5abdc and Zr-5abdc. The lowest maximum adsorption capacity (Q_0) for TeRh was however observed for Ce-5abdc. The highest Q_0 of TeRh was observed by Zr-5abdc with higher stronger interaction relative to Cu-5abdc. Favourable n values of 1.4767, 1.6388 and 1.7067 with $1/n$ values of 0.6772, 0.6102, and 0.5849 were also observed for Cu-5abdc, Ce-5abdc and Zr-5abdc for the Freundlich isotherm. The Zr-5abdc MOF was observed to have the highest K_f value of 5.8299 which indicates that it has the highest capacity to remove LGSF compared to Cu-5abdc and Ce-5abdc. The highest adsorption strength was also observed for Zr-5abdc with an n value of 1.7067 relative to Cu-5abdc with an n value of 1.4767 and Ce-5abdc with an n value of 1.6388. A slightly higher removal capacity by Ce-5abdc for TeRh was observed over Cu-5abdc.

Figure 84 the pseudo-first-order adsorption reaction rate of RBV5R by Cu-5abdc, Ce-5abdc and Zr-5abdc at varying initial RBV5R concentrations.

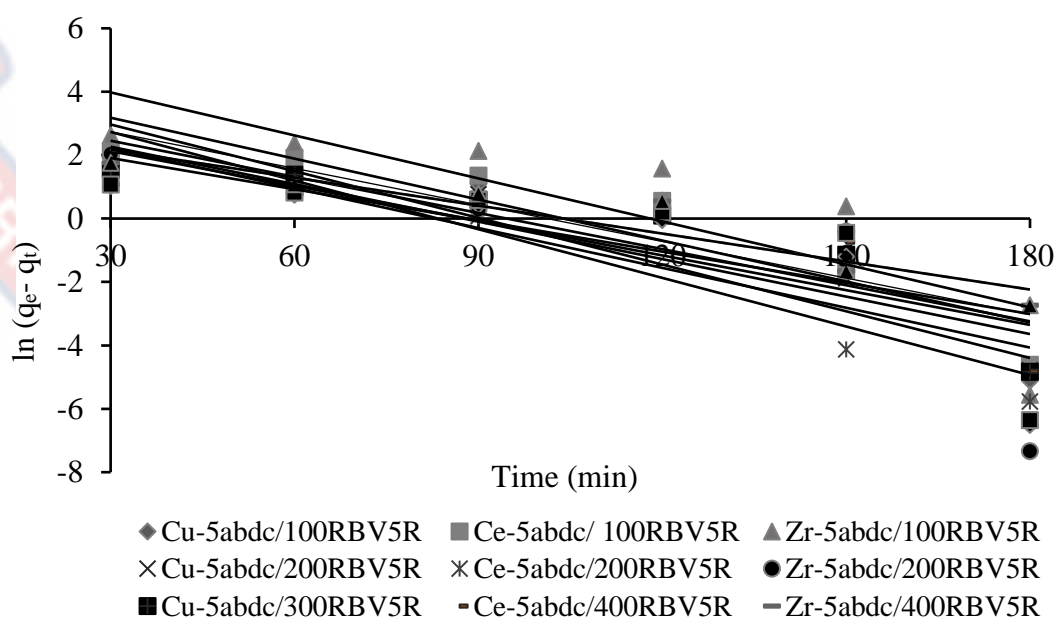


Figure 84: Pseudo-first-order graph for the adsorption of RBV5R by Cu-5abdc, Ce-5abdc and Zr-5abdc (MOF loading = 0.1g/L, Solution pH = 6)

A similar trend in the rate of adsorption of RBV5R was observed for the various MOFs. A summary of values for the parameters measured for the various MOFs is shown in Table 9. R^2 values below 0.9 and low experimental q_e values compared with the computed q_e values were observed.

Table 9: The Parameters for Pseudo-first-order Adsorption Kinetics of Cu-5abdc, Ce-5abdc and Zr-5abdc for RBV5R at Varying Concentration

Cu-5abdc/RBV5R				
[RBV5R]/g/L	K_1 (min ⁻¹)	R^2	q_e (mg/g)	q_{ecal} (mg/g)
0.1000	0.0387	0.7123	49.0775	84.4600
0.2000	0.0365	0.7836	25.0657	174.7700
0.3000	0.0380	0.8024	36.3866	276.7800
0.4000	0.0294	0.8855	21.2446	368.8500
Ce-5abdc/RBV5R				
[RBV5R]/g/L	K_1 (min ⁻¹)	R^2	q_e (mg/g)	q_{ecal} (mg/g)
0.1000	0.0430	0.8503	87.5666	92.2500
0.2000	0.0511	0.8617	71.1294	185.3800
0.3000	0.0419	0.6836	32.2785	280.5300
0.4000	0.0328	0.7107	18.0672	377.6900
Zr-5abdc/RBV5R				
[RBVR5]/g/L	K_1 (min ⁻¹)	R^2	q_e (mg/g)	q_{ecal} (mg/g)
0.1000	0.0452	0.6624	207.6596	98.7300
0.2000	0.0511	0.6741	84.8683	189.5500
0.3000	0.0394	0.6119	31.4784	282.4800
0.4000	0.0294	0.8855	21.2445	383.1500

Source: Experimental data (2022)

Figure 85 shows the pseudo-second-order adsorption reaction rate of RBV5R by Cu-5abdc, Ce-5abdc and Zr-5abdc at varying initial RBV5R concentrations. A similar trend of RBV5R adsorption rate was observed for the various MOFs. The R^2 values closer to 1 were observed for all the rates of adsorption reaction.

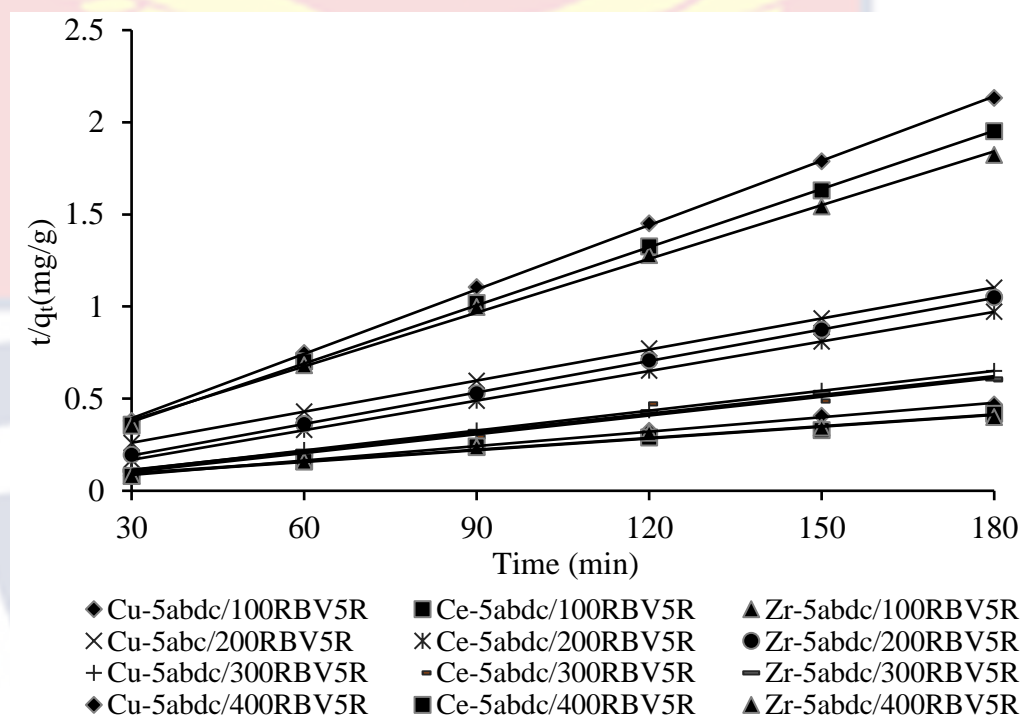


Figure 85: Pseudo-second-order graph for the adsorption of RBV5R by Cu-5abdc, Ce-5abdc and Zr-5abdc (MOF loading = 0.1g/L, Solution pH = 6).

A summary of values for the parameters measured for the various MOFs is shown in Table 10. A close experimental q_e values compared with the computed values were observed with increasing initial RBV5R concentration for each RBV5R concentration of 0.100g /L, 0.200 g/L and 0.300 g/L. larger q_e values were observed relative to q_{ecal} values, especially for the initial 0.400 g/L of RBV5R. The adsorption rate of RBV5R follows the pseudo-second-order adsorption rate reaction.

Table 10: The Parameters for Pseudo-second-order Adsorption Kinetics of Cu-5abdc, Ce-5abdc and Zr-5abdc for RBV5R at Varying Concentration

Cu-5abdc/RBV5R				
[RBV5R]/g/L	K_2 (min ⁻¹)	R^2	q_e (mg/g)	q_{ecal} (mg/g)
0.1000	0.0031	0.9997	86.2069	84.4600
0.2000	0.0003	0.9999	178.5714	174.7700
0.3000	0.0393	1.0000	277.7778	276.7800
0.4000	0.0009	0.9982	384.6154	368.8500
Ce-5abdc/RBV5R				
[RBV5R]/g/L	K_2 (min ⁻¹)	R^2	q_e (mg/g)	q_{ecal} (mg/g)
0.1000	0.0019	0.9996	95.2381	92.2500
0.2000	0.0016	1.0000	175.4386	185.3800
0.3000	0.0041	0.9737	238.0952	280.5300
0.4000	0.0016	0.9864	476.1905	377.6900
Zr-5abdc/RBV5R				
[RBVR5]/g/L	K_2 (min ⁻¹)	R^2	q_e (mg/g)	q_{ecal} (mg/g)
0.1000	0.0010	0.9992	103.0928	98.7300
0.2000	0.0039	0.9999	185.1852	189.5500
0.3000	0.0010	0.9974	294.1176	282.4800
0.4000	0.0001	0.9794	476.1905	383.1500

Source: Experimental data (2022)

The adsorption capacity of Cu-5abdc, Ce-5abdc and Zr-5abdc pseudo-second-order adsorption rate were further determined using the Langmuir and the Freundlich model. As shown in Figure 86, the pseudo-second-order

adsorption rate of RBV5R by Cu-5abdc, Ce-5abdc and Zr-5abdc fit the Langmuir adsorption model with R^2 values of 0.9118, 0.8202 and 0.9310.

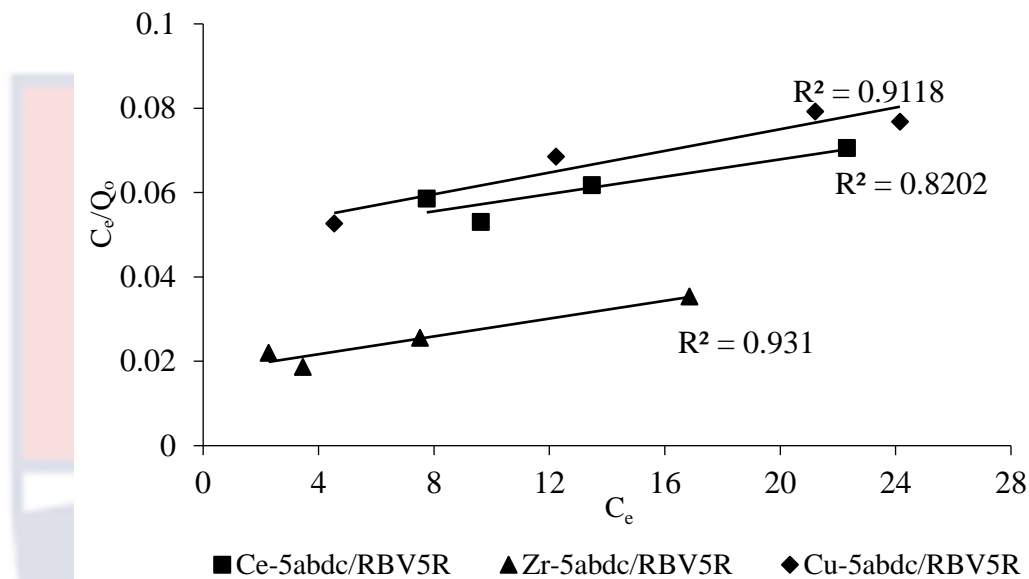


Figure 86: The Langmuir isotherm for the adsorption of RBV5R by Cu-5abdc, Ce-5abdc and Zr-5abdc

The adsorption capacity of Cu-5abdc, Ce-5abdc and Zr-5abdc observed for the Freundlich model is shown in Figure 87.

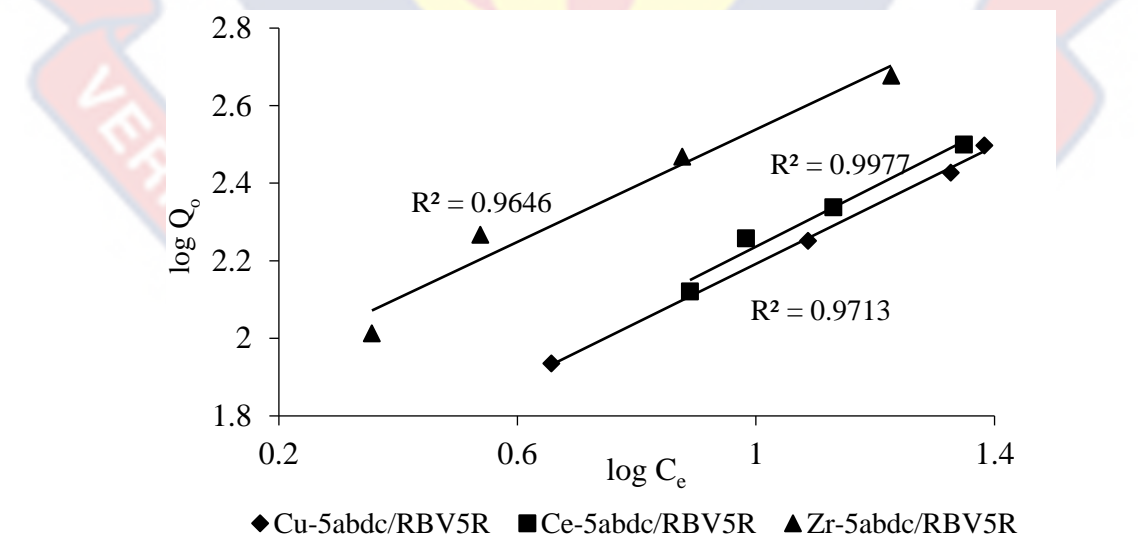


Figure 87: The Freundlich isotherm for the adsorption of RBV5R by Cu-5abdc, Ce-5abdc and Zr-5abdc

The pseudo-second-order adsorption rate of RBV5R by Cu-5abdc, Ce-5abdc and Zr-5abdc fit the Freundlich adsorption isotherm with high R^2 values of 0.9977, 0.9713 and 0.9646. Table 11 lists the parameters from the Langmuir isotherms and the Freundlich isotherms for the pseudo-second-order adsorption rate.

Table 11: The Parameters from Langmuir and Freundlich Isotherms of Cu-5abdc, Ce-5abdc and Zr-5abdc for RBV5R

		Langmuir		
Pseudo-second-order	R^2	K_L	Q_0	R_L
Cu-5abdc/RBV5R	0.9118	0.0264	769.2308	0.9896
Ce-5abdc/RBV5R	0.8202	0.0211	1000.0000	0.9916
Zr-5abdc/RBV5R	0.9310	0.0629	909.0909	0.9755
		Freundlich		
Pseudo-second-order	R^2	K_f	n	$1/n$
Cu-5abdc/RBV5R	0.9977	4.1929	1.3180	0.7587
Ce-5abdc/RBV5R	0.9713	4.2948	1.2837	0.7790
Zr-5abdc/RBV5R	0.9646	6.1331	1.3795	0.7249

Source: Experimental data (2022)

Favourable Langmuir adsorption isotherm was observed for the pseudo-second-order adsorption rate of RBV5R by Cu-5abdc, Ce-5abdc and Zr-5abdc with R_L values of 0.9896, 0.9916 and 0.9755. The lowest K_L value of 0.0211 was observed for Ce-5abdc which indicates that it has the weakest interaction towards RBV5R although it had the highest maximum adsorption

capacity (Q_0). The high Q_0 may have interfered with the interaction due to excess RBV5R. The Zr-5abdc had the highest interaction with the lower maximum adsorption capacity for RBV5R. The lowest separation was therefore observed between Zr-5abdc and RBV5R with R_L value of 0.9406 which makes it have the most favourable Langmuir adsorption isotherm relative to Cu-5abdc and Zr-5abdc.

Favourable n values of 1.3180, 1.2837 and 1.3795 with $1/n$ values of 0.7587, 0.7790 and 0.7249 were also observed for Cu-5abdc, Ce-5abdc and Zr-5abdc under the Freundlich isotherm. The Zr-5abdc MOF was observed to have the highest K_f value of 6.1331 which indicates its highest capacity to remove RBV5R compared to Cu-5abdc and Ce-5abdc. The highest adsorption strength was also observed for Zr-5abdc with an n value of 1.3795 relative to Cu-5abdc with an n value of 1.2837 and Ce-5abdc with an n value of 1.3180. A higher removal of RBV5R was observed for Ce-5abdc relative to Cu-5abdc.

Kinetic and Isotherm Study on the Adsorption of Coloured Organic Pollutants by Cu-BTC, Ce-BTC and Zr-BTC MOFs

The rate of adsorption of Lissamine green SF (LGSF), Tetraethylrhodamine (TeRh), and Remezol Brilliant Violet 5R (RBV5R) with time from water by Cu-BTC, Ce-BTC and Zr-BTC was examined using the pseudo-first-order adsorption and pseudo-second-order adsorption reaction rate equations. Figure 88 shows the pseudo-first-order adsorption reaction rate of LGSF by Cu-BTC, Ce-BTC and Zr-BTC at varying initial LGSF concentrations. A similar trend in the rate of adsorption of LGSF was

observed for the various MOFs. The R^2 values below 0.95 were observed for all the MOFs with varying initial LGSF concentrations.

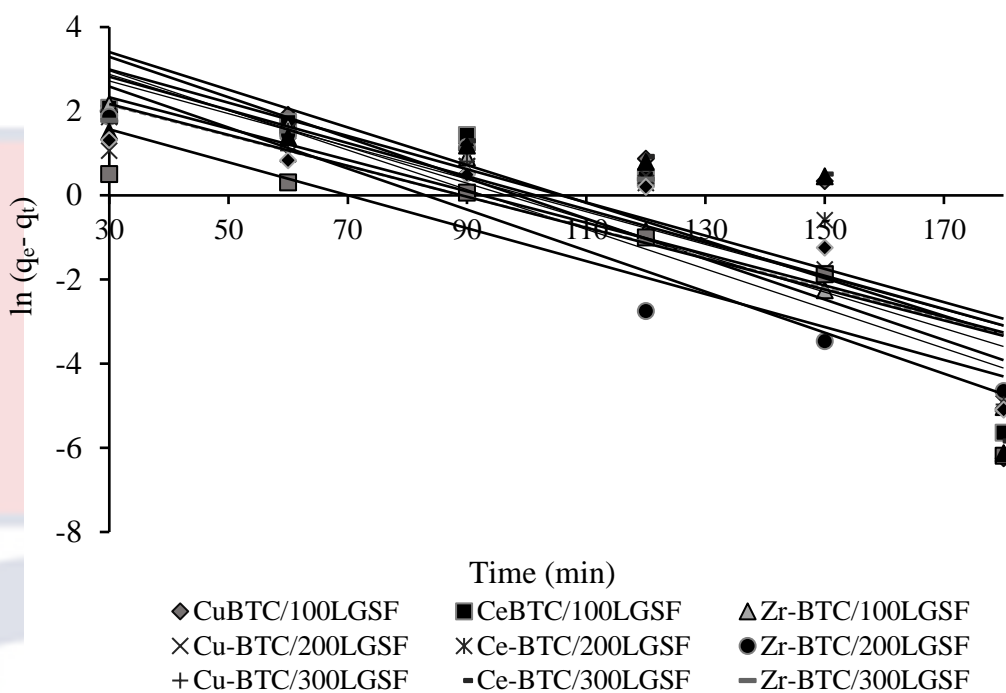


Figure 88: Pseudo-first-order graph for the adsorption of LGSF by Cu-BTC, Ce-BTC and Zr-BTC (MOF loading = 0.1g/L, Solution pH = 6).

A summary of values for the parameters measured for the various MOFs is shown in Table 12. Low experimental q_e values were observed with increasing initial LGSF concentration compared with the computed values for each LGSF concentration.

Table 12: The Parameters for Pseudo-first-order Adsorption Kinetics of Cu-BTC, Ce-BTC and Zr-BTC for LGSF at Varying Concentration

Cu-BTC/LGSF				
[LGSF]/g/L	K_1 (min^{-1})	R^2	q_e (mg/g)	q_{ecal} (mg/g)
0.1000	0.0445	0.6347	115.6074	93.7600
0.2000	0.0363	0.7514	25.4878	184.7900
0.3000	0.0373	0.7632	31.4847	282.5600
0.4000	0.0367	0.7540	26.4353	378.5700
Ce-BTC/LGSF				
[LGSF]/g/L	K_1 (min^{-1})	R^2	q_e (mg/g)	q_{ecal} (mg/g)
0.1000	0.0481	0.8214	113.8976	89.4800
0.2000	0.0388	0.7674	48.6669	183.7300
0.3000	0.0395	0.5798	65.17657	281.2700
0.4000	0.0392	0.7537	15.5666	370.7100
Zr-BTC/LGSF				
[LGSF]/g/L	K_1 (min^{-1})	R^2	q_e (mg/g)	q_{ecal} (mg/g)
0.1000	0.0471	0.9343	79.55113	99.5500
0.2000	0.0487	0.9083	57.3573	194.6400
0.3000	0.0431	0.8737	64.7090	292.4300
0.4000	0.0394	0.5573	54.7293	389.6000

Source: Experimental data (2022)

Figure 89 shows the pseudo-second-order adsorption reaction rate of LGSF by Cu-BTC, Ce-BTC and Zr-BTC at varying initial LGSF

concentrations. A similar trend of LGSF adsorption rate was observed for the various MOFs. The R^2 values closer to 1 were observed for all the rates of adsorption reaction. The adsorption rate of LGSF is observed to follow the pseudo-second-order adsorption.

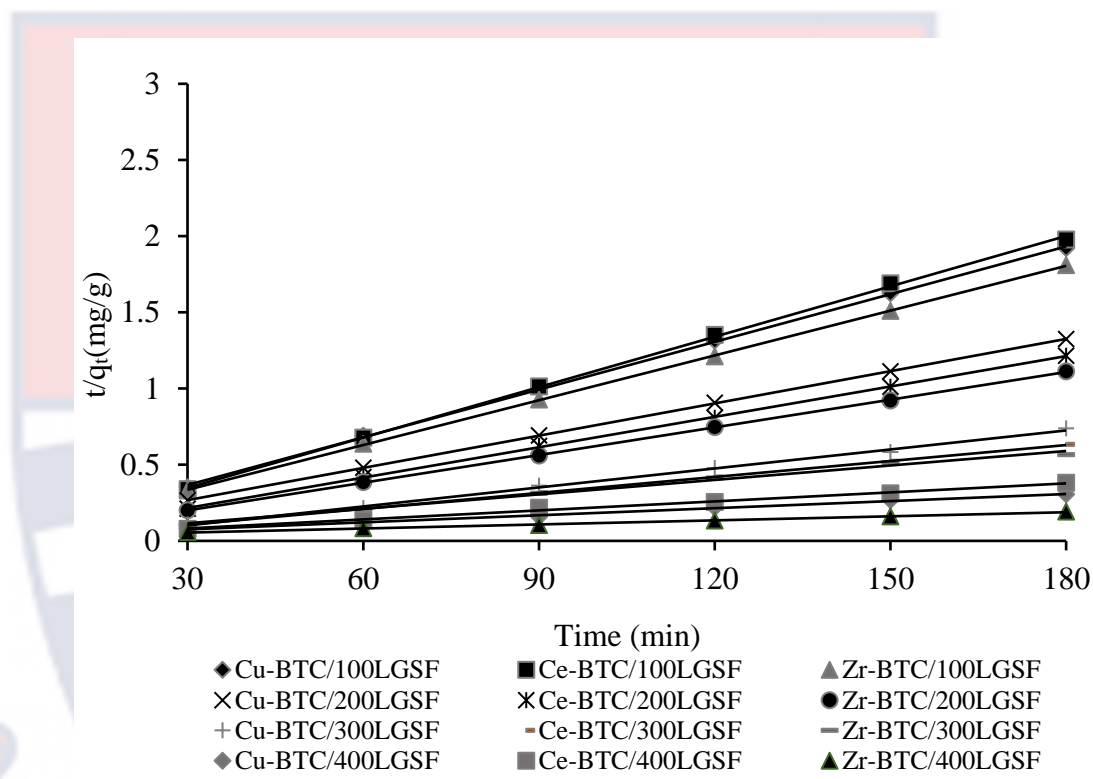


Figure 89: Pseudo-second-order graph for the adsorption of LGSF by Cu-BTC, Ce-BTC and Zr-BTC (MOF loading = 0.1g/L, Solution pH = 6).

A summary of values for the parameters measured for the various MOFs is shown in Table 13. Close experimental q_e values compared with the computed values were observed with increasing initial LGSF concentration for each LGSF concentration of 0.100g /L, 0.200 g/L and 0.300 g/L. A large difference in q_e values and q_{ecal} values was, however, observed for the 0.400 g/L initial concentrations.

Table 13: The Parameters for Pseudo-second-order Adsorption Kinetics of Cu-BTC, Ce-BTC and Zr-BTC for LGSF at Varying Concentration

Cu-BTC/LGSF				
[LGSF]/g/L	K_2 (min ⁻¹)	R^2	q_e (mg/g)	q_{ecal} (mg/g)
0.1000	0.0020	0.9996	96.1539	93.7600
0.2000	0.0009	1.0000	140.8451	184.7900
0.3000	0.0008	0.9971	238.0952	282.5600
0.4000	0.0001	0.9957	625.0000	378.5700
Ce-BTC/LGSF				
[LGSF]/g/L	K_2 (min ⁻¹)	R^2	q_e (mg/g)	q_{ecal} (mg/g)
0.1000	0.0072	0.9994	90.9091	89.4800
0.2000	0.0027	0.9998	151.5152	183.7300
0.3000	0.0204	0.9999	285.7143	281.2700
0.4000	0.0002	0.9944	500.0000	370.7100
Zr-BTC/LGSF				
[LGSF]/g/L	K_2 (min ⁻¹)	R^2	q_e (mg/g)	q_{ecal} (mg/g)
0.1000	0.0023	0.9999	102.0408	99.5500
0.2000	0.0020	0.9999	163.9344	194.6400
0.3000	0.0005	0.9923	312.5000	292.4300
0.4000	0.0001	0.9954	526.3158	389.6000

Source: Experimental data (2022)

The adsorption capacity of Cu-BTC, Ce-BTC and Zr-BTC for the pseudo-second-order adsorption rate which was the suitable adsorption reaction rate was further determined using the Langmuir and the Freundlich model. As shown in Figure 90, the pseudo-second-order adsorption rate of LGSF by Cu-BTC, Ce-BTC and Zr-BTC fit the Langmuir model although low R^2 values of 0.7978, 0.8920 and 0.8986 were observed.

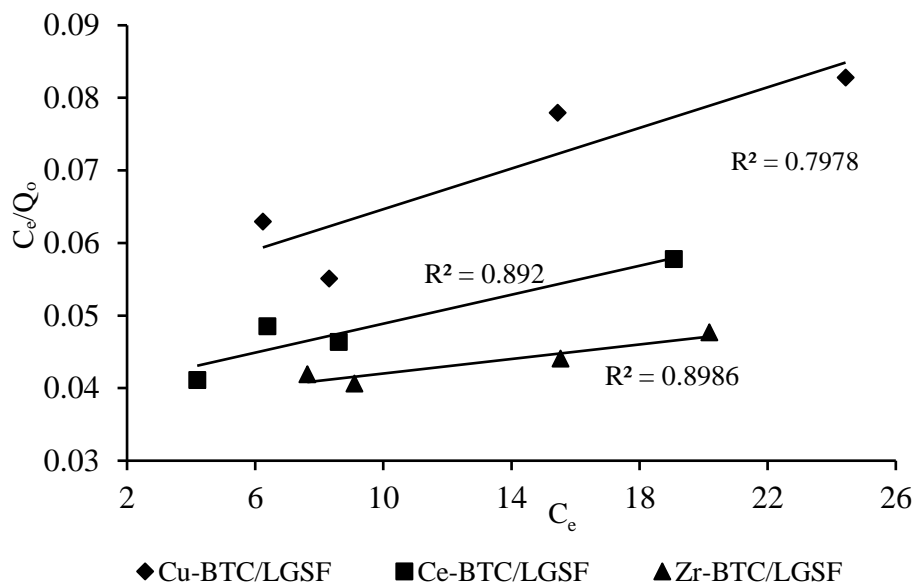


Figure 90: The Langmuir isotherm for the adsorption of LGSF by Cu-BTC, Ce-BTC and Zr-BTC

The adsorption capacity of Cu-BTC, Ce-BTC and Zr-BTC observed for the Freundlich model is as shown in Figure 91, the pseudo-second-order adsorption rate of LGSF by Cu-BTC, Ce-BTC and Zr-BTC fit the Freundlich model with R^2 values of 0.9588, 0.9919 and 0.9947.

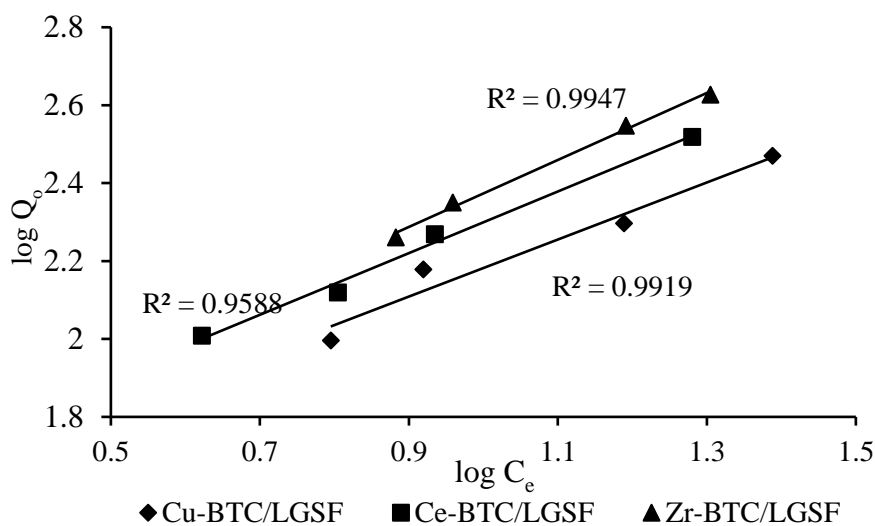


Figure 91: The Freundlich isotherm for the adsorption of LGSF by Cu-BTC, Ce-BTC and Zr-BTC

Table 14 shows the lists of the parameters from the Langmuir isotherms and the Freundlich isotherms for the pseudo-second-order adsorption rate of LGSF by Cu-BTC, Ce-BTC and Zr-BTC. Favourable Langmuir adsorption isotherm was observed for the pseudo-second-order adsorption rate of LGSF by Cu-BTC, Ce-BTC and Zr-BTC with R_L values of 0.9890, 0.9898 and 0.9946. The Zr-BTC was observed to have the weakest interaction with LGSF having a K_L value of 0.0135. The very low interaction may be due to the very high maximum adsorption capacity (Q_0) observed which may have interfered with the interaction due to excess LGSF adsorbed by Zr-BTC.

Table 14: The Parameters from Langmuir and Freundlich Isotherms of Cu-BTC, Ce-BTC and Zr-BTC for LGSF

		Langmuir		
Pseudo-second-order	R^2	K_L	Q_0	R_L
Cu-BTC/LGSF	0.7978	0.0277	714.2857	0.9890
Ce-BTC/LGSF	0.8920	0.0257	1000.0000	0.9898
Zr-BTC/LGSF	0.8986	0.0135	2000.0000	0.9946
		Freundlich`		
Pseudo-second order	R^2	K_f	n	1/n
Cu-BTC/LGSF	0.9588	4.2627	1.3659	0.7321
Ce-BTC/LGSF	0.9919	4.5177	1.2635	0.7915
Zr-BTC/LGSF	0.9947	4.5431	1.1629	0.8599

Source: Experimental data (2022)

The highest separation was therefore observed between Zr-BTC and LGSF with an R_L value of 0.9946 which makes it have the least favourable Langmuir adsorption isotherm relative to Cu-BTC and Zr-BTC due to the high separation effect. Cu-BTC had a slightly higher interaction relative to Ce-BTC with the lowest maximum adsorption capacity for LGSF among the MOFs. Favourable n values of 1.3659, 1.2635 and 1.1629 with $1/n$ values of 0.7321, 0.7915 and 0.8599 were also observed for the Freundlich isotherm. Close removal capacity of LGSF by Cu-BTC, Ce-BTC and Zr-BTC were observed with K_f values of 4.2627, 4.5177 and 4.5431. The highest adsorption strength was however observed for Cu-BTC with an n value of 1.3659 relative to Ce-BTC with an n value of 1.2635 and Zr-5abdc with an n value of 1.1629.

Figure 92 the pseudo-first-order adsorption reaction rate of TeRh by Cu-BTC, Ce-BTC and Zr-BTC at varying initial TeRh concentrations. A similar trend in the rate of adsorption of TeRh was observed for the various MOFs.

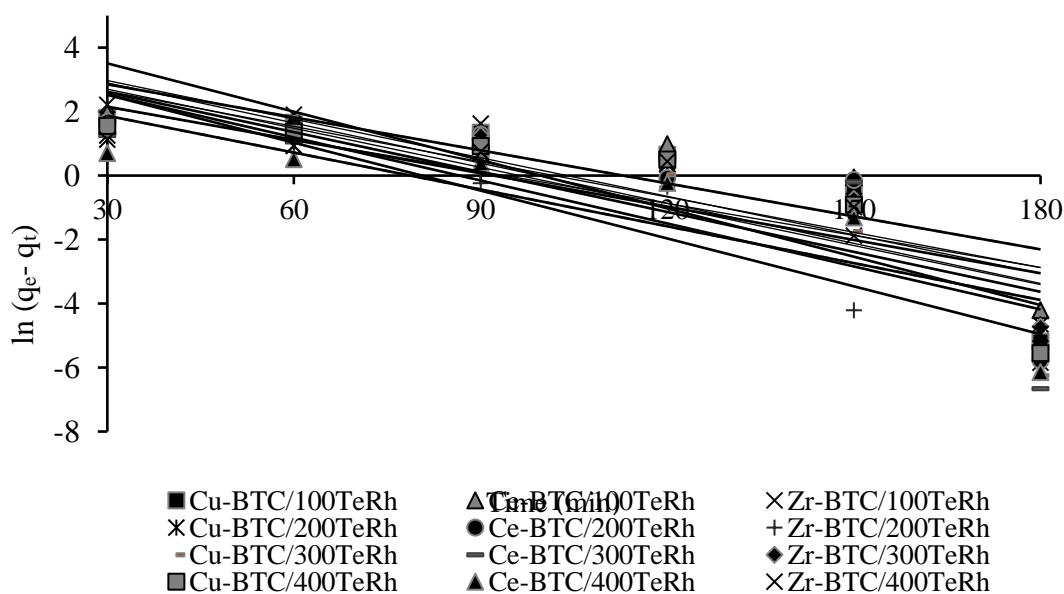


Figure 92: Pseudo-first-order graph for the adsorption of TeRh by Cu-BTC, Ce-BTC and Zr-BTC (MOF loading = 0.1g/L, Solution pH = 6)

A summary of parameters measured for the various MOFs is shown in Table 15. R^2 below 0.9 and low q_e values were generally observed.

Table 15: The Parameters for Pseudo-first-order Adsorption Kinetics of Cu-BTC, Ce-BTC and Zr-BTC for TeRh at Varying Concentration

Cu-BTC/TeRh				
[TeRh]/g/L	K_1 (min^{-1})	R^2	q_e (mg/g)	q_{ecal} (mg/g)
0.1000	0.0402	0.7191	65.0789	91.6400
0.2000	0.0334	0.7166	22.9267	185.7300
0.3000	0.0448	0.7626	48.2743	282.8400
0.4000	0.0407	0.7197	50.5418	378.5200
Ce-BTC/TeRh				
[TeRh]/g/L	K_1 (min^{-1})	R^2	q_e (mg/g)	q_{ecal} (mg/g)
0.1000	0.0344	0.7034	48.5746	94.8100
0.2000	0.0418	0.6852	63.4594	191.2500
0.3000	0.0416	0.5842	47.1484	286.6300
0.4000	0.0384	0.6777	20.5200	383.2800
Zr-BTC/TeRh				
[TeRh]/g/L	K_1 (min^{-1})	R^2	q_e (mg/g)	q_{ecal} (mg/g)
0.1000	0.0504	0.8229	150.9879	98.9600
0.2000	0.0499	0.8989	55.6121	193.2200
0.3000	0.0368	0.7332	42.2118	291.4400
0.4000	0.0347	0.6986	24.4370	386.1700

Source: Experimental data (2022)

Figure 93 shows the pseudo-second-order adsorption reaction rate of TeRh by Cu-BTC, Ce-BTC and Zr-BTC at varying initial TeRh concentrations. A similar trend of TeRh adsorption rate was observed for the various MOFs. The R^2 values closer to 1 were observed for all the rates of adsorption reaction. The adsorption rate of TeRh is seen to follow the pseudo-second-order adsorption.

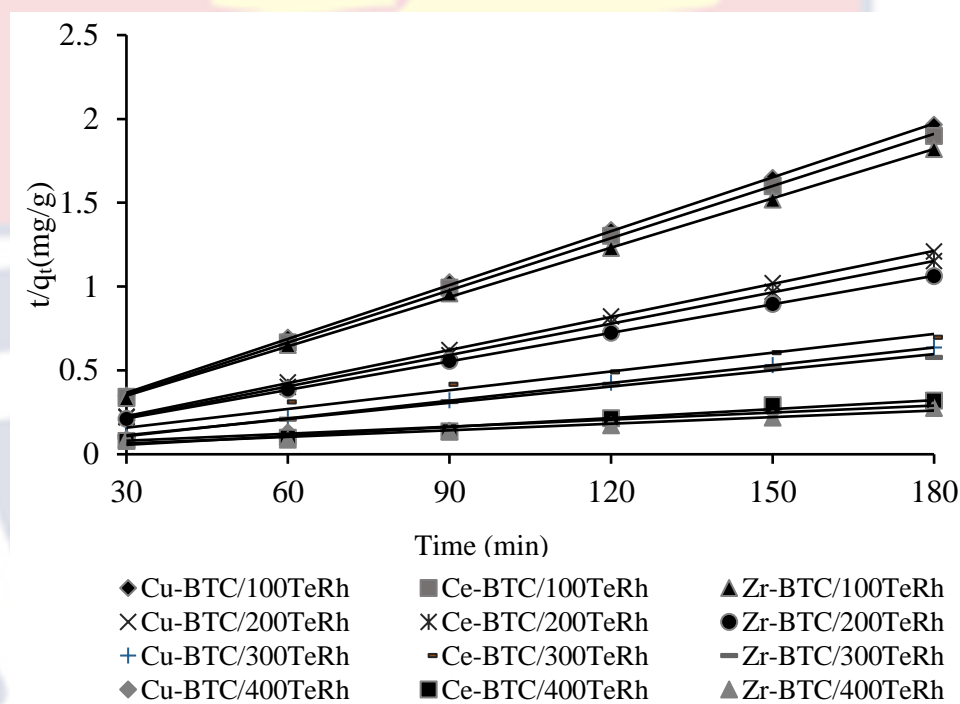


Figure 93: Pseudo-second-order graph for the adsorption of TeRh by Cu-BTC, Ce-BTC and Zr-BTC (MOF loading = 0.1g/L, Solution pH = 6)

A summary of values for the parameters measured for the various MOFs is shown in Table 16. Close experimental q_e values compared with the computed values were observed with increasing initial TeRh concentration for each TeRh concentration of 0.100g /L, 0.200 g/L and 0.300 g/L. A large difference in q_e values and q_{ecal} values was, however, observed for Cu-BTC and Ce-BTC at 0.400 g/L initial concentrations.

Table 16: The Parameters for Pseudo-second-order Adsorption Kinetics of Cu-BTC, Ce-BTC and Zr-BTC for TeRh at Varying Concentration

Cu-BTC/TeRh				
[TeRh]/g/L	K_2 (min ⁻¹)	R^2	q_e (mg/g)	q_{ecal} (mg/g)
0.1000	0.0025	0.9996	93.4580	91.6400
0.2000	0.0014	0.9999	151.5152	185.7300
0.3000	0.0047	1.0000	285.7143	282.8400
0.4000	0.0001	0.9716	714.2857	378.5200
Ce-BTC/TeRh				
[TeRh]/g/L	K_2 (min ⁻¹)	R^2	q_e (mg/g)	q_{ecal} (mg/g)
0.1000	0.0024	0.9996	96.1539	94.8100
0.2000	0.0013	1.0000	161.2903	191.2500
0.3000	0.0003	0.9732	270.2703	286.6300
0.4000	0.0012	0.9632	555.5556	383.2800
Zr-BTC/TeRh				
[TeRh]/g/L	K_2 (min ⁻¹)	R^2	q_e (mg/g)	q_{ecal} (mg/g)
0.1000	0.0017	0.9995	102.0408	98.9600
0.2000	0.0008	0.9999	175.4386	193.2500
0.3000	0.0006	0.9950	312.5000	286.2800
0.4000	0.0049	0.9543	395.2569	383.1900

Source: Experimental data (2022)

The adsorption capacity of Cu-BTC, Ce-BTC and Zr-BTC for pseudo-second-order adsorption rate was further determined using the Langmuir and the Freundlich model. As shown in Figure 94, the pseudo-second-order adsorption rate of TeRh by Cu-BTC, Ce-BTC and Zr-BTC fit the Langmuir adsorption model although with low R^2 values of 0.4115, 0.5195 and 0.8611.

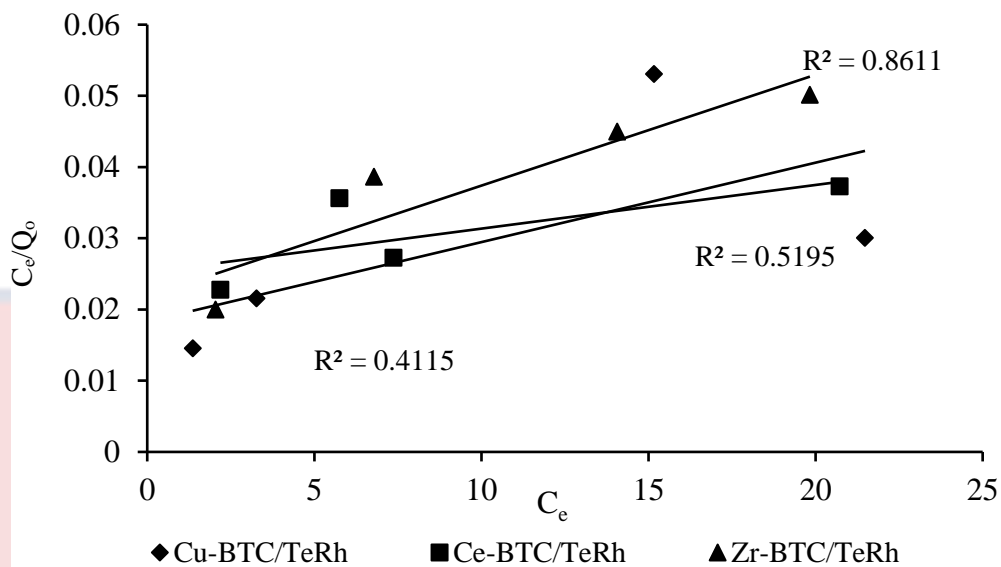


Figure 94: The Langmuir isotherm for the adsorption of TeRh by Cu-BTC, Ce-BTC and Zr-BTC

The adsorption capacity of Cu-BTC, Ce-BTC and Zr-BTC observed for the Freundlich model is as shown in Figure 95, the pseudo-second-order adsorption rate of TeRh by Cu-BTC, Ce-BTC and Zr-BTC fit the Freundlich model with R^2 values of 0.8942, 0.9662 and 0.9814.

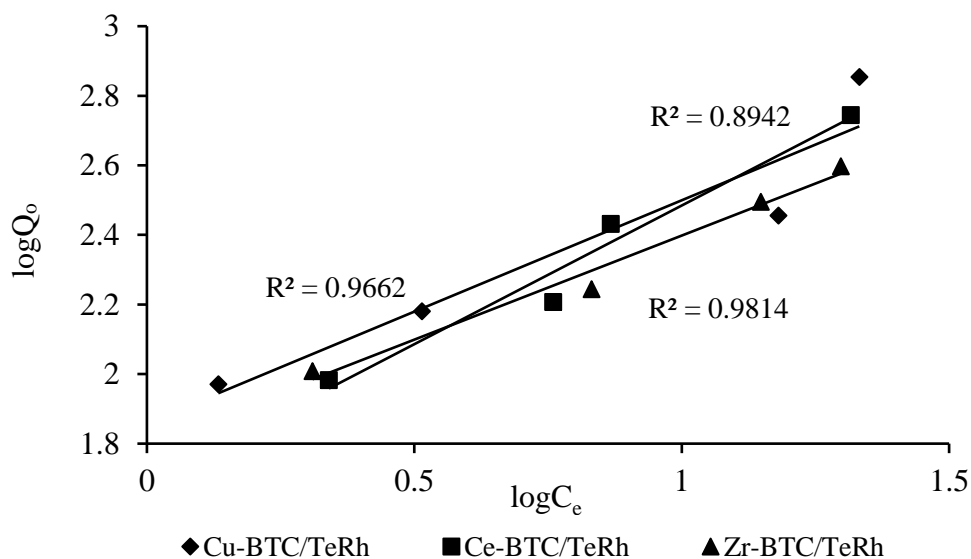


Figure 95: The Freundlich isotherm for the adsorption of TeRh by Cu-BTC, Ce-BTC and Zr-BTC

Table 17 lists the parameters from the Langmuir isotherm and the Freundlich isotherms for the pseudo-second-order adsorption rate of TeRh by Cu-BTC, Ce-BTC and Zr-BTC. The lowest K_L value of 0.0238 was observed for Ce-BTC which indicates that it has the weakest interaction towards TeRh. This may as a result of a very high maximum adsorption capacity (Q_0) observed due to excess TeRh which may have interfered with the interaction between Ce-BTC and TeRh yielding the highest separation from TeRh compared to Cu-BTC and Zr-BTC. Zr-BTC had the highest interaction with the lower maximum adsorption capacity for TeRh.

Table 17: The Parameters from Langmuir and Freundlich Isotherms of Cu-BTC, Ce-BTC and Zr-BTC for TeRh

		Langmuir		
Pseudo-second-order	R^2	K_L	Q_0	R_L
Cu-BTC/TeRh	0.4115	0.0601	909.0909	0.9765
Ce-BTC/TeRh	0.5195	0.0238	1666.6670	0.9906
Zr-BTC/TeRh	0.8611	0.1338	526.3158	0.9492
		Freundlich		
Pseudo-second-order	R^2	K_f	n	1/n
Cu-BTC/TeRh	0.8942	6.4199	1.5620	0.6402
Ce-BTC/TeRh	0.9662	5.4049	1.2544	0.7972
Zr-BTC/TeRh	0.9814	6.0484	1.6714	0.5983

Source: Experimental data (2022)

The lowest separation was therefore observed between Zr-BTC and TeRh with an R_L value of 0.9492 which makes it have the most favourable

Langmuir adsorption isotherm relative to Cu-5abdc and Zr-5abdc. Favourable Langmuir adsorption isotherm was observed for the pseudo-second-order adsorption rate of TeRh by Cu-BTC, Ce-BTC and Zr-BTC with R_L values of 0.9765, 0.9906 and 0.9492. Favourable n values of 1.5620, 1.2544 and 1.6714 with $1/n$ values of 0.6402, 0.7972 and 0.5983 were also observed for the Freundlich isotherm. The Cu-BTC was observed to have a slightly higher K_f value of 6.4199 relative to Zr-BTC with K_f value of 6.0484 which indicates a higher capacity for Cu-BTC to remove TeRh. A higher strength of adsorption was however observed for Zr-BTC with an n value of 1.6714 relative to Cu-BTC with an n value of 1.5620. The least removal of TeRh with the least strength of adsorption was observed for Ce-BTC among the MOFs.

Figure 96 the pseudo-first-order adsorption reaction rate of RBV5R by Cu-BTC, Ce-BTC and Zr-BTC at varying initial RBV5R concentrations.

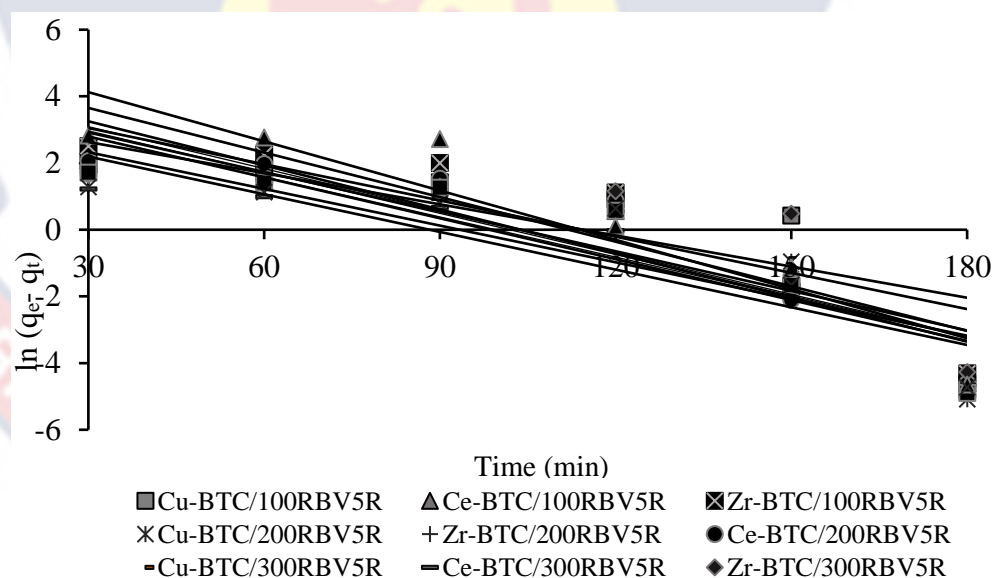


Figure 96: Pseudo-first-order graph for the adsorption of RBV5R by Cu-BTC, Ce-BTC and Zr-BTC (MOF loading = 0.1g/L, Solution pH = 6).

A similar trend in the rate of adsorption of RBV5R was observed for the various MOFs. A summary of values for the parameters measured for the

various MOFs is shown in Table 18. R^2 below 0.9 and low experimental q_e values were observed.

Table 18: The Parameters for Pseudo-first-order Adsorption Kinetics of Cu-BTC, Ce-BTC and Zr-BTC for RBV5R at Varying

Cu-BTC/RBV5R				
[RBV5R]/g/L	K_1 (min^{-1})	R^2	q_e (mg/g)	q_{ecal} (mg/g)
0.1000	0.0362	0.6628	62.5946	91.6000
0.2000	0.0419	0.7700	77.3701	185.8900
0.3000	0.0449	0.8098	54.4074	280.5500
0.4000	0.0409	0.7955	55.8741	372.7500
Ce-BTC/RBV5R				
[RBV5R]/g/L	K_1 (min^{-1})	R^2	q_e (mg/g)	q_{ecal} (mg/g)
0.1000	0.0412	0.8542	66.6797	90.9500
0.2000	0.0488	0.8276	35.4361	187.7600
0.3000	0.0377	0.8000	27.7962	280.5500
0.4000	0.0492	0.8524	27.3746	389.000
Zr-BTC/RBV5R				
[RBVR5]/g/L	K_1 (min^{-1})	R^2	q_e (mg/g)	q_{ecal} (mg/g)
0.1000	0.0446	0.8358	147.0981	97.4400
0.2000	0.0396	0.8036	60.8067	190.7400
0.3000	0.0311	0.5903	35.3253	287.1800
0.4000	0.0367	0.7596	30.8057	383.2800

Source: Experimental data (2022)

Figure 97 shows the pseudo-second-order adsorption reaction rate of RBV5R by Cu-BTC, Ce-BTC and Zr-BTC at varying initial RBV5R concentrations. A similar trend of RBV5R adsorption rate was observed for the various MOFs. The R^2 values closer to 1 were observed for all the rates of adsorption reaction.

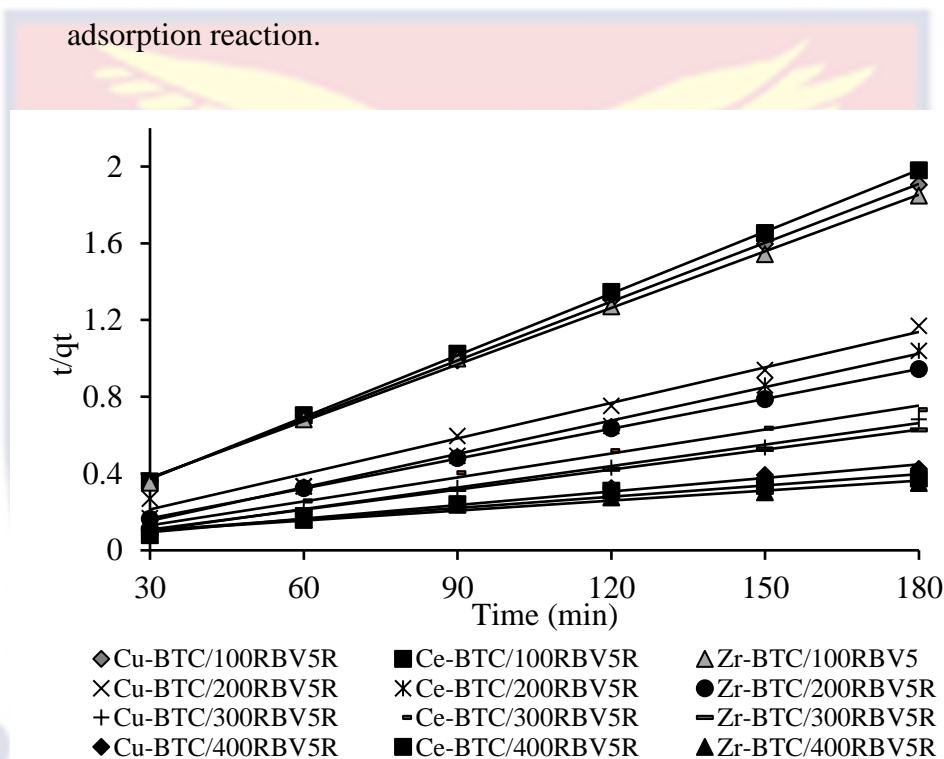


Figure 97: Pseudo-second-order graph for the adsorption of RBV5R by Cu-BTC, Ce-BTC and Zr-BTC (MOF loading = 0.1g/L, Solution pH = 6).

A summary of values for the parameters measured for the various MOFs is shown in Table 19. A close experimental q_e values compared with the computed values were observed with increasing initial RBV5R concentration for each RBV5R concentration of 0.100g /L, 0.200 g/L and 0.300 g/L. A large difference in q_e values and q_{ecal} values was, however, observed for Ce-BTC and Zr-BTC at 0.400 g/L initial concentrations. The adsorption rate of RBV5R is observed to follow the pseudo-second-order reaction rate.

Table 19: The Parameters for Pseudo-second-order Adsorption Kinetics of Cu-BTC, Ce-BTC and Zr-BTC for RBV5R at Varying Concentration

Cu-BTC/RBV5R				
[RBV5R]/g/L	K_2 (min ⁻¹)	R^2	q_e (mg/g)	q_{ecal} (mg/g)
0.1000	0.0017	0.9995	93.4579	91.6000
0.2000	0.0006	1.0000	163.9344	185.8900
0.3000	0.0036	0.9976	277.7778	280.5500
0.4000	0.0002	0.9845	416.6667	372.7500
Ce-BTC/RBV5R				
[RBV5R]/g/L	K_2 (min ⁻¹)	R^2	q_e (mg/g)	q_{ecal} (mg/g)
0.1000	0.0023	0.9997	93.4579	90.9500
0.2000	0.0012	1.0000	175.4386	187.7600
0.3000	0.0035	0.9958	238.0952	280.5500
0.4000	0.0001	0.9617	500.0000	389.0000
Zr-BTC/RBV5R				
[RBVR5]/g/L	K_2 (min ⁻¹)	R^2	q_e (mg/g)	q_{ecal} (mg/g)
0.1000	0.0010	0.99	102.0408	97.4400
0.2000	0.0039	0.6741	192.3077	190.7400
0.3000	0.0010	0.6119	285.7143	287.1800
0.4000	0.0001	0.8855	588.2353	383.2800

Source: Experimental data (2022)

The adsorption capacity of Cu-BTC, Ce-BTC and Zr-BTC were further determined using the Langmuir and the Freundlich model. As shown in Figure 98, the pseudo-second-order adsorption rate of RBV5R by Cu-BTC,

Ce- BTC and Zr-BTC fit the Langmuir model with R^2 values of 0.7633, 0.9294 and 0.9397.

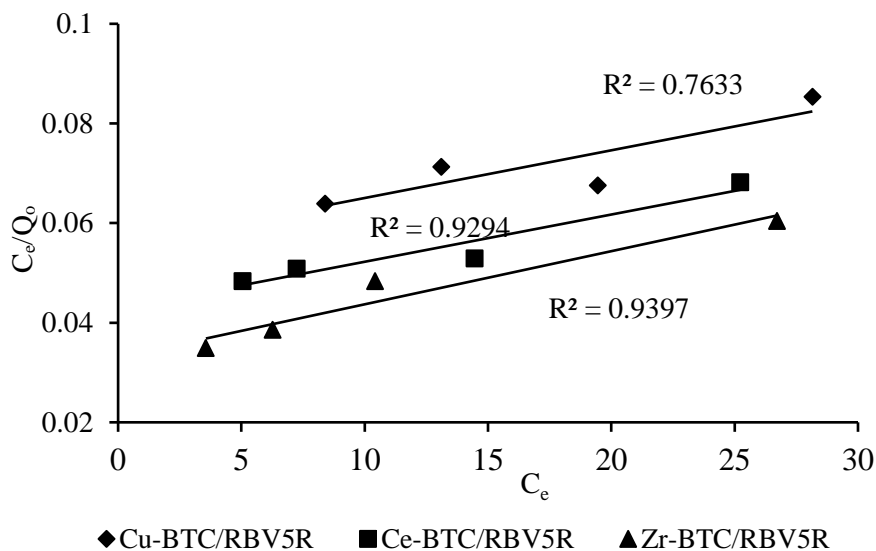


Figure 98: The Langmuir isotherm for the adsorption of RBV5R by Cu-BTC, Ce- BTC and Zr-BTC

The adsorption capacity of Cu-BTC, Ce-BTC and Zr-BTC observed for the Freundlich model is as shown in Figure 99.

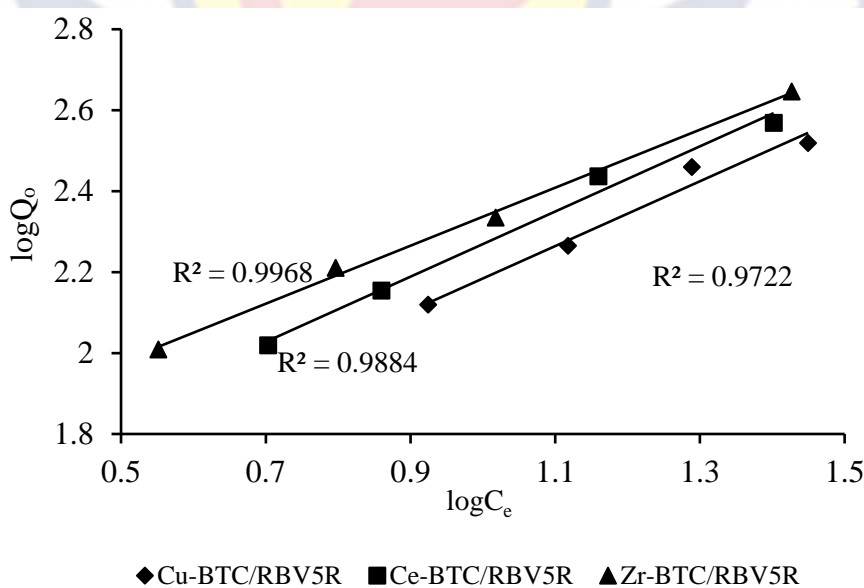


Figure 99: The Freundlich isotherm for the adsorption of RBV5R by Cu-BTC, Ce-BTC and Zr-BTC

The pseudo-second-order adsorption rate of RBV5R by Cu-BTC, Ce-BTC and Zr-BTC fit the Freundlich adsorption with R^2 values of 0.9722, 0.9884 and 0.9968. Table 20 lists the parameters from the Langmuir isotherms and the Freundlich isotherms for the pseudo-second-order adsorption rate.

Table 20: The Parameters from Langmuir and Freundlich Isotherms of Cu-BTC, Ce-BTC and Zr-BTC for RBV5R

		Langmuir		
Pseudo-first order	R^2	K_L	Q_0	R_L
Cu-BTC/RBV5R	0.7633	0.0180	1000.0000	0.9929
Ce-BTC/RBV5R	0.9294	0.0210	1111.1111	0.9917
Zr-BTC/RBV5R	0.9397	0.0211	909.0909	0.9916
		Freundlich		
Pseudo-second-order	R^2	K_f	n	1/n
Cu-BTC/RBV5R	0.9722	3.9896	1.2491	0.8006
Ce-BTC/RBV5R	0.9884	4.3232	1.2421	0.8051
Zr-BTC/RBV5R	0.9968	5.0536	1.3955	0.7166

Source: Experimental data (2022)

Favourable Langmuir adsorption isotherm was observed for the pseudo-second-order adsorption rate of RBV5R by Cu-BTC, Ce-BTC and Zr-BTC with an R_L value of 0.9929, 0.9917 and 0.9916. The lowest K_L value of 0.0180 was observed for Cu-BTC which indicates that it has the weakest interaction towards RBV5R although it had the highest maximum adsorption capacity (Q_0). The high Q_0 may have interfered with the interaction due to excess RBV5R adsorbed by Cu-BTC. The Zr-BTC and Ce-BTC were

observed to have very close higher interaction rates on RBV5R with K_L values of 0.0210 and 0.0211.

Favourable n values of 1.2491, 1.2421 and 1.3955 with $1/n$ values of 0.8006, 0.8051 and 0.7166 were also observed for the Freundlich isotherms.

The Cu-BTC was observed to have the lowest K_f value of 3.9896 among the MOFs which indicates a lower capacity for Cu-BTC to remove TeRh. A slightly higher strength of adsorption was however observed with an n value of 1.2491 relative to Ce-BTC with an n value of 1.2421. The highest removal of RBV5R with the highest strength of adsorption was observed for Zr-BTC among the MOFs.

Kinetic Study on the Removal of Coloured Organic Pollutants at

Optimum Parameter Set Conditions

The rate of removal of Lissamine green SF (LGSF), Tetraethylrhodamine (TeRh), and Remezol Brilliant Violet 5R (RBV5R) with time from water by the Cu-BTC, Cu-5abdc, Ce-BTC, Ce-5abdc, Zr-BTC and Zr-5abdc at optimum pollutant concentration of 0.2 g/L, optimum MOF loading of 0.01g/L and optimum pH of 6 or 8 was examine using the pseudo-first-order adsorption and pseudo-second-order adsorption reaction rate equations. Figure 100 shows the pseudo-first-order adsorption reaction rate of LGSF by Zr-BTC, Zr-5abdc, Ce-BTC, Ce-5abdc Cu-BTC and Cu-5abdc.

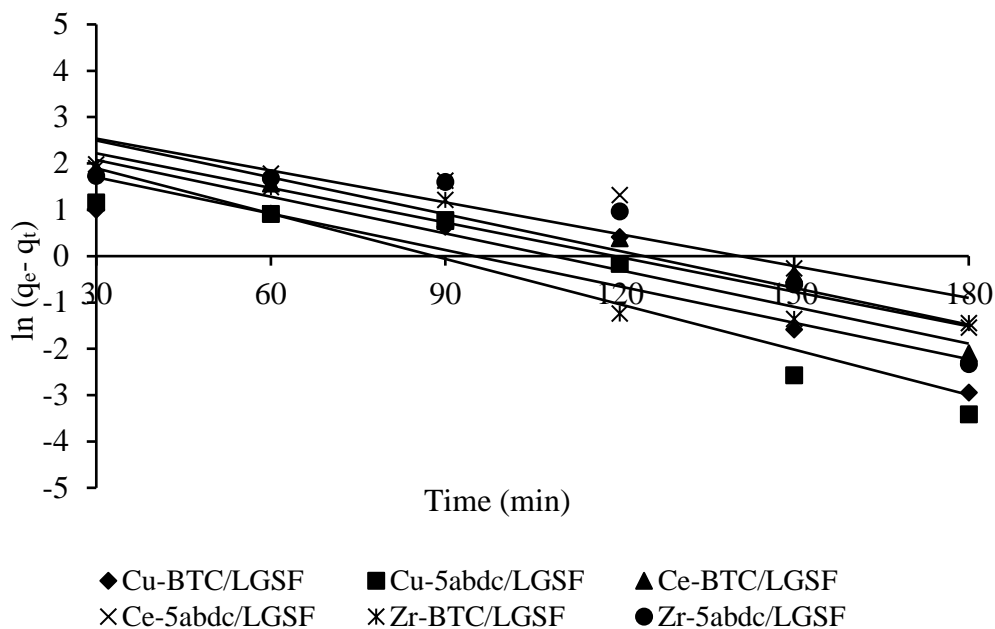


Figure 100: Pseudo-first-order graph for the adsorption of LGSF by MOFs ([LGSF] = 0.20 g/L, MOF loading = 0.01g/L, Solution pH =6)

The rate of adsorption of LGSF was observed for the various MOFs. A summary of values for the parameters measured for the various MOFs is shown in Table 21. The R^2 values of 0.8630, 0.8149, 0.9273, 0.8334, 0.8168 and 0.8705 as well as K_1 values of 0.0264, 0.0265, 0.0249, 0.0229, 0.0262 and 0.0326 were obtained for, Zr-BTC, Zr-5abdc, Ce-BTC, Ce-5abdc Cu-BTC and Cu-5abdc respectively. A low experimental values (q_e) of 17.5912, 26.8724, 19.4219, 25.1083, 12.0456 and 17.7378 compared with computed values (q_{ecal}) of 194.8657, 192.9889, 192.6559, 192.9859, 185.9547 and 184.9569 was observed for Zr-BTC, Zr-5abdc, Ce-BTC, Ce-5abdc Cu-BTC and Cu-5abdc under the pseudo-first-order adsorption reaction rate. The low R^2 values observed show the adsorption rate of LGSF does not follow the pseudo-first-order adsorption reaction rate.

Table 21: The Parameters for Pseudo-first-order Adsorption Kinetics of LGSF

Sample Solution	$K_1(\text{min}^{-1})$	R^2	$q_e(\text{mg/g})$	$q_{\text{ecal}}(\text{mg/g})$
Zr-BTC/LGSF	0.0264	0.8630	17.5912	194.8657
Zr-5abdc/LGSF	0.0265	0.8149	26.8724	192.9889
Ce-BTC/LGSF	0.0249	0.9273	19.4219	192.6559
Ce-5abdc/LGSF	0.0229	0.8334	25.1083	192.9859
Cu-BTC/LGSF	0.0262	0.8168	12.0456	185.9547
Cu-5abdc/LGSF	0.0326	0.8705	17.7378	184.9569

Source: Experimental data (2022)

Figure 101 shows the pseudo-second-order adsorption reaction rate of LGSF by Zr-BTC, Zr-5abdc, Ce-BTC, Ce-5abdc, Cu-BTC and Cu-5abdc. A similar trend of LGSF adsorption rate was observed for the various MOFs.

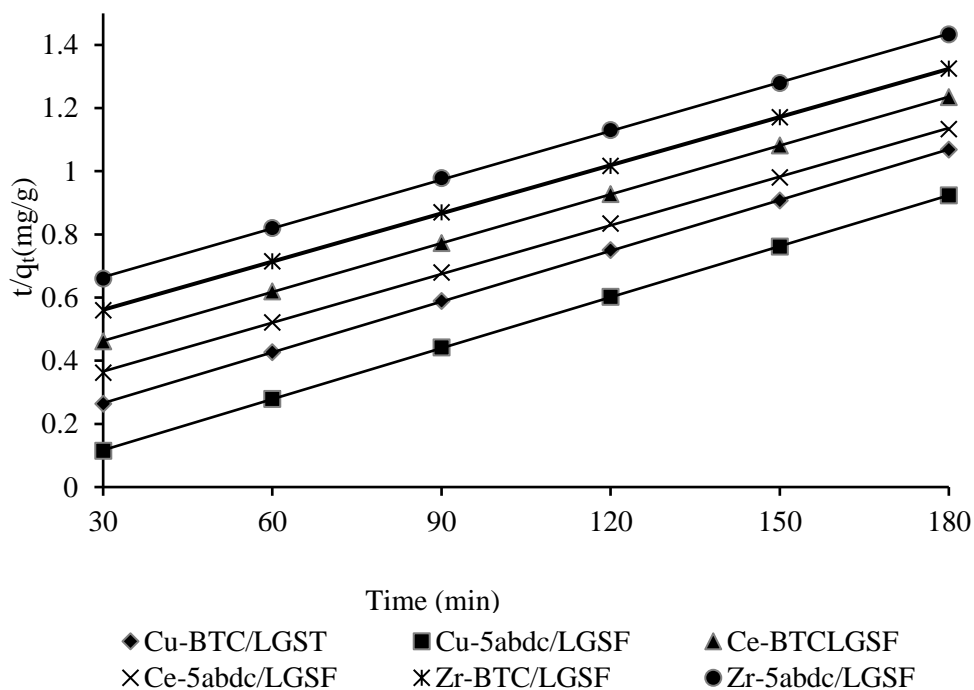


Figure 101: Pseudo-second-order graph for the adsorption of LGSF by MOFs ([LGSF] = 0.20 g/L, MOF loading = 0.1g/L, Solution pH = 6)

Table 22 shows a summary of values for the parameters measured for the various MOFs. The R^2 values of 0.9999, 0.9998, 1.0000, 0.9999, 1.0000 and 1.0000 as well as K_1 values of 0.0030, 0.0024, 0.0032, 0.0022, 0.0057 and 0.0052 were obtained for Zr-BTC, Zr-5abdc, Ce-BTC, Ce-5abdc Cu-BTC and Cu-5abdc respectively. A close experimental values (q_e) of 196.0785, 196.0784, 192.3076, 196.0784, 185.1852 and 185.1852 compared with computed values of 194.8657, 192.9889, 192.6559, 192.9856, 185.9547 and 184.9569 was observed for Zr-BTC, Zr-5abdc, Ce-BTC, Ce-5abdc Cu-BTC and Cu-5abdc under the pseudo-second-order adsorption reaction rate. The high R^2 values observed show the adsorption rate of LGSF follows a pseudo-second-order adsorption reaction rate.

Table 22: The Parameters for Pseudo-second-order Adsorption Kinetics of LGSF

Sample Solution	K_2 (min^{-1})	R^2	q_e (mg/g)	q_{ecal} (mg/g)
Zr-BTC/LGSF	0.0030	0.9999	196.0785	194.8657
Zr-5abdc/LGSF	0.0024	0.9998	196.0784	192.9889
Ce-BTC/LGSF	0.0032	1.0000	192.3076	192.6559
Ce-5abdc/LGSF	0.0022	0.9999	196.0784	192.9859
Cu-BTC/LGSF	0.0057	1.0000	185.1852	185.9547
Cu-5abdc/LGSF	0.0052	1.0000	185.1852	184.9569

Source: Experimental data (2022)

Figure 102 shows the pseudo-first-order adsorption reaction rate of TeRh by Zr-BTC, Zr-5abdc, Ce-BTC, Ce-5abdc Cu-BTC and Cu-5abdc at

0.20g/L initial TeRh concentration. A close adsorption rate trend of TeRh by the various MOFs was observed.

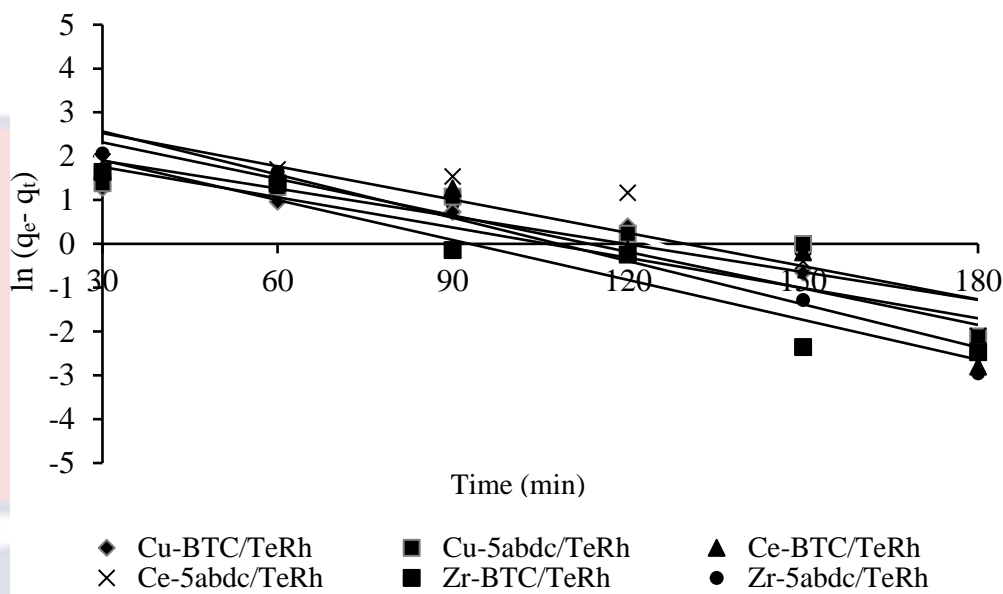


Figure 102: Pseudo-first-order graph for the adsorption of TeRh by MOFs ([TeRh] = 0.20 g/L, MOF loading = 0.1g/L, Solution pH = 6).

A summary of values for the parameters measured for the various MOFs is shown in Table 23. The R^2 values of 0.9397, 0.9275, 0.8759, 0.8537, 0.8586 and 0.8259 as well as K_1 values of 0.0262, 0.0343, 0.0237, 0.0205, 0.0207 and 0.0202 were obtained for, Zr-BTC, Zr-5abdc, Ce-BTC, Ce-5abdc, Cu-BTC and Cu-5abdc respectively. A low experimental values (q_e) of 13.4489, 38.2407, 18.0582, 20.0976, 10.0453 and 11.85678 compared with computed values of 193.3658, 193.2878, 191.2757, 190.6787, 185.88458 and 184.8265 was observed for Zr-BTC, Zr-5abdc, Ce-BTC, Ce-5abdc, Cu-BTC and Cu-5abdc under the pseudo-first-order adsorption reaction rate. The low R^2 values observed show the adsorption rate of TeRh does not follow the pseudo-first-order adsorption reaction rate.

Table 23: The Parameters for Pseudo-first-order Adsorption Kinetics of TeRh

Sample Solution	K_1 (min^{-1})	R^2	q_e (mg/g)	q_{ecal} (mg/g)
Zr-BTC/TeRh	0.0262	0.9397	13.4489	193.3658
Zr-5abdc/ TeRh	0.0343	0.9275	38.2407	193.2878
Ce-BTC/TeRh	0.0237	0.8759	18.0582	191.2757
Ce-5abdc/TeRh	0.0205	0.8537	20.0976	190.6787
Cu-BTC/TeRh	0.0207	0.8586	10.0453	185.8458
Cu-5abdc/TeRh	0.0202	0.8259	11.85678	184.8265

Source: Experimental data (2022)

Figure 103 shows the pseudo-second-order adsorption reaction rate of TeRh by Zr-BTC, Zr-5abdc, Ce-BTC, Ce-5abdc, Cu-BTC and Cu-5abdc. A similar rate of adsorption of TeRh trend was observed for the various MOFs.

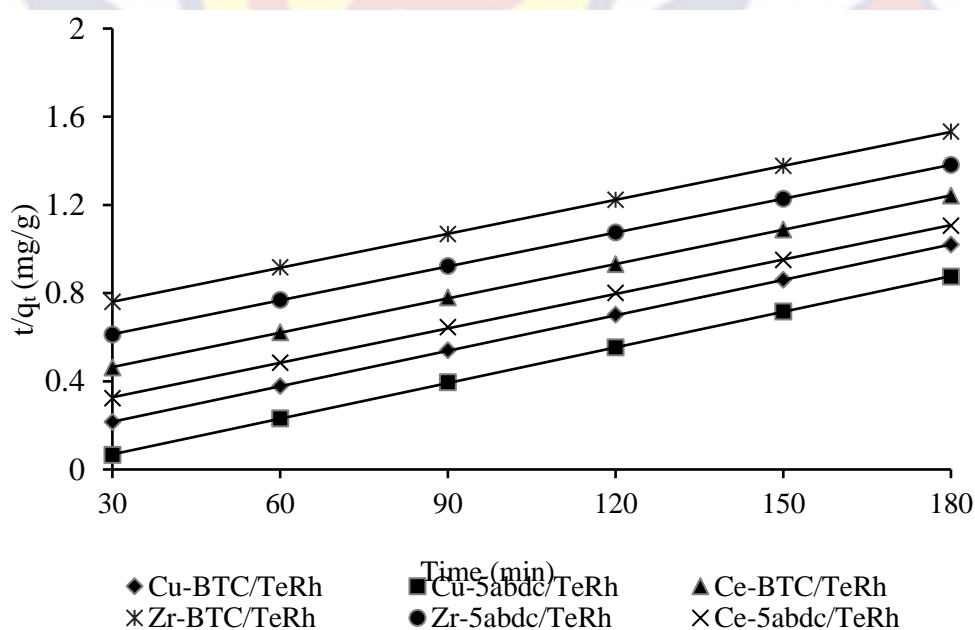


Figure 103: Pseudo-second-order graph for the adsorption of TeRh by MOFs ([TeRh] = 0.20 g/L, MOF loading = 0.1g/L, Solution pH = 8)

Table 24 shows a summary of values for the parameters measured for the various MOFs. The R^2 values of 1.0000, 1.0000, 0.9999, 0.9998, 1.0000 and 1.0000 as well as K_1 values of 0.0040, 0.0026, 0.0031, 0.0024, 0.0052 and 0.0042 were obtained for Zr-BTC, Zr-5abdc, Ce-BTC, Ce-5abdc Cu-BTC and Cu-5abdc respectively. A close experimental q_e values of 196.0780, 196.0780, 192.3077, 192.3077, 185.1852 and 185.1852 compared with computed values of 193.3658, 193.2878, 191.2757, 190.6787, 185.8458 and 185.8265 was observed for Zr-BTC, Zr-5abdc, Ce-BTC, Ce-5abdc Cu-BTC and Cu-5abdc under the pseudo-second-order adsorption reaction rate. The R^2 values observed show the adsorption rate of TeRh follows a pseudo-second-order adsorption reaction rate.

Table 24: The Parameters for Pseudo-second-order Adsorption Kinetics of TeRh

Sample Solution	K_2 (min^{-1})	R^2	q_e (mg/g)	q_{ecal} (mg/g)
Zr-BTC/TeRh	0.0040	1.0000	196.0780	193.3658
Zr-5abdc/TeRh	0.0026	1.0000	196.0780	193.2878
Ce-BTC/TeRh	0.0031	0.9999	192.3077	191.2757
Ce-5abdc/TeRh	0.0024	0.9998	192.3077	190.6787
Cu-BTC/TeRh	0.0052	1.0000	185.1852	185.8458
Cu-5abdc/TeRh	0.0042	1.0000	185.1852	184.8265

Source: Experimental data (2022)

Figure 104 the pseudo-first-order adsorption reaction rate of RBV5R by Zr-BTC, Zr-5abdc, Ce-BTC, Ce-5abdc, Cu-BTC and Cu-5abdc. A similar adsorption trend for RBV5R was observed with the various MOFs.

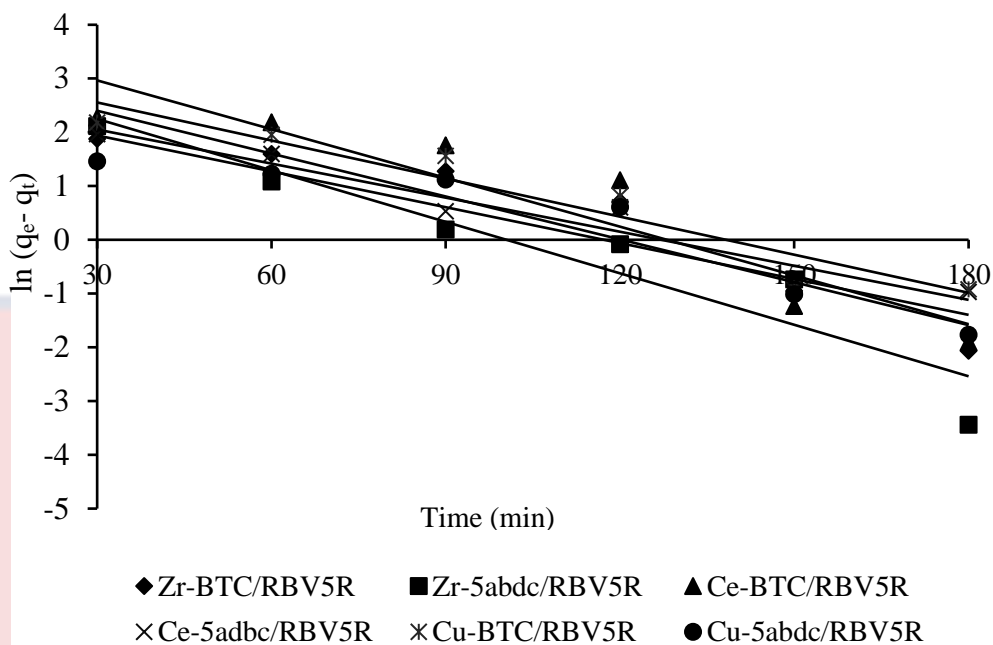


Figure 104: Pseudo-first-order graph for adsorption of RBV5R by MOFs ([RBV5R] = 0.20 g/L, MOF loading = 0.1g/L, Solution pH = 6)

A summary of values for the parameters measured for the various MOFs is shown in Table 25. The R^2 values of 0.9008, 0.8943, 0.8754, 0.9303, 0.9118 and 0.8697 as well as K_1 values of 0.0266, 0.0319, 0.0302, 0.0211, 0.0236 and 0.0223 were obtained for Zr-BTC, Zr-5abdc, Ce-BTC, Ce-5abdc, Cu-BTC and Cu-5abdc respectively. A low experimental q_e values of 25.7465, 22.3449, 39.3462, 11.9999, 20.3545 and 10.0613 compared with computed values of 190.8659, 189.3184, 187.8778, 185.6878, 185.6789 and 179.8879 was observed for Zr-BTC, Zr-5abdc, Ce-BTC, Ce-5abdc, Cu-BTC and Cu-5abdc under the pseudo-first-order adsorption reaction rate. The low R^2 values observed show the adsorption rate of RBV5R does not follow the pseudo-first-order adsorption reaction rate.

Table 25: The Parameters for Pseudo-first-order Adsorption Kinetics of RBV5R

Sample Solution	K_1 (min^{-1})	R^2	q_e (mg/g)	q_{ecal} (mg/g)
Zr-BTC/RBV5R	0.0266	0.9008	25.7465	190.8659
Zr-5abdc/RBV5R	0.0319	0.8943	22.3449	189.3184
Ce-BTC/RBV5R	0.0302	0.8754	39.3462	187.8778
Ce-5abdc/RBV5R	0.0211	0.9303	11.9999	185.6878
Cu-BTC/RBV5R	0.0236	0.9118	20.3545	185.6789
Cu-5abdc/RBV5R	0.0223	0.8697	10.0613	179.8879

Source: Experimental data (2022)

Figure 105 shows the pseudo-second-order adsorption reaction rate of RBV5R by Zr-BTC, Zr-5abdc, Ce-BTC, Ce-5abdc Cu-BTC and Cu-5abdc for 0.20 g/L initial RBV5R concentration. A close adsorption rate of RBV5R was observed for the various MOFs.

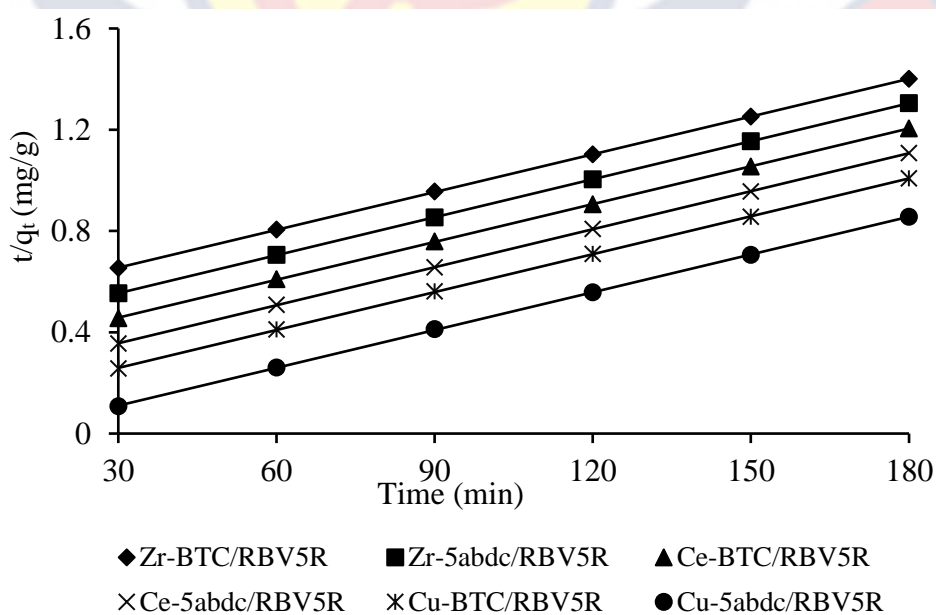


Figure 105: Pseudo-second-order graph for the adsorption of RBV5R by MOFs ([RBV5R] = 0.20 g/L, MOF loading = 0.1g/L, Solution pH = 6)

Table 26 shows a summary of the values of the parameters for the various MOFs. The R^2 values of 0.9999, 1.0000, 0.9998, 1.0000, 0.9999 and 1.0000 as well as K_1 values of 0.0026, 0.0038, 0.0020, 0.0039, 0.0025 and 0.0059 were obtained for, Zr-BTC, Zr-5abdc, Ce-BTC, Ce-5abdc Cu-BTC and Cu-5abdc respectively. A close experimental q_e values of 192.3077, 192.3677, 188.6792, 185.1852, 188.6792 and 181.8182 compared with computed values of 190.8659, 189.3184, 187.8778, 185.6878, 185.6789 and 179.8879 was observed for Zr-BTC, Zr-5abdc, Ce-BTC, Ce-5abdc Cu-BTC and Cu-5abdc under the pseudo-second-order adsorption reaction rate. The R^2 values observed show the adsorption rate of RBV5R follows a pseudo-second-order adsorption reaction rate.

Table 26: The Parameters for Pseudo-second-order Adsorption Kinetics of RBV5R

Sample Solution	K_2 (min^{-1})	R^2	q_e (mg/g)	q_{ecal} (mg/g)
Zr-BTC/RBV5R	0.0026	0.9999	192.3077	190.8659
Zr-5abdc/RBV5R	0.0038	1.0000	192.3977	189.3184
Ce-BTC/RBV5R	0.0020	0.9998	188.6792	187.8778
Ce-5abdc/RBV5R	0.0039	1.0000	185.1852	185.6878
Cu-BTC/RBV5R	0.0025	0.9999	188.6792	185.6989
Cu-5abdc/RBV5R	0.0059	0.9999	181.8182	179.8879

Source: Experimental data (2022)

The removal rate of LGSF, TeRh and RBV5R by Zr-BTC, Zr-5abdc, Ce-BTC, Ce-5abdc, Cu-BTC and Cu-5abdc all followed the pseudo-second-

order adsorption. The intramolecular force interactions during adsorption (physisorption) could be the limiting adsorption rate determining the pseudo-first-order adsorption trend (Liu et al., 2019; Sumalinog, Capareda, & de Luna, 2018). This is evidenced in the low experimental q_e values observed which indicates that low concentrations of LGSF, TeRh and RBV5R could be adsorbed by the various MOFs.

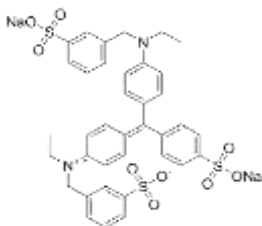
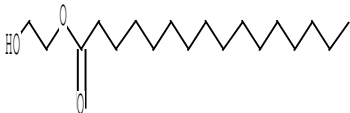
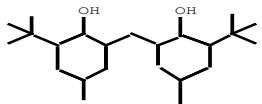
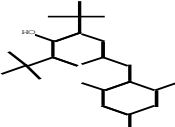
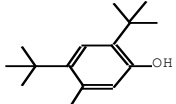
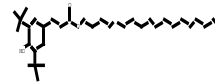
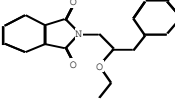
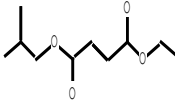
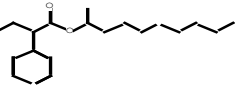
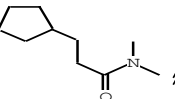

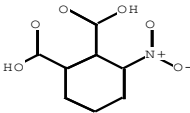
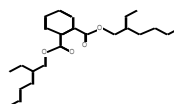
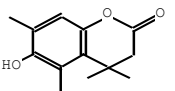
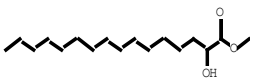
Intermediates Obtained from the Pollutant Transformation Process

Dye intermediates, when found in humans, may lead to acute and chronic toxicity (Affat, 2021; Al-Tohamy, et al., 2022; Avallone, et al., 2022; Berardi, et al., 2019; Chavan, 2013). Various intermediates were detected from the transformation of pollutants during their removal from the water after the 180 min light irradiation using the GC/MS. Table 27 lists the structures of the intermediates observed for the removal of Lissamine Green SF (LGSF) from water. Lissamine Green SF (LGSF) with a molar mass of 749.893g/mol was disintegrated into fragment compounds.

Fragment compounds such as 2,6-Di-tert-butyl-4-[(2-octadecyloxy carbonyl) ethyl]phenol (m/z 530), 1, 2-benzenedi carboxylic acid, bis(2-ethylhexyl) ester (m/z 390), Phenol, 2,2'-methylenebis [6-(1,1-dimethylethyl)-4-methyl (m/z 340), 2,6-di-tert-butyl-4-(2,4,6-trimethyl benzyl) phenol (m/z 338), Hexadecanoic acid, 2-hydroxyethyl ester (m/z 300), 3-Phenyl-2-ethoxypropylphthalimide (m/z 309) and Butyric acid-2-phenyl-dec-2-yl ester (m/z 304) were observed. Other lower fragments including Methyl 2-hydroxy hexadecanoate (m/z 286), 13-Tetradecenyl acetate (m/z 254), Phenol, 2, 4-bis(1,1-dimethylethyl)-5-methyl (m/z 220), 6-Hydroxy-4,4,5,7-tetramethyl-2-

chromanone (m/z 220), Fumaric acid-ethyl-2-methylallyl ester (m/z 198), 3-Cyclopentylpropionamide, N,N-dimethyl-ester (m/z 169), and 3-nitrophthalic acid (m/z 211) were also observed.

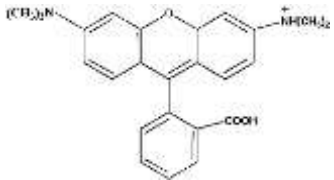
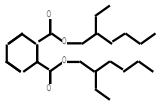
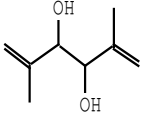
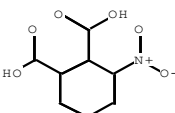
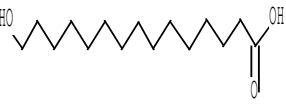
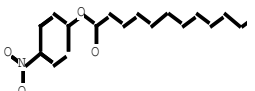
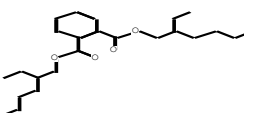
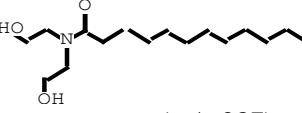
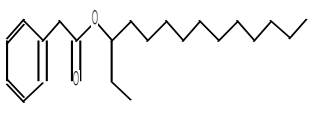
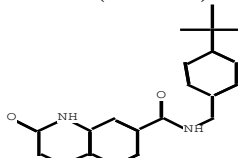
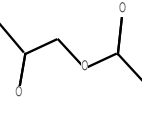
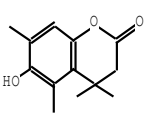
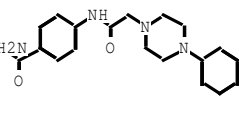
Table 27: Summary of Intermediates after 180 min Photoactivity on LGSF

Pollutant	Intermediates			
 (749.893g/mol) Lissamine green (LGSF)	 (m/z 300)	 (m/z 340)		
	 (m/z 338)	 (m/z 220)	 (m/z 530)	
	 (m/z 309)	 (m/z 198)	 (m/z 304)	
	 (m/z 169)	 (m/z 254)	 (m/z 211)	
	 (m/z 390)	 (m/z 220)	 (m/z 286)	

Source: Experimental data (2022)

Fragment compounds were also observed for TetraethylRhodamine (TeRh) with a molar mass of 479.02 g/mol as shown in Table 28.

Table 28: Summary of Intermediates after 180 min Photoactivity on TeRh

Pollutant	Intermediates		
 <p>(479.02 g/mol) Tetraethylrhodamine (Rhodamine B)</p>	 (m/z 390)	 (m/z 142)	 (m/z 211)
	 (m/z 258)	 (m/z 321)	
	 (m/z 390)	 (m/z 287)	
	 (m/z 332)	 (m/z 338)	
	 (m/z 116)	 (m/z 220)	 (m/z 338)

Source: Experimental data (2022)

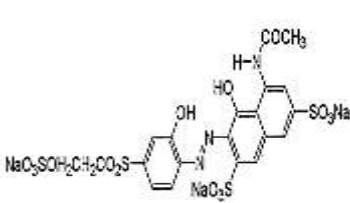
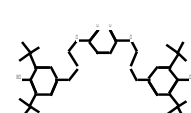
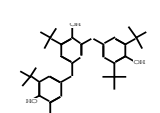
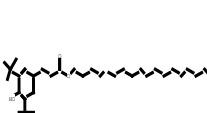
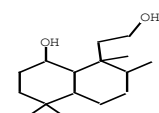
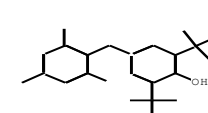
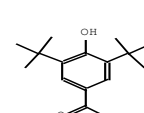
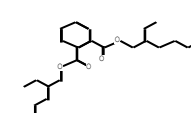
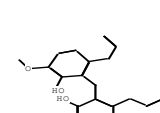
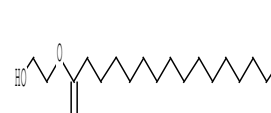
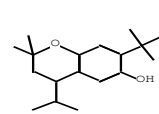
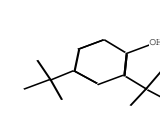
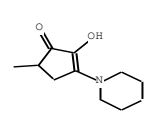
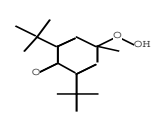
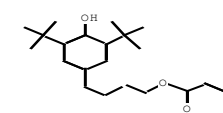
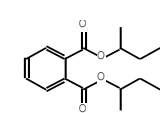
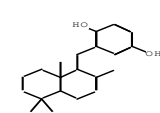
Fragment compounds such as 1,2-benzene dicarboxylic acid, bis(2-ethylhexyl) ester (m/z 390), Bis(2-ethylhexyl) phthalate (m/z 390), 4-([(4-phenyl-1-piperazinyl) acetyl]amino) benzamide (m/z 338), 2H-1,4-benzoxazine-6-carboxamide, n-[4-(1,1-dimethyl ethyl)phenyl] methyl]-3,4-dihydro-3-oxo (m/z 338), Benzeneacetic acid, 3-tetradecyl ester (m/z 332) and Dodecanoic acid, 4-nitrophenyl ester (m/z 321) were observed. The lower mass fragment which included N,N-bis (2-hydroxyethyl) dodecanamide (m/z 287), 15-Hydroxypentadecanoic acid (m/z 258), 6-Hydroxy-4,4,5,7-tetramethyl-2-chromanone (m/z 220), 3-nitrophthalic acid (m/z 211), 2,5-Dimethyl-1, 5-

hexadiene-3, 4-diol (m/z 142) and 2-oxopropyl acetate (m/z 116) were additionally observed.

Remazole Brilliant 5R (RBV5R) with a molar mass of 734.58 g/mol was disintegrated into fragments summarized in Table 29. Higher fragment masses such as Bis[3-(3,5-ditert-butyl-4-hydroxyphenyl)propyl] (2Z)-2-butenedioate (m/z 608), 2-tert-Butyl-4,6-bis(3,5-di-tert-butyl-4-hydroxybenzyl)phenol (m/z 586) and Benzenepropanoic acid, 3,5-bis(1,1-dimethylethyl)-4-hydroxy-, octadecyl ester (m/z 530) were observed. Other masses including 1, 2-benzenedicarboxylic acid, Bis (2-ethylhexyl) ester (m/z 390), Phenol, 2,2'-methylenebis*6-methoxy-3-(2-propenyl) (m/z 340), 2,6-Di-tert-butyl-4-(2,4,6-trimethylbenzyl) phenol (m/z 338), 4-(3,5-Di-tert-butyl-4-hydroxyphenyl) butyl acrylate (m/z 332), 1,4-Benzenediol,2-[(1,4,4a,5,6,7,8,8a-octahydro-2,5,5,8a-tetramethyl-1-naphthalenyl) methyl]-, [1R-(1.alpha.,4a.beta., 8a.alpha.)] (m/z 314) and Hexadecanoic acid, 2-hydroxyethyl ester (m/z 300) were observed.

Lower fragment masses such as, 1,2-Benzenedicarboxylic acid, di-sec-butyl ester (m/z 278), 2H-1-benzopyran-6-ol, 7-(1,1-dimethylethyl)-3,4-dihydro-2,2-dimethyl-4-(1-methylethyl) (m/z 276), (1R,2R,8S,8Ar)-8-hydroxy-1-(2-hydroxyethyl)-1,2,5,5-tetramethyl-cis-decalin (m/z 254), 2,5-cyclohexadien-1-one, 2,6-bis(1,1-dimethylethyl)-4-hydroperoxy-4-methyl (m/z 252), 3,5-di-tert-Butyl-4-hydroxyacetophenone (m/z 248), 1-hydroxy-2,4-di-tert-butylbenzene (m/z 206), 2-hydroxy-5-methyl-3-(piperidin-1-yl)cyclopent-2-en-1-one (m/z 195) were additionally observed.

Table 29: Summary of Intermediates after 180 min Photoactivity on RBV5R

Pollutants	Intermediate		
 <p>(734.58g/mol) Remazole brilliant violet 5R</p>			
	(m/z 608)	(m/z 586)	(m/z 530)
			
	(m/z 254)	(m/z 338)	(m/z 248)
			
(m/z 390)	(m/z 340)	(m/z 300)	
			
(m/z 276)	(m/z 206)	(m/z 195)	(m/z 252)
			
(m/z 332)	(m/z 278)	(m/z 314)	

Source: Experimental data (2022)

Photoactivity of Zr-BTC on Industrial Mixed Textile Dye

The Zr-BTC which had the highest adsorption activity on the removal of the selected coloured pollutants was used to investigate its effect to remove industrial textile dye. Figure 106 shows the removal of the dye with varying concentrations from 0.10g to 0.40g by Zr-BTC for 180 min. It was observed that Zr-BTC could effectively remove the mixed textile dye from water with the maximum dye percentage removal of 86.4% for the least concentration of

0.1g/L. A decrease in the removal dye percentage was observed with increasing dye concentration.

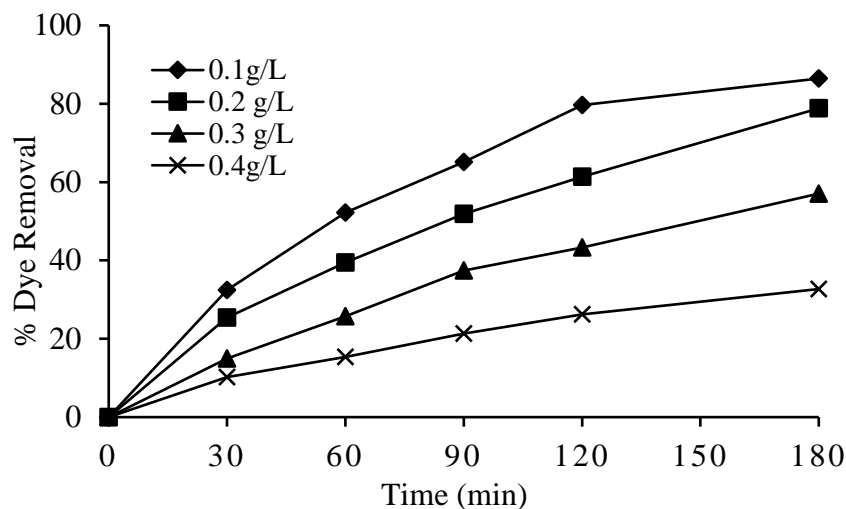


Figure 106: Effect of MTD concentration variation on removal activity of Zr-BTC (Zr-BTC Loading = 0.10 g/L; Solution pH = 6.2).

Figure 107 shows the UV-visible absorption spectra. Absorption peaks around 450 nm, 550 nm and 630 nm were identified. These peaks are the absorption regions of yellow, violet and blue which could indicate the dye is a mixture of these three colours. A gradual reduction of peaks at 30 min time intervals for 180 min was observed. This gradual reduction demonstrated that the dye was being removed from the sample solution.

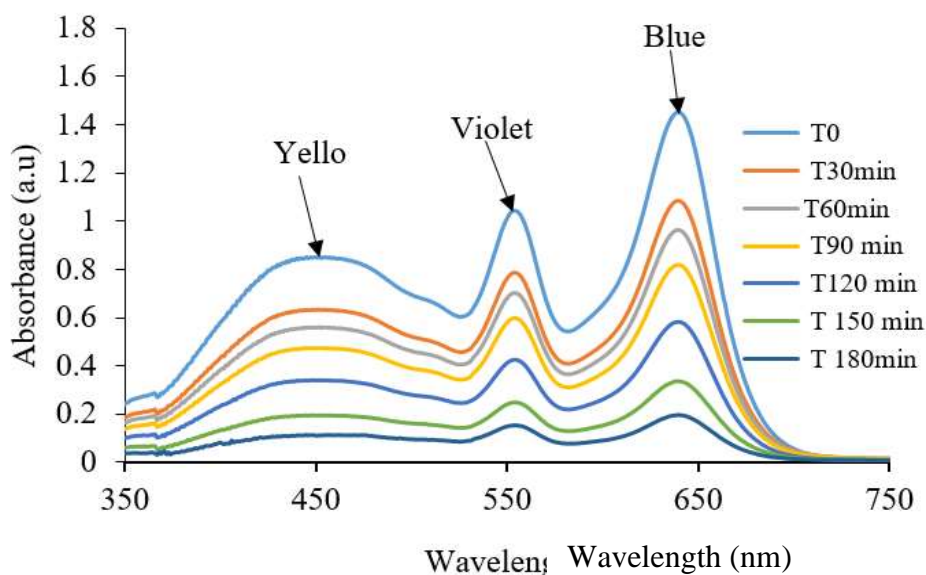


Figure 107: UV-visible absorption spectra showing the reduction of a mixed textile dye from water ($[dye] = 0.10 \text{ g/L}$; Zr-BTC amount = 0.010 g/L ; Solution pH = 6.2).

Effect of Initial Dye Concentration on Rate Adsorption of Mixed Textile Dye by Zr-BTC

The rate of adsorption of the mixed textile dye (MTD) with time from water by Zr-BTC was examined using the pseudo-first-order adsorption and pseudo-second-order adsorption reaction rate equations. Figure 98 shows the pseudo-first-order adsorption reaction rate of MTD by Zr-BTC. The values of R^2 below 9.5 indicate the adsorption rate of MTD by Zr-BTC does not follow the pseudo-first-order adsorption. A low decreasing experimental q_e trend of 86.8168, 26.3482, 16.7886 and 10.06942 with increasing dye concentration was observed relative to computed values.

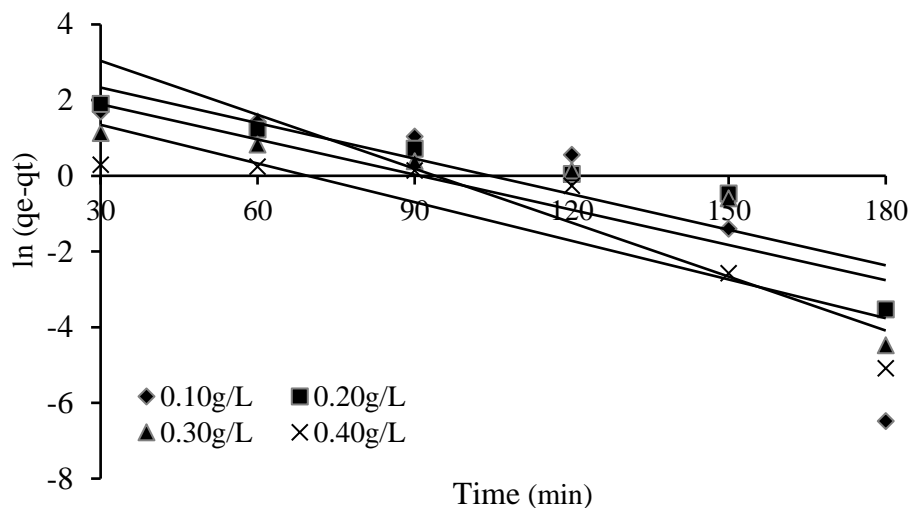


Figure 108: Pseudo-first-order graph for the removal of MTD by Zr-BTC (Zr-BTC loading = 0.1g/L, Solution pH = 8)

Figure 109 shows the pseudo-second-order adsorption reaction rate of MTD by Zr-BTC. The values R^2 were above 9.5 which is an indication that the adsorption rate of MTD by Zr-BTC follows the pseudo-second-order adsorption. Close experimental q_e values compared with computed values were observed for each MTD concentration.

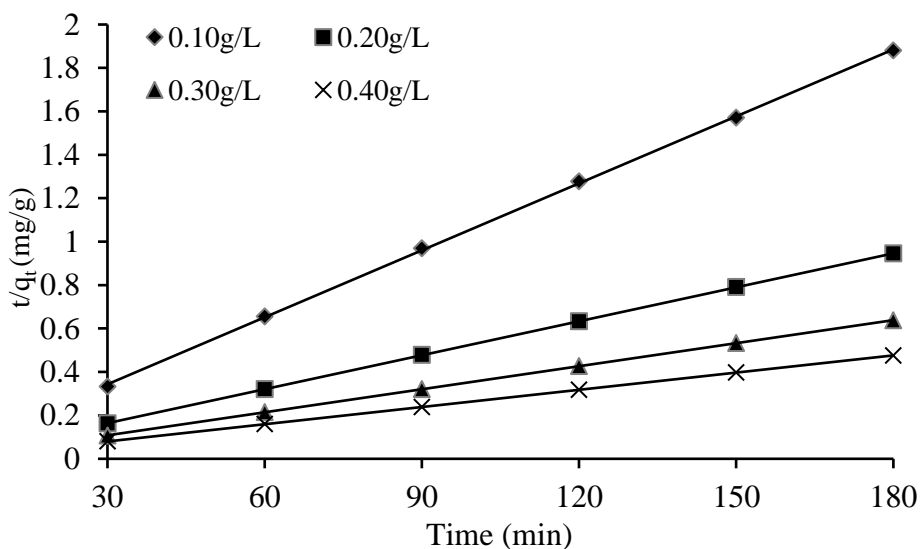


Figure 109: Pseudo-second-order graph for the removal of MTD by Zr-BTC (Zr-BTC loading = 0.1g/L, Solution pH = 8)

Table 30 shows the R^2 values, the K values, the experimental q_e value as well as the computed q_{ecal} values for the pseudo-first-order and the pseudo-second-order rate of adsorption.

Table 30: The Parameters for Pseudo-first-order and Pseudo-second-order Adsorption Mixed Textile Dye (MTD) by Zr-BTC

Pseudo Order	First	K_1 (min^{-1})	R^2	q_e (mg/g)	q_{ecal} (mg/g)
0.1g/L MTD		0.0420	0.8979	57.7487	99.5998
0.2g/L MTD		0.0307	0.8806	21.7954	190.3658
0.3g/L MTD		0.0221	0.8118	9.0585	281.98880
0.4g/L MTD		0.0096	0.8573	3.0423	384.6154
Pseudo Order	Second	K_2 (min^{-1})	R^2	q_e (mg/g)	q_{ecal} (mg/g)
0.1 g/L MTD		0.0026	0.9999	102.0408	99.5998
0.2 g/L MTD		0.0094	1.0000	142.8511	190.3658
0.3 g/L MTD		0.0102	1.0000	285.7143	281.9880
0.4 g/L MTD		0.0028	1.0000	384.6154	378.089

Source: Experimental data (2022)

The adsorption capacity of Zr-BTC was further investigated using the Langmuir-Hinshelwood and the Freundlich model. As shown in Figure 110, the Langmuir adsorption model favoured the pseudo-second-order (PSO) adsorption rate although with an extremely low R^2 value of 0.064. The pseudo-first-order (PFO) adsorption rate did not fit the Langmuir adsorption model although with a high R^2 value of 0.9212.

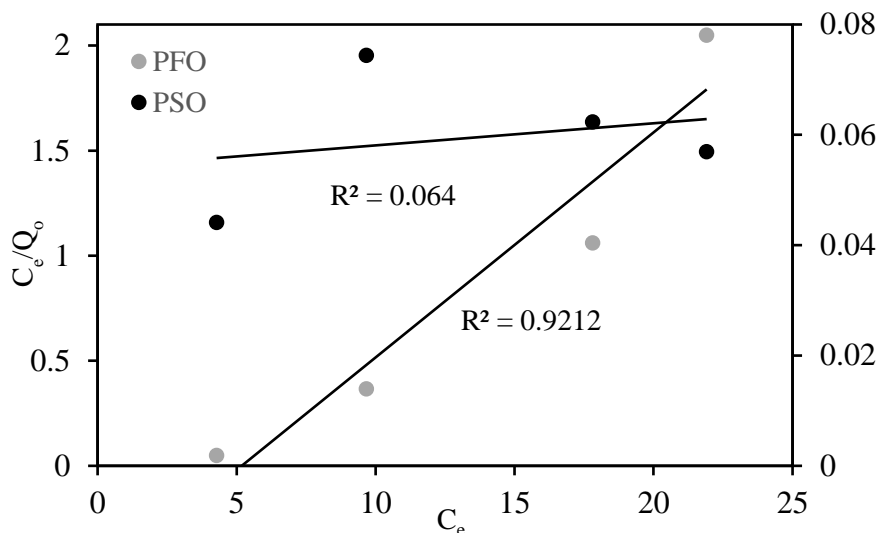


Figure 110: The Langmuir-Hinshelwood isotherm for the removal of MTD by Zr-BTC

Table 31 lists the parameters for the Langmuir isotherms. The adsorption isotherm is favourable for the Langmuir model when $0 < R_L < 1$, unfavourable when $R_L > 1$ and irreversible when $R_L = 0$ (Musah et al., 2022; Prasath, Muthirulan, & Kannan, 2014). A favourable isotherm was observed for pseudo-second-order adsorption with an R_L value of 0.9971. A favourable isotherm was observed for the pseudo-first-order adsorption with an R_L value of 1.0836.

Table 31: The Parameters from Langmuir Isotherms for Mixed Textile Dye (MTD)

MTD/Zr-BTC	R^2	Q_0	K_L	R_L
Pseudo-first-order	0.9212	9.3370	-0.1929	1.0836
Pseudo-second-order	0.0640	2500.000	0.0073	0.9971

Source: Experimental data (2022)

High R^2 values of 0.9623 and 0.9492 were observed for the pseudo-first-order adsorption and pseudo-second-order adsorption from the Freundlich adsorption isotherm in Figure 111. The pseudo-first-order adsorption however does not fit the Freundlich model.

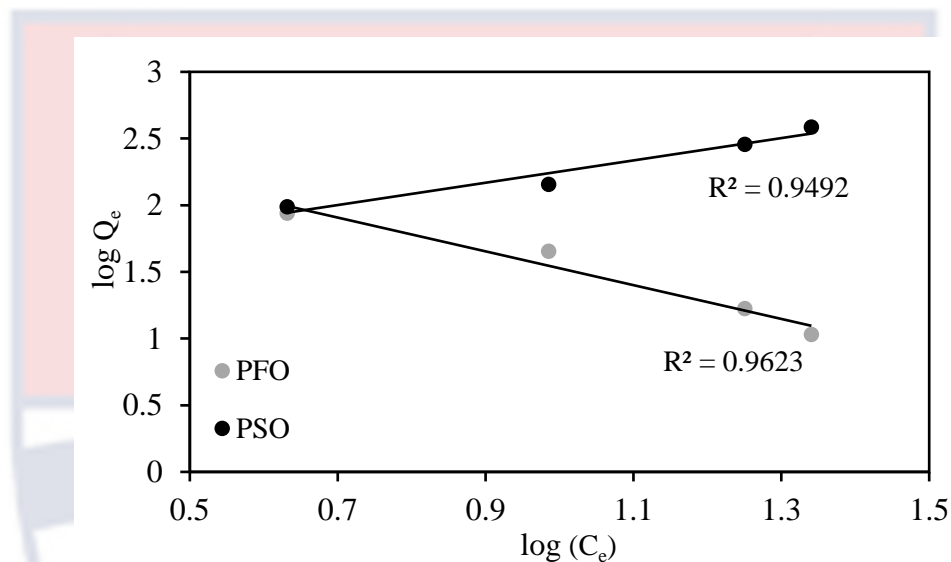


Figure 111: The Freundlich isotherm for the removal of MTD by Zr-BTC

Table 32 illustrates the parameters for the Freundlich isotherms. The adsorption isotherm is termed favourable for the Freundlich model when n has larger values (smaller $1/n$ value) and unfavourable when n has a smaller value (larger $1/n$ value) for $1 < n < 10$ (Anah, & Astrini, 2018; Ramadoss & Subramaniam, 2019). A favourable n value of 1.947 was observed for pseudo-second-order adsorption relative to the n value of -0.7893 for the pseudo-first-order adsorption rate which did not fit the model.

Table 32: The Parameters from Freundlich Isotherms for Mixed Textile Dye (MTD)

MTD/Zr-BTC	R^2	K_f	n	1/n
Pseudo-first-order	0.9623	16.3463	-0.7893	-1.2674
Pseudo-second-order	0.9492	4.1173	1.1947	0.8370

Source: Experimental data (2022)

Chapter Summary

The characterization Results from Fourier transform infrared (FTIR) analysis, X-ray diffraction (XRD) analysis, Scanning electron microscope and energy-dispersive X-ray spectroscopy (SEM-EDS) analysis, Single-crystal X-ray diffraction analysis and Thermogravimetric analysis on the synthesized metal-organic frameworks (MOFs) have been discussed. A discussion on the results of the photoactivity of the synthesized MOFs on the removal of coloured organic compounds as pollutants in water has been made. The kinetic and isotherm study on adsorption activity as well as intermediates obtained during the pollutant transformation activity was also discussed.

CHAPTER FIVE

SUMMARY, CONCLUSIONS AND RECOMMENDATIONS

Overview

This chapter is the conclusions of the research findings that have been provided. It deals with the summary of the entire work. Conclusions and relevant recommendations are also provided.

Summary

The solvothermal synthetic process was used to synthesize six metal-organic frameworks (MOFs) which included Zr-BTC, Zr-5abdc, Ce-BTC, Ce-5abdc, Cu-BTC and Cu-5abdc. Zirconium, cerium and copper were used as the metals while 5-amino benzene -1, 3 – dicarboxylic acid and Benzene-1, 3, 5- tricarboxylic acid were used as organic linkers. Different parameters relating to temperature and time with different solvents were used for the synthesis. The Zr-BTC, Zr-5abdc, Ce-BTC, Ce-5abdc, Cu-BTC and Cu-5abdc were characterized by Fourier transform infrared (FTIR), The X-ray diffraction (XRD), Scanning electron microscope-energy dispersive X-ray (SEM-EDX), Single crystal and Thermogravimetric analysis to determine whether expected metal-organic frameworks were formed.

Fourier transform infrared (FTIR) analysis done on Zr-BTC, Zr-5abdc, Ce-BTC, Ce-5abdc, Cu-BTC and Cu-5abdc revealed the various functional groups present and types of bonds formed between the metals and the linkers. The evidence of C=O and COH vibrational band in the linkers as well as the COO⁻ in all the synthesized metal-organic frameworks confirm the presence of the carboxylic acid groups in all the compounds. The presence of COO⁻

symmetric and asymmetric bands in Zr-BTC, Zr-5abdc, Ce-BTC, Ce-5abdc, Cu-BTC and Cu-5abdc indicates the deprotonation of the organic linkers for possible bond formation with the various metals. The bands from 673 cm^{-1} to 428 cm^{-1} revealed the presence of bonds between copper, cerium, zirconium and oxygen or nitrogen in the organic linkers.

The X-ray diffraction (XRD) analysis results for various synthesized metal-organic frameworks were detected to be crystalline except Zr-5abdc which was amorphous. Scanning electron microscope-energy-dispersive X-ray (SEM-EDX) analysis was used to study the morphologies of Zr-BTC, Zr-5abdc, Ce-BTC, Ce-5abdc, Cu-BTC and Cu-5abdc and confirmed the presence of the various element found in the frameworks. The SEM image shows different morphologies including irregular rockies, irregular flakes, rod-like pyramids, rod-like rectangular prisms, flowering and octahedral cubic crystals for Zr-BTC, Zr-5abdc, Ce-BTC, Ce-5abdc, Cu-BTC and Cu-5abdc. Single crystal analysis of Cu-BTC confirmed its geometry and the formation of bonds between the organic linkers and the metals. The thermogravimetric analysis of Zr-BTC, Zr-5abdc, Ce-BTC, Ce-5abdc, Cu-BTC and Cu-5abdc revealed that the complexes could withstand heat above $300\text{ }^{\circ}\text{C}$ and therefore thermally stable. The Zr-BTC decomposed around $600\text{ }^{\circ}\text{C}$ while Zr-5abdc decomposed between $350\text{ }^{\circ}\text{C}$ to $650\text{ }^{\circ}\text{C}$. The decomposition of Ce-BTC was observed around $600\text{ }^{\circ}\text{C}$ and that of Ce-5abdc around $650\text{ }^{\circ}\text{C}$. The Cu-BTC decomposed around $400\text{ }^{\circ}\text{C}$ and Cu-5abdc around $300\text{ }^{\circ}\text{C}$.

The photocatalytic activity of Zr-BTC, Zr-5abdc, Ce-BTC, Ce-5abdc, Cu-BTC and Cu-5abdc was investigated on Lissamine green SF (LGSF), Tetraethylrhodamine (TeRh), and Remezol Brilliant Violet 5R (RBV5R) using

solar and white light as the source of the irradiation light. A higher percentage removal of the LGSF, TeRh and RBV5R under solar light was observed as compared to that of relative to white light for all MOFs after the 180 min of irradiation. Percentage removal of LGSF removal between 70% and 95% under solar light and LGSF removal between 45 % and 75% in white light was observed. A TeRh removal between 80% and 96% in solar light and between 50 % and 79% in white light was achieved while RBV5R removal between 80% and 93% in solar light and between 50 % and 74% in white light was observed.

A high LGSF, TeRh and RBV5R removal was observed for all coloured pollutants when the amount of the MOFs was increased from 0.005 g/L to 0.010g/L. A slow removal of the LGSF, TeRh and RBV5R was however observed when the amount of the various MOFs was further increased from 0.015 g/L to 0.020 g/L. The percentage of LGSF removal between 30 % and 63% was observed for 0.005g/L of MOF between 70 % and 95 % for 0.010 g/L of MOF, between 85 % and 96 % for 0.015g/L of MOF and between 93 % and 96% for 0.020g/L of MOF. TeRh removal between 40 % and 65% were observed for 0.005g/L of MOF, between 78 % and 96 % for 0.010 g/L of MOF, between 84 % and 97 % for 0.015g/L of MOF t and between 91 % and 97% for 0.020g/L of MOF. RBV5R removal between 40% and 64% were also observed for 0.005g/L of MOF, between 76 % and 94 % for 0.010 g/L of MOF, between 85 % and 96 % for 0.015g/L of MOF and between 85 % and 96% for 0.020g/L of MOF.

A general decrease in the removal of LGSF, TeRh and RBV5R was observed with increasing concentrations of the pollutants. A percentage LGSF

removal between 79 % and 95% was observed for 0.10g/L of LGSF concentration, between 71 % and 93 % for 0.2 g/L of LGSF concentration, between 39 % and 52 % for 0.30 g/L of LGSF concentration and between 30 % and 45 % for 0.40 g/L of LGSF concentration. The percentage removal of TeRh between 83 % and 94% was observed for 0.10g/L TeRh concentration, between 77 % and 93 % for 0.2 g/L TeRh concentration, between 40 % and 64 % for 0.30 g/L TeRh concentration and between 30 % and 52 % for 0.40 g/L TeRh concentration. The percentage removal of RBV5R between 83 % and 96% was observed for 0.10g/L RBV5R concentration, between 73 % and 94 % for 0.2 g/L RBV5R concentration, between 40 % and 61 % for 0.30 g/L RBV5R concentration and between 35 % and 51 % for 0.40 g/L RBV5R concentration.

The removal of LGSF and RBV5R by Zr-BTC, Zr-5abdc, Ce-BTC, Ce-5abdc, Cu-BTC and Cu-5abdc was observed to generally decrease with increasing pH value from pH4 to pH10 after the 180 min photocatalysis. The removal of TeRh by Zr-BTC, Zr-5abdc, Ce-BTC, Ce-5abdc, Cu-BTC and Cu-5abdc was however seen to generally increase with increasing pH value from pH4 to pH10 after 180 min photocatalysis. The optimum pH determined for efficient removal of LGSF and RBV5R was determined to be pH6 and that of TeRh was pH8.

The rate of removal of LGSF, TeRh, and RBV5R from water with time by the Zr-BTC, Zr-5abdc, Ce-BTC, Ce-5abdc, Cu-BTC and Cu-5abdc was evaluated using the pseudo-first-order adsorption and pseudo-second-order adsorption reaction rate. Low R^2 values were observed for LGSF, TeRh and RBV5R by Zr-BTC, Zr-5abdc, Ce-BTC, Ce-5abdc, Cu-BTC and Cu-5abdc for

pseudo-first-order adsorption while high R^2 values were observed for the pseudo-second-order adsorption rate which is an indication that the removal rate of LGSF, TeRh and RBV5R by Zr-BTC, Zr-5abdc, Ce-BTC, Ce-5abdc, Cu-BTC and Cu-5abdc follows the pseudo-second-order adsorption. The adsorption rates of LGSF, TeRh and RBV5R by Zr-BTC, Zr-5abdc, Ce-BTC, Ce-5abdc, Cu-BTC and Cu-5abdc were further analyzed using the Langmuir-Hinshelwood and the Freundlich adsorption models. The Langmuir adsorption model and Freundlich adsorption isotherm favoured the pseudo-second-order adsorption rate.

Various intermediates were detected in the transformation of LGSF, TeRh, and RBV5R to remove these pollutants from water after the 180 min irradiation with light using the GC/MS. LGSF with a molar mass of 749.893g/mol during the transformation disintegrated into other fragment compounds of varying masses ranging from m/z 530 to m/z 211. TeRh with a molar mass of 479.02 g/mol TeRh also produced fragments with masses ranging from 390 m/z to 116 m/z and RBV5R with a molar mass of 734.58 g/mol had fragments with masses ranging from 608 m/z to 195 m/z.

The Zr-BTC which was determined to exhibit the highest adsorption capacity was used to investigate its ability to remove the industrial textile dye. It was observed that Zr-BTC could effectively remove the textile dye from water with the maximum dye percentage removal of 86.4% at a concentration of 0.10g/L. The rate of removal of the mixed textile dye (MTD) with time from water by Zr-BTC was evaluated using the pseudo-first-order adsorption and pseudo-second-order adsorption reaction rate equations. The R^2 values of below 9.5 were established for the pseudo-first-order adsorption which is an

indication that the rate of adsorption of MTD by Zr-BTC does not follow the pseudo-first-order adsorption. The R^2 values of above 9.5 were established for the pseudo-second-order adsorption rate which is an indication that the rate of adsorption of MTD by Zr-BTC satisfied the pseudo-second-order adsorption rate. The adsorption capacity of Zr-BTC was further evaluated using the Langmuir-Hinshelwood and the Freundlich model. The Langmuir adsorption model and Freundlich adsorption isotherm favoured the pseudo-second-order adsorption rate.

Conclusion

The solvothermal synthetic process was successfully used to synthesize Zr-BTC, Zr-5abdc, Ce-BTC, Ce-5abdc, Cu-BTC and Cu-5abdc MOFs. The results obtained from the various analytical techniques confirm the formation of metal-organic frameworks using the solvothermal technique. The Zr-BTC, Zr-5abdc, Ce-BTC, Ce-5abdc, Cu-BTC and Cu-5abdc were proven to be photoactive in the transformation of Lissamine green SF (LGSF), Tetraethylrhodamine (TeRh), and Remezol Brilliant Violet 5R (RBV5R) into less toxic compounds under solar and white light. The results from the solar light irradiation revealed a higher percentage removal of the LGSF, TeRh and RBV5R as compared to the white light. The removal efficiency of LGSF, TeRh and RBV5R by Zr-BTC, Zr-5abdc, Ce-BTC, Ce-5abdc, Cu-BTC and Cu-5abdc were shown to be dependent on adsorption parameters such as initial dye concentration, amount of MOF and the pH. The adsorption rate of LGSF, TeRh and RBV5R were observed to follow the pseudo-second-order adsorption. Further evaluation of the adsorption rate using the Langmuir

adsorption and Freundlich adsorption isotherm also revealed that the adsorption rate favoured the pseudo-second-order. The intermediate compounds formed during the transformation of LGSF, TeRh and RBV5R using the GC/MS into smaller fragments of compounds is an indication of the ability of Zr-BTC, Zr-5abdc, Ce-BTC, Ce-5abdc, Cu-BTC and Cu-5abdc to breakdown LGSF, TeRh and RBV5R. The results of Zr-BTC MOF provided the most promising tendency to effectively remove the mixed textile dye with the rate of adsorption following the pseudo-second-order adsorption at the optimum reaction condition of MOF amount, pollutant concentration and pH of the medium.

Recommendations

Upon completion of the present study, a few recommendations were drawn for future studies.

1. The performance of the photoactive metal-organic framework should be examined in the removal of inorganic pollutants such as magnesium and other persistent organic pollutants such as pharmaceuticals. This will help assess their efficiency as catalysts in degrading a wide range of pollutants.
2. The performance of the photoactive metal-organic framework should be examined in the conversion of pollutants into useful products. The conversion of pollutants to useful products will help reduce environmental pollution and add value.

3. Other photoactive metal-organic frameworks should be researched into using different metals and organic ligands for a higher photoactivity with the wide variety of metals and linkers available.



REFERENCES

- Aarti, A., Bhadauria, S., Nanoti, A., Dasgupta, S., Divekar, S., Gupta, P., & Chauhan, R. (2016). [Cu₃(BTC)₂]-polyethyleneimine: an efficient MOF composite for effective CO₂ separation. *Rsc Advances*, 6(95), 93003-93009.
- Abbasi, A. R., Karimi, M., & Daasbjerg, K. (2017). Efficient removal of crystal violet and methylene blue from wastewater by ultrasound nanoparticles Cu-MOF in comparison with mechanochemical synthesis method. *Ultrasonics Sonochemistry*, 37, 182-191.
- Abdelmoaty, A. S., El-Beih, A. A., & Hanna, A. A. (2022). Synthesis, characterization and antimicrobial activity of copper-metal organic framework (Cu-MOF) and its modification by melamine. *Journal of Inorganic and Organometallic Polymers and Materials*, 32(5), 1778-1785.
- Abdi, J., Vossoughi, M., Mahmoodi, N. M., & Alemzadeh, I. (2017). Synthesis of metal-organic framework hybrid nanocomposites based on GO and CNT with high adsorption capacity for dye removal. *Chemical Engineering Journal*, 326, 1145-1158.
- Abdollahi, N., Razavi, S. A. A., Morsali, A., & Hu, M. L. (2020). High capacity Hg (II) and Pb (II) removal using MOF-based nanocomposite: Cooperative effects of pore functionalization and surface-charge modulation. *Journal of hazardous materials*, 387, 121667.
- Abdullah, A. A. K. (2016). Photocatalytic Degradation of Rhodamine B Dye in Wastewater Using Gelatin/CuS/PVA Nanocomposites under Solar

Light Irradiation. *Journal of Biomaterials and Nanobiotechnology*, 8(01), 66-82.

Adegoke, K. A., & Maxakato, N. W. (2021). Porous metal-organic framework (MOF)-based and MOF-derived electrocatalytic materials for energy conversion. *Materials Today Energy*, 21, 100816.

Adhikari, S., Chandra, K. S., Kim, D. H., Madras, G., & Sarkar, D. (2018). Understanding the morphological effects of WO₃ photocatalysts for the degradation of organic pollutants. *Advanced Powder Technology*, 29(7), 1591-1600.

Affat, S. S. (2021). Classifications, advantages, disadvantages, toxicity effects of natural and synthetic dyes: a review. *University of Thi-Qar Journal of Science*, 8(1), 130-135.

Aghajanoloo, M., Rashidi, A. M., & Moosavian, M. A. (2014). Synthesis of zinc-organic frameworks nano adsorbent and their application for methane adsorption. *Journal of Chemical Engineering & Process Technology*, 5(5), 1.

Aghajanzadeh, M., Zamani, M., Molavi, H., Khieri Manjili, H., Danafar, H., & Shojaei, A. (2018). Preparation of metal-organic frameworks UiO-66 for adsorptive removal of methotrexate from aqueous solution. *Journal of Inorganic and Organometallic Polymers and Materials*, 28(1), 177-186.

Ahmadijokani, F., Molavi, H., Rezakazemi, M., Tajahmadi, S., Bahi, A., Ko, F., Aminabhavi, T. M., Li, J., & Arjmand, M. (2022). UiO-66 metal-organic frameworks in water treatment: A critical review. *Progress in Materials Science*, 125, 100904.

- Ahmed, I., & Jung, S. H. (2017). Applications of metal-organic frameworks in adsorption/separation processes via hydrogen bonding interactions. *Chemical Engineering Journal*, 310, 197-215.
- Ahmed, M. S., Begum, H., & Kim, Y. B. (2020). Iron nanoparticles implanted metal-organic-frameworks based Fe–N–C catalysts for high-performance oxygen reduction reaction. *Journal of Power Sources*, 451, 227733.
- Al Cheikh, J., Villagra, A., Ranjbari, A., Pradon, A., Antuch, M., Dragoe, D., & Assaud, L. (2019). Engineering a cobalt clathrochelate/ glassy carbon interface for the hydrogen evolution reaction. *Applied Catalysis B: Environmental*, 250, 292-300.
- Al Hageh, C., Al Assaad, M., El Masri, Z., Samaan, N., El-Sibai, M., Khalil, C., & Khnayzer, R. S. (2018). A long-lived cuprous bis-phenanthroline complex for the photodynamic therapy of cancer. *Dalton Transactions*, 47(14), 4959-4967.
- Alammar, T., Hlova, I. Z., Gupta, S., Balema, V., Pecharsky, V. K., & Mudring, A. V. (2018). Luminescence properties of mechanochemically synthesized lanthanide containing MIL-78 MOFs. *Dalton Transactions*, 47(22), 7594-7601.
- Al-Assy, W. H., Mahmoud, S. A., Husein, D. Z., & Mostafa, M. M. (2018). Synthesis, characterization and the role of ionic radii on the mechanistic of solvothermal for polyazine PtIV complexes: Reduction PtIV to PtII, DFT, x-ray single crystal and anticancer studies. *Beni-Suef University journal of basic and applied sciences*, 7(4), 575-586.

Alfè, M., Gargiulo, V., Lisi, L., & Di Capua, R. (2014). Synthesis and characterization of conductive copper-based metal-organic framework/graphene-like composites. *Materials Chemistry and Physics*, *147*(3), 744-750.

Alharbi, O. M., Khattab, R. A., & Ali, I. (2018). Health and environmental effects of persistent organic pollutants. *Journal of Molecular Liquids*, *263*, 442-453.

Al-Janabi, N., Deng, H., Borges, J., Liu, X., Garforth, A., Siperstein, F. R., & Fan, X. (2016). A facile post-synthetic modification method to improve hydrothermal stability and CO₂ selectivity of CuBTC metal-organic framework. *Industrial & Engineering Chemistry Research*, *55*(29), 7941-7949.

AlKaabi, K., Wade, C. R., & Dincă, M. (2016). Transparent-to-dark electrochromic behavior in naphthalene-diimide-based mesoporous MOF-74 analogs. *Chem*, *1*(2), 264-272.

Alkaykh, S., Mbarek, A., & Ali-Shattle, E. E. (2020). Photocatalytic degradation of methylene blue dye in aqueous solution by MnTiO₃ nanoparticles under sunlight irradiation. *Heliyon*, *6*(4).

Allendorf, M. D., Stavila, V., Witman, M., Brozek, C. K., & Hendon, C. H. (2021). What lies beneath a metal-organic framework crystal structure? New design principles from unexpected behaviors. *Journal of the American Chemical Society*, *143*(18), 6705-6723.

- Almáši, M., Zele nák, V.; Opanasenko, M.; Císarová, I. (2015). Ce (III) and Lu (III) metal–organic frameworks with Lewis acid metal sites: Preparation, sorption properties and catalytic activity in Knoevenagel condensation. *Catal. Today*, 243, 184-194.
- Almáši, M., Zeleňák, V., Kuchár, J., Bourrelly, S., & Llewellyn, P. L. (2016). New members of MOF-76 family containing Ho (III) and Tm (III) ions: Characterization, stability and gas adsorption properties. *Colloids and Surfaces A: Physicochemical and Engineering Aspects*, 496, 114-124.
- Al-Obaidy, G. S., Ibraheem, K. R., & Mesher, M. F. (2020). Metal complexes derived from dithiocarbamate ligand: formation, spectral characterization and biological activity. *Systematic Reviews in Pharmacy*, 11(6), 360-368.
- Al-Tohamy, R., Ali, S. S., Li, F., Okasha, K. M., Mahmoud, Y. A. G., Elsamahy, T., Jiao, H., Fu, Y., & Sun, J. (2022). A critical review on the treatment of dye-containing wastewater: Ecotoxicological and health concerns of textile dyes and possible remediation approaches for environmental safety. *Ecotoxicology and Environmental Safety*, 231, 113160.
- An, K., Ren, H., Yang, D., Zhao, Z., Gao, Y., Chen, Y., Tan, J., Wang, W., & Jiang, Z. (2021). Nitrogenase-inspired bimetallic metal organic frameworks for visible-light-driven nitrogen fixation. *Applied Catalysis B: Environmental*, 292, 120167.

Anah, L., & Astrini, N. (2018). Isotherm adsorption studies of Ni (II) ion removal from aqueous solutions by modified carboxymethyl cellulose hydrogel. In *IOP Conference Series: Earth and Environmental Science* (160) 012017.

Anandan, K., Rajesh, K., & Rajendran, V. (2017). Enhanced optical properties of spherical zirconia (ZrO₂) nanoparticles synthesized via the facile various solvents mediated solvothermal process. *Journal of Materials Science: Materials in Electronics*, 28(22), 17321-17330.

Andriamitantsoa, R. S., Dong, W., Gao, H., & Wang, G. (2017). Porous organic–inorganic hybrid xerogels for stearic acid shape-stabilized phase change materials. *New Journal of Chemistry*, 41(4), 1790-1797.

Anish Khan, A., Abu-Zied, B. M., Hussein, M., A., Asiri1, A.M., & Azam, M. (2019). Metal-Organic Framework Composites Volume I Materials Research Forum LLC Millersville, PA 17551, USA. Volume 53.1-285.

Ardila-Suárez, C., Alem, H., Baldovino-Medrano, V. G., & Ramírez Caballero, G. E. (2020). Synthesis of ordered microporous/macroporous MOF-808 through modulator-induced defect-formation, and surfactant self-assembly strategies. *Physical Chemistry Chemical Physics*, 22(22), 12591-12604.

Ardila-Suárez, C., Díaz-Lasprilla, A. M., Díaz-Vaca, L. A., Balbuena, P. B., Baldovino-Medrano, V. G., & Ramírez-Caballero, G. E. (2019). Synthesis, characterization, and post-synthetic modification of a micro/mesoporous zirconium–tricarboxylate metal–organic framework: Towards the addition of acid active sites. *CrystEngComm*, 21(19), 3014-3030.

- Arroussi, A., Gaffour, H., Mokhtari, M., & Boukli-Hacene, L. (2020). Investigating metal-organic framework based on nickel (II) and benzene 1, 3, 5-tri carboxylic acid (H3BTC) as a new photocatalyst for degradation of 4-nitrophenol. *International Journal of Environmental Studies*, 77(1), 137-151.
- Arumugam, J., Raj, A. D., Irudayaraj, A. A., & Thambidurai, M. (2018). Solvothermal synthesis of Bi₂S₃ nanoparticles and nanorods towards solar cell application. *Materials Letters*, 220, 28-31.
- Aslibeiki, B., Kameli, P., Ehsani, M. H., Salamati, H., Muscas, G., Agostinelli, E., Foglietti, V., Casciardi, S., & Peddis, D. (2016). Solvothermal synthesis of MnFe₂O₄ nanoparticles: the role of polymer coating on morphology and magnetic properties. *Journal of Magnetism and Magnetic Materials*, 399, 236-244.
- Assaad, N., Sabeih, G., & Hmadeh, M. (2020). Defect control in Zr-based metal-organic framework nanoparticles for arsenic removal from water. *ACS Applied Nano Materials*, 3(9), 8997-9008.
- Assat, G., & Manthiram, A. (2015). Rapid microwave-assisted solvothermal synthesis of non-olivine Cmc₂m polymorphs of LiMPO₄ (M= Mn, Fe, Co, and Ni) at low temperature and pressure. *Inorganic Chemistry*, 54(20), 10015-10022.
- Atta-Eyison, A. A., Anukwah, G. D., & Zugle, R. (2021). Photocatalysis using zinc oxide-zinc phthalocyanine composite for effective mineralization of organic pollutants. *Catalysis Communications*, 160, 106357.
- Atzori, C., Lomachenko, K. A., Øien-Ødegaard, S., Lamberti, C., Stock, N., Barolo, C., & Bonino, F. (2018). Disclosing the properties of a new Ce

(III)-Based MOF: $\text{Ce}_2(\text{NDC})_3(\text{DMF})_2$. *Crystal Growth & Design*, 19(2), 787-796.

Autie-Castro, G., Autie, M. A., Rodríguez-Castellón, E., Aguirre, C., & Reguera, E. (2015). Cu-BTC and Fe-BTC metal-organic frameworks: Role of the materials structural features on their performance for volatile hydrocarbons separation. *Colloids and Surfaces A: Physicochemical and Engineering Aspects*, 481, 351-357.

Avallone, B., Arena, C., Simoniello, P., Di Lorenzo, M., Vitale, E., Capriello, T., Ferrandino, I., Raggio, A., Sasso, M., Napolitano, G., De Bonis, S., Fogliano, C., Agnisola, C., & Motta, C. M. (2022). Comparative Toxicity of Vegan Red, E124, and E120 Food Dyes on Three Rapidly Proliferating Model Systems. *Environments*, 9(7), 89.

Bagherzadeh, E., Zebarjad, S. M., & Hosseini, H. R. M. (2018). Morphology Modification of the Iron Fumarate MIL-88A Metal–Organic Framework Using Formic Acid and Acetic Acid as Modulators. *European Journal of Inorganic Chemistry*, 2018(18), 1909-1915.

Bagherzadeh, E., Zebarjad, S. M., Hosseini, H. R. M., & Chagnon, P. (2019). Preparation, optimization and evolution of the kinetic mechanism of an Fe-MIL-88A metal–organic framework. *CrystEngComm*, 21(3), 544-553.

Bagherzadeh, E., Zebarjad, S. M., Hosseini, H. R. M., & Khodaei, A. (2022). Interplay between morphology and band gap energy in Fe-MIL-88A prepared via a high temperature surfactant-assisted solvothermal method. *Materials Chemistry and Physics*, 277, 125536.

Bahramzadeh, S., Abdizadeh, H., & Golobostanfard, M. R. (2015).

Controlling the morphology and properties of solvothermal synthesized Cu₂ZnSnS₄ nanoparticles by solvent type. *Journal of Alloys and Compounds*, 642, 124-130.

Baloch, H. A., Siddiqui, M. T. H., Nizamuddin, S., Riaz, S., Haris, M.,

Mubarak, N. M., Griffin, G., J., & Srinivasan, M. P. (2021). Effect of solvent on hydro-solvothermal co liquefaction of sugarcane bagasse and polyethylene for bio-oil production in ethanol–water system. *Process Safety and Environmental Protection*, 148, 1060-1069.

Balto, K. P., Gembicky, M., Rheingold, A. L., & Figueroa, J. S. (2021).

Crystalline Hydrogen-Bonding Networks and Mixed-Metal Framework Materials Enabled by an Electronically Differentiated Heteroditopic Isocyanide/Carboxylate Linker Group. *Inorganic Chemistry*, 60(16), 12545-12554.

Bao, S., Cai, X., Shi, Y., & Pang, M. (2017). Effect of modulators on size and

shape-controlled growth of highly uniform In–NDC–MOF particles. *CrystEngComm*, 19(14), 1875-1878.

Batten, S. R., & Champness, N. R. (2017). Coordination polymers and metal–

organic frameworks: materials by design. *Philosophical Transactions of the Royal Society A: Mathematical, Physical and Engineering Sciences*, 375(2084), 20160032.

Batten, S. R., Champness, N. R., Chen, X. M., Garcia-Martinez, J., Kitagawa,

S., Öhrström, L., O'Keeffe, M., Myunghyun Paik Suh, M. P., & Reedijk, J. (2012). Coordination polymers, metal–organic frameworks

and the need for terminology guidelines. *CrystEngComm*, 14(9), 3001-3004.

Berradi, M., Hsissou, R., Khudhair, M., Assouag, M., Cherkaoui, O., El Bachiri, A., & El Harfi, A. (2019). Textile finishing dyes and their impact on aquatic environs. *Heliyon*, 5(11), e02711.

Bhattacharya, S., Ayass, W. W., Taffa, D. H., Nisar, T., Balster, T., Hartwig, A., Wagner, V., Wark, M., & Kortz, U. (2020). Polyoxopalladate-loaded metal-organic framework (POP@ MOF): Synthesis and heterogeneous catalysis. *Inorganic Chemistry*, 59(15), 10512-10521.

Bhushan, R., Kumar, P., & Thakur, A. K. (2020). Catalyst-free solvothermal synthesis of ultrapure elemental N-and B-doped graphene for energy storage application. *Solid State Ionics*, 353, 115371.

Bincy, J. (2017). Temperature dependent solvothermal synthesis of Cu-Sb-S nanoparticles with tunable structural and optical properties. *Materials Research Bulletin*, 95, 267-276.

Bloch, W. M., Champness, N. R., & Doonan, C. J. (2015). X-ray Crystallography in Open-Framework Materials. *Angewandte Chemie International Edition*, 54(44), 12860-12867.

Bøjesen, E. D., & Iversen, B. B. (2016). The chemistry of nucleation. *CrystEngComm*, 18(43), 8332-8353.

Bon, V., Senkovska, I., Evans, J. D., Wöllner, M., Hölzel, M., & Kaskel, S. (2019). Insights into the water adsorption mechanism in the chemically stable zirconium-based MOF DUT-67—a prospective material for adsorption-driven heat transformations. *Journal of Materials Chemistry A*, 7(20), 12681-12690.

Bondesgaard, M., Becker, J., Xavier, J., Hellstern, H., Mamakhel, A., & Iversen, B. B. (2016). Guide to by-products formed in organic solvents under solvothermal conditions. *The Journal of Supercritical Fluids*, *113*, 166-197.

Bouider, B., Haffad, S., Bouakaz, B. S., Berd, M., Ouhnia, S., & Habi, A. (2023). MOF-5/Graphene Oxide Composite Photocatalyst for Enhanced Photocatalytic Activity of Methylene Blue Degradation Under Solar Light. *Journal of Inorganic and Organometallic Polymers and Materials*, 1-11.

Bour, J. R., Wright, A. M., He, X., & Dincă, M. (2020). Bioinspired chemistry at MOF secondary building units. *Chemical Science*, *11*(7), 1728-1737.

Brandi, F., Antonietti, M., & Al-Naji, M. (2021). Controlled lignosulfonate depolymerization via solvothermal fragmentation coupled with catalytic hydrogenolysis/hydrogenation in a continuous flow reactor. *Green Chemistry*, *23*(24), 9894-9905.

Broge, N. L. N., Søndergaard-Pedersen, F., Roelsgaard, M., Hassing-Hansen, X., & Iversen, B. B. (2020). Mapping the redox chemistry of common solvents in solvothermal synthesis through in situ X-ray diffraction. *Nanoscale*, *12*(15), 8511-8518.

Brozek, C. K., & Dincă, M. (2014). Cation exchange at the secondary building units of metal–organic frameworks. *Chemical Society Reviews*, *43*(16), 5456-5467.

Cao, G., Zhu, J., Li, Y., Zhou, Y., Jin, Z., Xu, B., Hai, C., & Zeng, J. (2020). Synthesis of a fine $\text{LiNi}_{0.88}\text{Co}_{0.09}\text{Al}_{0.03}\text{O}_2$ cathode material for

lithium-ion batteries via a solvothermal route and its improved high-temperature cyclic performance. *RSC advances*, 10(17), 9917-9923.

Carreon, M. A., & Venna, S. R. (2020). *Metal-Organic Framework Membranes for Molecular Gas Separations* (Vol. 6). World Scientific. 1-29.

Catala, L., & Mallah, T. (2017). Nanoparticles of Prussian blue analogs and related coordination polymers: From information storage to biomedical applications. *Coordination Chemistry Reviews*, 346, 32-61.

Catto, A. C., Ferrer, M. M., Lopes, O. F., Mastelaro, V. R., Andres, J., Da Silva, L. F., Longo, E., & Avansi Jr, W. (2020). The role of counterions in crystal morphology, surface structure and photocatalytic activity of ZnO crystals grown onto a substrate. *Applied Surface Science*, 529, 147057.

Cermelj, K., Ruengkajorn, K., Buffet, J. C., & O'Hare, D. (2019). Layered double hydroxide nanosheets via solvothermal delamination. *Journal of Energy Chemistry*, 35, 88-94.

Chang, W., Zheng, D., Zhao, C., & Yang, Y. (2019). Photocatalytic activity of MOF-derived Cu₂O/Cu/C/Ag porous composites. *South African Journal of Chemistry*, 72, 10-15.

Chanu, S. B., Raza, M. K., Musib, D., Pal, M., Pal, M., & Roy, M. (2020). Potent Photochemotherapeutic Activity of Iron (III) Complexes on Visible Light-induced Ligand to Metal Charge Transfer. *Chemistry Letters*, 49(6), 724-727.

Chavan, R. B. (2013). Health and environmental hazards of synthetic dyes. *Garment and Fashion Design at the University of Bahir Dar, Bahir Dar, Ethiopia*.

chemeurope.com (2023). Characterization definition. Retrieved from <https://q-more.chem-europe.com/>

Chemical Book Inc. (2017). 5-Aminoisophthalic acid IR1. CAS 99-31-0. Retrieved from https://www.Chemical-book.com/ContactUS_EN.aspx.

Chemicool Chemistry Dictionary (2023). Ligand. Retrieved from <http://www.chemicool.com/elements/ligand.html>.

Chen, B. W., Xu, L., & Mavrikakis, M. (2020). Computational methods in heterogeneous catalysis. *Chemical Reviews*, 121(2), 1007-1048.

Chen, C. X., Xiong, Y. Y., Zhong, X., Lan, P. C., Wei, Z. W., Pan, H., Su, P., Song, Y., Chen, Y., Nafady, A., Sirajuddin, & Ma, S. (2022). Enhancing photocatalytic hydrogen production via the construction of robust multivariate Ti-MOF/COF composites. *Angewandte Chemie International Edition*, 61(3), e202114071.

Chen, D. M., & Zhang, X. J. (2019). A polyoxometalate template metal-organic framework with unusual $\{Cu_8(\mu_4-OH)_6\}_{10+}$ secondary building unit for photocatalytic dye degradation. *Inorganic Chemistry Communications*, 108, 107523.

Chen, G., Zhou, M., Catanach, J., Liaw, T., Fei, L., Deng, S., & Luo, H. (2014). Solvothermal route based in situ carbonization to $Fe_3O_4@C$ as anode material for lithium ion battery. *Nano Energy*, 8, 126-132.

Chen, J., Zhang, M., Zhang, S., Cao, K., Mao, X., Zhang, M., He, L., Dong, X., Shu, J., Dong, H., Zhai, F., Shen, R., Yuan, M., Zhao, X., Wu, G.,

- Chai, Z., & Wang, S. (2022). Metal-Organic Framework@ Metal Oxide Heterostructures Induced by Electron-Beam Radiation. *Angewandte Chemie*, 134(47), e202212532.
- Chen, M. L., Lu, T. H., Long, L. L., Xu, Z., Ding, L., & Cheng, Y. H. (2022). NH₂-Fe-MILs for effective adsorption and Fenton-like degradation of imidacloprid: Removal performance and mechanism investigation. *Environmental Engineering Research*, 27(2).
- Chen, P., He, X., Pang, M., Dong, X., Zhao, S., & Zhang, W. (2020). Iodine capture using Zr-based metal-organic frameworks (Zr-MOFs): adsorption performance and mechanism. *ACS applied materials & interfaces*, 12(18), 20429-20439.
- Chen, Q., Chen, Q. W., Zhuang, C., Tang, P. P., Lin, N., & Wei, L. Q. (2017). Controlled release of drug molecules in metal-organic framework material HKUST-1. *Inorganic Chemistry Communications*, 79, 78-81.
- Chen, Y., Li, P., Modica, J. A., Drout, R. J., & Farha, O. K. (2018). Acid-resistant mesoporous metal-organic framework toward oral insulin delivery: protein encapsulation, protection, and release. *Journal of the American Chemical Society*, 140(17), 5678-5681.
- Chen, Y., Wang, D., Deng, X., & Li, Z. (2017). Metal-organic frameworks (MOFs) for photocatalytic CO₂ reduction. *Catalysis Science & Technology*, 7(21), 4893-4904.
- Chen, Z., Kirlikovali, K. O., Li, P., & Farha, O. K. (2022). Reticular chemistry for highly porous metal-organic frameworks: The chemistry and applications. *Accounts of chemical research*, 55(4), 579-591.

Chen, Z., Li, Z., Chen, J., Tan, H., Wu, J., & Qiu, H. (2022). Selective adsorption of rare earth elements by Zn-BDC MOF/graphene oxide nanocomposites synthesized via in situ interlayer-confined strategy. *Industrial & Engineering Chemistry Research*, 61(4), 1841-1849.

Chevinly, A. S., Mobtaker, H. G., Yousefi, T., Shirani, A. S., & Aghayan, H. (2017). $[\text{Ce}(\text{BTC})(\text{H}_2\text{O})] \cdot \text{DMF}$ metal organic framework as a new adsorbent for removal of neodymium ions. *Inorganica Chimica Acta*, 455, 34-40.

Coates, J. (2000). Interpretation of infrared spectra, a practical approach. *Encyclopedia of analytical chemistry*, 12, 10815-10837.

Corma (2016). Heterogeneous catalysis: understanding for designing, and designing for applications. *Angewandte Chemie International Edition*, 55(21), 6112-6113.

Corma, A., Iglesias, M., Llabrés i Xamena, F. X., & Sánchez, F. (2010). Cu and Au metal-organic frameworks bridge the gap between homogeneous and heterogeneous catalysts for alkene cyclopropanation reactions. *Chemistry—A European Journal*, 16(32), 9789-9795.

Cox, C. S., Slavich, E., Macreadie, L. K., McKemmish, L. K., & Lessio, M. (2023). Understanding the Role of Synthetic Parameters in the Defect Engineering of UiO-66: A Review and Meta-analysis. *Chemistry of Materials*, 35(8), 3057-3072.

Cui, J., Ren, S., Sun, B., & Jia, S. (2018). Optimization protocols and improved strategies for metal-organic frameworks for immobilizing

enzymes: Current development and future challenges. *Coordination Chemistry Reviews*, 370, 22-41.

Cui, Y., Zhang, J., He, H., & Qian, G. (2018). Photonic functional metal–organic frameworks. *Chemical Society Reviews*, 47(15), 5740-5785.

Cychosz, K. A., Guillet-Nicolas, R., García-Martínez, J., & Thommes, M. (2017). Recent advances in the textural characterization of hierarchically structured nanoporous materials. *Chemical Society Reviews*, 46(2), 389-414.

da Trindade, L. G., Zanchet, L., Dreon, R., Souza, J. C., Assis, M., Longo, E., Martini, E. M. A. Chiquito, A. J., & Pontes, F. M. (2020). Microwave-assisted solvothermal preparation of Zr-BDC for modification of proton exchange membranes made of SPEEK/PBI blends. *Journal of Materials Science*, 55, 14938-14952.

Dai, S., Tissot, A., & Serre, C. (2021). Metal-organic frameworks: from ambient green synthesis to applications. *Bulletin of the Chemical Society of Japan*, 94(11), 2623-2636.

Dalai, S. (2011). Coordination Polymers. *Journal of Physical Sciences*, Vol. 15, 2011, 223-230 ISSN: 0972-8791, www.vidyasagar.ac.in/journal Published on 22 December 2011.

d'Arras, L., Sassoie, C., Rozes, L., Sanchez, C., Marrot, J., Marre, S., & Aymonier, C. (2014). Fast and continuous processing of a new sub-micronic lanthanide-based metal–organic framework. *New Journal of Chemistry*, 38(4), 1477-1483.

- Das, A., Nikhil, S. K., & Nair, R. G. (2019). Influence of surface morphology on photocatalytic performance of zinc oxide: A review. *Nano-Structures & Nano-Objects*, *19*, 100353.
- Das, R., Manna, S. S., Pathak, B., & Nagaraja, C. M. (2022). Strategic Design of Mg-Centered Porphyrin Metal–Organic Framework for Efficient Visible Light-Promoted Fixation of CO₂ under Ambient Conditions: Combined Experimental and Theoretical Investigation. *ACS Applied Materials & Interfaces*, *14*(29), 33285-33296.
- Das, V., Kaushik, R., & Hussain, F. (2020). Heterometallic 3d-4f polyoxometalates: An emerging field with structural diversity to multiple applications. *Coordination Chemistry Reviews*, *413*, 213271.
- Datta, A., Guleria, M., Kumar, K., Agarwal, J., Singh, R., & Kaur, V. (2023). Copper (II) pseudoatranne appended heterobimetallic 2D-MOF: A multi-functional material with catalytic and sensing properties. *Applied Organometallic Chemistry*, *37*(6), e7083.
- Dawood, S. (2020). *Three-Dimensional Metal Organic Frameworks for Atomic Scale Patterning*. The University of North Carolina at Greensboro.
- De Marco, L., Carpenter, W., Liu, H., Biswas, R., Bowman, J. M., & Tokmakoff, A. (2016). Differences in the vibrational dynamics of H₂O and D₂O: observation of symmetric and antisymmetric stretching vibrations in heavy water. *The Journal of Physical Chemistry Letters*, *7*(10), 1769-1774.
- De Vos, A., Hendrickx, K., Van Der Voort, P., Van Speybroeck, V., & Lejaeghere, K. (2017). Missing linkers: an alternative pathway to UiO-

66 electronic structure engineering. *Chemistry of Materials*, 29(7), 3006-3019.

De, S., Devic, T., & Fateeva, A. (2021). Porphyrin and phthalocyanine-based metal organic frameworks beyond metal-carboxylates. *Dalton Transactions*, 50(4), 1166-1188.

Decker, G. E., Lorz, G. R., Deegan, M. M., & Bloch, E. D. (2020). MOF-mimetic molecules: Carboxylate-based supramolecular complexes as molecular metal-organic framework analogues. *Journal of Materials Chemistry A*, 8(8), 4217-4229.

Demazeau, G. (2010). Impact of high pressures in solvothermal processes. In *Journal of Physics: Conference Series* (Vol. 215, No. 1, p. 012124). IOP Publishing.

Demazeau, G. (2010). Solvothermal processes: definition, key factors governing the involved chemical reactions and new trends. *Zeitschrift für Naturforschung B*, 65(8), 999-1006.

Demazeau, G. (2011). Solvothermal and hydrothermal processes: the main physico-chemical factors involved and new trends. *Research on Chemical Intermediates*, 37, 107-123.

Demirkıran, M. (2016). *CoFe Prussian Blue Coordination Compounds Incorporating Metallopolymers: Investigation of Electrocatalytic Water Oxidation Activities* (Doctoral dissertation, Bilkent Universitesi (Turkey)).

Denisov, G. L., Primakov, P. V., Korlyukov, A. A., Novikov, V. V., & Nelyubina, Y. V. (2019). Solvothermal synthesis of the metal-organic

framework MOF-5 in autoclaves prepared by 3D printing. *Russian Journal of Coordination Chemistry*, 45, 836-842.

Denning, S., Majid, A. A., Lucero, J. M., Crawford, J. M., Carreon, M. A., & Koh, C. A. (2020). Metal–organic framework HKUST-1 promotes methane hydrate formation for improved gas storage capacity. *ACS Applied Materials & Interfaces*, 12(47), 53510-53518.

Dey, C., Kundu, T., Biswal, B. P., Mallick, A., & Banerjee, R. (2014). Crystalline metal-organic frameworks (MOFs): synthesis, structure and function. *Acta Crystallographica Section B: Structural Science, Crystal Engineering and Materials*, 70(1), 3-10.

Dhakshinamoorthy, A., Asiri, A. M., & Garcia, H. (2019). 2D metal–organic frameworks as multifunctional materials in heterogeneous catalysis and electro/photocatalysis. *Advanced Materials*, 31(41), 1900617.

Dhakshinamoorthy, A., Li, Z., & Garcia, H. (2018). Catalysis and photocatalysis by metal organic frameworks. *Chemical Society Reviews*, 47(22), 8134-8172.

Dhakshinamoorthy, A., Opanasenko, M., Čejka, J., & Garcia, H. (2013). Metal organic frameworks as heterogeneous catalysts for the production of fine chemicals. *Catalysis Science & Technology*, 3(10), 2509-2540.

Dhakshinamoorthy, A., Santiago-Portillo, A., Asiri, A. M., & Garcia, H. (2019). Engineering UiO-66 metal organic framework for heterogeneous catalysis. *ChemCatChem*, 11(3), 899-923.

Diercks, C. S., & Yaghi, O. M. (2017). The atom, the molecule, and the covalent organic framework. *Science*, 355(6328), eaal1585.

- Dimitrova, Y. (2006). Theoretical study of the changes in the vibrational characteristics arising from the hydrogen bonding between Vitamin C (l-ascorbic acid) and H₂O. *Spectrochimica Acta Part A: Molecular and Biomolecular Spectroscopy*, 63(2), 427-437.
- Ding, H., Wei, J. S., Zhang, P., Zhou, Z. Y., Gao, Q. Y., & Xiong, H. M. (2018). Solvent-controlled synthesis of highly luminescent carbon dots with a wide color gamut and narrowed emission peak widths. *Small*, 14(22), 1800612.
- Ding, M., Cai, X., & Jiang, H. L. (2019). Improving MOF stability: approaches and applications. *Chemical Science*, 10(44), 10209-10230.
- Dong, J. P., Shi, Z. Z., Li, B., & Wang, L. Y. (2019). Synthesis of a novel 2D zinc (II) metal–organic framework for photocatalytic degradation of organic dyes in water. *Dalton Transactions*, 48(47), 17626-17632.
- Dong, W., & Huang, Y. (2020). CeO₂/C nanowire derived from a cerium (III) based organic framework as a peroxidase mimic for colorimetric sensing of hydrogen peroxide and for enzymatic sensing of glucose. *Microchimica Acta*, 187(1), 1-10.
- Doveri, L., Dacarro, G., Fernandez, Y. A. D., Razzetti, M., Taglietti, A., Chirico, G., Collini, M., Sorzabal-Bellido, I., Esparza, M., Ortiz-de-Solorzano, C., Urteaga, X. M., Milanese, C., & Pallavicini, P. (2023). Prussian Blue nanoparticles: an FDA-approved substance that may quickly degrade at physiological pH. *Colloids and Surfaces B: Biointerfaces*, 113373.
- Dreischarf, A. C., Lammert, M., Stock, N., & Reinsch, H. (2017). Green synthesis of Zr-CAU-28: structure and properties of the first Zr-MOF

based on 2, 5-furandicarboxylic acid. *Inorganic chemistry*, 56(4), 2270-2277.

Dreischarf, A. C., Lammert, M., Stock, N., & Reinsch, H. (2017). Green synthesis of Zr-CAU-28: structure and properties of the first Zr-MOF based on 2, 5-furandicarboxylic acid. *Inorganic chemistry*, 56(4), 2270-2277.

Du, J., Chai, J., Li, Q., Zhang, W., & Tang, B. (2022). Application of two-dimensional layered Mo-MOF@ ppy with high valency molybdenum in lithium-ion batteries. *Colloids and Surfaces A: Physicochemical and Engineering Aspects*, 632, 127810.

Du, Q., Rao, R., Bi, F., Yang, Y., Zhang, W., Yang, Y., Liu, N., & Zhang, X. (2022). Preparation of modified zirconium-based metal-organic frameworks (Zr-MOFs) supported metals and recent application in environment: a review and perspectives. *Surfaces and Interfaces*, 28, 101647.

Dutta, A., Pan, Y., Liu, J. Q., & Kumar, A. (2021). Multicomponent isorecticular metal-organic frameworks: Principles, current status and challenges. *Coordination Chemistry Reviews*, 445, 214074.

Eassa, M. T. (2016). *Photocatalytic Degradation of Light Green Dye Using TiO₂ and Nano TiO₂ as Catalysts* (Doctoral dissertation, University of Kufa).

Ebrahimi, A. K., Sheikhshoae, I., & Mehran, M. (2017). Facile synthesis of a new metal-organic framework of copper (II) by interface reaction method, characterization, and its application for removal of Malachite Green. *Journal of Molecular Liquids*, 240, 803-809.

El-Berry, M. F., Sadeek, S. A., Abdalla, A. M., & Nassar, M. Y. (2021). Microwave-assisted fabrication of copper nanoparticles utilizing different counter ions: An efficient photocatalyst for photocatalytic degradation of safranin dye from aqueous media. *Materials Research Bulletin*, 133, 111048.

Electronic Supplementary Material (ESI) for CrystEngComm This journal is © The Royal Society of Chemistry 2009.

Elsaidi, S. K., Sinnwell, M. A., Devaraj, A., Droubay, T. C., Nie, Z., Murugesan, V., McGrail, P. B., & Thallapally, P. K. (2018). Extraction of rare earth elements using magnetite@ MOF composites. *Journal of Materials Chemistry A*, 6(38), 18438-18443.

Emam, H. E., Abdelhameed, R. M., & Ahmed, H. B. (2020). Adsorptive performance of MOFs and MOF containing composites for clean energy and safe environment. *Journal of Environmental Chemical Engineering*, 8(5), 104386.

Endashaw, M., & Girma, T. (2020). Review on the removal of dyes by photodegradation using metal-organic frameworks under light irradiation. *Chemistry and Materials Research*, 12(1), 14-21.

Engström, K., Johnston, E. V., Verho, O., Gustafson, K. P., Shakeri, M., Tai, C. W., & Bäckvall, J. E. (2013). Co-immobilization of an enzyme and a metal into the compartments of mesoporous silica for cooperative tandem catalysis: an artificial metalloenzyme. *Angewandte Chemie International Edition*, 52(52), 14006-14010.

Ethiraj, J., Bonino, F., Vitillo, J. G., Lomachenko, K. A., Lamberti, C., Reinsch, H., Lillerud, K. P., & Bordiga, S. (2016). Solvent-Driven

Gate Opening in MOF-76-Ce: Effect on CO₂ Adsorption. *ChemSusChem*, 9(7), 713-719.

Fakin, D., & Ojstršek, A. (2013). Optimization of removal of colour and organic pollutants from textile wastewater treated with UV/H₂O₂ adopting the Plackett–Burman factorial design. *Desalination and Water Treatment*, 51(7-9), 1584-1589

Fan, K., Zhang, C., Chen, Y., Wu, Y., & Wang, C. (2021). The chemical states of conjugated coordination polymers. *Chem*, 7(5), 1224-1243.

Fan, Z., Meng, F., Zhang, M., Wu, Z., Sun, Z., & Li, A. (2016). Solvothermal synthesis of hierarchical TiO₂ nanostructures with tunable morphology and enhanced photocatalytic activity. *Applied Surface Science*, 360, 298-305.

Fang, L., Xu, Q., Qi, Y., Wu, X., Fu, Y., Xiao, Q., Zhang, F., & Zhu, W. (2020). Fe/Fe₃C@ N-doped porous carbon microspindles templated from a metal–organic framework as highly selective and stable catalysts for the catalytic oxidation of sulfides to sulfoxides. *Molecular Catalysis*, 486, 110863.

Fang, Z., Bueken, B., De Vos, D. E., & Fischer, R. A. (2015). Defect-engineered metal–organic frameworks. *Angewandte Chemie International Edition*, 54(25), 7234-7254.

Farhadia, S., Manteghia, F., & Karimia, M. (2016). Application of a Zr-Metal Organic Framework in NCPE for Lithium Battery.

Feizbakhsh Bazargani, M. (2019) *Synthesis and characterization of ten new 1D, 2D and 3D-coordination polymers with oxygen or nitrogen*

containing ligands by using different metal cations (Doctoral dissertation). Friedrich-Schiller-Universität Jena

Feng, M., Zhang, P., Zhou, H. C., & Sharma, V. K. (2018). Water-stable metal-organic frameworks for aqueous removal of heavy metals and radionuclides: A review. *Chemosphere*, *209*, 783-800.

Feng, X., Jena, H. S., Krishnaraj, C., Leus, K., Wang, G., Chen, H., Jai, C., & Van Der Voort, P. (2021). Generating catalytic sites in UiO-66 through defect engineering. *ACS Applied Materials & Interfaces*, *13*(51), 60715-60735.

Feng, Y., Cai, S. L., Gao, Y., & Zheng, S. R. (2018). Construction of coordination polymers based on a rigid tripodal nitrogen-containing heterotopic ligand that designed by mixed-donors strategy. *Journal of Solid State Chemistry*, *265*, 64-71.

Ferreira da Rosa, P. P., Miyazaki, S., Sakamoto, H., Kitagawa, Y., Miyata, K., Akama, T., Kobayashi, M., Fushimi, K., Onda, K., Taketsugu, T., & Hasegawa, Y. (2021). Coordination geometrical effect on ligand-to-metal charge transfer-dependent energy transfer processes of luminescent Eu (III) complexes. *The Journal of Physical Chemistry A*, *125*(1), 209-217.

Ferrer, B., Alvaro, M., Baldovi, H. G., Reinsch, H., & Stock, N. (2014). Photophysical Evidence of Charge-Transfer-Complex Pairs in Mixed-Linker 5-Amino/5-Nitroisophthalate CAU-10. *ChemPhys Chem*, *15*(5), 924-928.

Fonseca, R. R., Gaspar, R. D., Raimundo Jr, I. M., & Luz, P. P. (2019). Photoluminescent Tb³⁺-based metal-organic framework as a sensor

for detection of methanol in ethanol fuel. *Journal of Rare Earths*, 37(3), 225- 231.

Friend, C. M., & Xu, B. (2017). Heterogeneous catalysis: a central science for a sustainable future. *Accounts of chemical research*, 50(3), 517-521.

Fromm, K. M., Sague, J. L., & Mirolo, L. (2010). Coordination polymer networks: an alternative to classical polymers?. In *Macromolecular symposia* (Vol. 291, No. 1, pp. 75-83). Weinheim: WILEY-VCH Verlag.

Fulton, J. R., Holland, A. W., Fox, D. J., & Bergman, R. G. (2002). Formation, reactivity, and properties of nondative late transition metal– oxygen and– nitrogen bonds. *Accounts of chemical research*, 35(1), 44-56.

Furukawa, H., Cordova, K. E., O’Keeffe, M., & Yaghi, O. M. (2013). The chemistry and applications of metal-organic frameworks. *Science*, 341(6149), 1230444.

Gabbott, P. (Ed.). (2008). *Principles and applications of thermal analysis*. John Wiley & Sons.

Ganesan, R., & Lee, J. S. (2006). An electrocatalyst for methanol oxidation based on tungsten trioxide microspheres and platinum. *Journal of Power Sources*, 157(1), 217-221.

Ganesh, M., Hemalatha, P., Peng, M. M., Cha, W. S., & Jang, H. T. (2014). Zr- fumarate MOF a novel CO₂-adsorbing material: Synthesis and characterization. *Aerosol and Air Quality Research*, 14(6), 1605-1612.

Gangu, K. K., Maddila, S., & Jonnalagadda, S. B. (2017). A review on synthesis, crystal structure and functionality of naphthalenedicarb

oxylate ligated metal-organic frameworks. *Inorganica Chimica Acta*, 466, 308-323.

Gao, G., Di, J. Q., Zhang, H. Y., Mo, L. P., & Zhang, Z. H. (2020). A magnetic metal organic framework material as a highly efficient and recyclable catalyst for synthesis of cyclohexenone derivatives. *Journal of catalysis*, 387, 39-46.

Gao, Q., Xu, J., & Bu, X. H. (2019). Recent advances about metal-organic frameworks in the removal of pollutants from wastewater. *Coordination Chemistry Reviews*, 378, 17-31.

Gao, X., Zhao, L., Ding, M., Wang, X., Zhai, L., & Ren, X. (2021). Insight understanding into influence of binding mode of carboxylate with metal ion on ligand-centered luminescence properties in Pb-based coordination polymers. *Chinese Chemical Letters*, 32(8), 2423-2426.

Gao, Z., Xu, B., Zhang, T., Liu, Z., Zhang, W., Sun, X., Liu, Y., Wang, X., Wang, Z., Yan, Y., Hu, F., Meng, X., & Zhao, Y. S. (2020). Spatially Responsive Multicolor Lanthanide-MOF Heterostructures for Covert Photonic Barcodes. *Angewandte Chemie*, 132(43), 19222-19226.

Garg, D., Rekhi, H., Kaur, H., Singh, K., & Malik, A. K. (2022). A novel method for the synthesis of MOF-199 for sensing and photocatalytic applications. *Journal of Fluorescence*, 32(3), 1171-1188.

Gautam, S., Agrawal, H., Thakur, M., Akbari, A., Sharda, H., Kaur, R., & Amini, M. (2020). Metal oxides and metal organic frameworks for the photocatalytic degradation: A review. *Journal of Environmental Chemical Engineering*, 8(3), 103726.

- Gautam, S., Singhal, J., Lee, H. K., & Chae, K. H. (2022). Drug delivery of paracetamol by metal-organic frameworks (HKUST-1): Improved synthesis and investigations. *Materials Today Chemistry*, 23, 100647.
- Gazulla, M. F., Rodrigo, M., Blasco, E., & Orduña, M. (2013). Nitrogen determination by SEM-EDS and elemental analysis. *X-Ray Spectrometry*, 42(5), 394-401.
- Ge, B., Xu, Y., Zhao, H., Sun, H., Guo, Y., & Wang, W. (2018). High performance gas separation mixed matrix membrane fabricated by incorporation of functionalized submicrometer -sized metal –organic framework. *Materials*, 11(8), 1421.
- Ge, R., Li, X. X., & Zheng, S. T. (2021). Recent advances in polyoxometalate-templated high-nuclear silver clusters. *Coordination Chemistry Reviews*, 435, 213787.
- Ghasempour, H., Wang, K. Y., Powell, J. A., ZareKarizi, F., Lv, X. L., Morsali, A., & Zhou, H. C. (2021). Metal–organic frameworks based on multicarboxylate linkers. *Coordination Chemistry Reviews*, 426, 213542.
- Głuchowska, H., Łyszczek, R., Mazur, L., & Kirillov, A. M. (2021). Structural and Thermal Investigations of Co (II) and Ni (II) Coordination Polymers Based on biphenyl-4, 4'-dioxydiacetate Linker. *Materials*, 14(13), 3545.
- Gorai, T., Schmitt, W., & Gunlaugsson, T. (2021). Highlights of the development and application of luminescent lanthanide based coordination polymers, MOFs and functional nanomaterials. *Dalton Transactions*, 50(3), 770-784.

Goswami, V., Deepika, S., Chandra, R., Babu, C. R., & Kothamasi, D. (2023).

Arbuscular mycorrhizas accelerate the degradation of colour containing organic pollutants present in distillery spent wash leachates. *Journal of Hazardous Materials*, 452, 131291.

Gu, J., Wen, M., Cai, Y., Shi, Z., Arol, A. S., Kirillova, M. V., & Kirillov, A.

M. (2019). Metal–organic architectures assembled from multifunctional polycarboxylates: hydrothermal self-assembly, structures, and catalytic activity in alkane oxidation. *Inorganic Chemistry*, 58(4), 2403-2412.

Gu, M., Ren, Y., Hu, Y., Tang, M., Kong, Z., Yue, B., & He, H. (2015). Three

Polyoxometalate-Based Coordination Polymers Constructed from the Same Dimetallic Cyclic Building Block. *European Journal of Inorganic Chemistry*, 2015(3), 488-493.

Gu, W., Gu, J., & Kirillov, A. M. (2020). A flexible aromatic tetracarboxylate

as a new linker for coordination polymers. *Crystals*, 10(2), 84..

Guan, D. (2021). Coordination polymers for high index of refraction and

ammonia sensing applications. Thesis Submitted in Partial Fulfillment of the Requirements for the Degree of Master of Science in the Department of Chemistry Faculty of Science. Simon Fraser University.

Günay, H., Çolak, A. T., Yeşilel, O. Z., Tunç, T., & Çolak, F. (2015).

Synthesis, structural characterization and microbial activity of 2D Ag (I)-5-aminoisophthalate coordination polymer with a new coordination mode. *Journal of Molecular Structure*, 1099, 108-113.

Guo, H., Wu, C., Xie, J., Zhang, S., Cao, G., & Zhao, X. (2014). Controllable

synthesis of high-performance LiMnPO₄ nanocrystals by a facile one-

spot solvothermal process. *Journal of Materials Chemistry A*, 2(27), 10581-10588.

Guo, J., Xue, X., Yu, H., Duan, Y., Li, F., Lian, Y., Liu, Y., & Zhao, M. (2022). Metal-organic frameworks based on infinite secondary building units: recent progress and future outlooks. *Journal of Materials Chemistry A*.

Guo, Q., Zhou, C., Ma, Z., & Yang, X. (2019). Fundamentals of TiO₂ photocatalysis: concepts, mechanisms, and challenges. *Advanced Materials*, 31(50), 1901997.

Guo, T., Mo, K., Zhang, N., Xiao, L., Liu, W., & Wen, L. (2021). Embedded homogeneous ultra-fine Pd nanoparticles within MOF ultra-thin nanosheets for heterogeneous catalysis. *Dalton Transactions*, 50(5), 1774-1779.

Guo, W., Liu, J., Dong, F., Chen, R., Das, J., Ge, W., Xu, X., & Hong, H. (2022). Deep learning models for predicting gas adsorption capacity of nanomaterials. *Nanomaterials*, 12(19), 3376.

Guo, X., Lin, C., Zhang, M., Duan, X., Dong, X., Sun, D. & You, T. (2021). 2D/3D Copper-Based Metal-Organic Frameworks for Electrochemical Detection of Hydrogen Peroxide. *Frontiers in Chemistry*, 9, 743637.

Guo, X., Zhu, N., Lou, Y., Ren, S., Pang, S., He, Y., Chen, X., Shi, Z. & Feng, S. (2020). A stable nanoscaled Zr-MOF for the detection of toxic mycotoxin through a pH-modulated ratiometric luminescent switch. *Chemical Communications*, 56(40), 5389-5392.

- Gupta, B. S., Jelle, B. P., & Gao, T. (2022). In vitro cell composition identification of wood decay fungi by Fourier transform infrared spectroscopy. *Royal Society Open Science*, 9(2), 201935.
- Gupta, P., & Paul, S. (2014). Solid acids: Green alternatives for acid catalysis. *Catalysis Today*, 236, 153-170.
- Gusain, R., Gupta, K., Joshi, P., & Khatri, O. P. (2019). Adsorptive removal and photocatalytic degradation of organic pollutants using metal oxides and their composites: A comprehensive review. *Advances in colloid and interface science*, 272, 102009.
- Gutiérrez, M., Di Nunzio, M. R., Caballero-Mancebo, E., Sánchez, F., Cohen, B., & Douhal, A. (2023). Disentangling the complex photodynamics of mixed-linker Zr-MOFs—efficient energy and charge transfer processes. *Journal of Materials Chemistry C*, 11(1), 183-195.
- Ha, J., Lee, J. H., & Moon, H. R. (2020). Alterations to secondary building units of metal–organic frameworks for the development of new functions. *Inorganic Chemistry Frontiers*, 7(1), 12-27.
- Haddad, A., Merouani, S., Hannachi, C., Hamdaoui, O., & Hamrouni, B. (2019). Intensification of light green SF yellowish (LGSFY) photodegradation in water by iodate ions: Iodine radicals implication in the degradation process and impacts of water matrix components. *Science of the Total Environment*, 652, 1219-1227.
- Hammond, O. S., Edler, K. J., Bowron, D. T., & Torrente-Murciano, L. (2017). Deep eutectic-solvothermal synthesis of nanostructured ceria. *Nature Communications*, 8(1), 14150.

- Han, M., Tang, X., Wang, P., Zhao, Z., Ba, X., Jiang, Y., & Zhang, X. (2022). Metal-Organic Frameworks Decorated Cu₂O Heterogeneous Catalysts for Selective Oxidation of Styrene. *Catalysts*, 12(5), 487.
- Hanafi, M. F., & Sapawe, N. (2020). A review on the water problem associate with organic pollutants derived from phenol, methyl orange, and remazol brilliant blue dyes. *Materials Today: Proceedings*, 31, A141-A150.
- Hang, M. T., Cheng, Y., Wang, Y. T., Li, H., Zheng, M. Q., He, M. Y., Chen, Q., & Zhang, Z. H. (2022). Rational synthesis of isomorphic rare earth metal-organic framework materials for simultaneous adsorption and photocatalytic degradation of organic dyes in water. *CrystEng Comm*, 24(3), 552-559.
- Hansen, R. E., & Das, S. (2014). Biomimetic di-manganese catalyst cage-isolated in a MOF: robust catalyst for water oxidation with Ce (IV), a non-O-donating oxidant. *Energy & Environmental Science*, 7(1), 317-322.
- Hariprasad, N., Anju, S. G., & Yesodharan, E. P. (2013). Sunlight induced removal of Rhodamine B from water through semiconductor photocatalysis: effects of adsorption, reaction conditions and additives. *Res. J. Mater. Sci*, 2320, 6055.
- Hashemi, S. H., & Kaykhali, M. (2022). Azo dyes: sources, occurrence, toxicity, sampling, analysis, and their removal methods. In *Emerging freshwater pollutants* (pp. 267-287). Elsevier.

- Hassaan, M. A., El Nemr, A., & Hassaan, A. (2017). Health and environmental impacts of dyes: mini review. *American Journal of Environmental Science and Engineering*, 1(3), 64-67.
- He, H., Hashemi, L., Hu, M. L., & Morsali, A. (2018). The role of the counterion in metal-organic frameworks' chemistry and applications. *Coordination Chemistry Reviews*, 376, 319-347.
- He, Y. P., Tan, Y. X., & Zhang, J. (2013). Gas sorption, second-order nonlinear optics, and luminescence properties of a series of lanthanide-organic frameworks based on nanosized tris ((4-carboxyl) phenylduryl) amine ligand. *Inorganic Chemistry*, 52(21), 12758-12762.
- He, Y., Chen, F., Li, B., Qian, G., Zhou, W., & Chen, B. (2018). Porous metal-organic frameworks for fuel storage. *Coordination Chemistry Reviews*, 373, 167-198.
- Hendon, C. H., & Walsh, A. (2015). Chemical principles underpinning the performance of the metal-organic framework HKUST-1. *Chemical Science*, 6(7), 3674-3683.
- Hendon, C. H., Rieth, A. J., Korzynski, M. D., & Dinca, M. (2017). Grand challenges and future opportunities for metal-organic frameworks. *ACS central science*, 3(6), 554-563.
- Heu, R., Ateia, M., & Yoshimura, C. (2020). Photocatalytic nanofiltration membrane using Zr-MOF/GO nanocomposite with high-flux and anti-fouling properties. *Catalysts*, 10(6), 711.
- Hou, C., Yuan, X., Niu, M., Li, Y., Wang, L., & Zhang, M. (2022). In situ composite of Co-MOF on a Ti-based material for visible light

multiphase catalysis: synthesis and the photocatalytic degradation mechanism. *New Journal of Chemistry*, 46(23), 11341-11349.

Hsieh, P. F., Law, Z. X., Lin, C. H., & Tsai, D. H. (2022). Understanding solvothermal growth of Metal–Organic Framework colloids for CO₂ capture applications. *Langmuir*, 38(14), 4415-4424.

Hu, D., Song, X., Wu, S., Yang, X., Zhang, H., Chang, X., & Jia, M. (2021). Solvothermal synthesis of Co-substituted phosphomolybdate acid encapsulated in the UiO-66 framework for catalytic application in olefin epoxidation. *Chinese Journal of Catalysis*, 42(2), 356-366.

Hu, Z., Kundu, T., Wang, Y., Sun, Y., Zeng, K., & Zhao, D. (2020). Modulated hydrothermal synthesis of highly stable MOF-808 (Hf) for methane storage. *ACS Sustainable Chemistry & Engineering*, 8(46), 17042-17053.

Hu, Z., Peng, Y., Tan, K. M., & Zhao, D. (2015). Enhanced catalytic activity of a hierarchical porous metal–organic framework CuBTC. *Cryst EngComm*, 17(37), 7124-7129.

Hua, Y., Lv, X., Cai, Y., Liu, H., Li, S., Wan, Y., & Wang, H. (2019). Highly selective and reproducible electroanalysis for histidine in blood with turn-on responses at a potential approaching zero using tetrahedral copper metal organic frameworks. *Chemical Communications*, 55(9), 1271-1274.

Huang, J. F., & Wu, Y. C. (2018). Making Ag present Pt-like activity for hydrogen evolution reaction. *ACS Sustainable Chemistry & Engineering*, 6(7), 8285-8290.

- Huang, K., Xu, Y., Wang, L., & Wu, D. (2015). Heterogeneous catalytic wet peroxide oxidation of simulated phenol wastewater by copper metal-organic frameworks. *RSC Advances*, 5(41), 32795-32803.
- Huang, W., Wang, X., Zhang, W., Zhang, S., Tian, Y., Chen, Z., Fang, W., & Ma, J. (2020). Intraligand charge transfer boosts visible-light-driven generation of singlet oxygen by metal-organic frameworks. *Applied Catalysis B: Environmental*, 273, 119087
- Hungerford, J. (2019). *Synthesis and stability: Metal-organic frameworks exposure to water, sulfur dioxide, and hydrogen sulfide* (Doctoral dissertation, Georgia Institute of Technology).
- Hunger, K. (2003). *Industrial dyes: chemistry application*. British Library cataloguing-in-publication data. Germany.
- Huo, P., Chen, T., Hou, J. L., Yu, L., Zhu, Q. Y., & Dai, J. (2016). Ligand-to-ligand charge transfer within metal-organic frameworks based on manganese coordination polymers with tetrathiafulvalene-bicarboxylate and bipyridine ligands. *Inorganic chemistry*, 55(13), 6496-6503.
- Huo, Y., Xiu, S., Meng, L. Y., & Quan, B. (2023). Solvothermal synthesis and applications of micro/nano carbons: A review. *Chemical Engineering Journal*, 451, 138572.
- Huskić, I., Pekov, I. V., Krivovichev, S. V., & Friščić, T. (2016). Minerals with metal-organic framework structures. *Science Advances*, 2(8), e1600621.

- Jacobsen, J., Ienco, A., D'Amato, R., Costantino, F., & Stock, N. (2020). The chemistry of Ce-based metal–organic frameworks. *Dalton Transactions*, 49(46), 16551-16586.
- Jallouli, N., Pastrana-Martínez, L. M., Ribeiro, A. R., Moreira, N. F., Faria, J. L., Hentati, O., Silva, A. M. T., & Ksibi, M. (2018). Heterogeneous photocatalytic degradation of ibuprofen in ultrapure water, municipal and pharmaceutical industry wastewaters using a TiO₂/UV-LED system. *Chemical Engineering Journal*, 334, 976-984.
- Jamil, U., Khoja, A. H., Liaquat, R., Naqvi, S. R., Omar, W. N. N. W., & Amin, N. A. S. (2020). Copper and calcium-based metal organic framework (MOF) catalyst for biodiesel production from waste cooking oil: A process optimization study. *Energy Conversion and Management*, 215, 112934.
- Janiak, C. (2013). Demonstration of permanent porosity in flexible and guest-responsive organic zeolite analogs (now called MOFs). *Chemical Communications*, 49(62), 6933-6937.
- Janicki, R., Mondry, A., & Starynowicz, P. (2017). Carboxylates of rare earth elements. *Coordination Chemistry Reviews*, 340, 98-133.
- Jensen, K. M., Tyrsted, C., Bremholm, M., & Iversen, B. B. (2014). In situ studies of solvothermal synthesis of energy materials. *ChemSus Chem*, 7(6), 1594-1611.
- Jeyaseelan, A., Albaqami, M. D., & Viswanathan, N. (2021). Facile design of metal ion fabricated benzene-1, 3, 5-tricarboxylic acid based metal organic frameworks for defluoridation of water. *Journal of Environmental Chemical Engineering*, 9(1), 104995.

- Ji, W., Hamachi, L. S., Natraj, A., Flanders, N. C., Li, R. L., Chen, L. X., & Dichtel, W. R. (2021). Solvothermal depolymerization and recrystallization of imine-linked two-dimensional covalent organic frameworks. *Chemical Science*, *12*(48), 16014-16022.
- Ji, W., Qu, J., Jing, S., Zhu, D., & Huang, W. (2016). Copper (I) halide clusters based upon ferrocenylchalcogenoether ligands: donors, halides and semi-rigidity effects on the geometry and catalytic activity. *Dalton Transactions*, *45*(3), 1016-1024.
- Jia, H., Han, Q., Luo, W., Cong, H., & Deng, H. (2022). Sequence control of metals in MOF by coordination number precoding for electrocatalytic oxygen evolution. *Chem Catalysis*, *2*(1), 84-101.
- Jia, J., Zhao, X., Hu, W., Wang, Y., Huang, J., Huang, J., Li, H., Peng, Y., Ma, H., & Xu, C. (2023). Role of cobalt phthalocyanine on the formation of high-valent cobalt species revealed by in situ Raman spectroscopy. *Journal of Materials Chemistry A*, *11*(15), 8141-8149.
- Jiang, H., Alezi, D., & Eddaoudi, M. (2021). A reticular chemistry guide for the design of periodic solids. *Nature Reviews Materials*, *6*(6), 466-487.
- Jiang, H., Wang, Q., Wang, H., Chen, Y., & Zhang, M. (2016). Temperature effect on the morphology and catalytic performance of Co-MOF-74 in low-temperature NH₃-SCR process. *Catalysis Communications*, *80*, 24-27.
- Jiang, L., Wang, Z., Bai, S. Q., & Hor, T. A. (2013). "Click-and-click"-hybridised 1, 2, 3-triazoles supported Cu (i) coordination polymers for azide-alkyne cycloaddition. *Dalton Transactions*, *42*(26), 9437-9443.

- Jiang, W., Yang, J., Yan, G., Zhou, S., Liu, B., Qiao, Y., Zhou, T., Wang, J., & Che, G. (2020). A novel 3-fold interpenetrated dia metal-organic framework as a heterogeneous catalyst for CO₂ cycloaddition. *Inorganic Chemistry Communications*, *113*, 107770.
- Jiao, L., Wang, Y., Jiang, H. L., & Xu, Q. (2018). Metal–organic frameworks as platforms for catalytic applications. *Advanced Materials*, *30*(37), 1703663.
- Jiku, M. A. S., Singha, A., Faruquee, M., Rahaman, M. A., Alam, M. A., & Ehsanullah, M. (2021). Toxic wastewater status for irrigation usage at Gazipur and Savar industrial vicinity of Bangladesh. *Acta Ecologica Sinica*, *41*(4), 358-364.
- Jin, H. G., Yan, Y. Z., Li, J., Gu, Z. G., Chen, J. H., Liu, Y. T., ... & Cai, Y. P. (2012). 1-D to 3-D lanthanide coordination polymers constructed from 5-aminoisophthalic acid and oxalic acid. *Inorganic Chemistry Communications*, *23*, 25-30.
- Jin, R., Chen, G., Pei, J., & Xu, H. (2012). Solvothermal synthesis and growth mechanism of ultrathin Sb₂Te₃ hexagonal nanoplates with thermoelectric transport properties. *RSC advances*, *2*(4), 1450-1456.
- Jing, C., Zhang, Y., Zheng, J., Ge, S., Lin, J., Pan, D., Naik, N., & Guo, Z. (2022). In-situ constructing visible light CdS/Cd-MOF photocatalyst with enhanced photodegradation of methylene blue. *Particuology*, *69*, 111-122.
- Jornet-Molla, V., & Romero, F. M. (2015). Synthesis of rigid ethynyl-bridged polytopic picolinate ligands for MOF applications. *Tetrahedron Letters*, *56*(44), 6120-6122.

- Julkapli, N. M., & Bagheri, S. (2015). Graphene supported heterogeneous catalysts: An overview. *International Journal of Hydrogen Energy*, 40(2), 948-979.
- Jurca, T., Marian, E., Vicaș, L. G., Mureșan, M. E., & Fritea, L. (2017). Metal complexes of pharmaceutical substances. *Spectrosc. Anal. Dev. Appl*, 123.
- Kalmutzki, M. J., Hanikel, N., & Yaghi, O. M. (2018). Secondary building units as the turning point in the development of the reticular chemistry of MOFs. *Science advances*, 4(10), eaat9180.
- Kar, A. K., & Srivastava, R. (2018). An efficient and sustainable catalytic reduction of carbon–carbon multiple bonds, aldehydes, and ketones using a Cu nanoparticle decorated metal organic framework. *New Journal of Chemistry*, 42(12), 9557-9567.
- Kareem, H. M., & Abd Alrubaye, R. T. (2019). Synthesis and characterization of metal organic frameworks for gas storage. In *IOP Conference Series: Materials Science and Engineering* (Vol. 518, No. 6, p. 062013). IOP Publishing.
- Karim, A. V., Krishnan, S., & Shriwastav, A. (2022). An overview of heterogeneous photocatalysis for the degradation of organic compounds: A special emphasis on photocorrosion and reusability. *Journal of the Indian Chemical Society*, 99(6), 100480.
- Kateshali, A. F., Dogaheh, S. G., Soleimannejad, J., & Blake, A. J. (2020). Structural diversity and applications of Ce (III)-based coordination polymers. *Coordination Chemistry Reviews*, 419, 213392.

Kaur, G., Anthwal, A., Kandwal, P., & Sud, D. (2023). Mechanochemical synthesis and theoretical investigations of Fe (II) based MOF containing 4, 4'-bipyridine with ordered intercalated p-aminobenzoic acid: Application as fluoroprobe for detection of carbonyl group. *Inorganica Chimica Acta*, 545, 121248.

Kaur, K., Badru, R., Singh, P. P., & Kaushal, S. (2020). Photodegradation of organic pollutants using heterojunctions: A review. *Journal of Environmental Chemical Engineering*, 8(2), 103666.

Kaur, M., Yusuf, M., & Malik, A. K. (2021). Synthesis of copper metal organic framework based on Schiff base tricarboxylate ligand for highly selective and sensitive detection of 2, 4, 6-trinitrophenol in aqueous medium. *Journal of Fluorescence*, 31, 1959-1973.

Khan, A., Valicsek, Z., & Horváth, O. (2021). Photocatalytic Degradation of Rhodamine B in Heterogeneous and Homogeneous Systems. *Hungarian Journal of Industry and Chemistry*, 49(1), 9-16.

Khan, N. A., Haque, M. M., & Jhung, S. H. (2010). Accelerated syntheses of porous isostructural lanthanide-benzenetricarboxylates (Ln-BTC) under ultrasound at room temperature.

Khasri, A., Jamir, M. R. M., Ahmad, A. A., & Ahmad, M. A. (2021). Adsorption of remazol brilliant violet 5R dye from aqueous solution onto melunak and rubberwood sawdust based activated carbon: interaction mechanism, isotherm, kinetic and thermodynamic properties. *DWT*, 216, 401-411.

Khatter, J., & Chauhan, R. P. (2020). Effect of temperature on properties of cadmium sulfide nanostructures synthesized by solvothermal

method. *Journal of Materials Science: Materials in Electronics*, *31*, 2676-2685.

Kitagawa, S. (2017). Future porous materials. *Accounts of chemical research*, *50*(3), 514-516.

Knebel, A., Geppert, B., Volgmann, K., Kolokolov, D. I., Stepanov, A. G., Twiefel, J., Heitjans, P., Volkmer, D., & Caro, J. (2017). Defibrillation of soft porous metal-organic frameworks with electric fields. *Science*, *358*(6361), 347-351.

Kohantorabi, M., & Gholami, M. R. (2017). M_xNi_{100-x} ($M = Ag$, and Co) nanoparticles supported on CeO_2 nanorods derived from Ce-metal organic frameworks as an effective catalyst for reduction of organic pollutants: Langmuir-Hinshelwood kinetics and mechanism. *New Journal of Chemistry*, *41*(19), 10948-10958.

Kokado, K. (2017). Network polymers derived from the integration of flexible organic polymers and rigid metal-organic frameworks. *Polymer journal*, *49*(4), 345-353.

Koohsaryan, E., & Anbia, M. (2016). Nanosized and hierarchical zeolites: A short review. *Chinese Journal of Catalysis*, *37*(4), 447-467.

Köse, D. A., & Necefoğlu, H. (2008). Synthesis and characterization of bis (nicotinamide) *m*-hydroxybenzoate complexes of $Co(II)$, $Ni(II)$, $Cu(II)$ and $Zn(II)$. *Journal of Thermal Analysis and Calorimetry*, *93*, 509-514.

Kostakis, G. E. (2018). *Structural Design and Properties of Coordination Polymers*. MDPI AG-Multidisciplinary Digital Publishing Institute.

- Kumar, I. A., Mezni, A., Periyasamy, S., & Viswanathan, N. (2022). Development of cerium-trimesic acid complexed 2D frameworks for effective nitrate and phosphate remediation. *Journal of Molecular Structure*, *1250*, 131873.
- Kumar, S., Malik, M. M., & Purohit, R. (2017). Synthesis methods of mesoporous silica materials. *Materials Today: Proceedings*, *4*(2), 350-357.
- Kuznetsova, A., Matveevskaya, V., Pavlov, D., Yakunenkov, A., & Potapov, A. (2020). Coordination polymers based on highly emissive ligands: Synthesis and functional properties. *Materials*, *13*(12), 2699.
- Lai, M. T. L., Lai, C. W., Lee, K. M., Chook, S. W., Yang, T. C. K., Chong, S. H., & Juan, J. C. (2019). Facile one-pot solvothermal method to synthesize solar active Bi₂WO₆ for photocatalytic degradation of organic dye. *Journal of Alloys and Compounds*, *801*, 502-510.
- Lai, S. Y., Ng, K. H., Cheng, C. K., Nur, H., Nurhadi, M., & Arumugam, M. (2021). Photocatalytic remediation of organic waste over Keggin-based polyoxometalate materials: A review. *Chemosphere*, *263*, 128244.
- Lalhriatzuala, & Agarwal, P. (2021). High-pressure solvothermal route to synthesize II–VI sulfide compounds. *Applied Physics A*, *127*, 1-8.
- Le, A. T., Duy, H. L. T., Cheong, K. Y., & Pung, S. Y. (2022). Immobilization of zinc oxide-based photocatalysts for organic pollutant degradation: A review. *Journal of Environmental Chemical Engineering*, 108505.
- Lee, J. Y., Tang, C. Y., & Huo, F. (2014). Fabrication of porous matrix membrane (PMM) using metal-organic framework as green template for water treatment. *Scientific reports*, *4*(1), 3740.

- Lestari, W. W., Inayah, W. C., Rahmawati, F., & Purwanto, A. (2020). Metal-Organic Frameworks Based on Zinc (II) and Benzene-1, 3, 5-Tricarboxylate Modified Graphite: Fabrication and Application as an Anode Material in Lithium-Ion Batteries. *Journal of Mathematical & Fundamental Sciences*, 52(1).
- Lestari, W. W., Winarni, I. D., & Rahmawati, F. (2017). Electrosynthesis of metal-organic frameworks (MOFs) based on nickel (II) and benzene 1, 3, 5-tri carboxylic acid (H3BTC): An optimization reaction condition. In *IOP Conference Series: Materials Science and Engineering* (Vol. 172, No. 1, p. 012064). IOP Publishing.
- Li, C. H., & Zuo, J. L. (2020). Self-healing polymers based on coordination bonds. *Advanced Materials*, 32(27), 1903762.
- Li, D., Ma, P., Niu, J., & Wang, J. (2019). Recent advances in transition-metal-containing Keggin-type polyoxometalate-based coordination polymers. *Coordination Chemistry Reviews*, 392, 49-80.
- Li, D., Wang, H., Zhang, X., Sun, H., Dai, X., Yang, Y., Ran, L., Li, X., Ma, X., & Gao, D. (2014). Morphology design of IRMOF-3 crystal by coordination modulation. *Crystal growth & design*, 14(11), 5856-5864.
- Li, H., Li, L., Lin, R. B., Zhou, W., Zhang, Z., Xiang, S., & Chen, B. (2019). Porous metal-organic frameworks for gas storage and separation: Status and challenges. *EnergyChem*, 1(1), 100006.
- Li, J., Wu, Q., & Wu, J. (2016). Synthesis of nanoparticles via solvothermal and hydrothermal methods. In *Handbook of nanoparticles* (pp. 295-328). Springer, Cham.

- Li, M., Huang, W., Tang, B., Song, F., Lv, A., & Ling, X. (2019). Preparation of a composite material AC/Cu-BTC with improved water stability and n-hexane vapor adsorption. *Journal of Nanomaterials*, 2019, 1-9.
- Li, Q., Dai, Z., Wu, J., Liu, W., Di, T., Jiang, R., & Zhou, J. (2020). Fabrication of ordered macro-microporous single-crystalline MOF and its derivative carbon material for supercapacitor. *Advanced Energy Materials*, 10(33), 1903750.
- Li, X., Cai, Z., Jiang, L. P., He, Z., & Zhu, J. J. (2019). Metal–ligand coordination nanomaterials for biomedical imaging. *Bioconjugate Chemistry*, 31(2), 332-339.
- Li, Y. (2013). *Lanthanide Luminescent Metal-Organic Frameworks with Linear Dicarboxylate Ligands: Synthesis, Structure and Sensing* (Doctoral dissertation).
- Li, Y. X., Han, Y. C., & Wang, C. C. (2021). Fabrication strategies and Cr (VI) elimination activities of the MOF-derivatives and their composites. *Chemical Engineering Journal*, 405, 126648.
- Li, Y., Liu, Y., Gao, W., Zhang, L., Liu, W., Lu, J., Wang, Z., & Deng, Y. J. (2014). Microwave-assisted synthesis of UIO-66 and its adsorption performance towards dyes. *CrystEngComm*, 16(30), 7037-7042.
- Li, Y., Miao, J., Sun, X., Xiao, J., Li, Y., Wang, H. & Li, Z. (2016). Mechanochemical synthesis of Cu-BTC@ GO with enhanced water stability and toluene adsorption capacity. *Chemical Engineering Journal*, 298, 191-197.
- Li, Z. J., Hofman, E., Davis, A. H., Khammang, A., Wright, J. T., Dzikovski, B., Meulenberg, R. W., & Zheng, W. (2018). Complete dopant

substitution by spinodal decomposition in Mn-doped two-dimensional CsPbCl₃ nanoplatelets. *Chemistry of Materials*, 30(18), 6400-6409.

Li, Z., Yang, J., Guang, T., Fan, B., Zhu, K., & Wang, X. (2021). Controlled Hydrothermal/Solvothermal Synthesis of High-Performance LiFePO₄ for Li-Ion Batteries. *Small Methods*, 5(6), 2100193.

Lian, X., Chen, Y. P., Liu, T. F., & Zhou, H. C. (2016). Coupling two enzymes into a tandem nanoreactor utilizing a hierarchically structured MOF. *Chemical science*, 7(12), 6969-6973.

Liang, L. L., Xu, L., Xue, H. B., Tao, Z. L., & Chen, F. J. (2016). Two metal-organic frameworks with different configurations constructed from a flexible tripodal triaromatic acid. *Journal of Molecular Structure*, 1125, 656-661.

Lin, A., Ibrahim, A. A., Arab, P., El-Kaderi, H. M., & El-Shall, M. S. (2017). Palladium nanoparticles supported on Ce-metal-organic framework for efficient CO oxidation and low-temperature CO₂ capture. *ACS Applied Materials & Interfaces*, 9(21), 17961-17968.

Lin, B., Xiang, S., Zhou, W., Chen, B. (2020) Microporous Metal-Organic Framework Materials for Gas Separation. *Chem*, 6, 337-363.

Lin, H., Lu, H., Le, M. A. O., Luan, J., Wang, X., & Liu, G. (2015). Three 2 D copper (II)/cadmium (II) coordination polymers based on semi-rigid/flexible bis-pyridyl-bis-amide ligands and 5-aminoisophthalate: Syntheses, structures and properties. *Journal of Chemical Sciences*, 127, 1275-1285.

Lin, L. D., Li, Z., Liu, J. H., Sun, Y. Q., Li, X. X., & Zheng, S. T. (2019). A new type of composite MOFs based on high-valent Sb (v)-based units

and cuprous-halide clusters. *Chemical Communications*, 55(100), 15113-15116.

Lin, S., Usov, P. M., & Morris, A. J. (2018). The role of redox hopping in metal–organic framework electrocatalysis. *Chemical Communications*, 54(51), 6965-6974.

Lin, Z. J., Lü, J., Hong, M., & Cao, R. (2014). Metal–organic frameworks based on flexible ligands (FL-MOFs): structures and applications. *Chemical Society Reviews*, 43(16), 5867-5895.

Liu, B., Li, Y., Oh, S. C., Fang, Y., & Xi, H. (2016). Fabrication of a hierarchically structured HKUST-1 by a mixed-ligand approach. *RSC advances*, 6(66), 61006-61012.

Liu, D., Purewal, J. J., Yang, J., Sudik, A., Maurer, S., Mueller, U., Ni, J., & Siegel, D. J. (2012). MOF-5 composites exhibiting improved thermal conductivity. *international journal of hydrogen energy*, 37(7), 6109-6117.

Liu, D., Zou, D., Zhu, H., & Zhang, J. (2018). Mesoporous metal–organic frameworks: synthetic strategies and emerging applications. *Small*, 14(37), 1801454.

Liu, G., Wang, Y., Xue, Q., Wen, Y., Hong, X., & Ullah, K. (2021). TiO₂/Cu-MOF/PPy composite as a novel photocatalyst for decomposition of organic dyes. *Journal of Materials Science: Materials in Electronics*, 32(4), 4097-4109.

Liu, J. Q., Luo, Z. D., Pan, Y., Singh, A. K., Trivedi, M., & Kumar, A. (2020). Recent developments in luminescent coordination polymers: Designing

strategies, sensing application and theoretical evidences. *Coordination chemistry reviews*, 406, 213145.

Liu, S., Qiu, Y., Liu, Y., Zhang, W., Dai, Z., Srivastava, D., Kumar, A., Pan, Y., & Liu, J. (2022). Recent advances in bimetallic metal–organic frameworks (BMOFs): Synthesis, applications and challenges. *New Journal of Chemistry*, 46(29), 13818-13837.

Liu, W., Zhao, G., An, M., & Chang, L. (2015). Solvothermal synthesis of nanostructured BiVO₄ with highly exposed (0 1 0) facets and enhanced sunlight-driven photocatalytic properties. *Applied Surface Science*, 357, 1053-1063.

Liu, X. L., Yin, Q., Huang, G., & Liu, T. F. (2018). Stable pyrazolate-based metal-organic frameworks for drug delivery. *Inorganic Chemistry Communications*, 94, 21-26.

Liu, X., Kirlikovali, K. O., Chen, Z., Ma, K., Idrees, K. B., Cao, R., Zhang, X., Islamoglu, T., Liu, Y., & Farha, O. K. (2021). Small molecules, big effects: tuning adsorption and catalytic properties of metal–organic frameworks. *Chemistry of Materials*, 33(4), 1444-1454.

Liu, X., Zhou, Y., Xie, W., Liu, S., Zhao, Q., & Huang, W. (2020). Construction of smart manganese dioxide-based all-in-one nanoplatform for cancer diagnosis and therapy. *Small Methods*, 4(12), 2000566.

Liu, Y., Ghimire, P., & Jaroniec, M. (2019). Copper benzene-1, 3, 5-tricarboxylate (Cu-BTC) metal-organic framework (MOF) and porous carbon composites as efficient carbon dioxide adsorbents. *Journal of colloid and interface science*, 535, 122-132.

Liu, Y., Gu, P., Jia, L., & Zhang, G. (2016). An investigation into the use of cuprous chloride for the removal of radioactive iodide from aqueous solutions. *Journal of hazardous materials*, *302*, 82-89.

Liu, Y., Wang, S., Li, Z., Chu, H., & Zhou, W. (2023). Insight into the surface-reconstruction of metal-organic framework-based nanomaterials for the electrocatalytic oxygen evolution reaction. *Coordination Chemistry Reviews*, *484*, 215117.

Liu, Y., Xu, X., & Shao, Z. (2020). Metal-organic frameworks derived porous carbon, metal oxides and metal sulfides-based compounds for supercapacitors application. *Energy Storage Materials*, *26*, 1-22.

Liu, Y., Zhou, L., Dong, Y., Wang, R., Pan, Y., Zhuang, S., Liu, D., & Liu, J. (2021). Recent developments on MOF-based platforms for antibacterial therapy. *RSC Medicinal Chemistry*, *12*(6), 915-928.

López-Magano, A., Jiménez-Almarza, A., Alemán, J., & Mas-Ballesté, R. (2020). Metal-organic frameworks (MOFs) and covalent organic frameworks (COFs) applied to photocatalytic organic transformations. *Catalysts*, *10*(7), 720.

Lu, F., & Astruc, D. (2020). Nanocatalysts and other nanomaterials for water remediation from organic pollutants. *Coordination Chemistry Reviews*, *408*, 213180.

Lu, L., Wang, J., Shi, C., Sun, Y., Wu, W., Pan, Y., & Muddassir, M. (2021). Four structural diversity MOF-photocatalysts readily prepared for the degradation of the methyl violet dye under UV-visible light. *New Journal of Chemistry*, *45*(2), 551-560.

- Lu, W., Wei, Z., Gu, Z. Y., Liu, T. F., Park, J., Park, J., Tian, J., Zhang, M., Zhang, Q., Gentle III, T., Boscha, M., & Zhou, H. C. (2014). Tuning the structure and function of metal–organic frameworks via linker design. *Chemical Society Reviews*, *43*(16), 5561-5593.
- Lu, X., Li, M., Hoang, S., Suib, S. L., & Gao, P. X. (2021). Solvent effects on the heterogeneous growth of TiO₂ nanostructure arrays by solvothermal synthesis. *Catalysis Today*, *360*, 275-283.
- Lu, Z., Karakoti, A., Velarde, L., Wang, W., Yang, P., Thevuthasan, S., & Wang, H. F. (2013). Dissociative binding of carboxylic acid ligand on nanoceria surface in aqueous solution: a joint in situ spectroscopic characterization and first-principles study. *The Journal of Physical Chemistry C*, *117*(46), 24329-24338.
- Luo, R., Xu, H., Gu, H. X., Wang, X., Xu, Y., Shen, X., Bao, W., & Zhu, D. R. (2014). Four MOFs with 2, 2'-dimethoxy-4, 4'-biphenyldicarboxylic acid: syntheses, structures, topologies and properties. *CrystEng Comm*, *16*(5), 784-796.
- Luo, S., Zeng, Z., Zeng, G., Liu, Z., Xiao, R., Chen, M., Tang, L., Tang, W., Lai, C., Cheng, M., Shao, B., Liang, Q., Wang, H., & Jiang, D. (2019). Metal organic frameworks as robust host of palladium nanoparticles in heterogeneous catalysis: synthesis, application, and prospect. *ACS applied materials & interfaces*, *11*(36), 32579-32598.
- Lv, X. L., Feng, L., Wang, K. Y., Xie, L. H., He, T., Wu, W., Li, J., & Zhou, H. C. (2021). A Series of Mesoporous Rare-Earth Metal–Organic Frameworks Constructed from Organic Secondary Building Units. *Angewandte Chemie International Edition*, *60*(4), 2053-2057.

- Ma, D., Huang, X., Zhang, Y., Wang, L., & Wang, B. (2023). Metal-organic frameworks: Synthetic methods for industrial production. *Nano Research*, *16*(5), 7906-7925.
- Ma, P., Hu, F., Wang, J., & Niu, J. (2019). Carboxylate covalently modified polyoxometalates: From synthesis, structural diversity to applications. *Coordination Chemistry Reviews*, *378*, 281-309.
- Ma, X., Wang, L., Wang, H., Deng, J., Song, Y., Li, Q., Li, Q., & Dietrich, A. M. (2022). Insights into metal-organic frameworks HKUST-1 adsorption performance for natural organic matter removal from aqueous solution. *Journal of Hazardous Materials*, *424*, 126918.
- Ma, Y., Gao, W., Zhang, Z., Zhang, S., Tian, Z., Liu, Y., Ho, J. C., & Qu, Y. (2018). Regulating the surface of nanoceria and its applications in heterogeneous catalysis. *Surface Science Reports*, *73*(1), 1-36.
- Ma, Y., Li, X., Li, A., Yang, P., Zhang, C., & Tang, B. (2017). H₂S-activable MOF nanoparticle photosensitizer for effective photodynamic therapy against cancer with controllable singlet-oxygen release. *Angewandte Chemie International Edition*, *56*(44), 13752-13756.
- Mahalakshmi, G., & Balachandran, V. (2014). FT-IR and FT-Raman spectra, normal coordinate analysis and ab initio computations of Trimesic acid. *Spectrochimica Acta Part A: Molecular and Biomolecular Spectroscopy*, *124*, 535-547.
- Mahata, P., Mondal, S. K., Singha, D. K., & Majee, P. (2017). Luminescent rare-earth-based MOFs as optical sensors. *Dalton Transactions*, *46*(2), 301-328.

- Mahmoodi, N. M. (2014). Synthesis of magnetic carbon nanotube and photocatalytic dye degradation ability. *Environmental monitoring and assessment*, 186(9), 5595-5604.
- Mahreni, M., & Ristianingsih, Y. (2020). A review on Metal-Organic Framework (MOF): synthesis and solid catalyst applications. In *Proceeding of LPPM UPN "Veteran" Yogyakarta Conference Series 2020–Engineering and Science Series* (Vol. 1, No. 1, pp. 638-645).
- Majee, P., Singha, D. K., Mondal, S. K., & Mahata, P. (2019). Effect of charge transfer and structural rigidity on divergent luminescence response of a metal organic framework towards different metal ions: luminescence lifetime decay experiments and DFT calculations. *Photochemical & Photobiological Sciences*, 18(5), 1110-1121.
- Majewski, M. B., Noh, H., Islamoglu, T., & Farha, O. K. (2018). NanoMOFs: little crystallites for substantial applications. *Journal of Materials Chemistry A*, 6(17), 7338-7350.
- Makal, Tegan. (2015). Re: Does the pH value have a significant role in MOFs synthesis? Retrieved from: <https://www.researchgate.net/post/Does-the-pH-value-have-a-significant-role-in-MOFssynthesis/55783c2f6307d9bed48b45b9/citation/download>
- Makhlouf, A. S. H., & Aliofkhazraei, M. (Eds.). (2015). *Handbook of materials failure analysis with case studies from the aerospace and automotive industries*. Butterworth-Heinemann.

Manousi, N., Giannakoudakis, D. A., Rosenberg, E., & Zachariadis, G. A. (2019). Extraction of metal ions with metal–organic frameworks. *Molecules*, *24*(24), 4605.

Mansouri, M., Sadeghian, S., Mansouri, G., & Setareshenas, N. (2021). Enhanced photocatalytic performance of UiO-66-NH₂/TiO₂ composite for dye degradation. *Environmental Science and Pollution Research*, *28*, 25552-25565.

Manyani, N., Siwath, P., Rana, S., Sharma, K., & Tripathi, S. K. (2023). Study of electrochemical behaviour of binder-free nickel metal-organic framework derived by benzene-1, 3, 5-tricarboxylic acid for supercapacitor electrode. *Materials Research Bulletin*, *165*, 112320.

Marinho, M. V., Reis, D. O., Oliveira, W. X., Marques, L. F., Stumpf, H. O., Deniz, M., Jorge Pasán, J., Ruiz-Pérez, C., Cano, J., Lloret, F., & Julve, M. (2017). Photoluminescent and slow magnetic relaxation studies on lanthanide (III)-2, 5-pyrazinedicarboxylate frameworks. *Inorganic Chemistry*, *56*(4), 2108-2123.

Marshall, C. R., Staudhammer, S. A., & Brozek, C. K. (2019). Size control over metal–organic framework porous nanocrystals. *Chemical science*, *10*(41), 9396-9408.

Mat Yusuf, S. N. A., Ng, Y. M., Ayub, A. D., Ngalim, S. H., & Lim, V. (2017). Characterisation and evaluation of trimesic acid derivatives as disulphide cross-linked polymers for potential colon targeted drug delivery. *Polymers*, *9*(8), 311.

McGraw-Hill Dictionary of Scientific & Technical Terms (2003).

Multidentate ligand. The McGraw-Hill Companies, Inc.

- McKinstry, C., Cathcart, R. J., Cussen, E. J., Fletcher, A. J., Patwardhan, S. V., & Sefcik, J. (2016). Scalable continuous solvothermal synthesis of metal organic framework (MOF-5) crystals. *Chemical Engineering Journal*, 285, 718-725.
- Mehra, S., Singh, M., & Chadha, P. (2021). Adverse impact of textile dyes on the aquatic environment as well as on human beings. *Toxicol. Int*, 28(2), 165.
- Meng, X., Song, S. Y., Song, X. Z., Zhu, M., Zhao, S. N., Wu, L. L., & Zhang, H. J. (2015). A tetranuclear copper cluster-based MOF with sulfonate-carboxylate ligands exhibiting high proton conduction properties. *Chemical Communications*, 51(38), 8150-8152.
- Mezenov, Y. A., Krasilin, A. A., Dzyuba, V. P., Nominé, A., & Milichko, V. A. (2019). Metal-organic frameworks in modern physics: Highlights and perspectives. *Advanced Science*, 6(17), 1900506.
- Mittal, A., Mittal, J., Malviya, A., Kaur, D., & Gupta, V. K. (2010). Decoloration treatment of a hazardous triarylmethane dye, Light Green SF (Yellowish) by waste material adsorbents. *Journal of colloid and interface science*, 342(2), 518-527.
- Miyasaka, H. (2013). Control of charge transfer in donor/acceptor metal-organic frameworks. *Accounts of chemical research*, 46(2), 248-257.
- Moghadam, P. Z., Li, A., Wiggin, S. B., Tao, A., Maloney, A. G., Wood, P. A., Ward, S. C., & Fairen-Jimenez, D. (2017). Development of a Cambridge Structural Database subset: a collection of metal-organic frameworks for past, present, and future. *Chemistry of Materials*, 29(7), 2618-2625.

Mohebali, H., Moussavi, G., Karimi, M., & Giannakis, S. (2023). Development of a magnetic Ce-Zr bimetallic MOF as an efficient catalytic ozonation mediator: Preparation, characterization, and catalytic activity. *Separation and Purification Technology*, 315, 123670.

Mohomed, K. (2016). Thermogravimetric Analysis (TGA) Theory and Applications. *TA Instruments*.

Mollabagher, H., Taheri, S., majid Mojtahedi, M., & Seyedmousavi, S. (2020). Cu-metal organic frameworks (Cu-MOF) as an environment-friendly and economical catalyst for one pot synthesis of tacrine derivatives. *RSC advances*, 10(4), 1995-2003.

Morris, W., Wang, S., Cho, D., Auyeung, E., Li, P., Farha, O. K., & Mirkin, C. A. (2017). Role of modulators in controlling the colloidal stability and polydispersity of the UiO-66 metal-organic framework. *ACS applied materials & interfaces*, 9(39), 33413-33418.

Morritt, G. H., Michaels, H., & Freitag, M. (2022). Coordination polymers for emerging molecular devices. *Chemical Physics Reviews*, 3(1), 011306.

Mosleh, S., Rahimi, M. R., Ghaedi, M., & Dashtian, K. (2016). HKUST-1-MOF-BiVO₄ hybrid as a new sonophotocatalyst for simultaneous degradation of disulfine blue and rose bengal dyes: Optimization and statistical modelling. *RSC advances*, 6(66), 61516-61527.

Mouchaham, G., Cooper, L., Guillou, N., Martineau, C., Elkaïm, E., Bourrelly, S., Llewellyn, P. L., Allain, C., Clavier, G., Serre, C., & Devic, T. (2015). A robust infinite zirconium phenolate building unit

to enhance the chemical stability of Zr MOFs. *Angewandte Chemie*, 127(45), 13495-13499.

Mouchaham, G., Wang, S., & Serre, C. (2018). The stability of metal–organic frameworks. *Metal-Organic Frameworks: Applications in Separations and Catalysis*, 1-28.

Mruthunjayappa, M. H., Kotrappanavar, N. S., & Mondal, D. (2022). New prospect on organic solvents, ionic liquids and eutectic mixtures assisted solvothermal carbonisation—A critical review. *Progress in Materials Science*, 100932.

Mugumo, R., Tichapondwa, S. M., & Chirwa, E. (2022). Effects of initial pH and CuS/ZnS loading in rhodamine B photodegradation under visible light irradiation.

Mukasyan, A. S. (2017). DTA/TGA-based methods. In *Concise Encyclopedia of Self-Propagating High-Temperature Synthesis* (pp. 93-95). Elsevier.

Murad, A., Yusoff, N. M., Liew, J. Y. C., Yaacob, M. H., Goh, C. S., & Mahdi, M. A. (2022). Nickel 1, 3, 5-benzene-tricarboxylic acid-metal organic framework polymer composite saturable absorber for femtosecond pulse generation. *Results in Physics*, 41, 105881.

Musah, M., Azeh, Y., Mathew, J. T., Umar, M. T., Abdulhamid, Z., & Muhammad, A. I. (2022). Adsorption kinetics and isotherm models: a review. *CaJoST*, 4(1), 20-26.

NaderiNasrabadi, M., Mortazavi, Y., & Khodadadi, A. A. (2016). Highly sensitive and selective Gd₂O₃-doped SnO₂ ethanol sensors synthesized by a high temperature and pressure solvothermal method in a microreactor. *Sensors and Actuators B: Chemical*, 230, 130-139.

Nandihalli, N., Gregory, D. H., & Mori, T. (2022). Energy-Saving Pathways for Thermoelectric Nanomaterial Synthesis: Hydrothermal/Solvothermal, Microwave-Assisted, Solution-Based, and Powder Processing. *Advanced Science*, 9(25), 2106052.

Nandiyanto, A. B. D., Oktiani, R., & Ragadhita, R. (2019). How to read and interpret FTIR spectroscopy of organic material. *Indonesian Journal of Science and Technology*, 4(1), 97-118.

Nandiyanto, A. B. D., Ragadhita, R., & Fiandini, M. (2023). Interpretation of Fourier Transform Infrared Spectra (FTIR): A Practical Approach in the Polymer/Plastic Thermal Decomposition. *Indonesian Journal of Science and Technology*, 8(1), 113-126.

Nemiwal, M., & Kumar, D. (2020). Metal organic frameworks as water harvester from air: Hydrolytic stability and adsorption isotherms. *Inorganic Chemistry Communications*, 122, 108279.

Nimmermark, A., Öhrström, L., & Reedijk, J. (2013). Metal-ligand bond lengths and strengths: are they correlated? A detailed CSD analysis.

Nivetha, R., Sajeev, A., Paul, A. M., Gothandapani, K., Gnanasekar, S., Bhardwaj, P., Jacob, G., Sellappan, R., Raghavan, V., Chandar, K., Pitchaimuthu, S., Jeong, S. K. & Grace, A. N. (2020). Cu based Metal Organic Framework (Cu-MOF) for electrocatalytic hydrogen evolution reaction. *Materials Research Express*, 7(11), 114001.

Noa, F. M. A., Abrahamsson, M., Ahlberg, E., Cheung, O., Göb, C. R., McKenzie, C. J., & Öhrström, L. (2021). A unified topology approach to dot-, rod-, and sheet-MOFs. *Chem*, 7(9), 2491-2512.

- Nohara, A., Takeshita, S., & Isobe, T. (2014). Mixed-solvent strategy for solvothermal synthesis of well-dispersed $\text{YBO}_3: \text{Ce}^{3+}, \text{Tb}^{3+}$ nanocrystals. *RSC Advances*, 4(22), 11219-11224.
- Nozohour Yazdi, M., Yamini, Y., Asiabi, H., & Alizadeh, A. (2018). A metal organic framework prepared from benzene-1, 3, 5-tricarboxylic acid and copper (II), and functionalized with various polysulfides as a sorbent for selective sorption of trace amounts of heavy metal ions. *Microchimica Acta*, 185, 1-8.
- Nunes, D., Pimentel, A., Santos, L., Barquinha, P., Pereira, L., Fortunato, E., & Martins, R. (2019). Synthesis, design, and morphology of metal oxide nanostructures. *Metal Oxide Nanostructures*, 21-57.
- Nzikayel, S., Akpan, I. J., & Adams, E. C. (2017). Synthesis, ftir and electronic spectra studies of metal (ii) complexes of pyrazine-2-carboxylic acid derivative. *Medicinal Chemistry*, 7(11), 2161-0444.
- Ohtani, B. (2010). Photocatalysis A to Z-What we know and what we do not know in a scientific sense. *Journal of Photochemistry and Photobiology C: Photochemistry Reviews*, 11(4), 157-178.
- Olas, B., Białecki, J., Urbańska, K., & Bryś, M. (2021). The effects of natural and synthetic blue dyes on human health: A review of current knowledge and therapeutic perspectives. *Advances in Nutrition*, 12(6), 2301-2311.
- Olatunde, O. C., & Onwudiwe, D. C. (2021). Temperature controlled evolution of pure phase Cu_9S_5 nanoparticles by solvothermal process. *Frontiers in Materials*, 8, 687562.

- Opanasenko, M. (2018). Zeolite constructor kit: Design for catalytic applications. *Catalysis Today*, 304, 2-11.
- Ortega-Guerrero, A., Fumanal, M., Capano, G., Tavernelli, I., & Smit, B. (2020). Insights into the electronic properties and charge transfer mechanism of a porphyrin ruthenium-based metal–organic framework. *Chemistry of Materials*, 32(10), 4194-4204.
- Osman, D. I., El-Sheikh, S. M., Sheta, S. M., Ali, O. I., Salem, A. M., Shousha, W. El- Khamisy, S. F., & Shawky, S. M. (2019). Nucleic acids biosensors based on metal-organic framework (MOF): paving the way to clinical laboratory diagnosis. *Biosensors and Bioelectronics*, 141, 111451.
- Oxford Languages (2023). Catalyst. Retrieved from <https://languages.oup.com/google-dictionary-en/>
- Ozdemir, J. A. (2022). *Fabrication of MOF Films of UiO or PCN Type through Layer-by-Layer Molecular Deposition as Well as Bulk Deposition for Catalytic Applications* (Doctoral dissertation, University of Arkansas).
- Pan, W., Li, Z., Qiu, S., Dai, C., Wu, S., Zheng, X., Guan, M., & Gao, F. (2022). Octahedral Pt-MOF with Au deposition for plasmonic effect and Schottky junction enhanced hydrogenothermal therapy of rheumatoid arthritis. *Materials Today Bio*, 13, 100214.
- Panda, D., Patra, S., Awasthi, M. K., & Singh, S. K. (2020). Lab cooked MOF for CO₂ capture: a sustainable solution to waste management. *Journal of Chemical Education*, 97(4), 1101-1108.

- Panda, D., Patra, S., Awasthi, M. K., & Singh, S. K. (2020). Lab cooked MOF for CO₂ capture: a sustainable solution to waste management. *Journal of Chemical Education*, 97(4), 1101-1108.
- Pang, C., Gao, L., Chaturvedi, A., Bao, N., Yanagisawa, K., Shen, L., & Gupta, A. (2015). High-temperature solvothermal synthesis and magnetic properties of nearly monodisperse CdCr₂S₄ nanocrystals. *Journal of Materials Chemistry C*, 3(46), 12077-12082.
- Park, B. H., Jung, Y., & Kim, S. (2021). Particle Size Control Influence on the Electrochemical Properties of Sulfur Deposited on Metal Organic Frameworks Host Electrodes. *Journal of Inorganic and Organometallic Polymers and Materials*, 31(5), 1931-1938.
- Patial, S., Raizada, P., Hasija, V., Singh, P., Thakur, V. K., & Nguyen, V. H. (2021). Recent advances in photocatalytic multivariate metal organic frameworks-based nanostructures toward renewable energy and the removal of environmental pollutants. *Materials Today Energy*, 19, 100589.
- Pei, J., Shao, K., Zhang, L., Wen, H. M., Li, B., & Qian, G. (2020). Current status of microporous metal–organic frameworks for hydrocarbon separations. *Metal-Organic Framework: From Design to Applications*, 305-338.
- Peng, C., Song, X., Yin, J., Zhang, G., & Fei, H. (2019). Intrinsic White-Light-Emitting Metal–Organic Frameworks with Structurally Deformable Secondary Building Units. *Angewandte Chemie*, 131(23), 7900-7904.

Peng, M. M., Ganesh, M., Vinodh, R., Palanichamy, M., & Jang, H. T. (2019). Solvent free oxidation of ethylbenzene over Ce-BTC MOF. *Arabian Journal of Chemistry*, 12(7), 1358-1364.

Peplow, M. (2015). The whole story. *Nature*, 520(7546), 148-151.

Peralta, R. A., Huxley, M. T., Albalad, J., Sumbly, C. J., & Doonan, C. J. (2021). Single-Crystal-to-Single-Crystal Transformations of Metal–Organic-Framework-Supported, Site-Isolated Trigonal-Planar Cu (I) Complexes with Labile Ligands. *Inorganic Chemistry*, 60(16), 11775-11783.

Pervez, M. N., Chen, C., Li, Z., Naddeo, V., & Zhao, Y. (2022). Tuning the structure of cerium-based metal-organic frameworks for efficient removal of arsenic species: The role of organic ligands. *Chemosphere*, 303, 134934.

Phan, D. P., Nguyen, T. H., Kim, H. B., Park, E. D., Kim, J., & Lee, E. Y. (2021). Effect of amino-defective-MOF materials on the selective hydrodeoxygenation of fatty acid over Pt-based catalysts. *Journal of Catalysis*, 400, 283-293.

Piciorus, M., Alexandru, P. O. P. A., Ianasi, C., Szerb, E. I., & Cretu, C. (2020). Zr (IV) mofs based on terephthalic acid and acetic acid modulator. *Scientific and Technical Bulletin, Series: Chemistry, Food Science and Engineering*, 17, 33-41.

Piernas Muñoz, M. J., Castillo Martínez, E., Piernas Muñoz, M. J., & Castillo Martínez, E. (2018). Prussian blue and its analogues. Structure, characterization and applications. *Prussian Blue Based Batteries*, 9-22.

- Prasath, R. R., Muthirulan, P., & Kannan, N. (2014). Agricultural wastes as a low cost adsorbents for the removal of Acid Blue 92 dye: A comparative study with commercial activated carbon. *IOSR Journal of Agriculture and Veterinary Science*, 7(2), 19-32.
- Pushie, M. J., Stefaniak, E., Sendzik, M. R., Sokaras, D., Kroll, T., & Haas, K. L. (2019). Using N-terminal coordination of Cu (II) and Ni (II) to isolate the coordination environment of Cu (I) and Cu (II) bound to His13 and His14 in Amyloid- β (4–16). *Inorganic Chemistry*, 58(22), 15138-15154.
- Qian, L. L., Wang, Z. X., Tian, H. X., Li, M., Li, B. L., & Li, H. Y. (2019). Synthesis, structure and photocatalytic degradation of organic dyes of a copper (II) metal–organic framework (Cu–MOF) with a 4-coordinated three-dimensional CdSO₄ topology. *Acta Crystallographica Section C: Structural Chemistry*, 75(8), 1053-1059.
- Qin, J. H., Qin, W. J., Xiao, Z., Yang, J. K., Wang, H. R., Yang, X. G., Li, D. S., & Ma, L. F. (2021). Efficient energy-transfer-induced high photoelectric conversion in a dye-encapsulated ionic pyrene-based metal–organic framework. *Inorganic Chemistry*, 60(24), 18593-18597.
- Qiu, J., Zhang, X., Feng, Y., Zhang, X., Wang, H., & Yao, J. (2018). Modified metal-organic frameworks as photocatalysts. *Applied Catalysis B: Environmental*, 231, 317-342.
- Qiu, Y., Deng, H., Yang, S., Mou, J., Daiguebonne, C., Kerbellec, N., Guillou, O & Batten, S. R. (2009). Syntheses, crystal structures, and gas storage studies in new three-dimensional 5-aminoisophthalate praseodymium polymeric complexes. *Inorganic chemistry*, 48(9), 3976-3981.

Rachuri, Y., Parmar, B., Bisht, K. K., & Suresh, E. (2017). Solvothermal self-assembly of Cd²⁺ coordination polymers with supramolecular networks involving N-donor ligands and aromatic dicarboxylates: synthesis, crystal structure and photoluminescence studies. *Dalton Transactions*, 46(11), 3623-3630.

Rafiq, A., Ikram, M., Ali, S., Niaz, F., Khan, M., Khan, Q., & Maqbool, M. (2021). Photocatalytic degradation of dyes using semiconductor photocatalysts to clean industrial water pollution. *Journal of Industrial and Engineering Chemistry*, 97, 111-128.

Ragon, F., Campo, B., Yang, Q., Martineau, C., Wiersum, A. D., Lago, A. & Clet, G. (2015). Acid-functionalized UiO-66 (Zr) MOFs and their evolution after intra-framework cross-linking: structural features and sorption properties. *Journal of Materials Chemistry A*, 3(7), 3294-3309.

Ramachandran, R., Xuan, W., Zhao, C., Leng, X., Sun, D., Luo, D., & Wang, F. (2018). Enhanced electrochemical properties of cerium metal-organic framework based composite electrodes for high-performance supercapacitor application. *RSC advances*, 8(7), 3462-3469.

Ramadoss, R., & Subramaniam, D. (2019). Removal of divalent nickel from aqueous solution using blue-green marine algae: adsorption modeling and applicability of various isotherm models. *Separation Science and Technology*, 54(6), 943-961.

Ramalingam, G., Pachaiappan, R., Kumar, P. S., Dharani, S., Rajendran, S., Vo, D. V. N., & Hoang, T. K. (2022). Hybrid metal organic

- frameworks as an Exotic material for the photocatalytic degradation of pollutants present in wastewater: a review. *Chemosphere*, 288, 132448.
- Ramanayaka, S., Vithanage, M., Sarmah, A., An, T., Kim, K. H., & Ok, Y. S. (2019). Performance of metal–organic frameworks for the adsorptive removal of potentially toxic elements in a water system: a critical review. *RSC advances*, 9(59), 34359-34376.
- Ramathulasamma, M., Bommakanti, S., & Das, S. K. (2023). Diverse coordination architectures based on a flexible multidentate carboxylate ligand and N-donor linkers: Synthesis, structure, supramolecular chemistry and related properties. *Polyhedron*, 230, 116216.
- Rápó, E., Aradi, L. E., Szabó, Á., Posta, K., Szép, R., & Tonk, S. (2020). Adsorption of remazol brilliant violet-5R textile dye from aqueous solutions by using eggshell waste biosorbent. *Scientific reports*, 10(1), 8385.
- Raptopoulou, C. P. (2021). Metal-organic frameworks: Synthetic methods and potential applications. *Materials*, 14(2), 310.
- Reddy, P. A. K., Reddy, P. V. L., Kwon, E., Kim, K. H., Akter, T., & Kalagara, S. (2016). Recent advances in photocatalytic treatment of pollutants in aqueous media. *Environment international*, 91, 94-103.
- Reza, K. M., Kurny, A. S. W., & Gulshan, F. (2017). Parameters affecting the photocatalytic degradation of dyes using TiO 2: a review. *Applied Water Science*, 7, 1569-1578.

- Rezaei, K. M. R., Oveisi, A. R., Kaykhaii, M., & Rezaei K. B. (2018). Determination of carbamazepine in urine and water samples using amino-functionalized metal-organic framework as sorbent. *Chemistry Central Journal*, 12(1), 1-12.
- Rhauderwiek, T., Heidenreich, N., Reinsch, H., Øien-Ødegaard, S., Lomachenko, K. A., Rütt, U., Soldatov, A. V., Lillerud, K. P., & Stock, N. (2017). Co-ligand dependent formation and phase transformation of four porphyrin-based cerium metal-organic frameworks. *Crystal Growth & Design*, 17(6), 3462-3474.
- Rocío-Bautista, P., González-Hernández, P., Pino, V., Pasán, J., & Afonso, A. M. (2017). Metal-organic frameworks as novel sorbents in dispersive-based microextraction approaches. *TrAC Trends in Analytical Chemistry*, 90, 114-134.
- Rocío-Bautista, P., Taima-Mancera, I., Pasán, J., & Pino, V. (2019). Metal-organic frameworks in green analytical chemistry. *Separations*, 6(3), 33.
- Rojas-Buzo, S., Bohigues, B., Lopes, C. W., Meira, D. M., Boronat, M., Moliner, M., & Corma, A. (2021). Tailoring Lewis/Brønsted acid properties of MOF nodes via hydrothermal and solvothermal synthesis: simple approach with exceptional catalytic implications. *Chemical Science*, 12(29), 10106-10115.
- Rowe, O. (2013). *Use of multiple functionalised ligand sets in metalorganic framework formation: synthesis, characterisation and gas uptake studies* (Doctoral dissertation, University of East Anglia).

Ru, J., Zhang, R. F., Wang, Y. X., Ma, X. X., Guo, Q., Du, X. M., Li. L. L., & Wang, Y. L. (2022). Water-stable Cd (II) metal-organic framework as multi-responsive luminescent sensor for CrO_4^{2-} , $\text{Cr}_2\text{O}_7^{2-}$ ions and picric acid as well as its mixed matrix membranes. *Journal of Solid State Chemistry*, 311, 123119.

Saadatkhan, N., Carillo Garcia, A., Ackermann, S., Leclerc, P., Latifi, M., Samih, S., & Chaouki, J. (2020). Experimental methods in chemical engineering: thermogravimetric analysis—TGA. *The Canadian Journal of Chemical Engineering*, 98(1), 34-43.

Saber-Samandari, S., & Gazi, M. (2015). Pullulan based porous semi-IPN hydrogel: Synthesis, characterization and its application in the removal of mercury from aqueous solution. *Journal of the Taiwan Institute of Chemical Engineers*, 51, 143-151.

Safaei, M., Foroughi, M. M., Ebrahimpoor, N., Jahani, S., Omid, A., & Khatami, M. (2019). A review on metal-organic frameworks: Synthesis and applications. *TrAC Trends in Analytical Chemistry*, 118, 401-425.

Saha, S., Chaudhary, N., Kumar, A., & Khanuja, M. (2020). Polymeric nanostructures for photocatalytic dye degradation: polyaniline for photocatalysis. *SN Applied Sciences*, 2, 1-10.

Sahil, K., Prashant, B., Akanksha, M., Premjeet, S. & Devashish, R. (2012). Interpretation of Infra Red Spectra. *International journal of pharmaceutical and chemical sciences*. Vol. 1 (1)175-200.

Saini, K., Jojeph, F., & Bhatia, S. S. (2018). Electrochemical synthesis of copper (II) based metal organic frameworks: Determination of

structure by Single X-ray diffraction crystallography and other supportive techniques. *Adv. Mater. Process*, 3, 469-474.

Samanta, P., Desai, A. V., Let, S., & Ghosh, S. K. (2019). Advanced porous materials for sensing, capture and detoxification of organic pollutants toward water remediation. *ACS Sustainable Chemistry & Engineering*, 7(8), 7456-7478.

Samuel, M. S., Savunthari, K. V., & Ethiraj, S. (2021). Synthesis of a copper (II) metal–organic framework for photocatalytic degradation of rhodamine B dye in water. *Environmental Science and Pollution Research*, 28, 40835-40843.

Sánchez-Serratos, M., Álvarez, J. R., González-Zamora, E., & Ibarra, I. A. (2016). Porous coordination polymers (Pcps): New platforms for gas storage. *Journal of the Mexican Chemical Society*, 60(2), 43-57.

Sangeetha, S., & Krishnamurthy, G. (2020). Electrochemical and photocatalytic applications of Ce-MOF. *Bulletin of Materials Science*, 43(1), 1-10.

Santos, P. F., & Luz, P. P. (2020). Synthesis of a Ce-based MOF-76 with high yield: a study of reaction parameters based on a factorial design. *Journal of the Brazilian Chemical Society*, 31, 566-573.

Saraci, F., Quezada-Novoa, V., Donnarumma, P. R., & Howarth, A. J. (2020). Rare-earth metal–organic frameworks: from structure to applications. *Chemical Society Reviews*, 49(22), 7949-7977.

Sarmadi, A., Msoudpanah, S. M., & Alamolhoda, S. (2022). Amino Acid-Assisted Solvothermal Synthesis of LiFePO₄ Cathode

Materials. *Journal of Ultrafine Grained and Nanostructured Materials*, 55(1), 37-44.

Saxena, A., & Gupta, S. (2022). Toxicological Impact of Azo Dyes Azo dyes and Their Microbial Degraded Byproducts on Flora and Fauna. In *Innovations in environmental biotechnology* (pp. 319-343). Singapore: Springer Nature Singapore.

Schlachter, A., Lapprand, A., Fortin, D., Strohmann, C., Harvey, P. D., & Knorr, M. (2020). From Short-Bite Ligand Assembled Ribbons to Nanosized Networks in Cu (I) Coordination Polymers Built Upon Bis (benzylthio) alkanes (BzS (CH₂)_n SBz; n= 1–9). *Inorganic Chemistry*, 59(6), 3686-3708.

Schlumberger, C., & Thommes, M. (2021). Characterization of hierarchically ordered porous materials by physisorption and mercury porosimetry—a tutorial review. *Advanced Materials Interfaces*, 8(4), 2002181.

Schoedel, A., Li, M., Li, D., O’Keeffe, M., & Yaghi, O. M. (2016). Structures of metal–organic frameworks with rod secondary building units. *Chemical Reviews*, 116(19), 12466-12535.

Schweighauser, L., Harano, K., & Nakamura, E. (2017). Experimental study on interconversion between cubic MOF-5 and square MOF-2 arrays. *Inorganic Chemistry Communications*, 84, 1-4.

Seetharaj, R., Vandana, P. V., Arya, P., & Mathew, S. (2019). Dependence of solvents, pH, molar ratio and temperature in tuning metal organic framework architecture. *Arabian journal of chemistry*, 12(3), 295-315.

Segneanu, A. E., Gozescu, I., Dabici, A., Sfirloaga, P., & Szabadai, Z. (2012). *Organic compounds FT-IR spectroscopy* (Vol. 145). Rijeka, Croatia: InTech.

Seidel, C., Lorbeer, C., Cybińska, J., Mudring, A. V., & Ruschewitz, U. (2012). Lanthanide coordination polymers with tetrafluoroterephthalate as a bridging ligand: thermal and optical properties. *Inorganic Chemistry*, 51(8), 4679-4688.

Semitut, E., Sukhikh, T., Filatov, E., Ryadun, A., & Potapov, A. (2017). Synthesis, crystal structure and luminescent properties of 2D zinc coordination polymers based on bis (1, 2, 4-triazol-1-yl) methane and 1, 3-bis (1, 2, 4-triazol-1-yl) propane. *Crystals*, 7(12), 354.

Senkovska, I., & Kaskel, S. (2014). Ultrahigh porosity in mesoporous MOFs: promises and limitations. *Chemical communications*, 50(54), 7089-7098.

Seoane, B., Castellanos, S., Dikhtiarenko, A., Kapteijn, F., & Gascon, J. (2016). Multi-scale crystal engineering of metal organic frameworks. *Coordination Chemistry Reviews*, 307, 147-187.

Servati Gargari, M., Stilinović, V., Bauzá, A., Frontera, A., McArdle, P., Van Derveer, D., Weng Ng, S., & Mahmoudi, G. (2015). Design of lead (II) metal-organic frameworks based on covalent and tetrel bonding. *Chemistry—A European Journal*, 21(49), 17951-17958.

Seyedpour, S. F., Dadashi Firouzjaei, M., Rahimpour, A., Zolghadr, E., Arabi Shamsabadi, A., Das, P., Afkhami, F. A., Sadrzadeh, M., Tiraferri, A., & Elliott, M. (2020). Toward sustainable tackling of biofouling implications and improved performance of TFC FO membranes

modified by Ag-MOF nanorods. *ACS applied materials & interfaces*, 12(34), 38285-38298.

Shan, B. (2019). *Synthesis and Characterization of 2D and 3D Metal Organic Frameworks*. A Dissertation Presented in Partial Fulfillment of the Requirements for the Degree Doctor of Philosophy Arizona State University.

Shan, B., James, J. B., Armstrong, M. R., Close, E. C., Letham, P. A., Nikkhah, K., Lin, Y. S., & Mu, B. (2018). Influences of deprotonation and modulation on nucleation and growth of UiO-66: Intergrowth and Orientation. *The Journal of Physical Chemistry C*, 122(4), 2200-2206.

Sharmin, E., & Zafar, F. (2016). Introductory chapter: metal organic frameworks (MOFs). In *Metal-organic frameworks*. IntechOpen.

Shearer, G. C., Chavan, S., Bordiga, S., Svelle, S., Olsbye, U., & Lillerud, K. P. (2016). Defect engineering: tuning the porosity and composition of the metal-organic framework UiO-66 via modulated synthesis. *Chemistry of Materials*, 28(11), 3749-3761.

Sheldrick, G.M., Crystal structure refinement with ShelXL, *Acta Cryst.*, (2015a), C71, 3-8.

Sheldrick, G.M., ShelXT-Integrated space-group and crystal-structure determination, *Acta Cryst.*, (2015b), A71, 3-8.

Shen, W., Guo, X., & Pang, H. (2022). Effect of Solvothermal Temperature on Morphology and Supercapacitor Performance of Ni-MOF. *Molecules*, 27(23), 8226.

Sheta, S. M., El-Sheikh, S. M., Abd-Elzaher, M. M., & Wassel, A. R. (2019). A novel nano-size lanthanum metal-organic framework based on 5-

amino-isophthalic acid and phenylenediamine: photoluminescence study and sensing applications. *Applied Organometallic Chemistry*, 33(4), e4777.

Shi, X., Cao, B., Liu, J., Zhang, J., & Du, Y. (2021). Rare-earth-based metal-organic frameworks as multifunctional platforms for catalytic conversion. *Small*, 17(22), 2005371.

Shi, Y., Yang, A. F., Cao, C. S., & Zhao, B. (2019). Applications of MOFs: Recent advances in photocatalytic hydrogen production from water. *Coordination Chemistry Reviews*, 390, 50-75.

Shi, Z. Q., Ji, N. N., Wang, M. H., & Li, G. (2020). A comparative study of proton conduction between a 2D Zinc (II) MOF and its corresponding organic ligand. *Inorganic chemistry*, 59(7), 4781-4789.

Shortall, K., Otero, F., Bendl, S., Soulimane, T., & Magner, E. (2022). Enzyme Immobilization on Metal Organic Frameworks: the Effect of Buffer on the Stability of the Support. *Langmuir*, 38(44), 13382-13391.

Siegelman, R. L., Kim, E. J., & Long, J. R. (2021). Porous materials for carbon dioxide separations. *Nature materials*, 20(8), 1060-1072.

Silmi, N., Febriyanti, E., Andriani, A., Arsyad, R., Steky, F. V., Mukti, R. R., & Suendo, V. (2021). Textural control of bicontinuous concentric lamellar nanostructured mesoporous silica via low-pressure solvothermal method. *Materials Chemistry and Physics*, 265, 124492.

Singh, A., Singh, A. K., Liu, J., & Kumar, A. (2021). Syntheses, design strategies, and photocatalytic charge dynamics of metal-organic

frameworks (MOFs): a catalyzed photo-degradation approach towards organic dyes. *Catalysis Science & Technology*, 11(12), 3946-3989.

Singh, G., Lee, J., Karakoti, A., Bahadur, R., Yi, J., Zhao, D., AlBahily, K., & Vinu, A. (2020). Emerging trends in porous materials for CO₂ capture and conversion. *Chemical Society Reviews*, 49(13), 4360-4404.

Singh, K. A. R. U. N. A., Kumar, P. A. N. K. A. J., & Srivastava, R. A. J. A. N. I. (2017). An overview of textile dyes and their removal techniques: Indian perspective. *Pollut. Res*, 36, 790-797.

Singha, D. K., & Mahata, P. (2015). Highly selective and sensitive luminescence turn-on-based sensing of Al³⁺ ions in aqueous medium using a MOF with free functional sites. *Inorganic chemistry*, 54(13), 6373-6379.

Soares, J. B., & Pérez, O. (2013). Coordination polymerization. *Handbook of Polymer Synthesis, Characterization, and Processing*, 85-104.

Soltani, B., Ghorbanpour, M., Bagheri, S., Ebadi-Nahari, M., & J Ziegler, C. (2023). Synthesis, Crystal Structure and Antibacterial Activity of Cu (II) Complex with Nitrogen Donor Pyrazolyl Borate Derivatives. *Pharmaceutical Sciences*, 29(2), 236-245.

Song, X., Hu, D., Yang, X., Zhang, H., Zhang, W., Li, J., Jia, M., & Yu, J. (2019). Polyoxomolybdic cobalt encapsulated within Zr-based metal-organic frameworks as efficient heterogeneous catalysts for olefins epoxidation. *ACS Sustainable Chemistry & Engineering*, 7(3), 3624-3631.

- Soni, S., Bajpai, P. K., & Arora, C. (2020). A review on metal-organic framework: Synthesis, properties and application. *Characterization and Application of Nanomaterials*, 3(2), 87-106.
- Sousa, J. C., Ribeiro, A. R., Barbosa, M. O., Pereira, M. F. R., & Silva, A. M. (2018). A review on environmental monitoring of water organic pollutants identified by EU guidelines. *Journal of hazardous materials*, 344, 146-162.
- Stuart, B. H. (2004). *Infrared spectroscopy: fundamentals and applications*. John Wiley & Sons.
- Su, X., Xu, T., Ye, R., Guo, C., Wabaidur, S. M., Chen, D. L., Aftab, S., Zhong, Y., & Hu, Y. (2023). One-pot solvothermal synthesis of In-doped amino-functionalized UiO-66 Zr-MOFs with enhanced ligand-to-metal charge transfer for efficient visible-light-driven CO₂ reduction. *Journal of Colloid and Interface Science*, 646, 129-140.
- Sud, D., & Kaur, G. (2021). A comprehensive review on synthetic approaches for metal-organic frameworks: From traditional solvothermal to greener protocols. *Polyhedron*, 193, 114897.
- Sugamata, K., Kobayashi, S., Iihama, T., & Minoura, M. (2021). Gas Adsorption in R₂-MOF-5 Difunctionalized with Alkyl Groups. *European Journal of Inorganic Chemistry*, 2021(31), 3185-3190.
- Sun, H., Zhang, H., Mao, H., Yu, B., Han, J., & Bhat, G. (2019). Facile synthesis of the magnetic metal-organic framework Fe₃O₄/Cu₃(BTC)₂ for efficient dye removal. *Environmental Chemistry Letters*, 17(2), 1091-1096.

- Sun, Y. X., & Sun, W. Y. (2015). Zinc (II)-and cadmium (II)-organic frameworks with 1-imidazole-containing and 1-imidazole-carboxylate ligands. *CrystEng Comm*, 17(22), 4045-4063.
- Surib, N. A., Kuila, A., Saravanan, P., Sim, L. C., & Leong, K. H. (2018). A ligand strategic approach with Cu-MOF for enhanced solar light photocatalysis. *New Journal of Chemistry*, 42(13), 11124-11130.
- Taghavi Fardood, S., Ramazani, A., & Woo Joo, S. (2017). Sol-gel synthesis and characterization of zinc oxide nanoparticles using black tea extract. *Journal of Applied Chemical Research*, 11(4), 8-17.
- Taher, A., Kim, D. W., & Lee, I. M. (2017). Highly efficient metal organic framework (MOF)-based copper catalysts for the base-free aerobic oxidation of various alcohols. *RSC advances*, 7(29), 17806-17812.
- Tajněšek, T. K., Zabukovec Logar, N., & Mazaj, M. (2023). Tuning Size and Properties of Zinc Ascorbate Metal-Organic Framework via Acid Modulation. *Molecules*, 28(1), 253.
- Tambat, S., Umale, S., & Sontakke, S. (2016). Photocatalytic degradation of Milling Yellow dye using sol-gel synthesized CeO₂. *Materials Research Bulletin*, 76, 466-472.
- Tan, A. D., Zhao, B., Liu, L., & Dai, J. C. (2015). Synthesis, structure, and characterization of polymeric lanthanide 2-aminoterephthalate frameworks [Ln₂ (atp)₃ (H₂O)₂]· dmf· 4H₂O. *Inorganic Chemistry Communications*, 61, 140-143.
- Tan, T. L., bin Mohammad Latif, M. A., & Rashid, S. A. (2022). One-pot solvothermal synthesis of Zr-based MOFs with enhanced adsorption

capacity for Cu^{2+} ions removal. *Journal of Solid State Chemistry*, 315, 123429.

Tatikonda, R. (2018). Multivalent N-donor ligands for the construction of coordination polymers and coordination polymer gels. *Research report/Department of Chemistry. University of Jyväskylä*, (208).

Tesh, S. J., & Scott, T. B. (2014). Nano-composites for water remediation: A review. *Advanced Materials*, 26(35), 6056-6068.

Tombesi, A., & Pettinari, C. (2021). Metal organic frameworks as heterogeneous catalysts in olefin epoxidation and carbon dioxide cycloaddition. *Inorganics*, 9(11), 81.

Tombesi, A., & Pettinari, C. (2021). Metal organic frameworks as heterogeneous catalysts in olefin epoxidation and carbon dioxide cycloaddition. *Inorganics*, 9(11), 81.

Treto-Suárez, M. A., Hidalgo-Rosa, Y., Ulecia, K. M., Páez-Hernández, D., Koivisto, B. D., Zarate, X., & Schott, E. (2023). Tuning the optical properties of a photocatalytic metal-organic framework by means of molecular modelling. *New Journal of Chemistry*, 47(7), 3430-3444.

Tripathy, S. P., Subudhi, S., & Parida, K. (2021). Inter-MOF hybrid (IMOFH): A concise analysis on emerging core-shell based hierarchical and multifunctional nanoporous materials. *Coordination Chemistry Reviews*, 434, 213786.

Tripathy, S. P., Subudhi, S., Ray, A., Behera, P., Bhaumik, A., & Parida, K. (2022). Mixed-valence bimetallic Ce/Zr MOF-based nanoarchitecture: a visible-light-active photocatalyst for ciprofloxacin degradation and hydrogen evolution. *Langmuir*, 38(5), 1766-1780.

- Tsivadze, A. Y., Aksyutin, O. E., Ishkov, A. G., Knyazeva, M. K., Solovtsova, O. V., Men'shchikov, I. E., ... & Grachev, V. A. (2019). Metal-organic framework structures: Adsorbents for natural gas storage. *Russian Chemical Reviews*, 88(9), 925.
- Tu, X., Xie, Y., Ma, X., Gao, F., Gong, L., Wang, D., Lu, L., Liu, G., Yu, Y., & Huang, X. (2019). Highly stable reduced graphene oxide-encapsulated Ce-MOF composite as sensing material for electrochemically detecting dichlorophen. *Journal of Electroanalytical Chemistry*, 848, 113268.
- Ullah, I., ul Haq, T., Khan, A. A., Inayat, A., Shoaib, M., Haider, A., Saleem, M., Abbas, S. M., Pope, M. A. & Hussain, I. (2023). Sodium decavanadate encapsulated Mn-BTC POM@ MOF as high-capacity cathode material for aqueous sodium-ion batteries. *Journal of Alloys and Compounds*, 932, 167647.
- Usman, M., Mendiratta, S., & Lu, K. L. (2017). Semiconductor metal-organic frameworks: future low-bandgap materials. *Advanced Materials*, 29(6), 1605071.
- Vakili, R. (2020). *Metal-organic frameworks (MOFs) for heterogeneous catalysis*. The University of Manchester (United Kingdom).
- Valvekens, P., Vandichel, M., Waroquier, M., Van Speybroeck, V., & De Vos, D. (2014). Metal-dioxidoterephthalate MOFs of the MOF-74 type: Microporous basic catalysts with well-defined active sites. *Journal of catalysis*, 317, 1-10.
- Van Santen, R. A. (2017). *Modern heterogeneous catalysis: an introduction*. John Wiley & Sons.

- Vaquero, F., Navarro, R. M., & Fierro, J. L. G. (2017). Influence of the solvent on the structure, morphology and performance for H₂ evolution of CdS photocatalysts prepared by solvothermal method. *Applied Catalysis B: Environmental*, 203, 753-767.
- Varga, M. (2016). Self-assembly of nanobiomaterials. In *Fabrication and Self-Assembly of Nanobiomaterials* (pp. 57-90). William Andrew Publishing.
- Varjani, S., Rakholiya, P., Ng, H. Y., You, S., & Teixeira, J. A. (2020). Microbial degradation of dyes: an overview. *Bioresour Technol*, 314, 123728.
- Varsha, M. V., & Nageswaran, G. (2020). Direct electrochemical synthesis of metal organic frameworks. *Journal of The Electrochemical Society*, 167(15), 155527.
- Védrine, J. C. (2017). Heterogeneous catalysis on metal oxides. *Catalysts*, 7(11), 341.
- Velegraki, T., Hapeshi, E., Fatta-Kassinos, D., & Poulios, I. (2015). Solar-induced heterogeneous photocatalytic degradation of methylparaben. *Applied Catalysis B: Environmental*, 178, 2-11.
- Vellingiri, K., Kumar, P., Deep, A., & Kim, K. H. (2017). Metal-organic frameworks for the adsorption of gaseous toluene under ambient temperature and pressure. *Chemical Engineering Journal*, 307, 1116-1126.
- Venkateshalu, S., Kumar, P. G., Kollu, P., Jeong, S. K., & Grace, A. N. (2018). Solvothermal synthesis and electrochemical properties of phase

pure pyrite FeS₂ for supercapacitor applications. *Electrochimica Acta*, 290, 378-389.

Villemot, V., Hamel, M., Pansu, R. B., Leray, I., & Bertrand, G. H. (2020). Unravelling the true MOF-5 luminescence. *RSC advances*, 10(31), 18418-18422.

Vizuet, J. P., Howlett, T. S., Lewis, A. L., Chroust, Z. D., McCandless, G. T., & Balkus Jr, K. J. (2019). Transition from a 1D coordination polymer to a mixed-linker layered MOF. *Inorganic Chemistry*, 58(8), 5031-5041.

Vizuet, J. P., Lewis, A. L., McCandless, G. T., & Balkus Jr, K. J. (2019). Synthesis and characterization of a holmium 2, 2'-bipyridine-5, 5'-dicarboxylate MOF: Towards the construction of a suitable holmium carrier. *Polyhedron*, 159, 12-17.

Vogel, D. J., Nenoff, T. M., & Rimsza, J. M. (2020). Tuned hydrogen bonding in rare-earth metal-organic frameworks for design of optical and electronic properties: an exemplar study of Y-2, 5-dihydroxyterephthalic acid. *ACS applied materials & interfaces*, 12(4), 4531-4539.

Wacławek, S., Padil, V. V., & Černík, M. (2018). Major advances and challenges in heterogeneous catalysis for environmental applications: a review. *Ecological Chemistry and Engineering S*, 25(1), 9-34.

Walsh, J. J., Bond, A. M., Forster, R. J., & Keyes, T. E. (2016). Hybrid polyoxometalate materials for photo (electro-) chemical applications. *Coordination Chemistry Reviews*, 306, 217-234.

Walton, R. I. (2020). Perovskite oxides prepared by hydrothermal and solvothermal synthesis: a review of crystallisation, chemistry, and compositions. *Chemistry—A European Journal*, 26(42), 9041-9069.

Wang R, Sivakumar V, Li Y, Redding K, Hastings G. 2003 Mutation induced modulation of hydrogen bonding to P700 studied using FTIR difference spectroscopy. *Biochemistry* 42, 9889–9897. (doi:10.1021/bi034230c)

Wang, C. C., Li, J. R., Lv, X. L., Zhang, Y. Q., & Guo, G. (2014). Photocatalytic organic pollutants degradation in metal–organic frameworks. *Energy & Environmental Science*, 7(9), 2831-2867.

Wang, C., Li, L., Bell, J. G., Lv, X., Tang, S., Zhao, X., & Thomas, K. M. (2015). Hysteretic gas and vapor sorption in flexible interpenetrated lanthanide-based metal–organic frameworks with coordinated molecular gating via reversible single-crystal-to-single-crystal transformation for enhanced selectivity. *Chemistry of Materials*, 27(5), 1502-1516.

Wang, C., Lin, G., Zhao, J., Wang, S., & Zhang, L. (2020). Enhancing Au (III) adsorption capacity and selectivity via engineering MOF with mercapto-1, 3, 4-thiadiazole. *Chemical Engineering Journal*, 388, 124221.

Wang, D., Ao, C., Liu, X., Fang, S., Lin, Y., Liu, W., Zhang, W., Zheng, X., Zhang, L., & Yao, T. (2019). Coordination-engineered Cu–N x single-site catalyst for enhancing oxygen reduction reaction. *ACS Applied Energy Materials*, 2(9), 6497-6504.

- Wang, F. K., Yang, S. Y., & Dong, H. Z. (2021). Solvent dependent Zinc (II) coordination polymers with 1, 3, 5-benzenetricarboxylic acid and the selective photocatalytic degradation for organic dyes. *Journal of Molecular Structure*, 1227, 129540.
- Wang, G. D., Wang, H. H., Shi, W. J., Hou, L., Wang, Y. Y., & Zhu, Z. (2021). A highly stable MOF with F and N accessible sites for efficient capture and separation of acetylene from ternary mixtures. *Journal of Materials Chemistry A*, 9(43), 24495-24502.
- Wang, H., Li, K. B., Xu, C., Xu, S. C., & Li, G. H. (2019). Large-scale solvothermal synthesis of Ag nanocubes with high SERS activity. *Journal of Alloys and Compounds*, 772, 150-156.
- Wang, J. J., Si, P. P., Yang, J., Zhao, S. S., Li, P. P., Li, B., Wang, S. Y., Lu, M., & Yu, S. X. (2019). La (III)-based MOFs with 5-aminoisophthalic acid for optical detection and degradation of organic molecules in water. *Polyhedron*, 162, 255-262.
- Wang, J., Lian, G., Si, H., Wang, Q., Cui, D., & Wong, C. P. (2016). Pressure-induced oriented attachment growth of large-size crystals for constructing 3D ordered superstructures. *ACS nano*, 10(1), 405-412.
- Wang, J., Wang, Z., Vieira, C. L., Wolfson, J. M., Pingtian, G., & Huang, S. (2019). Review on the treatment of organic pollutants in water by ultrasonic technology. *Ultrasonics sonochemistry*, 55, 273-278.
- Wang, L., Li, X., Yang, B., Xiao, K., Duan, H., & Zhao, H. (2022). The chemical stability of metal-organic frameworks in water treatments: Fundamentals, effect of water matrix and judging methods. *Chemical Engineering Journal*, 450, 138215.

- Wang, L., Ye, Y., Li, Z., Lin, Q., Ouyang, J., Liu, L., Zhang, Z., & Xiang, S. (2017). Highly selective adsorption of C₂/C₁ mixtures and solvent-dependent thermochromic properties in metal–organic frameworks containing infinite copper-halogen chains. *Crystal Growth & Design*, 17(4), 2081-2089.
- Wang, Q., Gao, Q., Al-Enizi, A. M., Nafady, A., & Ma, S. (2020). Recent advances in MOF-based photocatalysis: environmental remediation under visible light. *Inorganic Chemistry Frontiers*, 7(2), 300-339.
- Wang, S., Sun, B., Su, Z., Hong, G., Li, X., Liu, Y., Pan, Q., & Sun, J. (2022). Lanthanide-MOFs as multifunctional luminescent sensors. *Inorganic Chemistry Frontiers*, 9(13), 3259-3266.
- Wang, X. Z., Mao, X. Y., Zhang, Z. Q., Guo, R., Zhang, Y. Y., Zhu, N. J., Wang, K., Sun, P. P., Huo, J. Z., Wang, X. R., & Ding, B. (2020). Solvothermal and ultrasonic preparation of two unique cluster-based Lu and Y coordination materials: Metal–organic framework-based ratiometric fluorescent biosensor for an ornidazole and ronidazole and sensing platform for a biomarker of amoeba liver abscess. *Inorganic Chemistry*, 59(5), 2910-2922.
- Wang, Y., Li, L., Yan, L., Cao, L., Dai, P., Gu, X., & Zhao, X. (2018). Continuous synthesis for zirconium metal-organic frameworks with high quality and productivity via microdroplet flow reaction. *Chinese Chemical Letters*, 29(6), 849-853.
- Wang, Z., Li, Q., Su, R., Lv, G., Wang, Z., Gao, B., & Zhou, W. (2022). Enhanced degradation of bisphenol F in a porphyrin-MOF based

visible-light system under high salinity conditions. *Chemical Engineering Journal*, 428, 132106.

Wanigarathna, D. K., Gao, J., & Liu, B. (2020). Metal organic frameworks for adsorption-based separation of fluorocompounds: a review. *Materials Advances*, 1(3), 310-320.

Wasson, M. C., Otake, K. I., Gong, X., Strathman, A. R., Islamoglu, T., Gianneschi, N. C., & Farha, O. K. (2020). Modulation of crystal growth and structure within cerium-based metal-organic frameworks. *CrystEngComm*, 22(47), 8182-8188.

Wei, F. H., Chen, D., Liang, Z., Zhao, S. Q., & Luo, Y. (2017). Synthesis and characterization of metal-organic frameworks fabricated by microwave-assisted ball milling for adsorptive removal of Congo red from aqueous solutions. *RSC advances*, 7(73), 46520-46528.

Wei, F., Chen, D., Liang, Z., & Zhao, S. (2018). Comparison study on the adsorption capacity of Rhodamine B, Congo Red, and Orange II on Fe-MOFs. *Nanomaterials*, 8(4), 248.

Wei, L., Hui-Ming, L., Li, Y., Qing-Wei, W., & Lei, X. (2018). Synthesis, Crystal Structure, Theoretical Calculations, and Photoluminescent Property of a Mn (II) Complex Assembled by 5-Amino-isophthalic Acid and Phen Ligands. *Chinese Journal of Structural Chemistry*, 37(2), 286-291.

Wei, M., Wang, X., & Duan, X. (2013). Crystal Structures and Proton Conductivities of a MOF and Two POM-MOF Composites Based on CuII Ions and 2, 2'-Bipyridyl-3, 3'-dicarboxylic Acid. *Chemistry-A European Journal*, 19(5), 1607-1616.

- Weissenberger, T., Machoke, A. G., Reiprich, B., & Schwieger, W. (2021). Preparation and potential catalytic applications of hierarchically structured zeolites with macropores. *Advanced Materials Interfaces*, 8(4), 2001653.
- Weixia, D. O. N. G., Gaoling, Z. H. A. O., Qifu, B. A. O., & Xingyong, G. U. (2015). Solvothermal preparation of CaTiO₃ prism and CaTi₂O₄ (OH)₂ nanosheet by a facile surfactant-free method. *Materials Science*, 21(4), 583-585.
- Wißmann, G., Schaate, A., Lilienthal, S., Bremer, I., Schneider, A. M., & Behrens, P. (2012). Modulated synthesis of Zr-fumarate MOF. *Microporous and Mesoporous Materials*, 152, 64-70.
- Woo, H. C., & Jung, S. H. (2021). Adsorptive removal of nitro-or sulfonate-containing dyes by a functional metal–organic framework: quantitative contribution of hydrogen bonding. *Chemical Engineering Journal*, 425, 130598.
- Wu, M., Zhang, Y., Zhang, R., Ma, J., & Alonso-Vante, N. (2022). Highly active oxygen evolution reaction electrocatalyst based on defective-CeO_{2-x} decorated MOF (Ni/Fe). *Electrochimica Acta*, 403, 139630.
- Wu, X. P., Gagliardi, L., & Truhlar, D. G. (2018). Cerium metal–organic framework for photocatalysis. *Journal of the American Chemical Society*, 140(25), 7904-7912.
- Wu, Z., Yuan, X., Zhang, J., Wang, H., Jiang, L., & Zeng, G. (2017). Photocatalytic decontamination of wastewater containing organic dyes by metal–organic frameworks and their derivatives. *Chem CatChem*, 9(1), 41-64.

- Xie, J., Mu, Z., Yan, B., Wang, J., Zhou, J., & Bai, L. (2021). An electrochemical aptasensor for Mycobacterium tuberculosis ESAT-6 antigen detection using bimetallic organic framework. *Microchimica Acta*, 188(11), 1-10.
- Xie, R., Fang, K., Liu, Y., Chen, W., Fan, J., Wang, X., Ren, Y., & Song, Y. (2020). Z-scheme In $2\text{O}_3/\text{WO}_3$ heterogeneous photocatalysts with enhanced visible-light-driven photocatalytic activity toward degradation of organic dyes. *Journal of Materials Science*, 55, 11919-11937.
- Xin, L., Zhang, D., Qu, K., Lu, Y., Wang, Y., Huang, K., Wang, Z., Jin, W., & Xu, Z. (2021). Zr-MOF-enabled controllable ion sieving and proton conductivity in flow battery membrane. *Advanced Functional Materials*, 31(42), 2104629.
- Xing, J., Schweighauser, L., Okada, S., Harano, K., & Nakamura, E. (2019). Atomistic structures and dynamics of prenucleation clusters in MOF-2 and MOF-5 syntheses. *Nature communications*, 10(1), 3608.
- Xu, D., Yang, Y., Le, K., Wang, G., Ouyang, A., Li, B., Liu, W., Wu, L., Wang, Z., Liu, J., & Wang, F. (2021). Bifunctional $\text{Cu}_9\text{S}_5/\text{C}$ octahedral composites for electromagnetic wave absorption and supercapacitor applications. *Chemical Engineering Journal*, 417, 129350.
- Xu, H., Cao, C. S., Kang, X. M., & Zhao, B. (2016). Lanthanide-based metal-organic frameworks as luminescent probes. *Dalton transactions*, 45(45), 18003-18017.

- Xu, J., Yang, Y., Wang, Y., Cao, J., & Chen, Z. (2019). Enhanced electrochemical properties of manganese-based metal organic framework materials for supercapacitors. *Journal of Applied Electrochemistry*, 49(11), 1091-1102.
- Xu, L. J., Wang, C. M., Yu, K., Wang, C. X., & Zhou, B. B. (2023). Research progress of POMs constructed by 1, 3, 5-benzene-tricarboxylic acid: From synthesis to application. *Coordination Chemistry Reviews*, 481, 215044.
- Xu, S. Y., Wu, Y. N., Chen, B. C., Huang, P. W., Zhang, Z. Z., Zhong, Y., Zhao, Y., Huang, X. Y., & Du, K. Z. (2022). Electrochemical Thin Film Deposition of Copper (I) Halides in Aqueous Solution: Substrate Extension and Structure Transformation. *Advanced Materials Interfaces*, 9(10), 2102239.
- Yaghi, O. M. (2019). Reticular chemistry in all dimensions. *ACS central science*, 5(8), 1295-1300.
- Yaghi, O. M. (2019). Reticular chemistry: molecular precision in infinite 2D and 3D. *Molecular Frontiers Journal*, 3(01), 66-83.
- Yakuphanoglu, F. (2019). Thermal analysis methods used in solid state physics and chemistry to obtain kinetics and thermodynamics parameters of solid materials by TGA, DTA and DSC analyses. *Journal of Materials and Electronic Devices*, 1(1), 17-23.
- Yamjala, K., Nainar, M. S., & Ramiseti, N. R. (2016). Methods for the analysis of azo dyes employed in food industry—a review. *Food chemistry*, 192, 813-824.

- Yan, J., Sun, Y., Ji, T., Zhang, C., Liu, L., & Liu, Y. (2022). Room-temperature synthesis of defect-engineered Zirconium-MOF membrane enabling superior CO₂/N₂ selectivity with zirconium-oxo cluster source. *Journal of Membrane Science*, 653, 120496.
- Yan, Q. Q., Li, B., & Yong, G. P. (2021). Four new coordination polymers with a Y-shaped tricarboxylic acid ligand: Structural diversities, luminescence sensing and magnetic properties. *Journal of Molecular Structure*, 1228, 129453.
- Yan, Y. T., Zhang, W. Y., Zhang, F., Cao, F., Yang, R. F., Wang, Y. Y., & Hou, L. (2018). Four new metal–organic frameworks based on diverse secondary building units: sensing and magnetic properties. *Dalton Transactions*, 47(5), 1682-1692.
- Yan, Y., Li, C., Wu, Y., Gao, J., & Zhang, Q. (2020). From isolated Ti-oxo clusters to infinite Ti-oxo chains and sheets: recent advances in photoactive Ti-based MOFs. *Journal of Materials Chemistry A*, 8(31), 15245-15270.
- Yanai, N., Uemura, T., Inoue, M., Matsuda, R., Fukushima, T., Tsujimoto, M., Isoda, S., & Kitagawa, S. (2012). Guest-to-host transmission of structural changes for stimuli-responsive adsorption property. *Journal of the American Chemical Society*, 134(10), 4501-4504.
- Yang, C., Yang, X., Li, F., Li, T., & Cao, W. (2016). Controlled synthesis of hierarchical flower-like Sb₂WO₆ microspheres: photocatalytic and superhydrophobic property. *Journal of Industrial and Engineering Chemistry*, 39, 93-100.

- Yang, D., Chen, Y., Su, Z., Zhang, X., Zhang, W., & Srinivas, K. (2021). Organic carboxylate-based MOFs and derivatives for electrocatalytic water oxidation. *Coordination Chemistry Reviews*, 428, 213619.
- Yang, K., Yan, Y., Chen, W., Kang, H., Han, Y., Zhang, W & Li, Z. (2018). Nut-like MOF/hydroxylated graphene hybrid materials for adsorptive desulfurization of thiophene. *RSC advances*, 8(42), 23671-23678.
- Yang, L. M., Fang, G. Y., Ma, J., Ganz, E., & Han, S. S. (2014). Band gap engineering of paradigm MOF-5. *Crystal growth & design*, 14(5), 2532-2541.
- Yang, L., Ruess, G. L., & Carreon, M. A. (2015). Cu, Al and Ga based metal organic framework catalysts for the decarboxylation of oleic acid. *Catalysis Science & Technology*, 5(5), 2777-2782.
- Yang, P., Zhuang, Q., Li, Y., & Gu, J. (2019). Green separation of rare earth elements by valence-selective crystallization of MOFs. *Chemical Communications*, 55(99), 14902-14905.
- Yang, S., Hu, W., Nyakuchena, J., Fiankor, C., Liu, C., Kinigstein, E. D., Zhang, J., Zhang, X., & Huang, J. (2020). Unravelling a long-lived ligand-to-metal cluster charge transfer state in Ce–TCPP metal organic frameworks. *Chemical Communications*, 56(90), 13971-13974.
- Yang, X. Y., Chen, L. H., Li, Y., Rooke, J. C., Sanchez, C., & Su, B. L. (2017). Hierarchically porous materials: synthesis strategies and structure design. *Chemical Society Reviews*, 46(2), 481-558.
- Yang, X., Jiang, X., Huang, Y., Guo, Z., & Shao, L. (2017). Building nanoporous metal–organic frameworks “armor” on fibers for high-

performance composite materials. *ACS applied materials & interfaces*, 9(6), 5590-5599.

Yang, Y., Shukla, P., Wang, S., Rudolph, V., Chen, X. M., & Zhu, Z. (2013).

Significant improvement of surface area and CO₂ adsorption of Cu-BTC via solvent exchange activation. *Rsc Advances*, 3(38), 17065-17072.

Yao, Q., Bermejo Gómez, A., Su, J., Pascanu, V., Yun, Y., Zheng, H., Chen,

H., Liu, L., Abdelhamid, H. N., Martín-Matute, B., & Zou, X. (2015). Series of highly stable isorecticular lanthanide metal-organic frameworks with expanding pore size and tunable luminescent properties. *Chemistry of Materials*, 27(15), 5332-5339.

Yao, Y., Wang, C., Na, J., Hossain, M. S. A., Yan, X., Zhang, H., Amin, M.

A., Qi, J., Yamauchi, Y., & Li, J. (2022). Macroscopic MOF architectures: Effective strategies for practical application in water treatment. *Small*, 18(8), 2104387.

Ye, Z., Kong, L., Chen, F., Chen, Z., Lin, Y., & Liu, C. (2018). A comparative

study of photocatalytic activity of ZnS photocatalyst for degradation of various dyes. *Optik*, 164, 345-354.

Yin, M. R., Li, B., Yan, Q. Q., & Yong, G. P. (2021). From zero-dimensional

complexes to one-dimensional coordination polymers adjusted by the solvents or ligand substituent groups. *Nano-Structures & Nano-Objects*, 26, 100690.

Yin, R., Chen, Y., Hu, J., Lu, G., Zeng, L., Choi, W., & Zhu, M. (2021).

Complexes of Fe (III)-organic pollutants that directly activate Fenton-

like processes under visible light. *Applied Catalysis B: Environmental*, 283, 119663.

Yu, L., Ullah, S., Zhou, K., Xia, Q., Wang, H., Tu, S., Huang, J., Xia, H. L., Liu, X. Y., Thonhauser, T., & Li, J. (2022). A Microporous Metal–Organic Framework Incorporating Both Primary and Secondary Building Units for Splitting Alkane Isomers. *Journal of the American Chemical Society*, 144(9), 3766–3770.

Yu, S., Pang, H., Huang, S., Tang, H., Wang, S., Qiu, M., Chen, Z., Yang, H., Song, G., Fu, D., Hu, B., & Wang, X. (2021). Recent advances in metal-organic framework membranes for water treatment: A review. *Science of the Total Environment*, 800, 149662.

Yuan, S., Feng, L., Wang, K., Pang, J., Bosch, M., Lollar, C., Sun, Y., Qin, J., Yang, X., Zhang, P., Wang, Q., Zou, L., Zhang, Y., Zhang, L., Fang, Y., Li, J., & Zhou, H. C. (2018). Stable metal–organic frameworks: design, synthesis, and applications. *Advanced Materials*, 30(37), 1704303.

Yuan, S., Qin, J. S., Lollar, C. T., & Zhou, H. C. (2018). Stable metal–organic frameworks with group 4 metals: current status and trends. *ACS central science*, 4(4), 440–450.

Zahn, G., Zerner, P., Lippke, J., Kempf, F. L., Lilienthal, S., Schröder, C. A., Schneider, A. M. & Behrens, P. (2014). Insight into the mechanism of modulated syntheses: in situ synchrotron diffraction studies on the formation of Zr-fumarate MOF. *CrystEngComm*, 16(39), 9198–9207.

Zainal, N. F. A., Saiter, J. M., Halim, S. I. A., Lucas, R., & Chan, C. H. (2021). Thermal analysis: basic concept of differential scanning

calorimetry and thermogravimetry for beginners. *Chemistry Teacher International*, 3(2), 59-75.

Zainip, V. J., Adna, L. A., & Elshikh, M. S. (2021). Decolorization of remazol brilliant violet 5R and procion red MX-5B by *Trichoderma* species. *Tropical Aquatic and Soil Pollution*.

Zango, Z. U., Jumbri, K., Sambudi, N. S., Ramli, A., Abu Bakar, N. H. H., Saad, B., Rozaini, M. N. H., Isiyaka, H. A., Jagaba, A. H., Aldaghri, O., & Sulieman, A. (2020). A critical review on metal-organic frameworks and their composites as advanced materials for adsorption and photocatalytic degradation of emerging organic pollutants from wastewater. *Polymers*, 12(11), 2648.

Zarei-Shokat, S., & Ganjali, F. (2023). Overview of Metal Organic Frameworks. In *Physicochemical Aspects of Metal-Organic Frameworks: A New Class of Coordinative Materials* (pp. 1-14). Cham: Springer International Publishing.

Zarrouk, S. J., & Mclean, K. (2019). Advanced analytical pressure-transient analysis relevant to geothermal wells. *Geothermal Well Test Analysis*, 89.

Zhan, C. H., Huang, D. P., Wang, Y., Mao, W. T., Wang, X. J., Jiang, Z. G., & Feng, Y. L. (2021). Four anionic Ln-MOFs for remarkable separation of C₂H₂-CH₄/CO₂-CH₄ and highly sensitive sensing of nitrobenzene. *CrystEngComm*, 23(15), 2788-2792.

Zhang, C., Xu, Y., Lv, C., Zhou, X., Wang, Y., Xing, W., Meng, Q., Kong, Y., & Chen, G. (2019). Mimicking π backdonation in Ce-MOFs for solar-

driven ammonia synthesis. *ACS applied materials & interfaces*, 11(33), 29917-29923.

Zhang, H. X., Hong, Q. L., Li, J., Wang, F., Huang, X., Chen, S., Chen, S., Tu, W., Yu, D., Xu, R., Zhou, T., & Zhang, J. (2019). Isolated square-planar copper center in boron imidazolate nanocages for photocatalytic reduction of CO₂ to CO. *Angewandte Chemie International Edition*, 58(34), 11752-11756.

Zhang, H., Si, S., Zhai, G., Li, Y., Liu, Y., Cheng, H., Wang, Z., Wang, P., Zheng, Z., Dai, Y., Liu, T. X., Huang, B., & Huang, B. (2023). The long-distance charge transfer process in ferrocene-based MOFs with FeO₆ clusters boosts photocatalytic CO₂ chemical fixation. *Applied Catalysis B: Environmental*, 122909.

Zhang, J. W., Hu, M. C., Li, S. N., Jiang, Y. C., & Zhai, Q. G. (2017). Ligand Torsion Triggered Two Robust Fe-Tetratopic Carboxylate Frameworks with Enhanced Gas Uptake and Separation Performance. *Chemistry–A European Journal*, 23(27), 6693-6700.

Zhang, J., Chen, L., & Yang, K. (2019). In situ synthesis of CuO nanoparticles decorated hierarchical Ce-metal-organic framework nanocomposite for an ultrasensitive non-enzymatic glucose sensor. *Ionics*, 25(9), 4447-4457.

Zhang, J., Xiang, Q., Zhu, Y., Yang, J., Song, Y., & Zhang, C. (2021). Two W/S/Cu-cluster-containing metal-organic frameworks fabricated by multidentate organic ligands: New topologies, strong NLO properties, and efficient luminescent detection. *Crystal Growth & Design*, 21(6), 3225-3233.

Zhang, Q., Chen, M., Zhong, L., Ye, Q., Jiang, S. & Huang, Z. (2018). Highly effective removal of metal cyanide complexes and recovery of palladium using quaternary-ammonium-functionalized

MOFs. *Molecules*, 23(8), 2086.

Zhang, W., Huang, W., Jin, J., Gan, Y., & Zhang, S. (2021). Oxygen-vacancy-mediated energy transfer for singlet oxygen generation by diketone-anchored MIL-125. *Applied Catalysis B: Environmental*, 292, 120197.

Zhang, W., Huang, W., Jin, J., Gan, Y., & Zhang, S. (2021). Oxygen-vacancy-mediated energy transfer for singlet oxygen generation by diketone-anchored MIL-125. *Applied Catalysis B: Environmental*, 292, 120197.

Zhang, X., Chen, J., Jiang, S., Zhang, X., Bi, F., Yang, Y., Wang, Y., & Wang, Z. (2021). Enhanced photocatalytic degradation of gaseous toluene and liquid tetracycline by anatase/rutile titanium dioxide with heterophase junction derived from materials of Institut Lavoisier-125 (Ti): Degradation pathway and mechanism studies. *Journal of Colloid and Interface Science*, 588, 122-137.

Zhang, X., Hou, F., Li, H., Yang, Y., Wang, Y., Liu, N., & Yang, Y. (2018). A strawshave-like metal organic framework Ce-BTC derivative containing high specific surface area for improving the catalytic activity of CO oxidation reaction. *Microporous and Mesoporous Materials*, 259, 211-219.

Zhang, X., Lv, X., Bi, F., Lu, G., & Wang, Y. (2020). Highly efficient Mn₂O₃ catalysts derived from Mn-MOFs for toluene oxidation: The influence of MOFs precursors. *Molecular Catalysis*, 482, 110701.

- Zhang, X., Wang, J., Dong, X. X., & Lv, Y. K. (2020). Functionalized metal-organic frameworks for photocatalytic degradation of organic pollutants in environment. *Chemosphere*, *242*, 125144.
- Zhang, Y., Liu, W., Chen, S., Gao, Q., Li, Q., & Zhu, X. (2020). Ionic liquids for the controllable preparation of functional TiO₂ nanostructures: a review. *Ionics*, *26*, 5853-5877.
- Zhang, Y., Wang, F., Liu, C., Wang, Z., Kang, L., Huang, Y., Dong, K., Ren, J., & Qu, X. (2018). Nanozyme decorated metal-organic frameworks for enhanced photodynamic therapy. *ACS nano*, *12*(1), 651-661.
- Zhang, Y., Yang, X., & Zhou, H. C. (2018). Synthesis of MOFs for heterogeneous catalysis via linker design. *Polyhedron*, *154*, 189-201.
- Zhao, L., Azhar, M. R., Li, X., Duan, X., Sun, H., Wang, S., & Fang, X. (2019). Adsorption of cerium (III) by HKUST-1 metal-organic framework from aqueous solution. *Journal of colloid and interface science*, *542*, 421-428.
- Zhao, S. N., Wang, G., Poelman, D., & Voort, P. V. D. (2018). Luminescent lanthanide MOFs: A unique platform for chemical sensing. *Materials*, *11*(4), 572.
- Zhao, X., Zheng, M., Gao, X., Zhang, J., Wang, E., & Gao, Z. (2021). The application of MOFs-based materials for antibacterials adsorption. *Coordination Chemistry Reviews*, *440*, 213970.
- Zhao, Y., Chai, Y. H., Ding, L., Wang, S., Wang, Y. N., Ma, L. F., & Zhao, B. T. (2023). A stable N-containing heterocyclic carboxylic acid ligand Co-MOF for photoelectric performance and anionic dyes adsorption. *Arabian Journal of Chemistry*, *16*(8), 104878.

Zhao, Y., Wang, J., & Pei, R. (2022). Guest Molecules with Amino and Sulfhydryl Groups Enhance Photoluminescence by Reducing the Intermolecular Ligand-to-Metal Charge Transfer Process of Metal–Organic Frameworks. *Applied Sciences*, *12*(22), 11467.

Zhao, Y., Wang, J., Zhu, W., Liu, L., & Pei, R. (2021). The modulation effect of charge transfer on photoluminescence in metal–organic frameworks. *Nanoscale*, *13*(8), 4505-4511.

Zhao, Z., Ma, X., Kasik, A., Li, Z., & Lin, Y. S. (2013). Gas separation properties of metal organic framework (MOF-5) membranes. *Industrial & Engineering Chemistry Research*, *52*(3), 1102-1108.

Zheng, G., Chen, M., Yin, J., Zhang, H., Liang, X., & Zhang, J. (2019). Metal organic frameworks derived nano materials for energy storage application. *International Journal of Electrochemical Science*, *14*(3), 2345-2362.

Zheng, M., Xu, L., Chen, C., Labiadh, L., Yuan, B., & Fu, M. L. (2022). MOFs and GO-based composites as deliberate materials for the adsorption of various water contaminants. *Separation and Purification Technology*, *294*, 121187.

Zheng, S., Li, Q., Xue, H., Pang, H., & Xu, Q. (2020). A highly alkaline-stable metal oxide@ metal–organic framework composite for high-performance electrochemical energy storage. *National science review*, *7*(2), 305-314.

Zheng, Z., Nguyen, H. L., Hanikel, N., Li, K. K. Y., Zhou, Z., Ma, T., & Yaghi, O. M. (2023). High-yield, green and scalable methods for

producing MOF-303 for water harvesting from desert air. *Nature Protocols*, 18(1), 136-156.

Zhong, G., Liu, D., & Zhang, J. (2018). Incorporation of Functional Groups Expands the Applications of UiO-67 for Adsorption, Catalysis and Thiols Detection. *ChemistrySelect*, 3(25), 7066-7080.

Zhou, J. M., Shi, W., Xu, N., & Cheng, P. (2013). Highly selective luminescent sensing of fluoride and organic small-molecule pollutants based on novel lanthanide metal-organic frameworks. *Inorganic Chemistry*, 52(14), 8082-8090.

Zhou, S., Shekhah, O., Jia, J., Czaban-Józwiak, J., Bhatt, P. M., Ramírez, A., Gascon, J., & Eddaoudi, M. (2021). Electrochemical synthesis of continuous metal-organic framework membranes for separation of hydrocarbons. *Nature Energy*, 6(9), 882-891.

Zhou, X., Zhang, J., Ma, Y., Tian, H., Wang, Y., Li, Y., Jiang, L., & Cui, Q. (2017). The solvothermal synthesis of γ -AlOOH nanoflakes and their compression behaviors under high pressures. *RSC advances*, 7(9), 4904-4911.

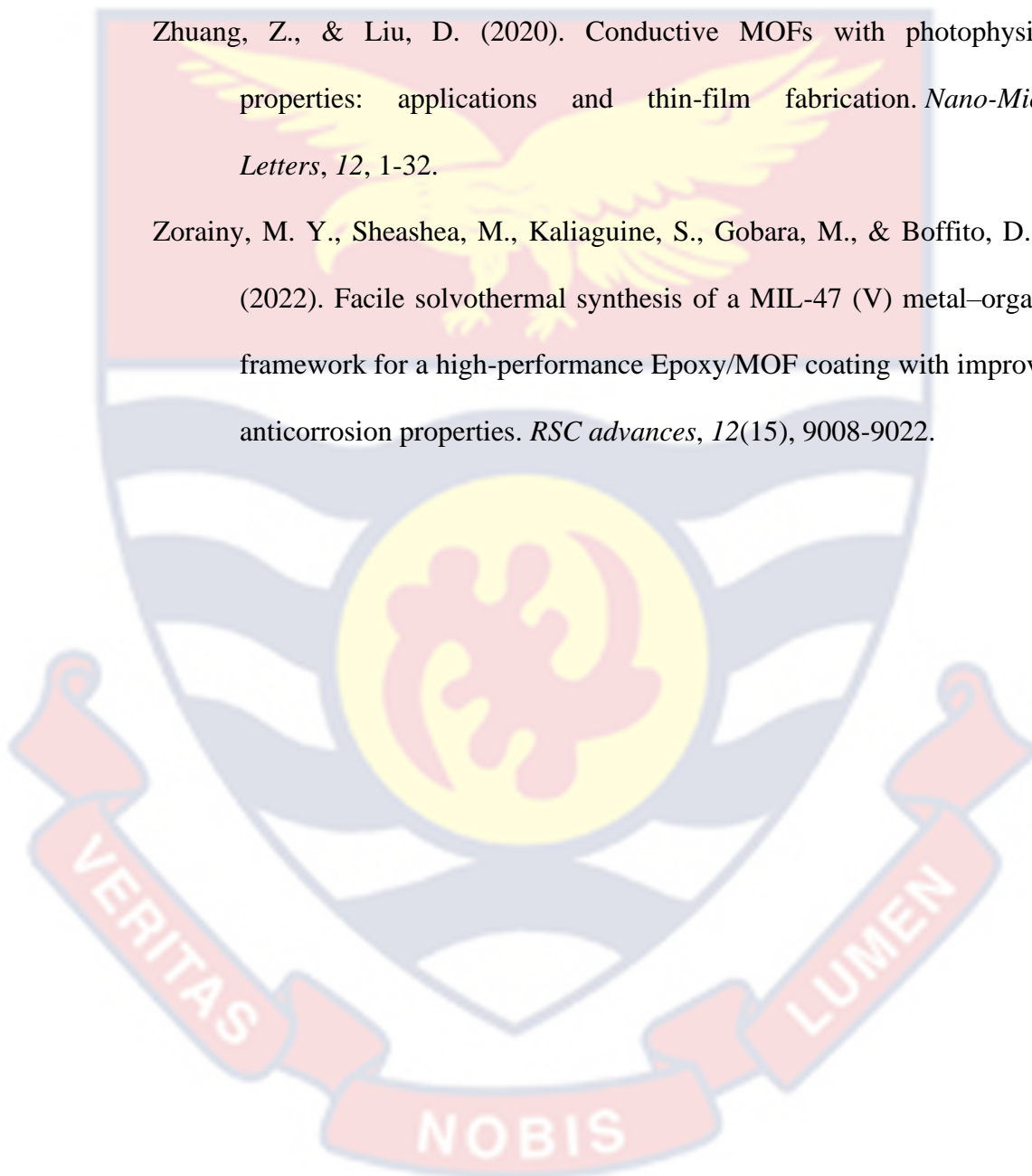
Zhou, Y. Y., Geng, B., Zhang, Z. W., & Bo, Q. B. (2016). Synthesis, structures and photoluminescence of three d10 5-aminonicotinate and 5-aminoisophthalate coordination polymers with bilayer structures. *Inorganica Chimica Acta*, 444, 150-158.

Zhou, Z., Mukherjee, S., Warnan, J., Li, W., Wannapaiboon, S., Hou, S., Rodewald, K., Rieger, B., Weidler, P.G., Wöll, C., & Fischer, R. A. (2020). Porphyrin based metal-organic framework films: nucleation and growth. *Journal of Materials Chemistry A*, 8(48), 25941-25950.

Zhou, Z., Wang, T., Hu, T., Cheng, C., Yu, S., Li, H., Liu, S., Ma, L., Zhao, M., Liang, R., & Tan, C. (2023). Facile synthesis of 2D Al-TCPP MOF nanosheets for efficient sonodynamic cancer therapy. *Materials Chemistry Frontiers*, 7(8), 1684-1693.

Zhuang, Z., & Liu, D. (2020). Conductive MOFs with photophysical properties: applications and thin-film fabrication. *Nano-Micro Letters*, 12, 1-32.

Zorainy, M. Y., Sheashea, M., Kaliaguine, S., Gobara, M., & Boffito, D. C. (2022). Facile solvothermal synthesis of a MIL-47 (V) metal-organic framework for a high-performance Epoxy/MOF coating with improved anticorrosion properties. *RSC advances*, 12(15), 9008-9022.

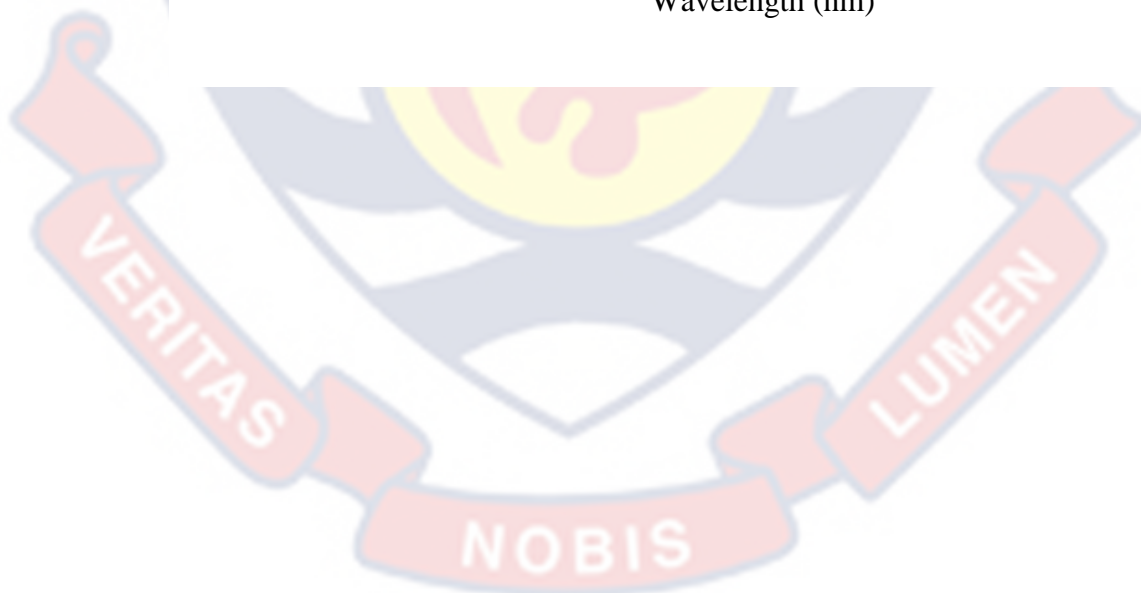
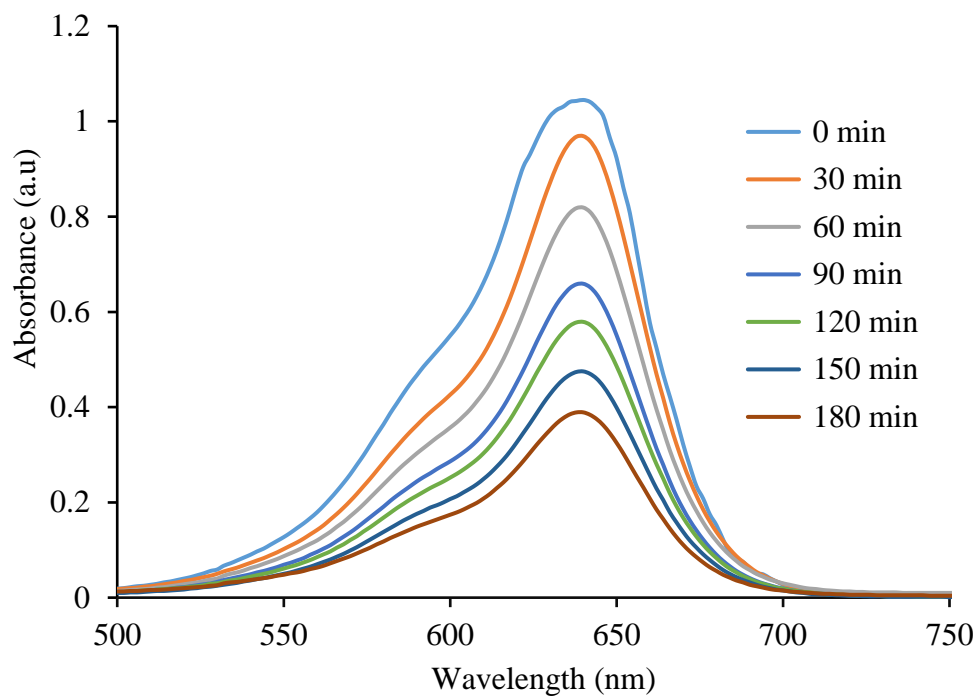


APPENDICES

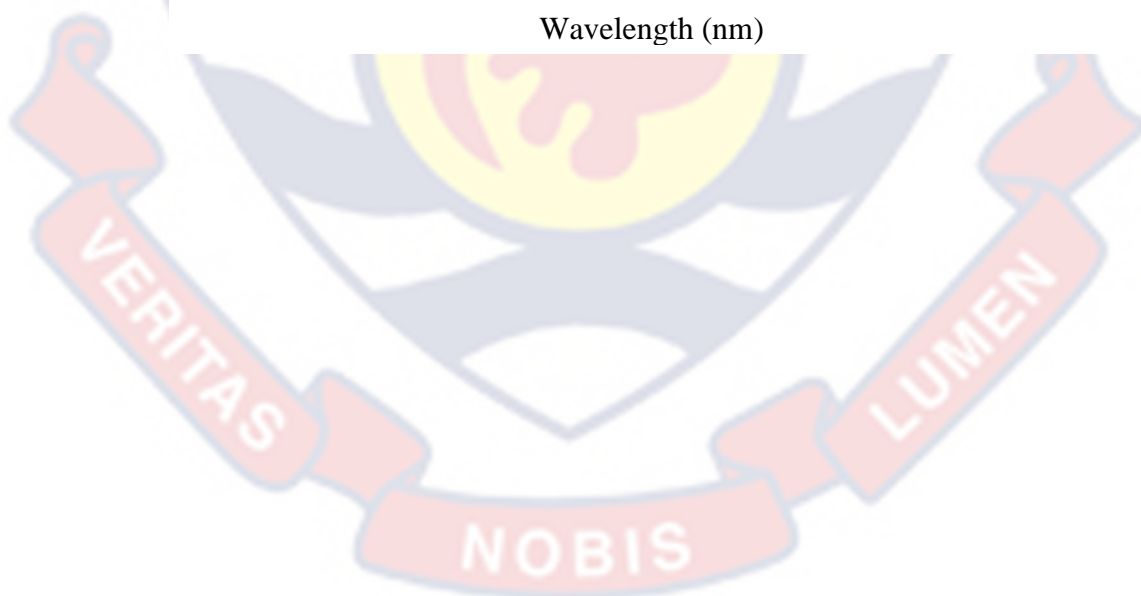
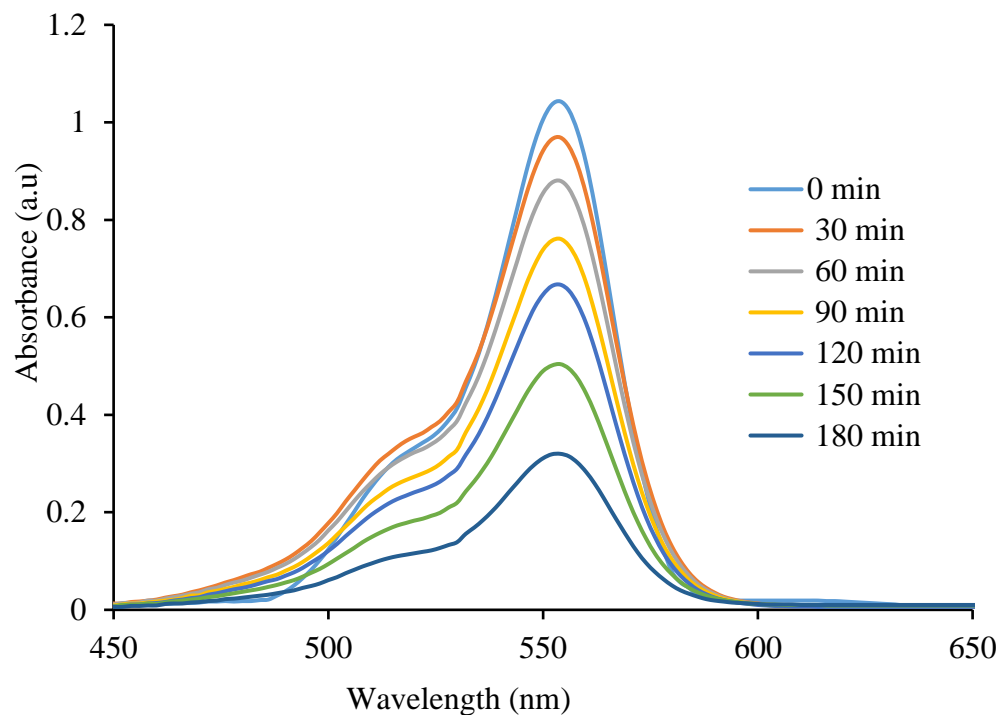
APPENDIX A

UV-VISIBLE ABSORPTION SPECTRA OF LISSAMINE GREEN SF

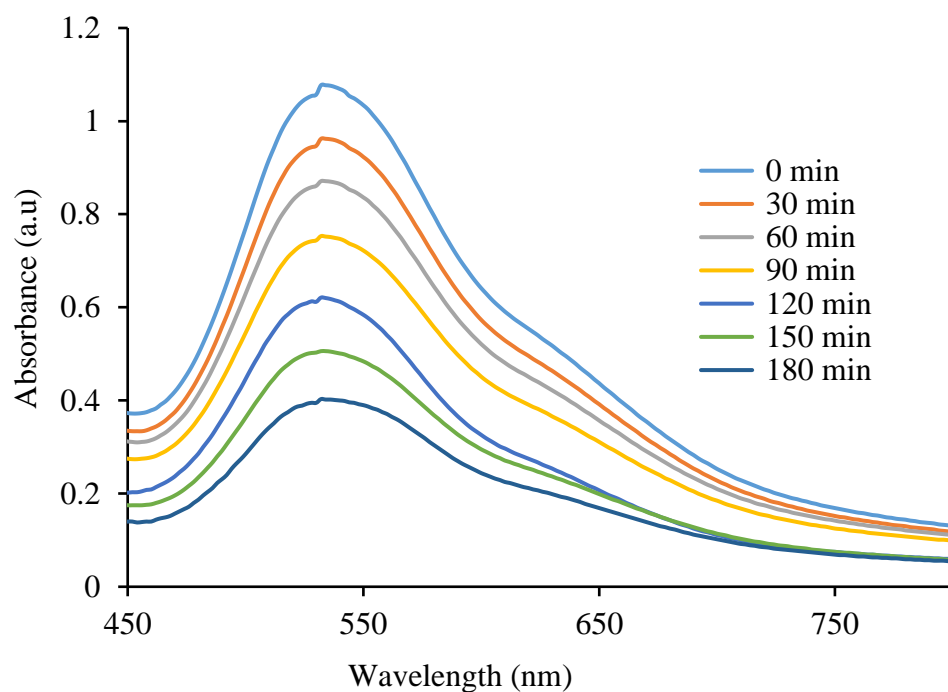
(LGSF) AT 640 nm UNDER PHOTODEGRADATION.



APPENDIX B

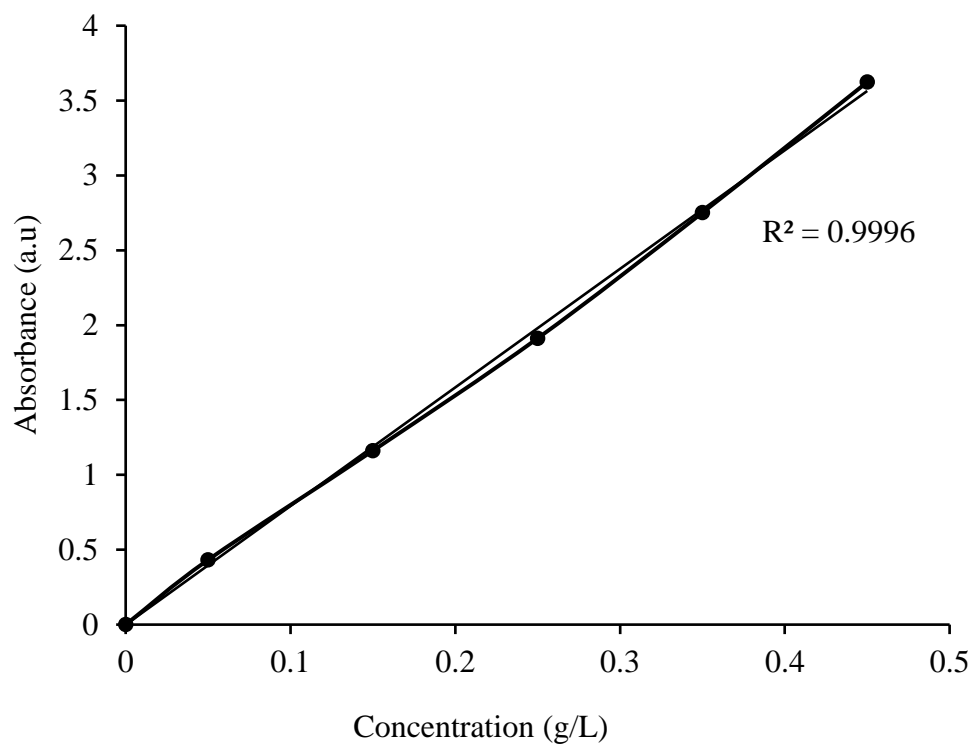
UV-VISIBLE ABSORPTION SPECTRA OF
TETRAETHYLRHODAMINE (TeRh) AT 554 nm UNDER
PHOTODEGRADATION.

APPENDIX C

UV-VISIBLE ABSORPTION SPECTRA OF RAMAZOLE BRILLIANT
VIOLET 5R (RBV5R) AT 540 nm UNDER PHOTODEGRADATION.

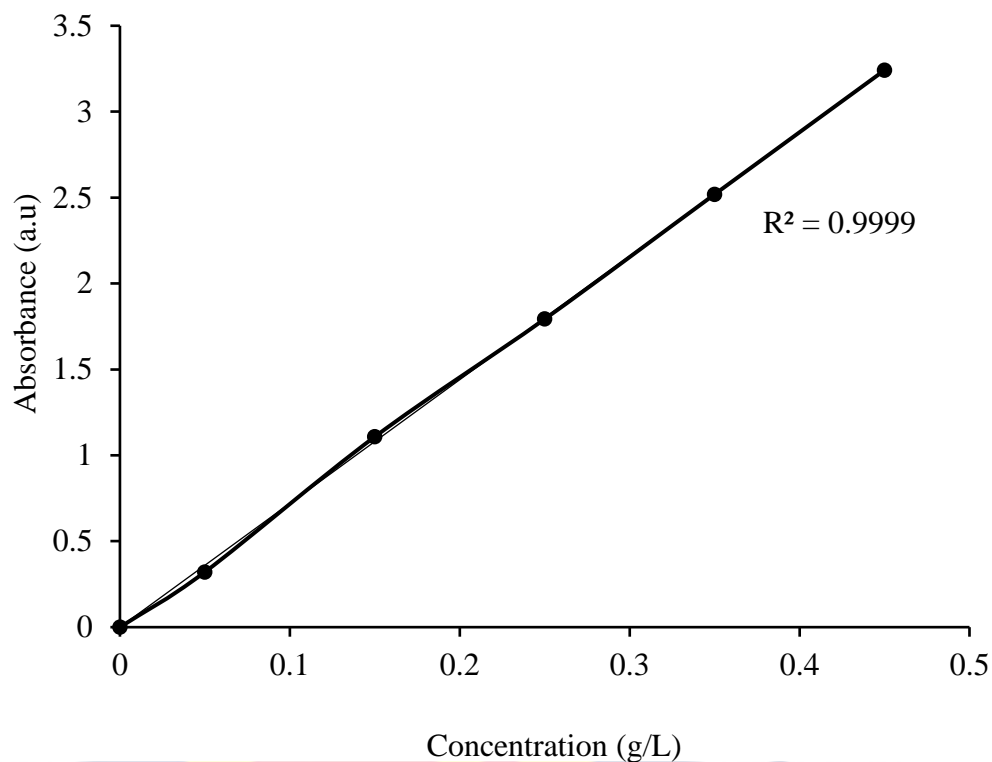
APPENDIX D

LISSAMINE GREEN SF (LGSF) CALIBRATION CURVE



APPENDIX E

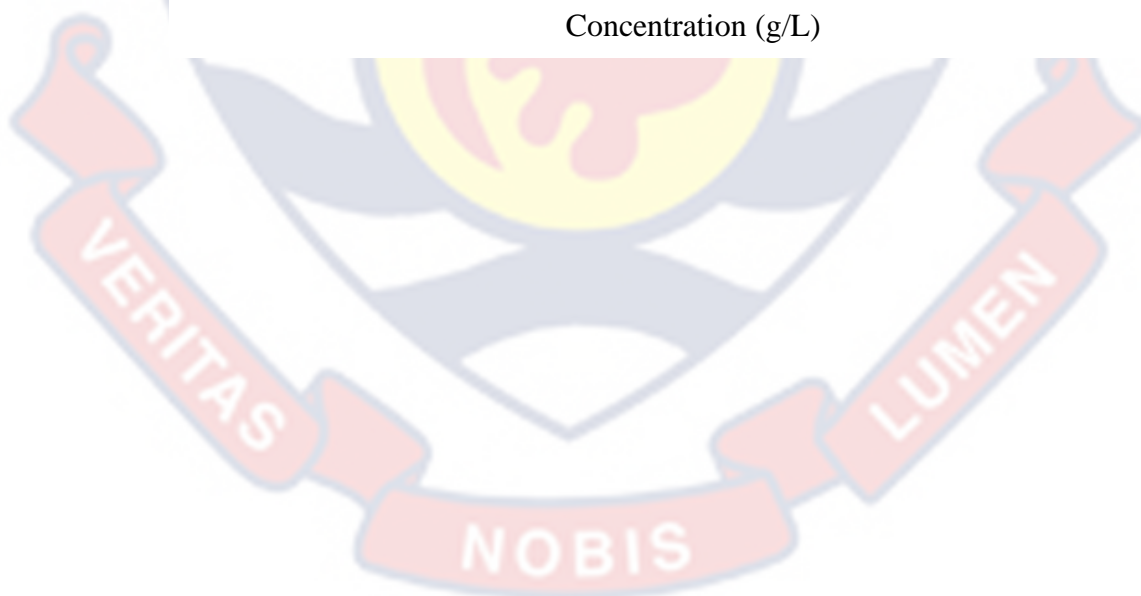
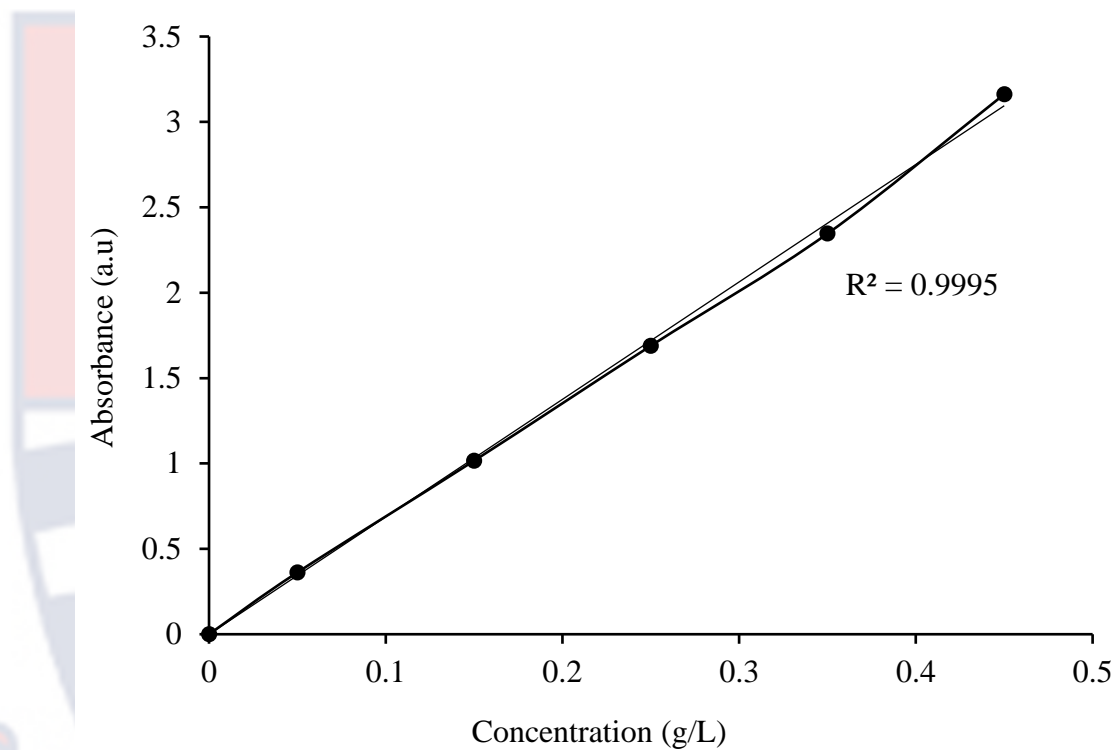
TETRAETHYLRHODAMINE (TeRh) CALIBRATION CURVE



APPENDIX F

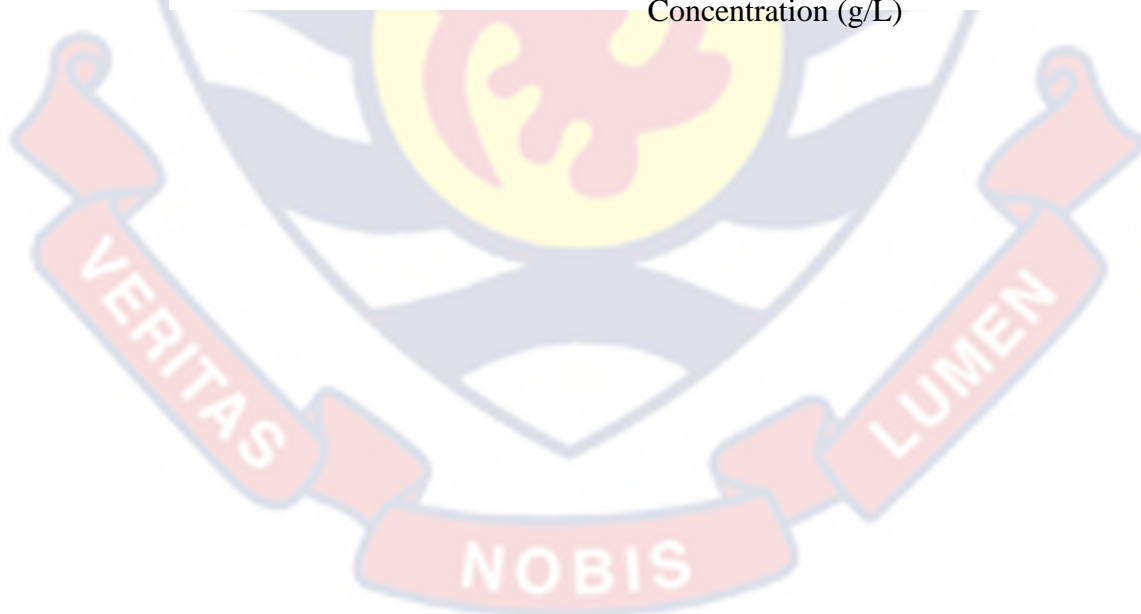
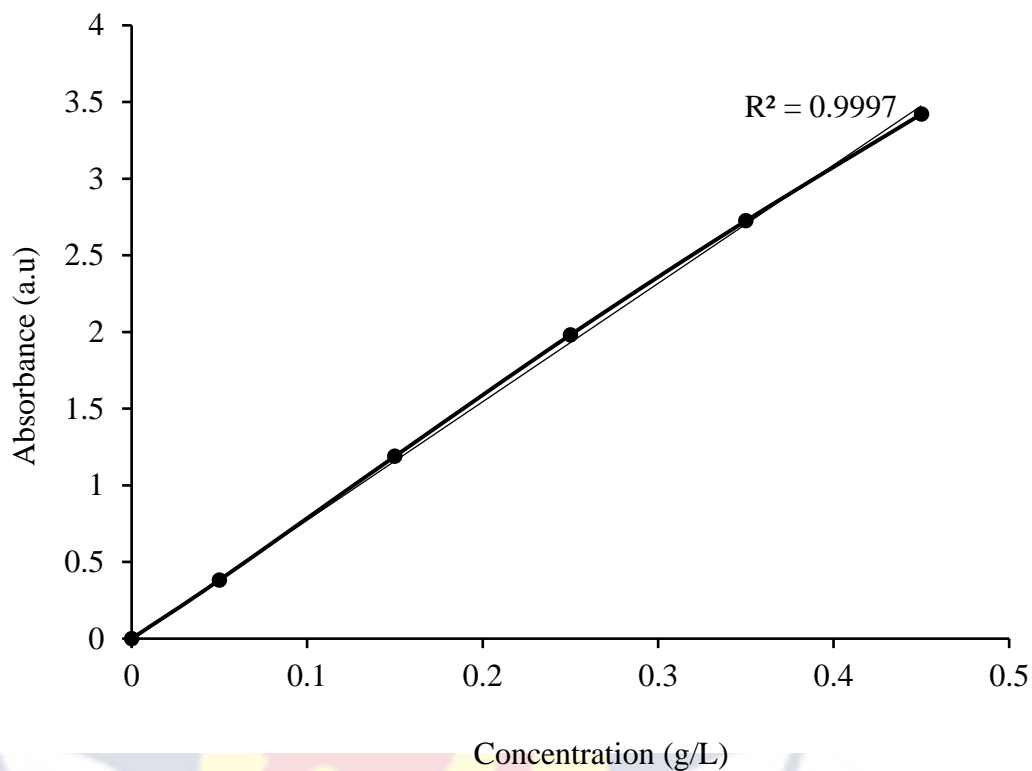
RAMAZOLE BRILLIANT VIOLET 5R (RBV5R) CALIBRATION

CURVE



APPENDIX G

MIXED TEXTILE DYE CALIBRATION CURVE

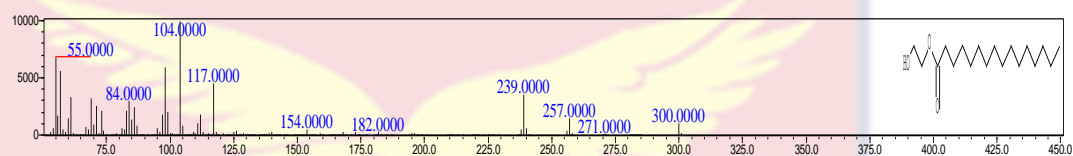


APPENDIX H

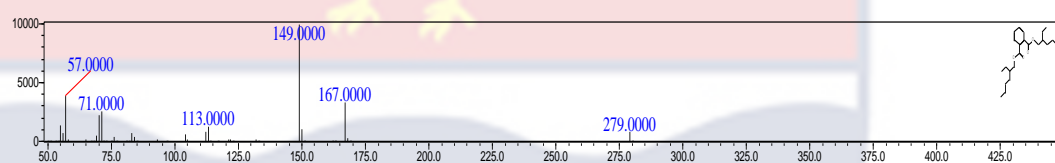
INTERMEDIATES OBTAINED FROM GC/MS FOR LISSAMINE

GREEN SF (LGSF)

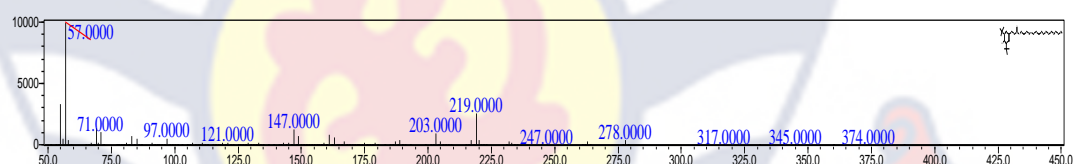
Hexadecanoic acid, 2-hydroxyethyl ester



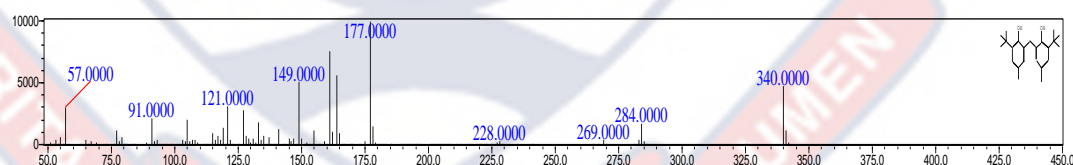
1, 2-Benzenedicarboxylic acid, bis (2-ethylhexyl) ester



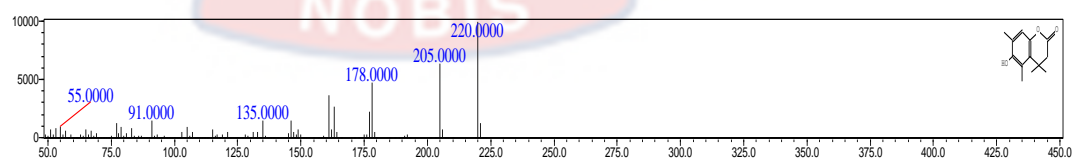
2, 6-Di-tert-butyl-4-[(2-octadecyloxycarbonyl) ethyl] phenol



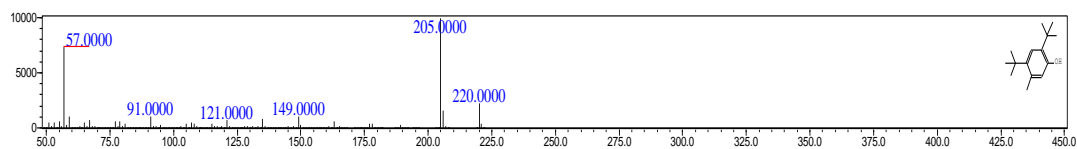
Phenol, 2, 2'-methylenebis [6-(1,1-dimethylethyl)-4-methyl



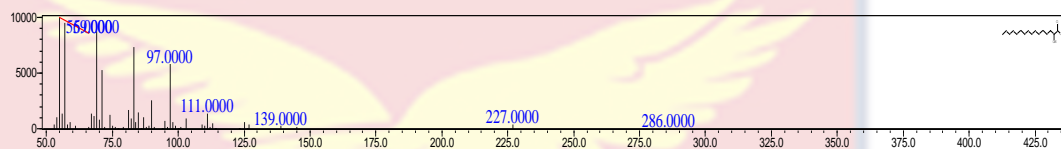
6-Hydroxy-4, 4, 5, 7-tetramethyl-2-chromanone



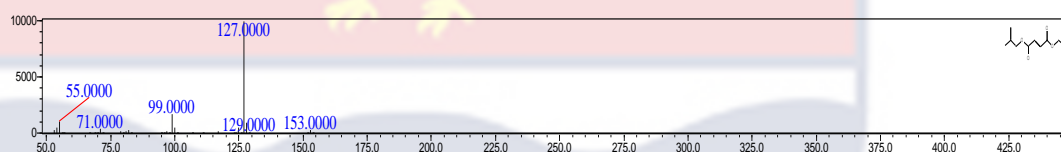
Phenol, 2, 4-bis (1,1-dimethylethyl)-5-methyl



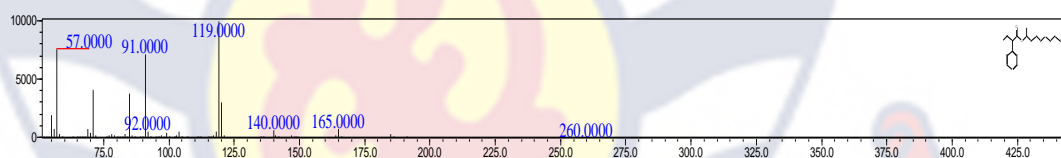
Methyl 2-hydroxyhexadecanoate



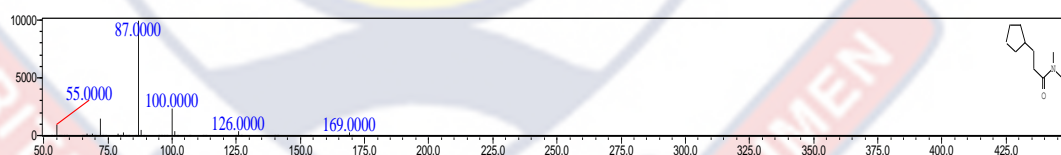
Fumaric acid, ethyl 2-methylallyl ester



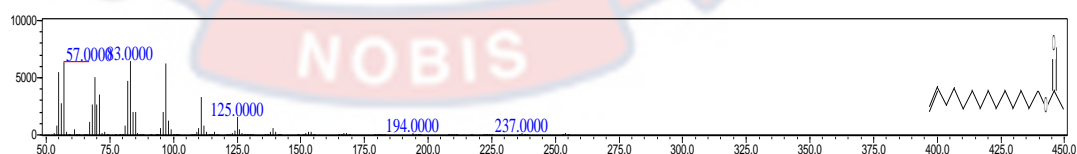
Butyric acid-2-phenyl-, dec-2-yl ester



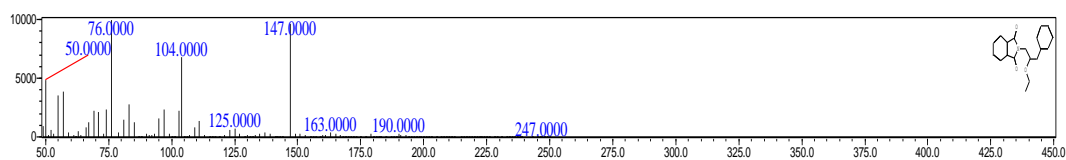
3-Cyclopentylpropionamide, N, N-dimethyl-ester



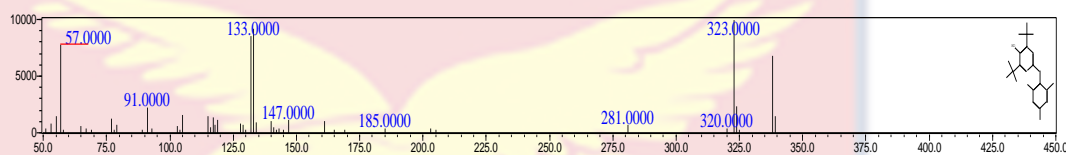
13-Tetradecenyl acetate



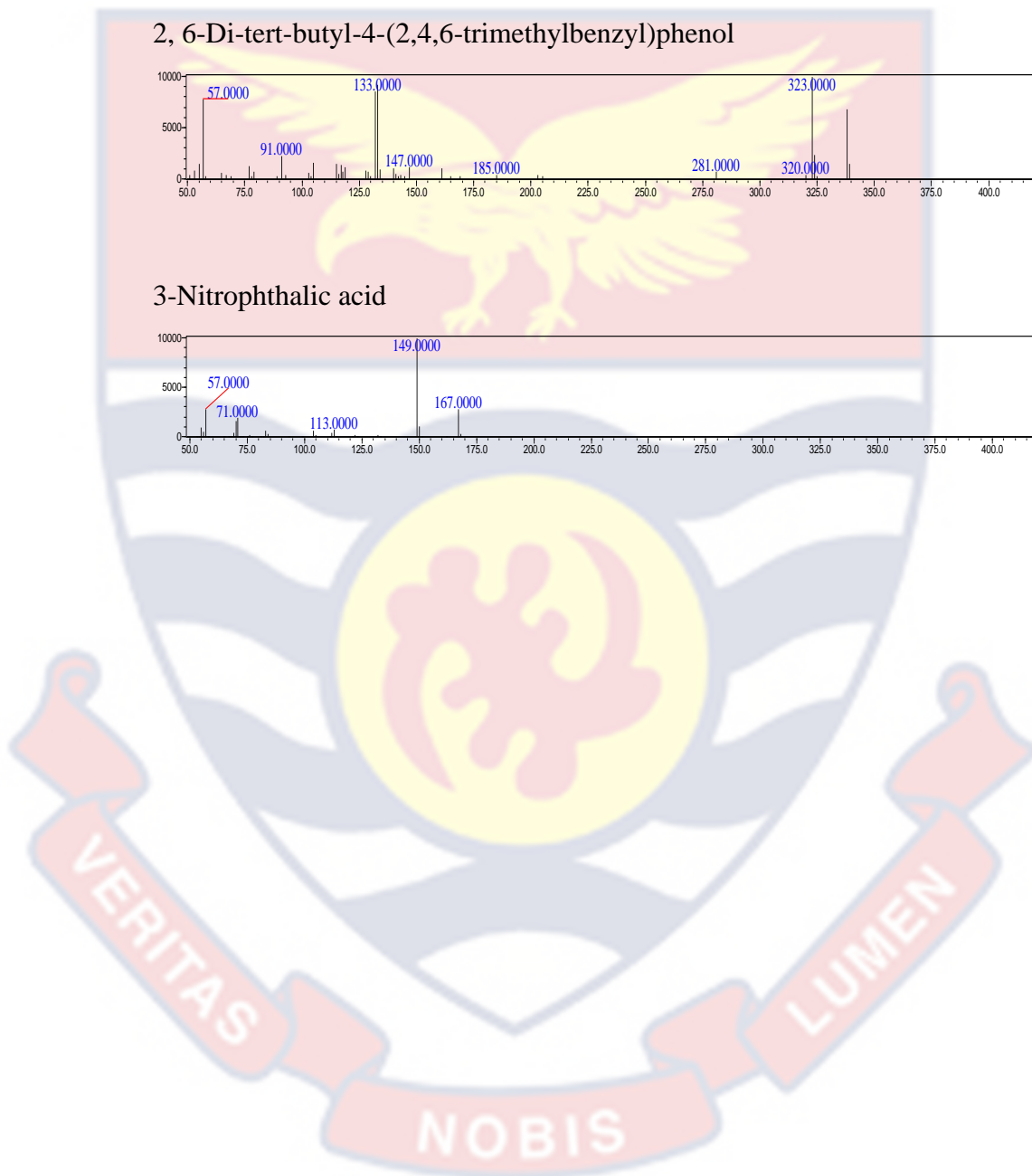
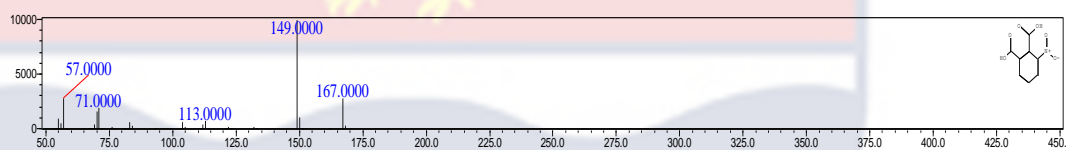
3-Phenyl-2-ethoxypropylphthalimide



2, 6-Di-tert-butyl-4-(2,4,6-trimethylbenzyl)phenol



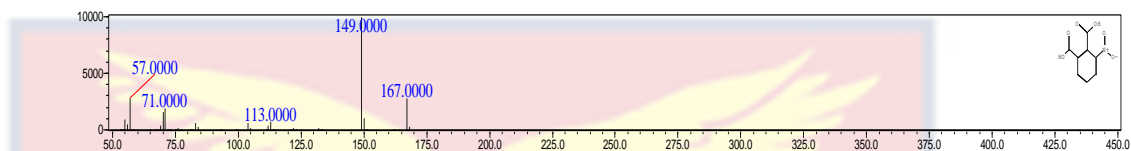
3-Nitrophthalic acid



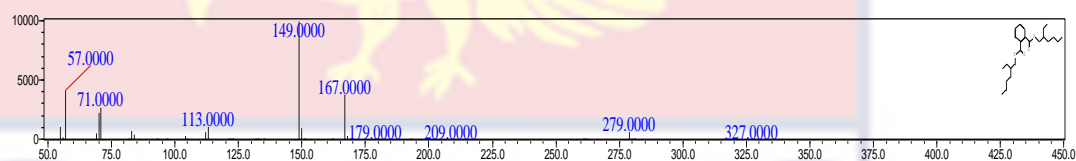
APPENDIX I

INTERMEDIATES OBTAINED FROM GC/MS FOR TETRAETHYL
RHODAMINE (TeRh)

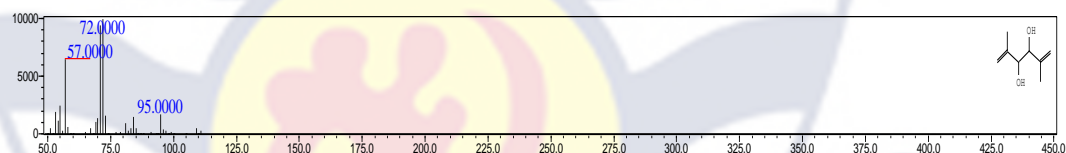
3-Nitrophthalic acid



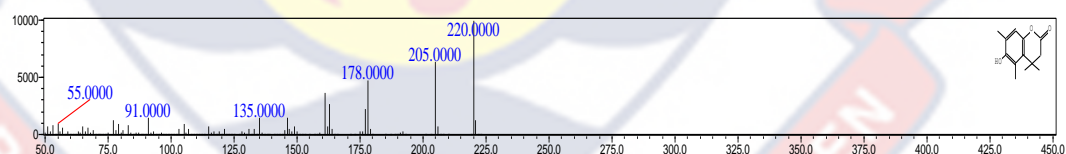
1, 2-Benzenedicarboxylic acid, bis (2-ethylhexyl) ester



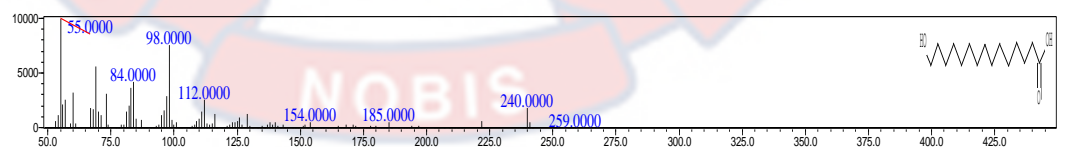
2, 5-Dimethyl-1, 5-hexadiene-3, 4-diol



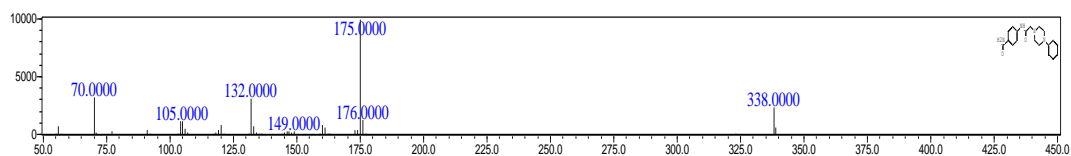
6-Hydroxy-4, 4, 5, 7-tetramethyl-2-chromanone



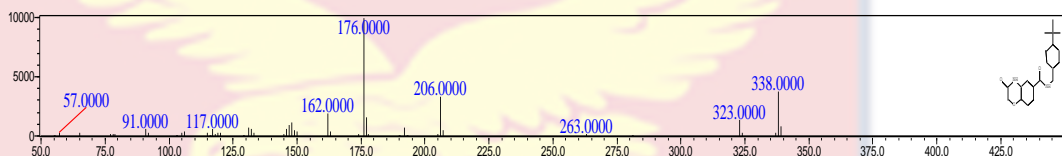
15-Hydroxypentadecanoic acid



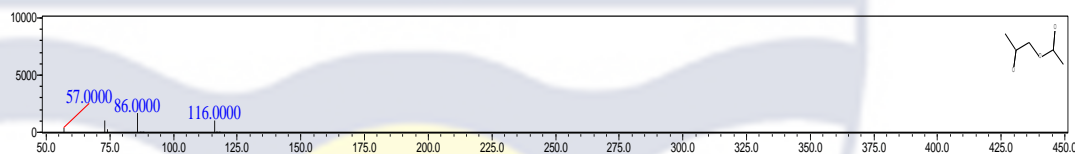
4-((4-phenyl-1-piperazinyl) acetyl) amino) benzamide



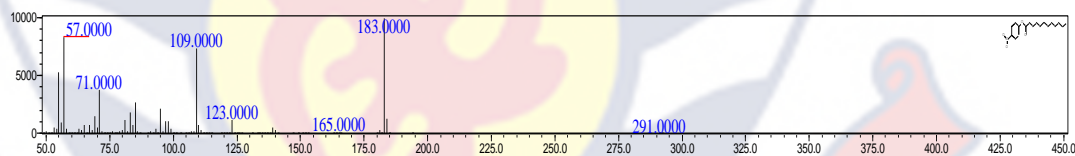
2H-1, 4-benzoxazine-6-carboxamide, n-[[4-(1, 1-dimethylethyl) phenyl] methyl]-3, 4-dihydro-3-oxo



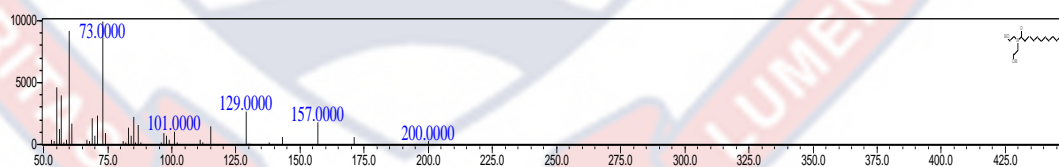
2-Oxopropyl acetate



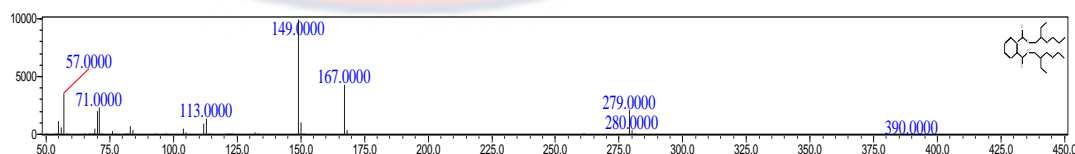
Dodecanoic acid, 4-nitrophenyl ester



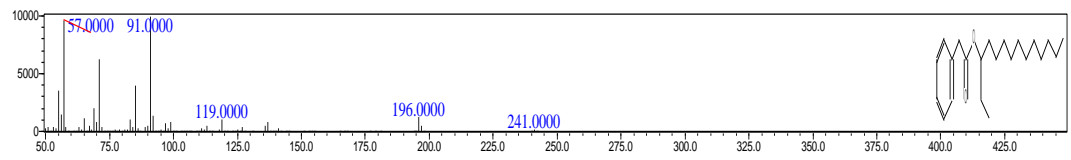
N, N-Bis (2-hydroxyethyl) dodecanamide



Bis (2-ethylhexyl) phthalate



Benzeneacetic acid, 3-tetradecyl ester

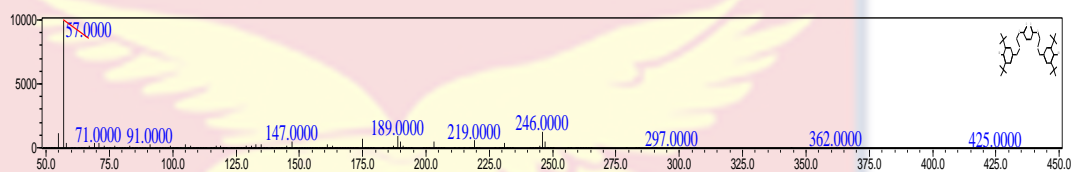


APPENDIX J

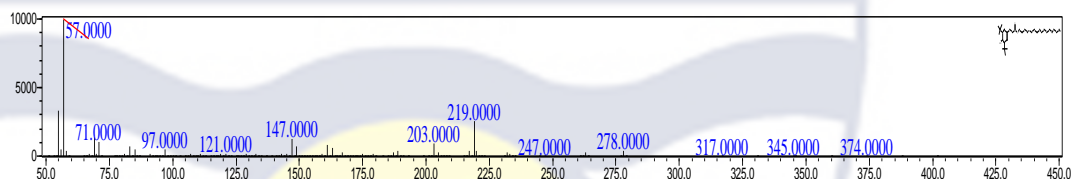
INTERMEDIATES OBTAINED FROM GC/MS FOR RAMAZOLE

BRILLIANT VIOLET 5R (RBV5R)

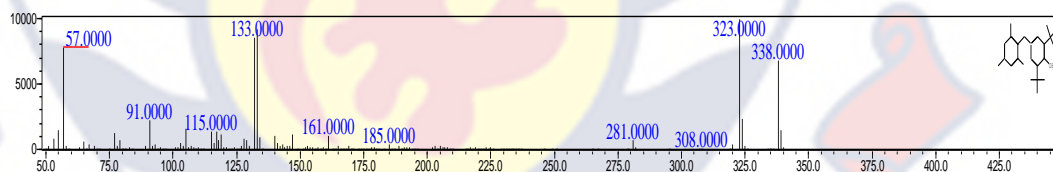
Bis [3-(3, 5-ditert-butyl-4-hydroxyphenyl) propyl] (2Z)-2-butenedioate



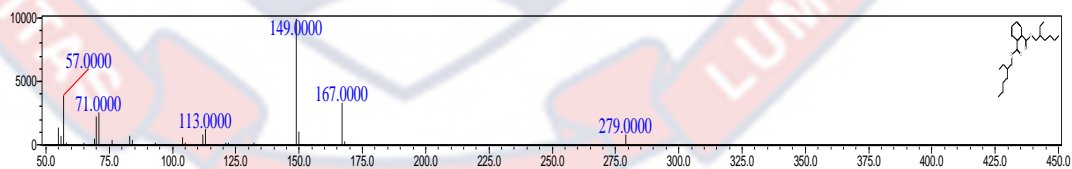
Benzenepropanoic acid, 3, 5-bis (1, 1-dimethylethyl)-4-hydroxy-, octadecyl ester



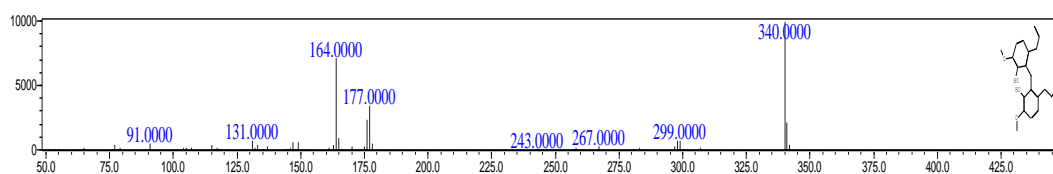
2, 6-Di-tert-butyl-4-(2, 4, 6-trimethylbenzyl) phenol



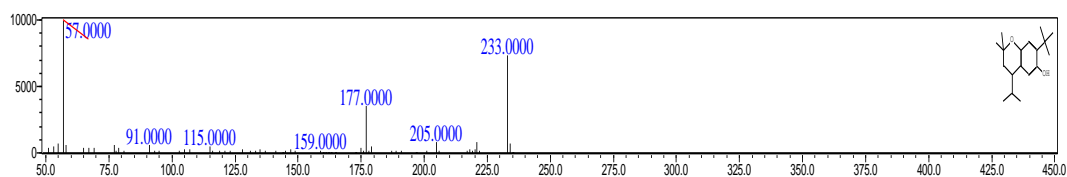
1, 2-Benzenedicarboxylic acid, bis (2-ethylhexyl) ester



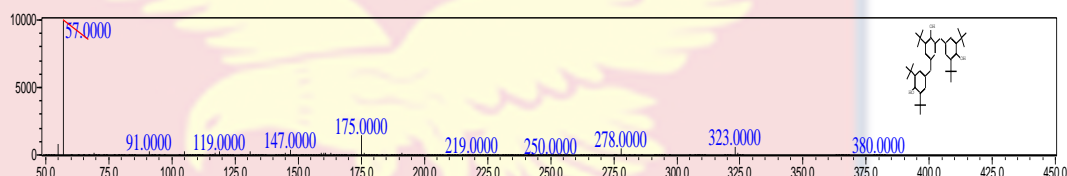
Phenol, 2, 2'-methylenebis*6-methoxy-3-(2-propenyl)



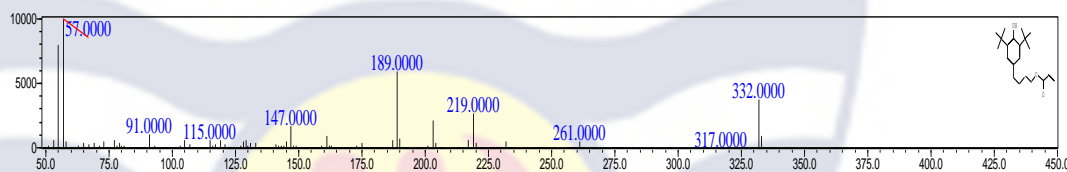
2H-1-benzopyran-6-ol, 7-(1,1-dimethylethyl)-3,4-dihydro-2,2-dimethyl-4-(1-methylethyl)



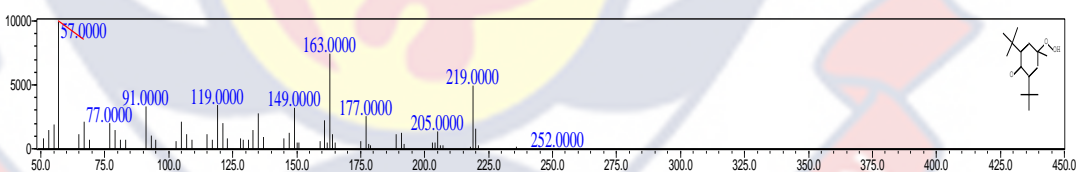
2-tert-Butyl-4, 6-bis (3, 5-di-tert-butyl-4-hydroxybenzyl) phenol



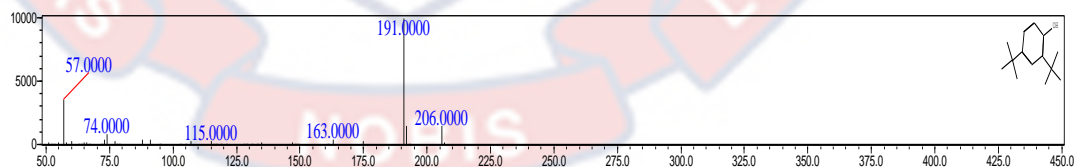
4-(3, 5-Di-tert-butyl-4-hydroxyphenyl) butyl acrylate



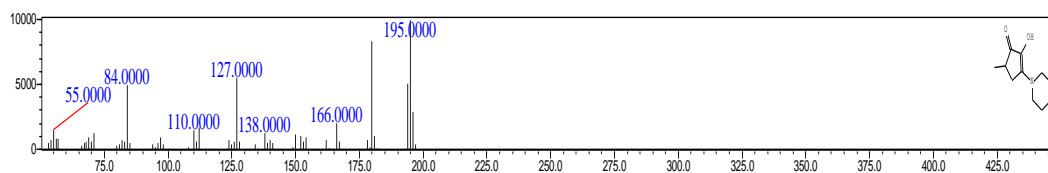
2, 5-cyclohexadien-1-one, 2, 6-bis (1, 1-dimethylethyl)-4-hydroperoxy-4-methyl



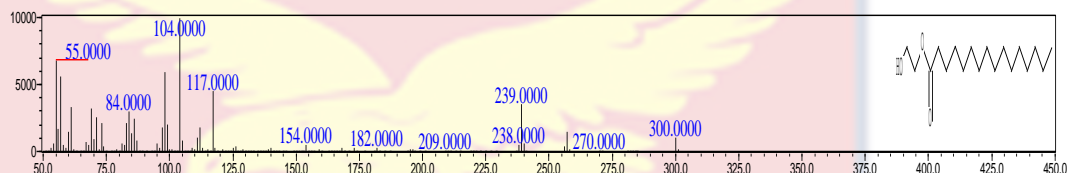
1-Hydroxy-2, 4-di-tert-butylbenzene



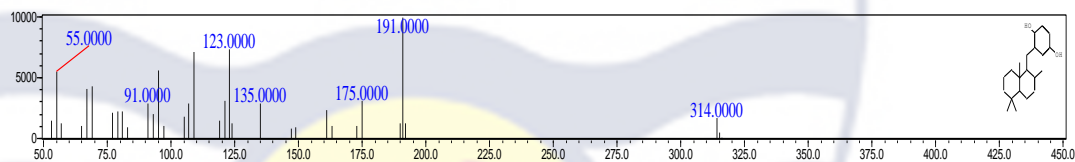
2-hydroxy-5-methyl-3-(piperidin-1-yl) cyclopent-2-en-1-one



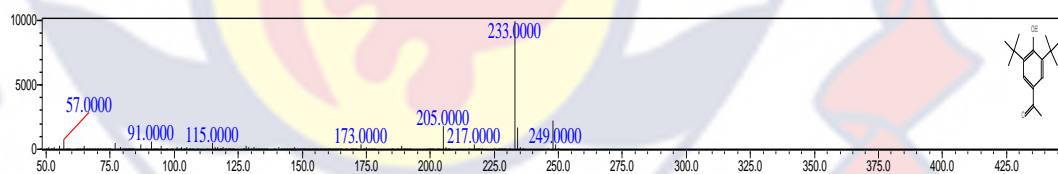
Hexadecanoic acid, 2-hydroxyethyl



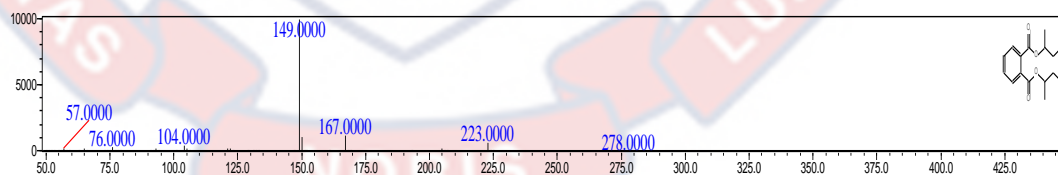
1,4-Benzenediol, 2-[(1,4,4a,5,6,7,8,8a-octahydro-2,5,5,8a-tetramethyl-1-naphthalenyl)methyl]-, [1R-(1.alpha.,4a.beta.,8a.alpha.)]



3, 5-di-tert-Butyl-4-hydroxyacetophenone \$ 1-(3,5-Ditert-butyl-4-hydroxyphenyl) ethanone



1, 2-Benzenedicarboxylic acid, di-sec-butyl ester



(1R, 2R, 8S, 8Ar)-8-hydroxy-1-(2-hydroxyethyl)-1, 2, 5, 5-tetramethyl-cis-decalin

